Adsorption and Transport in Zeolites : Molecular Simulation and Neutron Scattering Experiments

Wanda Kellouai

To cite this version:

Wanda Kellouai. Adsorption and Transport in Zeolites : Molecular Simulation and Neutron Scattering Experiments. Physics [physics]. Université Grenoble Alpes [2020-..], 2022. English. NNT : 2022GRALY082 . tel-04076253

HAL Id: tel-04076253
https://theses.hal.science/tel-04076253v1

Submitted on 20 Apr 2023

THÈSE

Pour obtenir le grade de

DOCTEUR DE L'UNIVERSITÉ GRENOBLE ALPES

École doctorale : PHYS - Physique
Spécialité : Nanophysique
Unité de recherche : Laboratoire Interdisciplinaire de Physique

Adsorption et Transport dans des Zéolithes : Simulation Moléculaire et Expériences de Diffusion Neutronique

Adsorption and Transport in Zeolites: Molecular Simulation and Neutron Scattering Experiments

Présentée par :

Wanda KELLOUAI

Direction de thèse :

Benoît COASNE DIRECTEUR DE RECHERCHE, Université Grenoble Alpes	Directeur de thèse
Patrick JUDEINSTEIN Directeur de recherche, Université Paris-Saclay GS Chimie	Co-directeur de thèse

Rapporteurs :

NATALIE MALIKOVA
Chargé de recherche HDR, CNRS DELEGATION PARIS CENTRE
LAURENT JOLY
Professeur des Universités, UNIVERSITE LYON 1 - CLAUDE BERNARD

Thèse soutenue publiquement le **8 décembre 2022**, devant le jury composé de :

NATALIE MALIKOVA Chargé de recherche HDR, CNRS DELEGATION PARIS CENTRE	Rapporteure
LAURENT JOLY Professeur des Universités, UNIVERSITE LYON 1 - CLAUDE BERNARD	Rapporteur
ISABELLE BEURROIES Professeur des Universités, AIX-MARSEILLE UNIVERSITE	Examinatrice
NOEL JAKSE Professeur des Universités, GRENOBLE INP	Président
VIRGINIE MARRY Professeur des Universités, UNIVERSITE PARIS 6 -PIERRE & MARIE CURIE	Examinatrice

Invités :

MARIE PLAZANET
Chargé de recherche HDR, CNRS DELEGATION ALPES

Abstract

Porous materials science is at the heart of processes impacting our societies with applications in energy storage/conversion, environmental protection, gas separation, etc. The separation of small molecules such as CH_4 and CO_2 - relevant for greenhouse gas reduction - remains a challenge as they interact weakly and not very specifically. In this context, nanoporous silica materials such as zeolites are promising as they are permeable materials through which gases are separated according to their size, diffusivity and concentration. However, despite a growing number of studies on these materials, the coupling mechanisms between adsorption, diffusion and transport remain poorly understood in many aspects.

This thesis aims at elucidating the fundamentals of adsorption and transport in zeolite materials using a coupled experimental and modeling approach. In this context we will focus on the behavior of methane (CH_4) in silicalite-1 zeolites by combining adsorption and neutron scattering experiments with molecular simulations such as Monte Carlo and molecular dynamics.In a first step we study the influence of pressure and temperature on methane adsorption in zeolite crystals and thin layers. A model based on the Frenkel-Halsey-Hill approximation and the Polanyi model is developed to reproduce the adsorption isotherms at different temperatures. In a second step, we study the individual diffusion of methane molecules and its dependence on the loading and on the temperature. We show that a free volume theory reproduces the diffusive behavior including its anisotropic components in the different crystal directions. Finally, in a third step, we study the collective diffusion and the flux of methane in the zeolite on different time and space scales. Collective diffusion coefficients are calculated as a function of the loading. We use the De Gennes narrowing model - which relates the confined methane structure factor to the collective diffusion coefficient - to successfully describe our results.

In conclusion, the analysis of our results allows to propose models to explain and predict the behavior of fluids in a zeolite and in particular the coupling between structural, thermodynamic and dynamic aspects. This subject at the interface between physics and physical chemistry is a fundamental research but has a strong applicative potential. Based on an approach combining experiment and theory, this subject bring a deep molecular understanding of these systems which could allow to optimize their design and use.

Résumé

La science des matériaux poreux est au cœur de procédés impactant nos sociétés avec des applications en stockage/conversion d'énergie, protection de l'environnement, séparation des gaz, etc. La séparation de petites molécules comme CH_4 et CO_2 – pertinente pour la réduction des gaz à effet de serre – reste un défi car elles interagissent faiblement et peu spécifiquement. Dans ce contexte, les matériaux nanoporeux de silice tels que les zéolithes sont prometteurs car ce sont des matériaux perméables au travers desquels les gaz sont séparés selon leur taille, diffusivité et concentration. Pourtant, malgré un nombre croissant d'études sur ces matériaux, les mécanismes de couplage entre adsorption, diffusion et transport restent mal compris par de nombreux aspects.

Cette thèse vise à élucider les éléments fondamentaux de l'adsorption et du transport dans des matériaux zéolithiques en utilisant une approche couplant expériences et modélisations. Dans ce contexte nous nous intéresserons au comportement du méthane (CH_4) dans des zéolithes de type silicalite-1 en associant des expériences d'adsorption et de diffusion neutronique à des simulations moléculaires de type Monte Carlo et dynamique moléculaire. Dans un premier temps nous étudions l'influence de la pression et de la température sur l'adsorption du méthane dans des cristaux de zéolithes et des films minces. Un modèle se basant sur les approximations de Frenkel-Halsey-Hill ainsi que sur le modèle de Polanyi est développé afin de reproduire les isothermes d'adsorption à différentes températures. Dans un second temps nous étudions la diffusion individuelle des molécules de méthane et sa dépendance en fonction du taux de remplissage de la zéolithe ainsi que de la température. Nous montrons qu'une théorie de volume libre reproduit le comportement diffusif y compris dans ses composantes anisotropes dans les différentes directions cristallines. Enfin dans un troisième temps, nous étudions la diffusion collective et le flux de méthane dans la zéolithe sur différentes échelles de temps et d'espace. Les coefficients de diffusion collectifs sont calculés en fonction du taux de remplissage des zéolithes. Nous utilisons le modèle du rétrécissement de De Gennes – qui relie le facteur de structure du méthane confiné au coefficient de diffusion collectif – pour décrire nos résultats avec succès.

En conclusion, l'analyse de nos résultats permet de proposer des modèles pour expliquer et prédire le comportement de fluides dans une zéolithe et notamment le couplage entre les aspects structuraux, thermodynamiques et dynamiques. Ce sujet à l'interface entre physique et physico-chimie relève de la recherche fondamentale mais présente un fort potentiel applicatif. En reposant sur une approche alliant expérience et théorie, ce sujet apporte une compréhension moléculaire approfondie sur ces systèmes qui pourrait permettre d'optimiser leur conception et leur utilisation.

Acknowledgement

When you start a PHD, you never know how will be the person that you are going to be at the end. My three years of PHD were a whole life full of encounters, doubts and joy, fights, failures and victories. I can't acknowledge all the people that I met and who has contributed to make the person that I am today. But there are people that I can't forget.

Thanks Benoit for your supervision during these three years. This scientific adventure, we have done it together, and our discussions, our thoughts and all the knowledge that you shared with me helped me to become the scientist that I actually am – for the good and the bad! But being a supervisor is not only about science and I thank you for your wise and well-balanced supervision. Thanks Patrick for the help during this thesis. For sharing with me your sharp sense of experiments. Thanks also for having corrected my manuscript; it was a long and hard period and we did pretty well! Marie, even if you were not in the official direction of my thesis, you took on your time and energy to guide me through neutrons experiments and analysis. Even if sometimes fitting some curves seemed to be the end of the world, it was a really nice part of my thesis and I really enjoyed working with you.

I also would like to thank my colleagues and friends – specially the non-permanents – working at the LIPhy during my thesis who have made my time here really nice and full of distractions. Thanks to my officemates and friends from the team: Raja, Nikolas, Alan for your nice company, you become a friend and I am looking forward to see you again, Vishnu for all the talks, the breaks and your patience when I was grumpy. Antrea, Laila, Cecile, Saranath, Caroline, Camille, Markus, Dandara, Edouardo thanks for all the really nice time, the out of LIPhy activities and talks – the day to day life through the smoking breaks, lunches together which gave me the will to get up every morning and come to the lab. Lieve Maaike, thanks for all of this and for all the smiles and the energy that you brought me through the many facets of our relationship.

Merci à tous-tes les camarades rencontré-es dans les luttes et mouvements sociaux, de la fac et d'ailleurs. Ces trois ans de thèse, c'est aussi un engagement militant, des rencontres et des batailles pour faire respecter nos droits qui ont aussi changé ma vision de la recherche.

Cette thèse c'est aussi un travail collectif mené avec tout mes proches qui m'ont permis de garder la tête hors de l'eau. Merci à mes ami-es, particulièrement Ulysse, Cyprien, Chloé, Perrine, Hippolyte et Livia pour m'avoir distraite de la thèse. Vous m'avez apporté beaucoup d'énergie bien que peu de sommeil. Je voudrais particulièrement remercier mes trois colocataires de thèse : Ulysse pour tes talents en recettes de tartes et en informatique, Hippolyte pour m'avoir patiemment écouté me plaindre pendant cette fin de thèse, Livia pour tous ces bons conseils sur l'arrangement des placards qui m'ont fait gagner un temps précieux le matin.

Merci à ma famille pour m'avoir toujours soutenue. Si je suis là aujourd'hui, c'est grâce à vous.

Enfin, je voudrais remercier la personne qui a été à mes côtés pendant ces trois ans. Ces quelques phrases me paraissent bien maigres au regard de tout ce que tu m'as aidé à traverser. Merci Oriane pour tout ton soutien et ton affection.

Contents

Introduction

In its last report, the IPCC ("Intergovernmental Panel on Climate Change") warned on the inefficiencies of the policies in place to mitigate global warming and climate change. Without any drastic change in these public policies, experts from IPCC predict an increase of Earth's temperature by 1.5°C by the end of this century with catastrophic consequences for humans and ecosystems. The IPCC report also highlights industrial processes as one of the main sources of greenhouse production. As an example, distillation processes, which are widely used to separate chemical compounds, are an important part of industrial energy consumption. Typically, in the United States, between 45% and 55% of the industrial energy is consumed on separation processes (data from 2015 reported in [1]). Among these processes, distillation corresponds to the half - in term of the energy consumption. For example, in oil and gas companies, most refineries use distillation to separate hydrocarbons from crude oil. This process involves 230 GW per day, which is the United Kingdom consumption for a year [2].
In order to reduce the impact of energy-consuming chemical separation processes, solutions have been proposed to separate chemical components and, more generally, to reduce the associated energy consumption in industrial processes. A known efficient alternative to distillation consists of using nanoporous materials to separate hydrocarbons according to their molecular size. As a result, nanoporous materials and membranes receive increasing attention as the broad class of available materials allow tuning and adjusting the permeability to gas and separation properties. However, even if many of such materials are already used in industrial applications, extension of their use to a large spectrum of separation processes requires a better knowledge of the basic mechanisms at play within these materials. Indeed, optimizing separation processes within such nanoconfined environments requires to unravel how fluid molecules behave inside their complex nanoporosity - which includes deciphering the dependence on pressure, temperature, etc. of fluid adsorption and transport in nanoporous solids. Beyond the issue of process optimizing, this work is part of fundamental research which should bring - we believe - its own contributions to public knowledge as it draws a picture of possibilities and solutions that are available for facing social and environmental challenges.

In this framework, my thesis work is aimed at investigating gas adsorption and transport mechanisms in a well-known, prototypical nanoporous material: zeolites. In general, porous media have a strong permeability to gas with a porosity consisting of voids present in a solid matrix. These solids possess a large internal surface where guest fluid molecules interact with the host matrix. These molecular interactions are strongly dependent on the chemical properties of both the solid surface and the guest molecules. These interactions are responsible for adsorption mechanisms as they stabilize guest molecules that accumulate at the solid surface inside the porosity. From a transport point of view, due to thermal motion, these molecules are constantly in motion so that jump between adsorption sites, molecule collisions and energy exchanges with other molecules, etc occur. Diffusion and transport mechanisms describe the individual and collective motions of these molecules as a result of these events through which molecules explore their environment. In the case of nanoporous materials, this environment is strongly confined as the pore dimension is of the order of 1 to 100 molecular sizes (according to IUPAC, nanopores refer to pores between 1 and 100 nm). Such confinement strongly impacts the thermodynamics and dynamics of fluid molecules.

Early discoveries of nanoporous materials are quite old as zeolites were described by Alex Cronstedt in 1756. If a large variety of porous materials exists naturally, progress in synthesis methods in chemistry have allowed scientists to manufacture nanoporous materials with an almost infinite variety of chemical compositions, porous volume and shape. In turn, this versatility allows covering a very broad range of properties and applications. The knowledge gain in this field has led to classify nanoporous materials according to their chemical composition and pore size. In parallel to the discovery and synthesis of nanoporous solids, adsorption phenomena in pores started to be observed at the end of the XVIIIth century – with the first measurement of adsorption on charcoals and clays. Nowadays, adsorption is routinely used as a characterization method which allows one to assess key material properties such as their porous volume, specific surface area, pore size, etc. Significant work has been devoted to this subject and adsorption isotherms are standard data to classify porous materials according to their pore size and porous architecture [3]. As far as dynamical properties are concerned, theoretical frameworks describing diffusion and transport were first developed by Fick and Stokes in the XIXth century. These pioneer scientists brought new concepts and tools to understand matter diffusion which, in turn, opened new areas in research. Later, in the XXth century, new formalisms such as Onsager's theory were developed to link thermodynamic and dynamic properties through the same framework – including the case of transport in porous media.

The large body of experimental and theoretical studies dedicated to adsorption and diffusion in nanoporous materials has been already reviewed [4, 5]. However, the coupling mechanisms between adsorption, diffusion and transport within nanoporous materials remains poorly understood. In particular, only few studies have reported consistent models to predict the behavior of fluids in these solids. Within this context, the present thesis focuses on the three following aspects:

- The individual trajectory of molecules - known as self diffusivity or tracer diffusivity - is dependent on the loading as steric repulsion between molecules combine with thermodynamic and geometric effects within the confining material. In such particular environments, the loading dependence of the diffusion coefficient remains to be fully rationalized. Such an aspect challenges existing models such as the Reed-Ehrlich model [6] - also known as surface diffusion model - which does not fully predict all diffusivities observed experimentally.

- The collective diffusivity of molecules in such nanoconfined environments depends on the length and time scales considered experimentally. This dependence has been already related to the microscopic/mesoscopic structure of the geometry of the confining solid with strong correlations between dynamic and structural properties [7, 8]. Moreover, in contrast to self diffusivity, a simple consistent theoretical picture of the collective transport of fluids in very narrow, anisotropic geometries is still missing.

- Most nanoporous materials present external surfaces (i.e. interfaces between the host solid and its external environment) where adsorption, diffusion and transport mechanisms remain poorly understood. The impact of such external surfaces is already documented with striking examples in adsorption uptakes measurements [9, 10] as well as in separation/chromatography where it plays a key role in the balance between intra-particle diffusion and hydraulic transport [11, 12]. However, very practical questions remain unanswered such as the influence on gas adsorption/transport coupling of the surface geometry (orientation, flexibility, etc.). Moreover, a unified formalism to model in a consistent fashion adsorption, diffusion and transport in the zeolite core and at its external surface is lacking.

The aim of the present manuscript is to elucidate the fundamental mechanisms driving adsorption and transport in zeolite materials using a coupled experimental and modeling approach. In this context, we will focus on the behavior of a simple gas - methane (CH_4) - in a pure silica zeolite by combining adsorption volumetry and neutron scattering (QENS) experiments with molecular simulations (Monte Carlo, molecular dynamics). Silicalite-1, the form of zeolite that will be considered throughout this document, possesses a strong anisotropic structure with different pore geometries. The manuscript is organized as follows.

- The first chapter provides a short summary of the basic concepts involved in this work. We present the main characteristics of porous materials and some application examples in which porous materials are involved. We also introduce the fundamentals of adsorption, diffusion and transport with the underlying theoretical frameworks which are at the heart of this study.

- The second chapter presents the principles of the experimental and numerical methods used in this thesis. We introduce the basics of the molecular simulation techniques employed in this work (Monte Carlo and Molecular Dynamics). For the experimental part, we describe the volumetric adsorption technique and also present general principles of neutron scattering.

- The third chapter is dedicated to the study of methane adsorption in zeolite crystals and zeolite layers. As a first step, experimental and simulation results allow us to probe the influence of pressure and temperature on adsorption isotherms. In a second step, a model based on the Frenkel-Halsey-Hill approximation and Polanyi's adsorption potential theory is developed and applied to both zeolite crystals and external surfaces as present in zeolite layers.

- The fourth chapter focuses on the dynamical properties of methane molecules confined with the zeolite nanoporosity. We illustrate that neutron scattering experiments combined with molecular simulations provide valuable information on the pressure and temperature dependence of the self diffusion coefficients within such extremely confined environments. We compare these two approaches to study the effect of the anisotropic porous geometry. Finally, a simple free volume theory is applied to the simulation data in order to rationalize the self diffusion behavior of the guest molecules.

- The fifth chapter is dedicated to the collective and transport diffusivities inside the zeolite porous network. In a first part, macroscopic collective diffusion coefficients - at vanishing wave vectors – are calculated as a function of the methane loading inside the zeolite. In a second part, we use the concept of De Gennes narrowing - which relates the structure factor of confined methane to its collective diffusivity – to describe the transport of methane. We also present the preliminary analysis of an original neutron scattering experiment performed to probe collective diffusion in zeolites.

We wish to mention that a significant part of Chapter 3 in this manuscript is taken from our published article "*Gas Adsorption in Zeolite and Thin Zeolite Layers: Molecular Simulation, Experiment and Adsorption Potential Theory*" published in Langmuir in 2022 [13].

1 General overview

This chapter presents fundamental concepts for understanding adsorption and transport of gas in porous materials. In a first part, we will introduce the main properties that characterize porous materials and also some examples of applications in which porous materials are involved. We will describe more specifically zeolites and its Silicalite-1 structure which is going to be used in this work. In a second time, we will present the fundamentals of adsorption and some physical models currently used to rationalize and predict adsorption isotherms. In a last part, we will introduce fundamentals of diffusion and transport through the definition of diffusion coefficients. We will also present more specifically the different transport regimes observed in porous media and a short literature review on diffusion and transport in zeolites.

1.1 Porous materials

Porous solids are common compounds in nature which have led to extensive research since the middle of the 20^{th} century. They encompass a large spectrum of structures with different chemical compositions leading to interesting properties for many industrial applications [3, 14, 15, 16]. Among them, we can cite catalysis, gas separation, gas storage, etc. Zeolites constitute a specific type of porous materials; they are aluminosilicates as they are made up of SiO_4 tetrahedra in which some of the Si atoms can be substituted by an Al atom. Used in industry for many years [17, 18, 19], they are a key element in various area such as oil industry for refining or for xylene separation (plastic precursors) [20]. In the first section, we introduce some definitions and concepts about porous materials and their applications. After some generalities, we focus on the specific case of zeolites since they are at the heart of this thesis. Then, we will briefly introduce the Mobil FIve (MFI) structure which corresponds to the specific zeolite structure considered in this thesis.

1.1.1 Definitions

Porous materials are like Gruyere cheese. They are made up of a solid skeleton which coexists with empty cavities – the so-called “pores”. These pores can be of different sizes, typically from the molecular scale ($\sim$ nm) to the macroscopic scale ($\sim$ mm). They can be of different shapes, from a regular geometry (spherical, cylindrical, etc.) to more complex geometries with distorted pore shapes. Moreover, they can be connected to each other to form a porous network or isolated from each other. In porous materials with an “open” porosity, the pore network is accessible from the external environment of the material. In contrast, in a porous material with a “closed” or “occluded” porosity, the pore network is not accessible from the external environment of the material [21]. A schematic representation of porous materials and their internal surface is shown in Figure 1.1(a).

The intrinsic properties of a given porous material depend on the morphology and topology of its porous framework but also on the chemical composition of its solid skeleton. The morphology refers to the geometry of the pores while the topology refers to the way the pores are connected together in the porous network (independent versus connected pores, number of connections per pore, etc.). The following paragraphs present the main basic concepts that allow characterizing porous materials such as the porosity ϕ, the porous volume V_p, the pore size D_p, the internal specific surface S_p. We also present other key elements that are relevant to the pore morphology and topology.

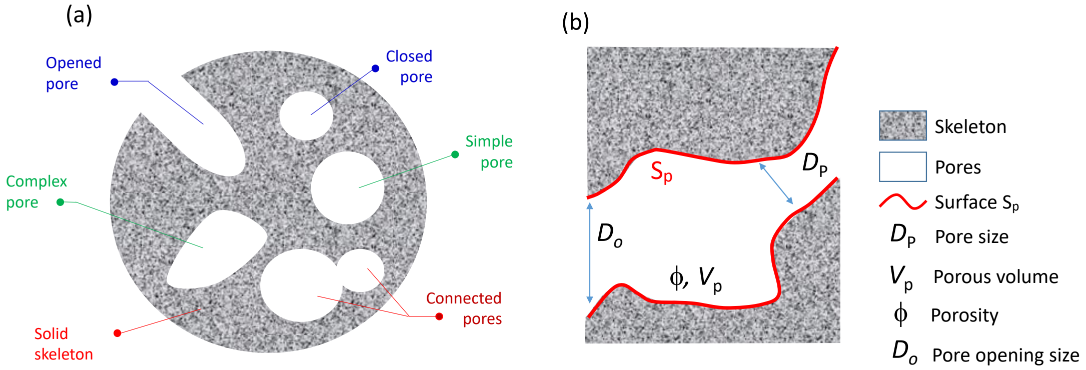

Figure 1.1: (a) Schematic representation of a porous material. Pores can be of different shapes, from a simple spherical/cylindrical geometry to a complex geometry with a distorted pore shape. Pores can be connected to form a porous network or isolated from each other. If a pore is not accessible from the external environment of the material, it is said to be "closed". Otherwise, it is said to be "open". (b) Representation of different porous material properties. The porous volume V_p is defined as the pore volume accessible to a fluid that would be set in contact with the material. The porosity ϕ corresponds to the ratio between the porous volume and the total volume V (i.e porous volume V_p + solid skeleton volume V_s). The internal surface S_p is defined as the surface of the pore walls. The pore size D_p and the pore opening size D_o are important parameters to determine whether or not the pore is accessible to a given molecule.

Porosity ϕ and porous volume V_p. The porosity ϕ is an important property of porous materials because it scales with the amount of fluid that can be contained inside the material. It is defined as the ratio between the pore volume V_p and the total volume V in the material (with the total volume V defined as the sum of the pore volume V_p and the solid skeleton volume V_s):

$$\phi = \frac{V_p}{V} = \frac{V_p}{V_p + V_s} \tag{1.1}$$

V_p is the pore volume accessible to the fluid while V is the total volume of the material as shown in Figure 1.1(b). The pore volume, skeleton volume and total volume are specific properties, which means that these quantities are expressed in m^3/g. Typically, zeolite materials have a porous volume V_p comprised between 0.1 and 0.35 10^{-6} m^3 per gram of material [22]. As will be discussed later in this section, such large porous volumes confer some interesting storage properties to this class of materials.

Pore size D_p. The pore size D_p is another important parameter that characterizes porous materials. According to IUPAC (International Union of Pure and Applied Chemistry) [23], porous materials can be subdivided into three categories [24, 21] illustrated with practical examples in Figure 1.2:

Microporous solids with $D_p \leq 2$ nm
Mesoporous solids with $2nm < D_p \leq 50$ nm
Macroporous solids with $D_p > 50$ nm

Nanoporous materials, which are defined as solids with pores having dimensions in the nanometric range – typically between 1 and 100 nm – encompass both microporous and mesoporous materials as exemplified in Figure 1.2 (a) and (b).

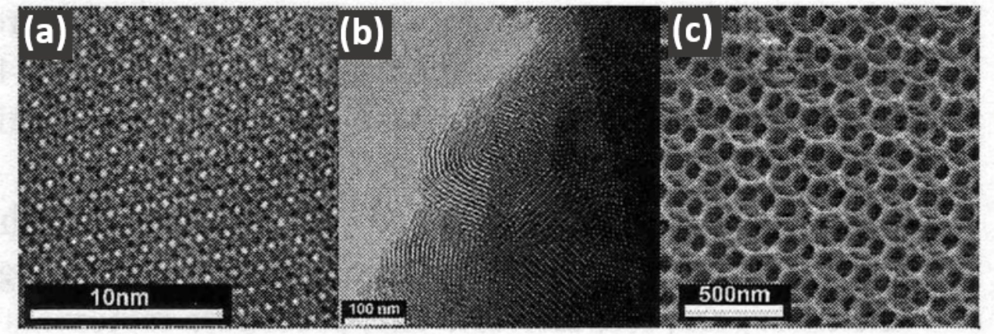

Figure 1.2: Typical porous materials as observed using electronic microscopy: (a) microporous material consisting of zeolite Y, (b) mesoporous material and (c) macroporous material [25]. [Adapted from Ref [25].]

Internal specific surface S_p. Porosity leads to another important feature of porous materials: a large internal specific surface S_p. The specific surface is defined as the ratio of the actual surface (including both the internal and external surfaces) normalized to the sample mass (S_p is in m^2/g). Zeolites possess an internal specific surface varying between 300 and 700 m^2/g [22]. For Metal Organic Frameworks (MOF), this surface is often comprised between 1000 and 2000 m^2/g but it can reach 7000 m^2/g [26, 27] (almost the surface of a football field!).

The concept of large internal surfaces can be pictured using a sheet of paper curled up to form a paper ball. The ball holds in your hand but the sheet exceeds the size of your hand when unfolded. Typically, the material surface is proportional to the inverse of the pore size: $S_p \sim 1/\ D_p$. Thus, $D_p \sim 1$ nm yields typical specific surfaces between 100 and 1000 m^2/g! Molecules adsorbed at the zeolite surface go inside the pores and stick to the surface because of molecular interactions between gas molecules and the host porous material. This property is very important: a large internal surface allows capturing many molecules. At the microscopic scale, the interactions that drive such adsorption phenomena between the guest molecules and the atoms of the porous material are dispersion interactions, dipolar interactions, etc. The generic term interactions responsible for adsorption are discussed in the next section.

Topology. Pores can be connected in different ways. Some simple network notions allow classifying porous materials: connectivity and tortuosity. The connectivity can be defined as the average number of connections between pores. Typical displacements within the porous network increases with connectivity. The tortuosity τ corresponds to the ratio between the physical length travelled by molecules, L, and the geometrical distance between the start/end points of their displacement, L_0 [28].

$$\tau = \frac{L}{L_0} \tag{1.2}$$

However, this definition is often difficult to probe/assess. On the other hand, another definition relevant to the physics of diffusion/transport can be used for the tortuosity τ. The tortuosity can be defined as the ratio of the bulk and confined diffusivities (D_s^0 and D_s, respectively).

$$\tau = \frac{D_s^0}{D_s} \tag{1.3}$$

where D_s is the self diffusion coefficient of the fluid inside the porous material while D_s^0 is the self diffusion coefficient of the fluid in the bulk phase taken under the same thermodynamic conditions. The two definitions are not compatibles as the first one do not consider the proportion of molecules which take the length path L considered. In the other hand, we can notice that the second definition consider the tortuosity dependent of the number of molecules. In general, $\tau > 1$ as fluid diffusion in the pores is hindered by confinement and surface interactions lead to reduced diffusivities. Some exceptions exists when one consider slipping surfaces in confined media.

The porous network in a given porous solid is organized more or less regularly. Porous materials can be divided into three categories according to the morphology and topology of their porous network as illustrated in Figure 1.4:

- Porous materials with a crystalline network (i.e. where the solid atoms are located periodically in space on a Bravais lattice). This includes materials such as zeolites, clays and MOFs as shown in Figure 1.4 (c) and (d)).
- Porous materials with regular networks (but no underlying crystalline atomic structure) such as MCM-41 (Mobil Composition of Matter) which are ordered mesoporous silica.
- Porous materials with a disordered porous structure (i.e. with irregular pore shapes and pore sizes). This includes active carbons which have an amorphous structure obtained after a pyrolysis step at high temperature and an activation step of organic matter (Figure 1.4 (b)).

1.1.2 Properties and Applications

The nanometric scale of the pore size in nanoporous materials is an important property as this characteristic lengthscale is of the same order of magnitude as the range of microscopic interactions in molecular liquids. As a result, the guest molecules properties, when confined in the porosity, are very different from those for non-confined molecules. Some interesting effects can be highlighted:

- Capillary condensation: gases liquefy inside the pores at a capillary pressure P_c which depends on pore size D_p. The smaller the pore size, the lower the pressure needed to liquefy the gas. This can be described using the Kelvin equation which states that the chemical potential corresponding to capillary condensation is proportional to surface tension and inverse proportional to the pore size:

$$RT \ln\left(\frac{P_c}{P_0}\right) \sim \frac{\gamma}{D_p} \tag{1.4}$$

where P_0 is the saturating vapor pressure and γ the liquid/gas surface tension.

- Another thermodynamic effect is the shift of the melting temperature T_f of water in porous materials depending on their pore size D_p. This effect is described by Gibbs-Thomson equation [29]. Such melting point shift is the topic of intense research as it is involved in cement degradation upon thawing/unthawing cycles [30].

As discussed above, porous materials possess a large internal surface that is the host of interactions and, in some cases, reactions between the guest molecules and the host structure (Figure 1.3 (a)). Many applications rely on these combined properties:

- Large internal surfaces that yield significant interactions between the host structure and the fluid
- Broad variability in terms of interaction type which depends on the fluid/solid couple (dipole-dipole interactions, hydrogen bonding, Van der Waals interactions, etc.)

There are many applications that rely on the remarkable properties of nanoporous materials. In practice, we will only discuss three important examples here: catalysis, gas storage, and fluid separation. The characteristics of the porous material (pore size D_p, etc.) are very important parameters in these applications. They can be obtained by synthesising specific porous materials according to required specifications [31, 32].

Catalysis. Catalysis is an important application where nanoporous materials are involved [33]. It is the most important economical activity of zeolites where these materials are used. Catalysis often relies on the acid properties of the porous structure. The large variety of zeolites in term of chemical nature, location of acid sites, density and thus selectivity make them very interesting candidates for numerous catalytic applications [34]. Nowdays, by tunning their porous topology and composition, they can reach very high performances in many processes [35]. An important example is the Y-type zeolite used in catalytic process for the oil refinery industry [36]. It is typically used for the so-called fluid catalytic craking or hydro-craking where long hydrocarbon chains are broken into smaller chains (for example to produce gasoline).

Gas capture and storage. As already explained, the large internal surface in nanoporous materials are at the heart of some important adsorption properties. Indeed, the strength of molecular interactions between the host and guest atoms vary according to their chemical nature. Adsorption can be selective or not (Figure 1.3(b)). While adsorption concepts will be explained later in this overview chapter, we provide some practical examples here. Storage of CO_2 in coal mines is an important economical and environmental application. To mitigate the amount of CO_2 released in the atmosphere, a practical solution consists of capturing CO_2 in coal mines thanks to Van der Waals interactions between this greenhouse gas molecule and the host carbon structure [37]. The CO_2 sequestrated in abandoned coal mines is then monitored to avoid CO_2 leaks through the atmosphere.

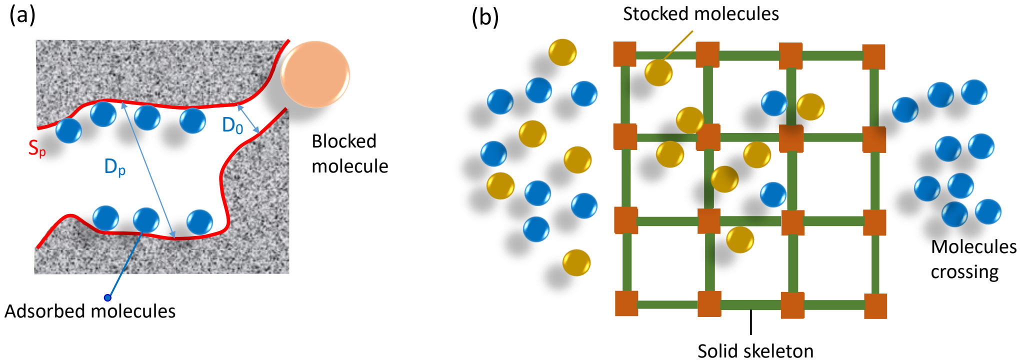

Figure 1.3: (a) Adsorption at the pore scale and confinement effects. Molecules in blue are adsorbed inside the pore and stick to the wall due to molecular interactions with the host pore surface. Owing to the large internal surface S_p, a large amount of molecules can be stored inside the pores. The molecular size of the orange molecule is larger than the pore opening size D_o: it is blocked and therefore cannot be adsorbed. (b) Selective adsorption. The interaction strength between the zeolite framework and the guest fluid varies with the nature of the guest fluid molecules. The adsorption can be selective which leads to the adsorption of different amounts of molecules according to their nature (interactions are stronger with yellow molecules than with the blue molecules in the cartoon shown here). The selectivity of adsorption is used to do separation.

Microporous materials such as zeolites can also be used to store solar energy. In summer, some heat can be removed by desorbing water from the porosity of hydrophilic zeolites. In winter, zeolites adsorb water molecules as the temperature decreases and release heat towards the external environment as adsorption is exothermal [38]. There are currently significant efforts being devoted to increasing the porous volume and explore new materials for such applications. Indeed, if the porous volume increases, the number of fluid molecules that can be stored also increases.

Separation and purification. Natural gas separation is also an important economical and environmental application of nanoporous materials. To retrieve methane from natural or synthetic gas steams, the natural gas has to be purified from CO_2, water and other gases (N_2, O_2, etc.). This separation can be realized using porous materials such as zeolites or MOFs [39].
Zeolites can also be used to soften water by exchanging ions. Typically, in water softening, the zeolite material removes Ca^{2+} and Mg^{2+} ions while releasing Na^+ ions from aqueous solutions [40].
Zeolites are also used to separate and capture radioactive cations as cesium 137 for waste treatment in nuclear industry. It lies on the availability of cations to transfer between the zeolite structure and the radioactive element. After Fukushima accident, large amounts of zeolite were dropped in the ocean near the nuclear plant to adsorb cesium 137 isotopes (which have a quite long life time of 30 years) [41].

In general, porous materials can be classified according to their nature (i.e their chemical composition). They can be divided into three categories: organic (typically solids with carbonaceous structures), inorganic (compounds with inorganic atoms in their structure) and hybrid (both organic and inorganic) materials [27] (Figure 1.4).

Organic materials. This category includes materials such as polymers, carbon nanotubes and active carbons. Carbon nanotubes are made up of one or more carbon sheets rolled on itself. It provides to these materials many properties including important mechanical strength. In this family, we also find polymers of intrinsic microporosity (PIMs) which are polymers with porosity generated by the voids formed between their rigid chains. Finally, active carbons are carbonaceous materials which undergo a specific treatment to obtain an amorphous porous structure. Their large adsorption capacity is used for gas masks, air filtration, etc.

Inorganic materials. In this category, the most important sub-category is composed of porous oxides which are materials made up of titanium oxide, silica or alumina. This thesis will be devoted to the following inorganic material category: porous aluminosilicates and, more precisely, zeolites. Aluminosilicates are minerals made up of Si linked with O to form silica tetrahedra. Some Si may be replaced by Al atoms which will induce charge defects in the structure framework (these defects are compensated by the presence of extra-framework cations). The two important families of aluminosilicates are the tectosilicates and phyllosilicates. We will not further introduce zeolites here because as il will be done in the next section of this chapter.

Hybrid materials. This family, which is composed of solids made up of both organic and inorganic parts, includes materials such as Metal Organic Frameworks (MOFs). MOFs are made up of metal ions that are linked by organic molecules. These materials were discovered recently at the end of the XXth century. They are considered as promising candidates for practical applications in industry. Indeed, their large internal specific surface makes them good candidates for gas storage, transport and separation [3].

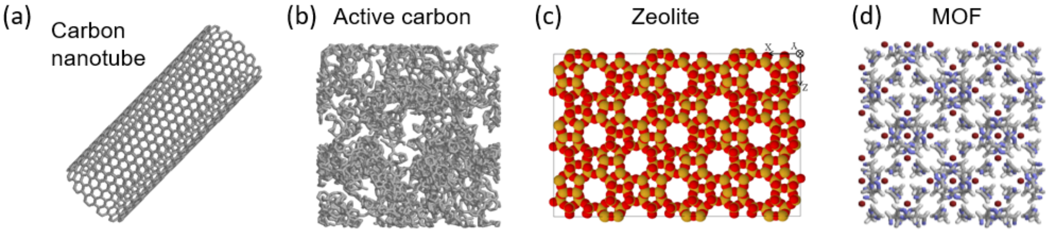

Figure 1.4: Examples of porous materials with different pore networks and belonging to different chemical categories: (a) Organic solids with regular network such as carbon nanotubes. (b) Organic solids with disordered pore network such as active carbon. (c) Inorganic solids with a crystalline network such as zeolites. (d) Hybrid solids with a crystalline network such as MOFs. [Courtesy Benoit Coasne]

1.1.3 Zeolites

History and definitions. Zeolites were discovered by Alex Cronstedt, a swedish chemist, in 1756. During his experimentation over stilbite, a natural mineral, he observed that the mineral surface seems to be “boiling” upon heating up to 150°C. Indeed, upon heating, this mineral expels the water trapped under ambient temperature in its hydrophilic porous structure. The mineral was named zeolite as it derives from the Greek zeo ("which boils") and lithos ("stone") [3]. Today, there are about 250 identified zeolite structures, including 67 natural structures. The International Zeolite Association (IZA) provides a website which lists all discoveries about zeolites [42]. The large number of industrial applications (oil industry, catalysis, etc.) have boosted significant research efforts to create new zeolite structures such as zeolite films [43], nanozeolites [44], hollow zeolites [45], hierarchical zeolites [46], etc. Such intense research helped to develop the field of zeolite synthesis and engineering.

Microscopic structures. Zeolites are microporous materials ($D_p \leq 2$ nm). They exhibit different pore sizes according to the specific zeolite type. They possess different connections between their pores which generate different network structures. They are aluminosilicates as they are composed of silicon and aluminium atoms. The ratio Si/Al significantly affects the properties of the structure. Zeolites possess a crystalline structure as atoms occupy positions that repeat periodically in space to form a macroscopic crystal. At the microscopic scale, zeolites are arranged in the three space dimensions as tetrahedra TO_4 (SiO_4 or AlO_4) [3]. These tetrahedra, coined as Basic Building Units (BBU) are connected by oxygens to form Secondary Building Units (SBU). The latter can arrange over 23 different forms such as square, octagon or dodecagon, etc. For this reason, there is a limited number of zeolite types even if this number is extremely large. At the mesoscopic scale, the arrangement of these bricks forms Composit Building Units (CBU) such as polyhedra, cubes, prisms, etc. They constitute the solid framework of zeolites [47]. The arrangement of different CBU allows building the elementary lattice, whose repetition according to symmetry operations generates the macroscopic crystal (Figure 1.5).

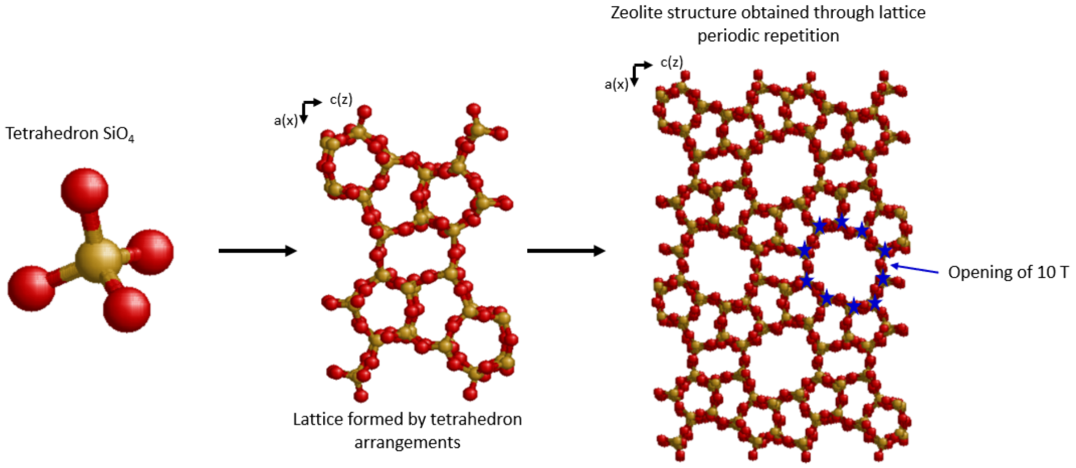

Figure 1.5: Silicon and oxygen atoms are linked to form a tetrahedron, the basic building unit in zeolite. These tetrahedra are arranged to form the lattice with its specific periodicity repetition in space forming the zeolite crystal (here, we show the silicalite-1 zeolite structure). The 10 T atoms which build the channel opening are represented by blue stars.

The microporous pore size (≤ 2 nm) in zeolites is roughly of the order of magnitude of the molecular size of many small molecules such as CO_2, CH_4, etc. For a guest molecule to enter in a zeolite pore, the pore opening has to be composed of more than 8 T atoms (which means, an arrangement of at least 8 tetrahedra) as shown in Figure 1.6. According to the atoms layout, which defines the zeolite structure type, the structure presents different pore diameters D_p and pore opening sizes D_o. They can be classified as follows [24]:

- Small pore sizes with an opening of 8 T atoms leading to a window size between 3 and 4.5 Å
- Intermediate pore sizes with an opening of 10 T atoms leading to a window size between 4.5 and 6 Å
- Large pore sizes with an opening of 12 T atoms leading to a window size between 6 and 8 A
- Extra-large pore sizes with an opening of at least 14 T atoms leading to a window size larger than 8 Å

According to their pore size, the zeolite structure is built of three pore categories:

- **Cages:** Polyhedra can arrange to form a pore with an opening smaller than 8 T atoms. Such pores only host small molecules such as water, methane and carbon dioxide. For example, the LTA zeolite possesses cages with an opening of 6 T atoms and a pore diameter of 6.1 Å (Figure 1.6(a).)
- **Cavities**: Like cages, cavities are formed by polyhedra arrangement. However, their pore opening D_o is larger than 8 T atoms so that they can host many guest molecules including large molecules such as xylene, kerosene, olefin, etc. For example, FAU zeolites possess cavities with an opening with 12 T atoms and a pore opening D_o of 7.5 Å and a pore diameter D_p of 13 Å (Figure 1.6(b).
- **Channels**: Channels are cavities but extended to infinity in one dimension. For example in MFI zeolites, right channels have an opening of 10 T atoms which corresponds to a pore opening size of 5.4 Å (Figure 1.6(c)).

Chemical nature. The chemical composition of zeolites is an important parameter, which can vary from a zeolite to another. The general chemical composition of a zeolite writes: $\mathrm{M}^{n+}_{x/n}\mathrm{Al}_x(\mathrm{SiO}_2)_{1-x}$. In this chemical formula, x the stoechiometric number of Al, $1-x$ the stoechiometric number of Si, x/n the number of cations and M^{n+} the nature of cations M with a positive charge n. The ratio between Si and Al is the ratio between the numbers of Si and Al atoms which is noted $r_{Si/Al} = (1-x)/x$. The Lowenstein rule [48] states that two Al atoms cannot be adjacent without making the structure unstable. We note that recent studies have reported in some cases a violation of the Lowenstein rule (typically under water loading conditions) [49]. The Lowenstein rule implies that $r_{Si/Al}$ varies between ∞ (pure silica material) and 1 (equal Si/Al content). When an Al atom substitutes an Si atom, a charge defect is induced because of the lower valency number for Al (+III) than for Si (+IV). This extra charge has to be compensated by cations; if there are x Al atoms, the zeolite neutrality requires x positive charges (if one cation has n positive charges, the zeolite requires x/n cations outside the skeleton). These cations can be alkaline metal ions (Na^+, Ca^{2+}), transition metal ions (Ag^+, Ni^{2+}), protons H^+, etc. These cations lead to zeolites with some important properties for catalysis, ion exchange, gas separation, etc. as explained earlier in this chapter.

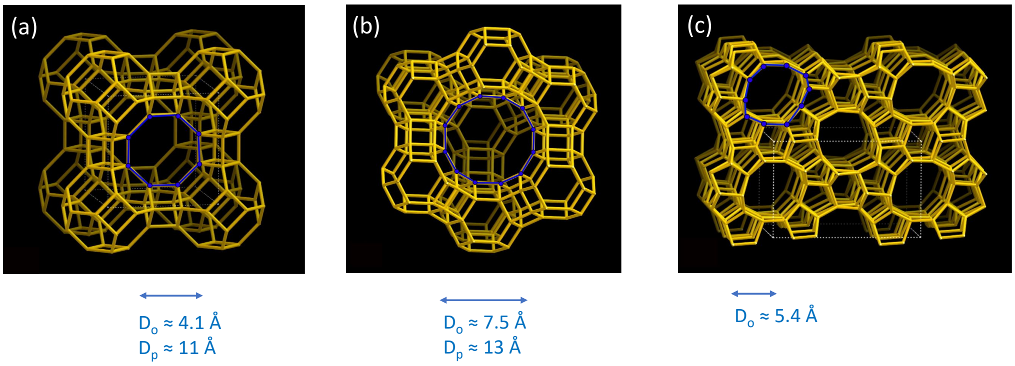

Figure 1.6: Three different zeolites with various pore diameters and pore openings [taken from Ref. [42]]: (a) LTA structure with cages, (b) FAU structure with cavities, and (c) MFI structure with channels.

1.1.4 MFI structure

Composition. As discussed in the previous section, zeolites encompass many structures which have different crystalline frameworks and porous network organizations. Faujasite (FAU), Mobile FIve (MFI), Beta Zeolite (BEA), Zeolite A (LTA), which are among the most widely used zeolites, possess their own (i.e. unique) crystalline structure with different characteristics, pore sizes, and networks. The MFI structure (Mobile FIve) was discovered in 1972 thanks to significant developments made in the field of zeolite synthesis. It is nowadays used in chemical industry and oil industry for cracking for instance [3]. This zeolite material is characterized by a strong content in silica: the ratio $r_{Si/Al}$ is very high from 12 to infinity. The MFI family can be divided into two categories. If the solid contains aluminium atoms, the zeolite belongs to the ZSM-5 (Zeolite Socony Mobil 5: Z**S**M-**FI**ve) subcategory. If the solid does not contain aluminium atoms, MFI zeolite is coined as silicalite-1 (in practice, silicalite-1 has a ratio $r_{Si/Al} > 100$).

Figure 1.7: Composite Building Units CBU involved in the formation of the MFI zeolite structure. The arrangement of these units allows building channels [42].

Structural organisation. Depending on the thermodynamic conditions (pressure, temperature, etc.), the MFI crystallizes either in the orthorhombic system ($\alpha = \beta = \gamma = 90$) or in the monoclinic system (but with an angle very close to an orthorhombic lattice). The unit cell is composed of 96 silicon and 192 oxygen. The volume of the unit cell is 5211.3 Å and the MFI density is 18.4 T/1000 Å^3 [42] which leads to a density of about 2811 kg/m^3.

The arrangement of CBU (Figure 1.7) generates a microporous structure composed of channels and small pores. There are two channel types characterizing the MFI structure: straight channels and sinusoidal (or zigzag) channels which are crossing in intersection areas (Figure 1.8). The straight channels, which are parallel to the y-axis, possess an opening of 10 tetrahedra linked between them (Figure 1.4) and a pore opening D_o comprised between 5.1 and 5.6 Å. The pores have an opening of 5 tetrahedra which can accept small molecules only such as water, CO$_2$, CH$_4$, etc.

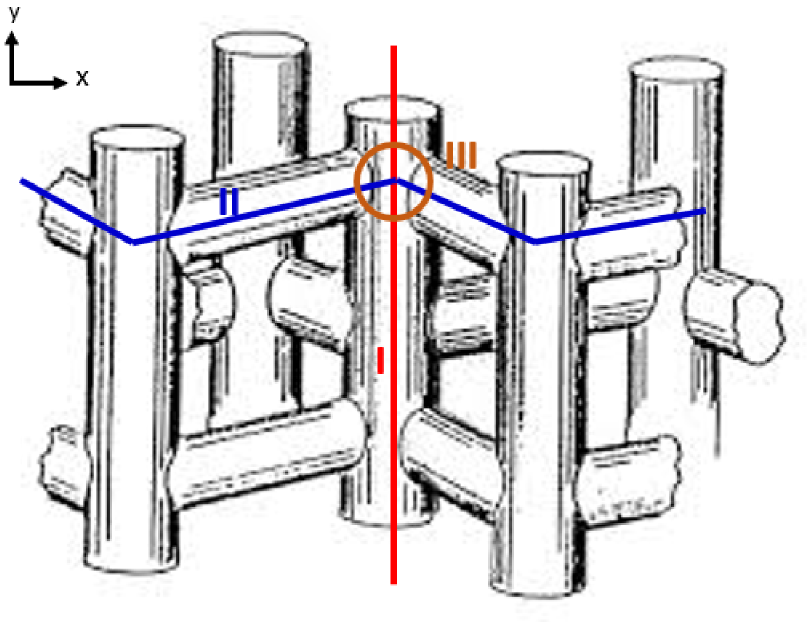

Figure 1.8: Channels and intersections in the MFI structure [adapted from Ref. [50]]: (I-red) straight channels, (II-blue) sinusoidal channels, (III-orange) intersections between straight and sinusoidal channels.

1.2 Adsorption phenomena

Adsorption is a phenomenon which has been studied since the XVIII$^{\text{th}}$ century. At the beginning, some pioneering experiments allowed the scientists to make the first discoveries on adsorption. Typically, in 1773, Scheele and Fontana observed and measured gas adsorption by charcoal and clay. Then, in 1783, Lowitz managed to bleach an acid solution by removing the organic impurities through adsorption in charcoals [51]. Important developments in physics, chemistry, and physical chemistry have led to physical models which allow to rationalize and describe adsorption. In this section, we first introduce the general principles related to the physics and chemistry of adsorption. Then, we discuss the main adsorption models together with their limitations.

1.2.1 Concepts

The adsorption phenomenon is defined by the International Union of Pure and Applied Chemistry (IUPAC) as the increase in the concentration of molecular species – the so-called adsorbate – at the interface with a solid or a liquid phase – the so-called adsorbent [23]. This molecular accumulation at interfaces is due to attractive forces that occur at the microscopic level which bind the adsorbed molecules with the adsorbent. It forms a layer whose density departs from the bulk phase counterpart as illustrated in Figure 1.9. Adsorption is involved in many processes which can involve very different adsorbent/adsorbate couples: solid/liquid, liquid/liquid, liquid/gas, solid/gas. In the framework of this thesis, we will only consider the last case even if many of our conclusions could be readily extended to other situations.

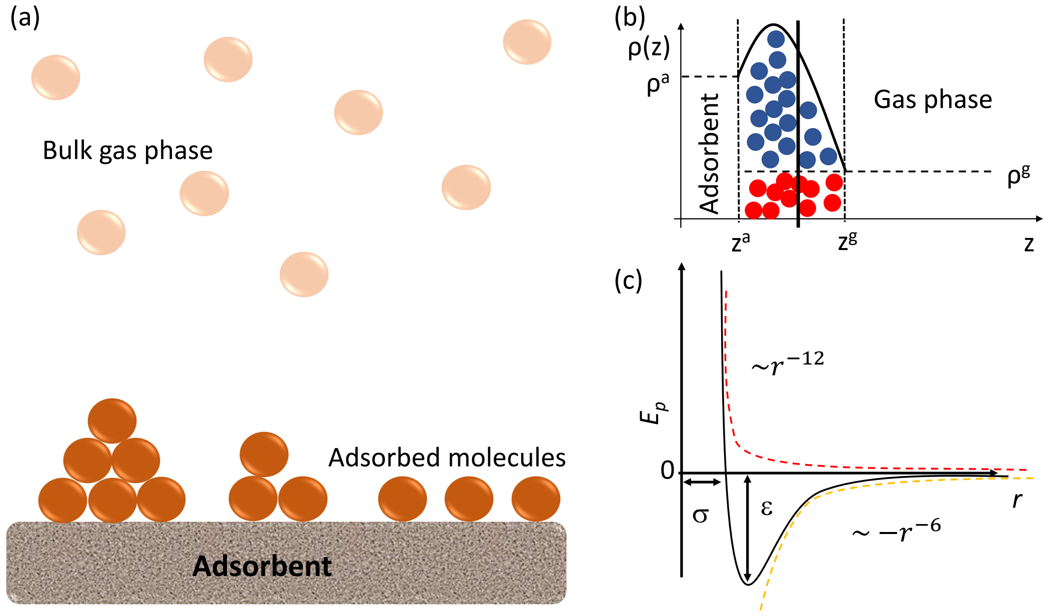

Figure 1.9: (a) Schematic representation of gas adsorption onto a solid surface (adsorbent). In this molecular description, the solid is coined as adsorbent with the fluid adsorbed at its surface forming an adsorbed layer. Far from the solid surface, the fluid molecules form the bulk gas phase as they do not experience any molecular interactions with the atoms of the solid. (b) Schematic picture of the concepts of the Gibbs dividing surface and surface excess concentration. The interface i.e. adsorbed layer is spatially located between the two vertical dashed lines; in this region, the density of the molecular species adsorbed at the solid surface departs from (1) the density within the adsorbent at the position z^a and (2) the density in the gas phase at the position z^g. The Gibbs dividing surface (GDS) can be taken anywhere within the interfacial layer. In this schematic view, it is represented by the black vertical line. The surface excess concentration n_a^{exc} (molecules shown in blue) corresponds to the number of molecules in the interfacial i.e. adsorbed layer once the concentration of the bulk phase is subtracted (molecules in red). (c) Schematic representation of Lennard-Jones potential energy E_p that would feel an molecule located at a distance r from another atom. It is the sum of the repulsive (red dashed line) and the attractive (yellow dashed line) terms.

Physisorption versus chemisorption. Depending on the energy involved in adsorption processes, we can define two adsorption types: physical adsorption (physisorption) and chemical adsorption (chemisorption) [3]. Chemisorption involves chemical bonds between the adsorbent and the adsorbate at the interface. It is characterized by large interaction energies which lead to high adsorption heats ($\sim$ 1 eV). This type of adsorption is irreversible as the energy involved is much larger than the thermal energy at room temperature. In contrast, physisorption, which will be considered throughout this thesis, involves intermolecular forces such as Van der Waals forces with corresponding interaction energies much lower than for chemical bonds. Typically, the following features apply for physisorption:

- Physisorption is exothermic so that physical adsorption is spontaneous. At constant T and P, $\Delta G < 0$ for the system made up of the bulk gas phase and the adsorbed phase). The free enthalpy can be written as $\Delta \mathrm{G} = \Delta \mathrm{H} - \mathrm{T}\Delta \mathrm{S}$ so that the adsorption enthalpy $\Delta \mathrm{H}$ must be negative (since the entropy decreases upon adsorption due to the decrease in the degree of freedom of the adsorbed molecules) [52].
- The heat of physisorption is of the order of $\sim$ 0.1 eV (few times the thermal energy $k_B T$).
- Physisorption leads to multilayer adsorption and is reversible.

Interfaces and surface excess concentrations. Considering a solid surface as shown in Figure 1.9(a), an interface can be defined as a particular zone which separates two different thermodynamic phases. We will use the term “bulk” phase to refer to the volumetric part of these two phases. They have their own thermodynamic properties which are independent from each other. In contrast, the properties of the interface depends on the properties of the two phases in contact. Gibbs was one of the first scientists to introduce a thermodynamic model for the interface by using the concept of surface excess [51]. The interfacial layer is the region of space where the density of the molecular species considered departs from those for the bulk phases [i.e. the region between the two vertical dashed lines in Figure 1.9(b)]. There is an infinite number of possibilities for the position of the Gibbs dividing surface (GDS) as it can be positioned anywhere within the interface layer. The surface excess amount n_a^{exc} is the number of molecules in the interface layer once the concentration of the bulk phase is subtracted. Mathematically, it can be expressed as: $n_a^{exc} = n_a^{tot} - \rho^g V_{int}$ where n_a^{tot} is the total number of molecules at the interface, ρ^g is the gas phase density and V_{int} the volume of the interface. In Figure 1.9(b), the surface excess amount is represented by the blue spheres while the red spheres correspond to the term $\rho^g V_{int}$. The surface excess concentration is the surface excess amount divided by the surface of the GDS. These excess quantities, which are expressed as relative quantities with respect to the same quantities for the bulk phases, depart from absolute quantities.

Intermolecular interactions and forces. Considering the system in Figure 1.9(a), we now focus on the intermolecular interactions which occur at the interface. Such interactions are responsible for the adsorption of molecules on the adsorbent surface. Their origin can be found in intermolecular forces e.g. Van der Waals interactions. In the XIX$^{\text{th}}$ century, Laplace (1806-1807) discovered the existence of intermolecular forces which apply at short distances and are stronger than gravitational forces. This discovery gave a first explanation for the cohesion of liquids as well as for condensation phenomena and adsorption of fluids into solids at surfaces. In 1814, Saussure produces a first theory of physical adsorption in which the intermolecular forces are assumed to occur at the surface of solids and modify the behavior of fluids in its vicinity. Among important contributions to such intermolecular interactions, the dispersion interactions find their origin in fluctuations of the electronic cloud around its equilibrium in atoms and molecules [53]. Such fluctuations generate non permanent electrical moments (dipolar, quadrupolar, etc.) which lead to the so-called dispersion interactions. The atoms situated at a distance r from these fluctuating electrical moments feel an attractive interaction with an energy proportional to $-r^{-6}$. On the other hand, at very short distances, this energy is counterbalanced by Pauli repulsion which decays exponentially with the distance r. In practice, for the sake of convenience, this repulsive interaction is often approximated using a scaling in r^{-12} – in fact, for mathematical reasons as this scaling is the square of the dispersion term in r^{-6}. This is the spirit of the Lennard-Jones potential which is illustrated in Figure 1.9(c):

$$V(r) = 4\epsilon\left[\left(\frac{\sigma}{r}\right)^{12} - \left(\frac{\sigma}{r}\right)^{6}\right] \tag{1.5}$$

In this equation, r is the distance between the two interacting atoms while ϵ is the potential well-depth and σ the distance at which the repulsive and attractive forces compensate each other. In the system gas/solid considered here, Lennard-Jones potential applies between particles in the gas phase and at the interface between atoms that compose the solid and gas particles.

Thermodynamics of adsorption. Simple thermodynamical ingredients allow describing the evolution of the system and its equilibrium state upon adsorption. Let us start with some basic definitions. The free enthalpy G of a system at a temperature T and pressure P can be defined from the internal energy U and entropy S of the system:

$$\mathrm{G} = \mathrm{U} + \mathrm{PV} - \mathrm{TS} \tag{1.6}$$

where V is the volume of the system. The free enthalpy is a state function which is defined at equilibrium. Considering that G is an additive function, the free enthalpy of a system is equal to the sum of the free enthalpy for each phase. In parallel, we can introduce the chemical potential μ which is defined as the internal energy variation dU of the system when the number of molecules N varies by a quantity dN:

$$\mathrm{dU} = \mathrm{TdS} - \mathrm{PdV} + \mu\mathrm{dN} \tag{1.7}$$

For a single component fluid, the free enthalpy G is also equal by definition to the chemical potential $\mathrm{G} = \mu\mathrm{N}$. Therefore, by differentiating the equation Eq. (1.6), we obtain:

$$\mathrm{dG} = \mathrm{dU} + \mathrm{PdV} + \mathrm{VdP} - \mathrm{TdS} - \mathrm{SdT} = \mathrm{VdP} - \mathrm{SdT} + \mu\mathrm{dN} \tag{1.8}$$

where the second equality is obtained by inserting Eq. (1.7) into Eq. (1.8). Comparison between this last expression and $d\mathrm{G} = \mu d\mathrm{N} + \mathrm{N}d\mu$ leads to the Gibbs-Duhem equation:

$$\mathrm{N}d\mu = \mathrm{VdP} - \mathrm{SdT} \tag{1.9}$$

At constant temperature, $d\mathrm{T} = 0$, the Gibbs-Duhem equation simplifies to:

$$\mathrm{d}\mu = \mathrm{V}_m dP \tag{1.10}$$

where V_m is the molecular volume. Integration of the Gibbs-Duhem equation between a known reference point (P_0, μ_0) and some specific conditions corresponding to a point (P, μ) leads to:

$$\mu - \mu_0 = \int_{P_0}^{P} V_m\, \mathrm{dP} \tag{1.11}$$

Upon assuming that the fluid behaves as an ideal gas, i.e. $V_m = k_\mathrm{B}T/P$, we obtain:

$$\mu = \mu_0 + k_\mathrm{B}T \ln\left(\frac{P}{P_0}\right) \tag{1.12}$$

In contrast, for an non-ideal gas, the pressure must be replaced by the fugacity f. The fugacity can be seen as an effective pressure which corresponds to the gas pressure of an ideal gas at the same chemical potential.

Using Eq. (1.8), upon transforming a system involving a single molecular species at constant temperature T and pressure P (so that the chemical potential μ is also constant), the variation in the free enthalpy G is equal to dG = μ dN. If we now consider the two fluid phases in presence (i.e. the bulk gas phase denoted 'g' and the adsorbed phase denoted 'a'), we can write $\mathrm{dG} = \mu^a \mathrm{dN}^a + \mu^g \mathrm{dN}^g$. At equilibrium, the function G is minimal so that dG = 0 so that the transfer of dN molecules from the gas phase into the adsorbed phase at constant T and P writes ($\mathrm{dN}^g = -\mathrm{dN}^a$):

$$\mathrm{dG} = -\mathrm{dN}(\mu^g - \mu^a) = 0 \tag{1.13}$$

which leads to:

$$\mu^g = \mu^a$$

Therefore, at equilibrium, the chemical potential of a given compound is the same in all coexisting phases (extension to multicomponent systems is straightforward).

Gibbs extended the thermodynamic of surfaces by associating to the interface phase excess thermodynamic variables that allow to define the free surface energy: $dG^s = -Ad\gamma - S^s dT + A\sum_i \mu_i dn_i^s$ with A the area of the surface, γ is the superficial tension (in J.m^{-2}), S^s the surface entropy, μ_i and dn_i^s the chemical potential and density of the i species respectively. Gibbs-Duhem equation for two dimension system can be established using the last equation and $dG^s = A\big(\sum_i \mu_i dn_i^s + \sum_i n_i^s d\mu_i\big)$. It is also called the Gibbs adsorption equation:

$$s^s dT + d\gamma + \sum_i n_i^s d\mu_i = 0 \tag{1.14}$$

with s^s=S^s/A. At constant temperature, we get the Gibbs adsorption isotherm. For a single component:

$$\frac{d\gamma}{d\mu} = -n^s \tag{1.15}$$

The superficial tension decreases when the chemical potential increases. The superficial tension is due to Van der Waals forces which insure a stability in the system by the cohesion of a liquid. However, at the surface, these forces are not compensated. Adsorption is the thermodynamic phenomena which allows to stabilize the surface, and decrease the superficial tension.

1.2.2 Simple physical models

The equilibrium observed when setting in contact an adsorbent and an adsorbate is characterized by the characteristic adsorption isotherm. This important quantity describes the adsorbed amount n_a as a function of pressure P (or fugacity f) at constant temperature T. At equilibrium, each point along the adsorption isotherm corresponds to a unique chemical potential μ which is the same in both the adsorbed and gas phases as explained above. Several physical models were proposed in the XX$^{\mathrm{th}}$ century to provide a general framework to rationalize adsorption. In what follows, we only focus on three important theories which are can be used to predict adsorption isotherms regardless the type of the intermolecular interactions at play [51, 54].

Langmuir model. The Langmuir model was developed in 1918 using a kinetic description of the adsorption of gas molecules onto a flat solid surface [55]. This model treats the adsorbent surface as an interface made up of a number N_a of adsorption sites. These sites, which are assumed to be energetically equivalent, can adsorb a single gas molecule as illustrated in Figure 1.10. Using the kinetic theory of gases, Langmuir expressed the adsorption v_{ads} and desorption v_{des} rates as a function of pressure P and the number of adsorption sites N_a. At equilibrium, the condition $v_{ads} = v_{des}$ allows expressing the fraction of occupied solid sites as a function of pressure P:

$$\theta = \frac{K_A P_A}{1 + K_A P_A} \tag{1.16}$$

where K_A is the adsorption coefficient which describes the competition between adsorption and desorption processes (i.e. the larger K_A, the faster the sites get occupied). In practice, K_A describes the slope of the adsorption isotherm in the low pressure range (with a maximum adsorbed amount being reached at low pressures). Historically, the Langmuir model is considered as a very important model as it opened the field of kinetic studies on adsorption. However, it is important to note that this model assumes localized adsorption restricted to monomolecular adsorption. The assumption that all sites are energetically equivalent imply that it only applies to homogeneous surfaces – a picture that departs from reality for many experimental situations. Moreover, because of the hypothesis that all sites are independent, this model fails to include lateral interactions between adsorbed molecules. While this is a reasonable approximation – to some extent – for small adsorbed amounts (low pressure range), this is known to fail at high pressures but also for complex molecules. Despite such weaknesses, the Langmuir model allows one to describe many systems in a very simple manner. In particular, this model is routinely used to describe adsorption phenomena in many practical applications (e.g. reaction kinetics at surfaces).

Brunauer, Emmett and Teller theory. Brunauer Emmet and Teller model (BET) was developed in 1938 to extend the Langmuir model to multilayer adsorption [56]. In this model, one models adsorption in the first layer (i.e. nearest layer from the surface) using the Langmuir model. Then, it is assumed that the molecules adsorbed in the first layer form adsorption sites for the second layer [and so on so that the i^{th} layer provides sites for adsorption in the $i + 1^{th}$ layer]. This model therefore allows the formation of layers beyond the first layer as illustrated in Figure 1.10(b). The BET equation that express the adsorbed volume in function of the pressure can be written:

$$\frac{1}{V\left[\left(\frac{P}{P_0}\right) - 1\right]} = \frac{1}{V_m C} + \frac{C-1}{V_m C}\frac{P}{P_0} \tag{1.17}$$

with V and V_m the volume of gas adsorbed at the pressure P and saturation pressure P_0 respectively. C is the BET constant and can be linked to the fraction of surface unoccupied $\theta_0 = \sqrt{C} - 1/(C-1)$ [3]. In addition to the approximations made using the Langmuir model, the BET model assumes that the adsorption energy beyond the first layer is equal to the heat of liquefaction (in fact, this hypothesis is not necessary but it is often assumed as it makes the application of the model easier). While this is a reasonable approximation far from the solid surface, it becomes questionable close to the surface as interactions with the adsorbent surface cannot be neglected. Moreover, like for the

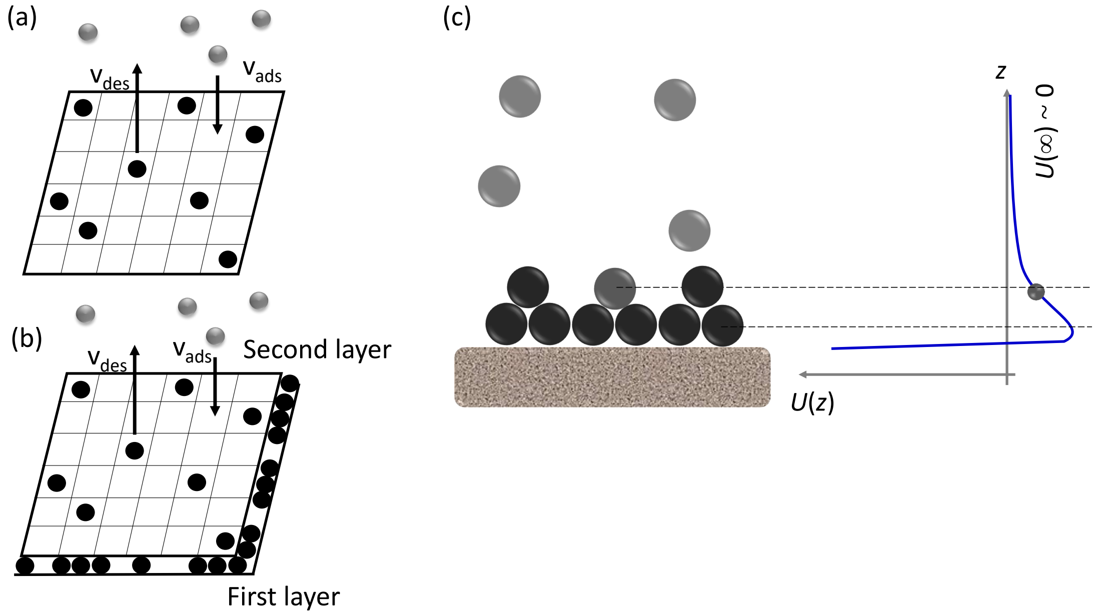

Figure 1.10: (a) Schematic description of the Langmuir adsorption theory. The solid surface is made up of adsorption sites which can adsorb a single adsorbate molecule. The surface is homogeneous so that each site adsorbs with the same adsorption energy. Molecules from the bulk (fluid) phase adsorb with a rate which depends on the pressure and the number of available sites. (b) Schematic description of the BET adsorption model. The first adsorbate layer at the solid surface simply forms according to the Langmuir adsorption model. Then, beyond the first layer, the adsorption energy is equal to the gas liquefaction energy. (c) Polanyi model which describes the multilayer film adsorbed at the solid surface. The density and thickness of the adsorbed layer depends on the interaction potential between the adsorbate molecules and the solid surface. The characteristic curve is represented in blue.

Langmuir model, the BET approach does not take into account lateral interactions between adsorbed molecules within the same layer. Despite such strong approximations, the BET model is extensively used in both fundamental and practical research for the determination of specific surface areas. Indeed, using Eq. (1.17), ones can plot the left side of the equation versus P/P_0. This yields to a straight line where the slope and the intercept can lead to extract V_m and to calculate the surface area. This was done for the first time by Brunauer and Emmett themselves in their two papers [57, 58].

Adsorption potential theory. This theory was proposed by Polanyi in 1914 through a series of seminal papers [59, 60]. This important adsorption model relies on two main concepts: the adsorption potential and the characteristic curve. In contrast to the Langmuir and BET models, there is no underlying kinetic description as it simply relies on a thermodynamic approach. The bulk gas molecules which are adsorbed on the solid surface, form a multilayer film whose thickness depends on the adsorption potential as illustrated in Figure 1.10(c). This adsorption potential, which is not exactly known, derives from intermolecular interactions such as Van der Waals interactions between the adsorbent and the adsorbate. Because it corresponds to an adsorption energy (and not an adsorption free energy), the adsorption potential is assumed to be temperature independent. Without being known a priori, the relation between the adsorption potential and the distance from the adsorbed molecule and the solid surface is coined as the characteristic curve. The characteristic curve f can be expressed by the equation [54, 51]:

$$E = f[V] \tag{1.18}$$

with E the adsorption potential and V the adsorbed volume which can be described as $V = Nv$ with N the amount of molecules adsorbed and v the molar volume of the species. Moreover, in this model, lateral interactions between adsorbed molecules are included in an effective fashion through the adsorption potential. While the assumption of a temperature-independent adsorption potential is not always valid, it allows modeling adsorption isotherms for a broad range of porous materials; typically, using a reference adsorption isotherm at a given temperature, one extracts the adsorption potential which is then used to predict adsorption at various temperatures [61]. For the sake of brevity, we do not present in detail this model as it will be at the heart of Chapter 3 on adsorption within zeolite materials and at their external surfaces.

1.2.3 Adsorption classification

In 1985, the International Union of Pure and Applied Chemistry (IUPAC) proposed a classification of the typical physisorption isotherms existing in the literature. This convention is based on a simple pore/surface classification as illustrated in Figure 1.11 [3].

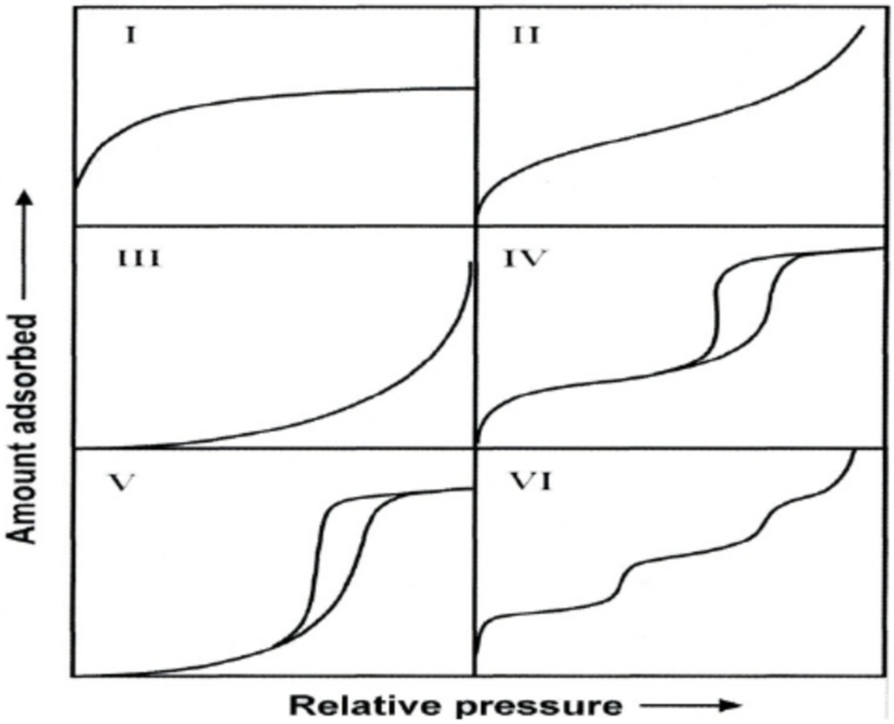

Figure 1.11: IUPAC classification of adsorption isotherms [taken from Ref. [62]]. The classification is clarified in the core of the text.

- Type I adsorption isotherm, which corresponds to the Langmuir adsorption isotherm, is usually observed for microporous solids with small external surfaces. The saturation plateau refers to the maximum adsorbed amount (i.e. saturation capacity) which is driven by the pore volume accessible to the adsorbate fluid. As will be seen in this thesis, this adsorption type is typical of adsorption in zeolite systems.

- Type II adsorption isotherm also corresponds to adsorption as observed for gases in non porous or macroporous adsorbents. The shape of the curve corresponds to an unrestricted monolayer or multilayer adsorption regime until very high pressures P/P^0 (P^0 is the bulk saturating vapor pressure at which all bulk gas molecules transform into the liquid phase).

- Type III adsorption isotherm also corresponds to adsorption in non-porous or macroporous adsorbents but with weak interactions between the adsorbent and the adsorbate phase. This adsorption type is typically observed when the monolayer/multilayer adsorption only occurs at high pressures but below the saturating vapor pressure.

- Type IV adsorption isotherm corresponds to mesoporous adsorbents. It starts like type II adsorption isotherms (pores size is larger than the molecular size in both mesoporous and macroporous solids which drives the adsorption at small pressure) but is followed by pore capillary condensation (i.e. the gas/liquid condensation pressure is shifted due to confinement in the porosity).

- Type V adsorption is similar to type IV but corresponds to weak adsorbate/adsorbent interactions so that film adsorption does not occur at low pressures.

- Type VI adsorption corresponds to layer by layer adsorption. This very unusual adsorption type can be observed when very uniform, i.e. homogeneous, non-porous surfaces are considered (e.g. graphite).

1.3 Fundamentals of transport

In this part, we introduce the fundamental principles of diffusion and transport of a molecular species in a porous media. The motion of molecules can be described using different mechanisms: diffusion, advection, convection and reaction. While reaction is not strictly speaking a transport mechanism, it is involved in the displacement of molecules in a porous material as chemical reactions can occur (e.g. catalysis). Reaction processes refer to the creation or deletion of molecules over time. It can be the consequence of a chemical reaction or an adsorption/desorption process; in the latter case, an adsorbed molecule can be seen as a molecule with no displacement for a given lapse of time which can extend to very long times. Diffusion corresponds to the motion of the molecules from high concentration to low concentration. Diffusion can occur even if no global concentration gradient is applied; it is the result of local concentration gradients as induced by thermal fluctuations in the system. However, diffusion also occurs when a global concentration gradient is imposed on the system. As will be seen below, several diffusion coefficients can be introduced: self, collective and transport diffusivities. Advection refers to the displacement of the fluid when it is set in motion by a thermodynamical gradient (e.g. pressure gradient, temperature gradient) or any combination of thermodynamic gradients. Convection refers to the creation of a velocity field by the displacement of molecules which drives molecules in motion. However, in nanoporous media, friction with the solid is the main mechanism which drives the motion and imposes a laminar advective regime. In the rest of the manuscript, the convective term is neglected.

The change in concentration c over time of a given molecular species can be described using the following advection–diffusion–reaction equation [63]:

$$\frac{\partial c}{\partial t} = \nabla \cdot (D_s \nabla c) - \nabla \cdot (uc) + R \tag{1.19}$$

With u the Stokes velocity of the fluid, D_s the self diffusion coefficient. The first term in the right hand side of the equation refers to diffusive transport, while the second term corresponds to advective transport. Finally, the last term, R is the reaction term which acts as a sink/source for the transported molecules. The competition between the diffusion and advection mechanisms is classically described using Peclet number: $P_e = uD_p/D_s$ where D_p is the pore size and u the fluid velocity. For very small Peclet number $P_e << 1$, the advective contribution is negligible so that transport mostly occurs through diffusion.

1.3.1 Self, collective and transport diffusivity

In few words, self diffusivity refers to the displacement of one, tagged molecule while collective and transport diffusivities correspond to the collective motion of molecules. If the self diffusivity is measured when the system is at equilibrium, the collective and transport diffusivities can be measured by both equilibrium and out of equilibrium methods. In order to define the self, collective and transport diffusivities more formally, we briefly introduce Onsager's theory of transport. This phenomenological theory allows combining the formalism of thermodynamics with transport linear equations.

Onsager coefficient

Considering a thermodynamic system made up of a single compound, we can define the so-called affinities F_i through Gibbs entropy equation:

$$\mathrm{d}S = \frac{1}{T}\mathrm{d}U + \frac{P}{T}\mathrm{d}V - \frac{\mu}{T}\mathrm{d}N \tag{1.20}$$

The different affinities F_U, F_V, F_N are the conjugated variables of the different extensive variables $\mathrm{d}U$, $\mathrm{d}V$, $\mathrm{d}N$. Thus, we can write $F_U = 1/T$, $F_V = P/T$ and $F_N = \mu/T$. At thermodynamic equilibrium, the entropy is maximal and the affinities are homogeneous over the whole system. However, if we induce a perturbation to shift the system with respect to its equilibrium state, any affinity gradient will induce a flux J corresponding which depends on the induced perturbation. For small gradients ∇F_i, the induced flux J_i can be assumed to follow a linear relation $J \sim \nabla F_i$ with $i = U, V, N$ [64, 65]. Formally, this linear response model can be expressed as:

$$J_i = \sum L_{i,j} \nabla F_j \tag{1.21}$$

where the quantities $L_{i,j}$ – the so-called Onsager transport coefficients – are symmetrical (i.e. $L_{i,j} = L_{j,i}$).

This formalism has been already develop to express transport properties - this will be developed in the following lines. For example, for a system subjected to a temperature gradient, Onsager's theory leads to $J_U = L_{UU}\nabla F_U = -L_{UU}/T^2 \nabla T$ which can be recast as Fourier's law $J = -\lambda \nabla T$ (where $\lambda = L_{UU}/T^2$, known as the material's conductivity). An interesting example – particularly relevant for this thesis – is the case of a system at constant temperature/pressure subjected to a chemical potential gradient. Using

Onsager's theory of transport, the molecule flux induced by a chemical potential gradient can be written:

$$J_N = -L_{NN}\nabla\left(\frac{\mu}{T}\right) = -\frac{L_{NN}}{T}\nabla\mu \tag{1.22}$$

where the second equality holds if the system is at constant temperature. As introduced in the rest of this paragraph, this equation allows defining the different diffusivity coefficients (self D_s, collective D_0 and transport D_T) at constant temperature and pressure.

Self diffusivity

Even when no thermodynamic gradient is applied to the system, diffusion occurs under equilibrium conditions as molecules explore their environment through thermal motion and collisions. In this context, self diffusivity refers to tracer diffusion where one follows a single, i.e. tagged, molecule [66]. Such tracer diffusion and its associated transport coefficient known as self diffusivity D_s can be studied considering a very diluted system where $\mu = k_B T ln(c)$. Eq. (1.22) leads to Fick's law:

$$J(\mathbf{r},t) = -D_s(c)\nabla c(\mathbf{r},t) \tag{1.23}$$

where $c(\mathbf{r},t)$ is the local concentration at a position $\mathbf{r}$ at time t and $D_s = L_{NN}k_B/c$. By adding mass conservation, i.e. $\partial c(\mathbf{r},t)/\partial t + \nabla \cdot J(\mathbf{r},t) = 0$, and considering that the diffusivity is concentration independent (i.e. $D_s(c)$ ∼cst), one arrives at Fick's second law:

$$\frac{\partial c(\mathbf{r},t)}{\partial t} - D_s\Delta c(\mathbf{r},t) = 0 \tag{1.24}$$

The space and time-dependent solution of Eq. (1.24) has the form of the so-called Gaussian propagator:

$$c(\mathbf{r},t) = N\frac{\exp(-\mathbf{r}^2/4D_s t)}{(4\pi D_s t)^{3/2}} \tag{1.25}$$

with N the number of particles which is assumed to be constant. The Gaussian propagator corresponds to the probability that the particle moves over a distance r in a time t. Here, we note that we consider D_s independent of the concentration c. The Fickian regime is defined as the times and distances where the molecule displacements follow the Gaussian propagator.

Mean square displacement At this stage, it is useful to introduce the mean square displacements of the molecules which is defined as the root mean square of the position of a molecule at time t [66]. From Eq. (1.25), it can be shown that the mean square displacement (MSD) follows Einstein's equation:

$$< \mathbf{r}^2(t) >= |\mathbf{r}(t) - \mathbf{r}(0)|^2 = 6D_s t \tag{1.26}$$

where $r(t)$ and $r(0)$ are the position of the molecule at the time t and the origin $t = 0$ respectively. For an anisotropic medium, this equation becomes $< \mathbf{r}_\alpha^2(t) >= 2D_{s,\alpha}t$ where $\alpha = x$, y or z.

Figure 1.12(a) shows the mean square displacements (MSD) as function of time for a molecule entrapped in a porous network (here a zeolite). Several regimes can be observed when monitoring the MSD. The first part of the curve corresponds to the ballistic regime where $< \Delta x^2(t) >$ is proportional to t^2. Then, the molecule can be stuck in a pore until the typical escape time τ_c is reached. Thus, $< \Delta x^2(t) >$ associated to the plateau is roughly equal to the characteristic pore size. Finally, after a certain time, the molecule trajectory becomes fickian with the typical diffusion regime where $< \Delta x^2(t) >$

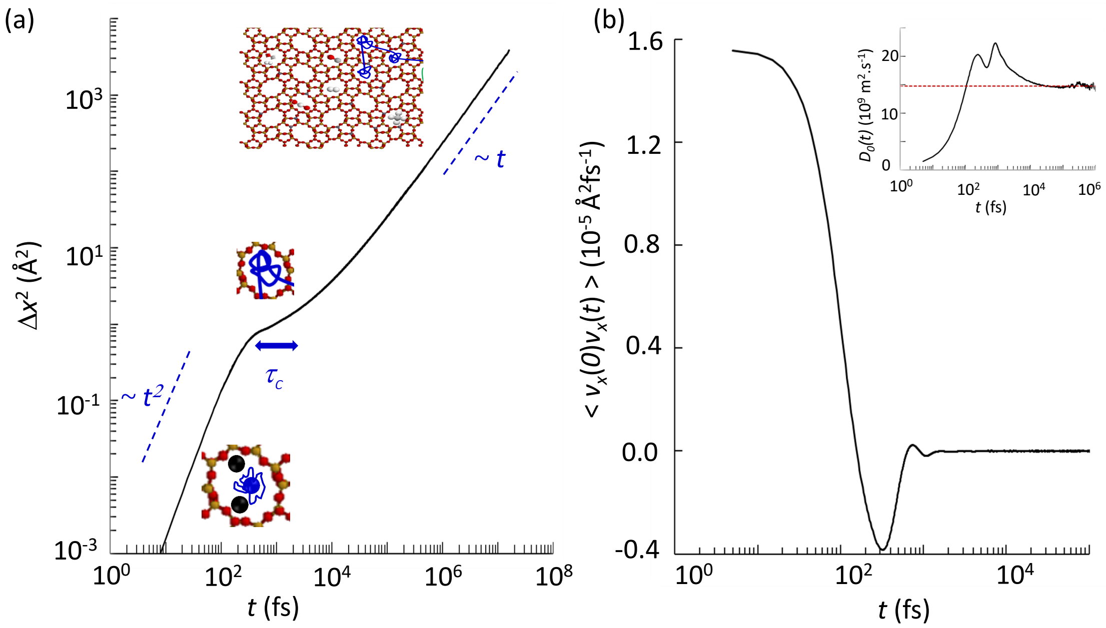

Figure 1.12: (a) Mean square displacement $< \Delta x^2(t) >$ as a function of time t for a fluid confined in a porous media. The first part of the curve corresponds to the ballistic regime where $< \Delta x^2(t) >$ is proportional to t^2. This regime is valid only in the very short time before molecules collide with its neighbors. In the intermediate time range, the molecule can remain trapped in a pore until the typical escape time τ_c is reached. Thus, $< \Delta x^2(t) >$ associated to the plateau is roughly equal to the characteristic pore size. Finally, after a certain time, the molecule trajectory becomes fickian as diffusion becomes homogeneous: $< \Delta x^2(t) >$ is proportional to time t. (b) Velocity autocorrelation function (VACF) as function of time t. The insert shows the self diffusion coefficient extracted from the integration of the VACF. The plateau indicates that the system reached the Fickian regime with a value corresponding to D_s as obtained from the mean square displacements in the long time limit.

is proportional to time t.

Green Kubo formalism. The Green Kubo formalism allows linking any transport coefficient to statistical fluctuations in a corresponding microscopic quantity [67, 68]. This is a general formalism which is applicable in order to compute numerous and various coefficients such as the thermal conductivity [69, 70], the Navier Stokes friction coefficient [71] or the viscosity [72]. Using this formalism, the self diffusion coefficient D_s can be related to the velocity autocorrelation function (VACF) $< \mathbf{v}(0) \cdot \mathbf{v}(t) >$ where v is the molecule velocity (which is taken at time $t = 0$ and a time t later). The brackets indicate that statistical average over the different molecules in the system and over many different configurations is considered. The self diffusion coefficient is then obtained using the following Green-Kubo equation relation:

$$D_s = \frac{1}{d} \int_0^{\infty} < \mathbf{v}(0) \cdot \mathbf{v}(t) > \mathrm{d}t \tag{1.27}$$

with d the dimensionality of the system. As can be found in the book by Hansen and McDonald [73], the self diffusion coefficient D_s given by the mean square displacement formula in Eq. (1.26) and the Green-Kubo formalism in Eq. (1.27) are mathematically equivalent. As an illustration of this equivalence, Figure 1.12(b) shows the typical VACF obtained for methane confined in the silicalite-1 zeolite at room temperature.

The insert also shows the self diffusion coefficient extracted from the integration of the VACF using the Green-Kubo relationship defined above. The plateau indicates that the system reaches the Fickian regime with a value corresponding to self diffusion coefficient D_s obtained from the MSD.

This formalism was also used in order to compute D_0 the collective diffusion coefficient. We would draw the attention of the reader here. Indeed, D_0 describes a collective motion; however, in the Green Kubo approach, the system is at equilibrium and thus, the average velocity of the fluid is $u = 0$. But D_0 is an information contained in statistical fluctuations of the average velocity. This will be discussed in the chapter dedicated to collective diffusion.

Incoherent scattering function. The intermediate incoherent scattering function describes the correlations between the positions of a given particle i at different times:

$$F_{\text{inc}}(\mathbf{q}, t) = 1/N \sum_i \rho_i(\mathbf{q}, 0)\rho_i^*(\mathbf{q}, t) \tag{1.28}$$

where $\rho_i(\mathbf{q}, t) = \int \exp[-i\mathbf{q}\cdot\mathbf{r}]\rho_i(\mathbf{r}, t)\mathrm{d}r$ is the Fourier transform of the density distribution for particle i: $\rho_i(\mathbf{r}, t) = \delta(\mathbf{r}(t) - \mathbf{r}_i(t))$. This density distribution function has the form of a dirac which becomes non-zero when $\mathbf{r}(t) = \mathbf{r}_i(t)$. In the above equation, the $*$ indicates the conjugate value since $\rho_i(\mathbf{q}, t)$ is an imaginary quantity. From the latter definition, it is straightforward to show that:

$$\begin{aligned}\rho_i(\mathbf{q}, t) = \int &\exp[-i\mathbf{q}\cdot\mathbf{r}]\delta(\mathbf{r}(t) - \mathbf{r}_i(t))\mathrm{d}r \\ &= \exp[-i\mathbf{q}\cdot\mathbf{r}_i(t)]\end{aligned} \tag{1.29}$$

so that:

$$F_{\text{inc}}(\mathbf{q}, t) = 1/N \sum_i \exp[-i\mathbf{q}\cdot(\mathbf{r}_i(t) - \mathbf{r}_i(0))] \tag{1.30}$$

We can also obtain an expression for the intermediate incoherent scattering function by solving Eq. (1.24) in Fourier space: $\partial\rho_i(\mathbf{q}, t)/\partial t + D_s\mathbf{q}^2\rho_i(\mathbf{q}, t) = 0$ (here $\mathbf{q}$ is the wave vector so that $\mathbf{q} \sim 1/\mathbf{r}$). In so doing, one arrives at the following solution:

$$\rho_i(\mathbf{q}, t) = \rho_i(\mathbf{q}, 0)\exp[-D_s\mathbf{q}^2 t] \tag{1.31}$$

Because $\rho_i^*(\mathbf{q}, 0)\rho_i(\mathbf{q}, 0) = 1$, by multiplying the last equation by $\rho_i^*(\mathbf{q}, 0)$, we obtain the intermediate incoherent scattering function [74, 75]:

$$F_{\text{inc}}(\mathbf{q}, t) = \exp^{-D_s\mathbf{q}^2 t} \tag{1.32}$$

We notice that this exponential form assumes that the system is to be considered at large distances (i.e. small $\mathbf{q}$ values) and/or long times to consider that the Fickian regime is reached.

Incoherent dynamic structure factor The incoherent dynamic structure factor $S_{inc}(\mathbf{q}, \omega)$ is the time Fourier transform of the intermediate incoherent scattering function $F_{inc}(\mathbf{q}$,t) given in Eq. (1.32):

$$S_{inc}(\mathbf{q}, \omega) = \int \exp(-i\omega t)F_{inc}(\mathbf{q}, t)\mathrm{d}t \tag{1.33}$$

Using the exponential form as defined in Eq. (1.32), we get:

$$S_{inc}(\mathbf{q}, \omega) = \frac{1}{\pi}\frac{D_s\mathbf{q}^2}{\omega^2 + (D_s\mathbf{q}^2)^2} \tag{1.34}$$

which corresponds to a Lorentzian function whose Half Width at Half Maximum (HWHM) is $D_s q^2$.

Collective diffusion

The collective and transport diffusivities are Onsager coefficients corresponding to the system's response when subjected to a chemical potential or a density gradient respectively. The general form of Eq. (1.22) has to be considered by writing the flux as the average velocity/flow rate:

$$J_N = \rho v = \frac{1}{V} \sum_i \vec{v} \tag{1.35}$$

where the sum is performed over each i molecule in the system. Here, we can use the linear response theory [76] to determine D_0. Let us consider the system under a perturbation ΔH. In the linear response theory, we consider:

$$\Delta H(t) = -AF_0 \exp(-i\omega t) \tag{1.36}$$

with $F_0 = -\nabla\mu$ the force corresponding to the chemical potential gradient applied to the system. The conjugated thermodynamical variable to this chemical potential gradient is $A(t) = \sum_i x_i(t)$ i.e. the displacement of the particles. The observable of interest is the flux that we will call $B = J_N$. The linear response theory states that the change in the observable $< B >$ induced by the perturbation can be written:

$$< \Delta B >= M_{BA}(\omega) F_0 \exp(-i\omega t) \tag{1.37}$$

with

$$M_{BA}(\omega) = \frac{1}{k_B T} \int < B(t) A' > \exp(-i\omega t) \mathrm{d}t \tag{1.38}$$

If we consider the expression of the flux as given in Eq. (1.35) and the derivative of $A(t)$, we get:

$$M_{BA}(\omega) = \frac{1}{3Vk_B T} \int < \sum_{i,j} \mathbf{v}_i(t) \cdot \mathbf{v}_j(0) > \exp(-i\omega t) \mathrm{d}t \tag{1.39}$$

If we now consider a stationary perturbation, $\omega \longrightarrow 0$, we have from Eq. (1.37):

$$< \Delta B >= -M_{BA}(0) \nabla\mu \tag{1.40}$$

By definition, using the velocity autocorrelation function, D_0 corresponds to the correlation between the velocity of a given molecule at a time $t = 0$ and the velocity of another molecule at a time t later. It includes the self diffusion contribution but also crossed terms between particles $i \neq j$:

$$D_0 = \frac{1}{3N} \int_0^\infty \Big\langle \sum_{i,j} \mathbf{v}_i(0) \cdot \mathbf{v}_j(t) \Big\rangle \mathrm{d}t \tag{1.41}$$

We can therefore write D_0 as the sum of the self diffusion contribution and all collective contributions [77]:

$$D_0 = \frac{1}{3N} \int_0^\infty \Big\langle \sum_{i=1}^{N} \mathbf{v}_i(0) \cdot \mathbf{v}_i(t) \Big\rangle \mathrm{d}t + \frac{1}{3N} \int_0^\infty \Big\langle \sum_{i\neq j}^{N} \mathbf{v}_i(0) \cdot \mathbf{v}_j(t) \Big\rangle \mathrm{d}t \tag{1.42}$$

with the first term corresponding to Eq. (1.27).

We can notice here that in the limit of very diluted system, the hydrodynamic term is negligible and $D_s \sim D_0$. However, in many cases, this assumption is not verified and we usually get $D_0 > D_s$ as cross-terms are positive. This term means that the velocity of a molecule creates a velocity field which favors the diffusion of the other neighboring molecules.

Now, by replacing B by the observable J_N in Eq. (1.40), we can compare Eq. (1.40) and Eq. (1.22) to identify:

$$M_{BA}(0) = \frac{L_{NN}}{T} \tag{1.43}$$

From Eq. (1.39) and Eq. (1.41), we can define a relation between $M_{BA}(0)$ and D_0:

$$M_{BA}(0) = D_0 \frac{\rho}{k_B T} \tag{1.44}$$

with ρ the fluid average density. Thus, D_0 can be defined as follows:

$$J_N = -D_0 \frac{\rho}{k_B T} \nabla \mu \tag{1.45}$$

Therefore, D_0 is the collective diffusion coefficient which corresponds to the response of the system to a chemical gradient which is characterized by individual motions and collective transport (see Eq.(1.41)).

Transport and thermodynamic (Darken) factor. In many experiments, the transport is described as the response to a pressure or concentration gradient. In any case, for small gradients, we can assume a linear response of the flux to write:

$$J_N = -D_T \nabla \rho \tag{1.46}$$

Comparison between Eq. (1.46) and Eq. (1.45) leads to:

$$D_T = D_0 \frac{\rho}{k_B T} \frac{\partial \mu}{\partial \rho}\bigg|_T \tag{1.47}$$

where $\nabla\mu/\nabla\rho \sim \partial\mu/\partial\rho$. By invoking $\mu = k_B T \ln(f\Lambda^3/k_B T)$, where f is the fugacity (i.e. f=P for an ideal gas) and Λ is the thermal de Broglie wavelength, we have that $\partial\mu = k_B T \partial \ln f$. [The latter equation derives from the definition of the Helmholtz free energy $F = U - TS$ with U, T and S the internal energy, temperature and entropy respectively of a thermodynamical system. It can be shown that the chemical potential is the derivative of F with N the number of particles: $(\partial F/\partial N)|T, V$. The physical statistic provides a definition for F: $dF = k_B T \ln(Q(N, V, T)$ with $Q(N, V, T)$ the partition function of the canonical ensemble which will be detailed in Chapter 2. This partition function brings out Λ and f.] We also have $\partial \ln \rho = \partial\rho/\rho$ so that Eq. (1.47) can be written as:

$$D_T = D_0 \frac{\partial \ln f}{\partial \ln \rho}|_T \tag{1.48}$$

In the latter equation, the term $\partial \ln f/\partial \ln \rho$ is known as the thermodynamic factor [78, 79] (sometimes referred to as Darken factor). It can be linked to the isothermal compressibility of the fluid - the derivation will be provided in Chapter 5 where we will consider the theory of De Gennes narrowing. In particular, as will be seen later, the thermodynamic factor can be measured using the adsorption isotherm: it corresponds to the slope of the adsorption isotherm at a given (P, ρ) adsorption condition.

Coherent scattering function and coherent dynamic structur factor. The coherent scattering function $F_{\mathrm{coh}}(\mathbf{q},t)$, which is linked to the collective diffusivity, characterizes correlations between molecules at different times t:

$$F_{\mathrm{coh}}(\mathbf{q},t) =< \rho(\mathbf{q},0)\rho^*(\mathbf{q},t) > \tag{1.49}$$

Of particular interest, the structure factor $S(\mathbf{q})$ corresponds to the intermediate coherent scattering function at $t=0$: $S(\mathbf{q}) = F_{\mathrm{coh}}(\mathbf{q},0)$. Let us now determine an expression for $F_{\mathrm{coh}}(\mathbf{q},t)$. By replacing the flux from Eq. (1.46) in the mass conservation equation $\partial\rho(\mathbf{r},t)/\partial t + \nabla\cdot J(\mathbf{r},t) = 0$, one gets:

$$\frac{\partial\rho(\mathbf{r},t)}{\partial t} - D_T\Delta\rho(\mathbf{r},t) = 0 \tag{1.50}$$

Considering that D_T does not depend on $\mathbf{r}$, we can do a spatial Fourier transform to obtain:

$$\frac{\partial\rho(\mathbf{r},t)}{\partial t} - D_T\mathbf{q}^2\rho(\mathbf{r},t) = 0 \tag{1.51}$$

which leads to:

$$\rho(\mathbf{q},t) = \rho(\mathbf{q},0)\exp[-D_T\mathbf{q}^2 t] \tag{1.52}$$

As done earlier for the self diffusivity/incoherent function, multiplying by $\rho(\mathbf{q},0)$ the above equation leads to:

$$F_{coh}(\mathbf{q},t) = S(\mathbf{q})\exp[-D_T\mathbf{q}^2 t] \tag{1.53}$$

The coherent dynamic structure factor is obtained by the time Fourier transform of the coherent scattering function:

$$S_{coh}(\mathbf{q},\omega) = \frac{S(\mathbf{q})}{\pi}\frac{D_T\mathbf{q}^2}{\omega^2 + (D_T\mathbf{q}^2)^2} \tag{1.54}$$

which corresponds to a Lorentzian function whose Half Width at Half Maximum (HWHM) is $D_T q^2$.

1.3.2 Diffusion in porous materials

This subsection presents the different transport regimes that can be observed in porous materials depending on pore size D_p. As illustrated in Figure 1.13(a), let us consider a fluid with some simple parameters such as its molecular size σ and its mean free path λ_f (the latter is linked to the density of the fluid by the relation $\lambda_f = 1/\rho\sigma^2$). The different following transport mechanisms can be considered [77, 80].

Molecular sieving occurs when the pore size is smaller than the molecular size $D_p < \sigma$ as illustrated in Figure 1.13(b). This condition leads to molecular blocking at the pore entrance. Molecular sieving may be used to separate different molecule types in a mixture (based on their molecular sizes). In this context, the synthesis of new porous materials with controlled pore sizes is useful to separate gas or liquid mixtures for industrial applications [81, 2].

Knudsen diffusion occurs for rarefied gases when the pore size is smaller than the mean free path $D_p < \lambda_f$. In this case, the main transport phenomena is the diffusion of individual particles which occurs mainly through collisions of the molecules with the surface atoms as illustrated in Figure 1.13(c). In other words, collisions between fluid particles can be neglected. At the opposite, for high density fluid, the flow is mainly

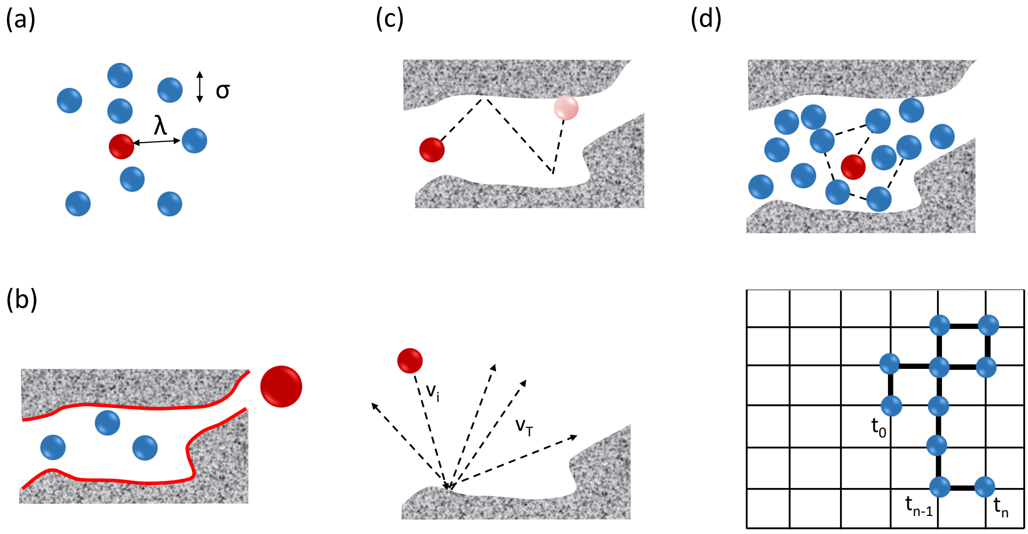

Figure 1.13: [Adapted from Ref[77]](a) A bulk fluid which consists of molecules with a molecular size σ. The mean free path λ_f, which corresponds to the distance traveled by a molecule between two collisions, depends on density. (b) Molecular sieving regime when $D_p < \sigma$. The fluid molecule is blocked at the pore entrance; this mechanism allows one to separate different types of molecules. (c) Knudsen regime when $D_p < \lambda$. In the case of rarefied gases, diffusion of the molecules arises from the collisions with the surface. It is considered as a diffusive regime, a molecule has a collision with the surface at a velocity v_i. It is adsorbed, thermalized and released to the pore volume with a velocity v_T independent from its initial velocity. (d) Molecular diffusion regime when $D_p > \lambda$. The diffusion arises from the collisions with the other fluid molecules. It can be modelled as a random walk process where the walker moves from a site to another site in a time $\delta t = t_n - t_{n-1}$.

advective in the laminar regime and the collective diffusion is predominant. In order to determine how important Knudsen diffusion is, the Knudsen number can be assessed:

$$K_n = \frac{\lambda_f}{D_p} \tag{1.55}$$

with $\lambda_f = k_B T / \sqrt{2} P \pi \sigma^2$. We can notice that σ can be taken as the Lennard-Jones parameter for the fluid/fluid interaction (the latter will be defined more rigorously later).

- For $K_n >> 10$, Knudsen diffusion is the main process through which diffusion occurs.

- For $K_n << 0.1$, Knudsen diffusion can be neglected as diffusion is mainly due to molecular diffusion.

- For $0.1 < K_n < 10$, both Knudsen and molecular diffusion occur in parallel.

The Knudsen number was computed from the simulation data in our system. It varies on 6 order of magnitude (between 10^{-2} and 10^{4}) depending on the pressure considered (indeed, we consider pressure from 10^{-3} to 10^3 bars). This means that our system passes through the different regimes listed before. We now present in more details the Knudsen regime and the molecular diffusion regime.

Knudsen regime

In the Knudsen regime (which is the main process for $K_n >> 10$), one only considers collisions of fluid molecules with the atoms of the wall. Let us consider a cylindrical pore. Any applied gradient $\nabla\rho$ induces a flux J_K directly linked to the thermal velocity (i.e $v_T = \sqrt{(8k_BT/\pi m)}$) with the probability that the molecule passes through the pore ω. The flux can be written $J_K = -\omega v_T \nabla\rho$. We can also define the diffusion coefficient associated to this Knudsen regime D_K as $J_K = -D_K\nabla\rho$ (i.e. Fick's law). By comparing the different equations, we can write:

$$D_K \sim \sqrt{T} \tag{1.56}$$

Some important comments are in order here:

- There is no activation barrier here. The self diffusion coefficient follows a continuous and linear relation with $\sqrt{T}$.

- Because of the definition of the velocity (i.e. through the thermal velocity), we assume that collisions correspond to diffusive scattering phenomena. Indeed, a molecule collides with the wall with a velocity v_i. Then, it is adsorbed, thermalized and released with an isotropic direction and a velocity independent of v_i (which only depends on T as shown in Figure 1.13(c) bottom).

- One can introduce a degree of specular reflections (elastic collisions) with the number f. f is the fraction of molecules which undergo diffusive scattering while $1-f$ undergo specular reflection. It is assumed here that f is T-independent. This contribution has the form of a factor $2 - f/f$ in Eq. (1.56) [77].

Molecular diffusion

Molecular diffusion occurs when the pore size is larger compared to the distance between molecules $D_p > \lambda$. It implies that the diffusion process occurs through the collisions between fluid particles. It happens for sufficient large pores or considering an important density of the fluid. In this regime there is no general model but the random walk model gives a good framework in order to find an expression for D_s. Let us take a lattice as shown in Figure 1.13(d). A particle, the walker, jumps from one site to another randomly. The distance between two sites is constant and equal to a. $\delta t = t_n - t_{n-1}$ is the time between two jumps. Solving this problem is equivalent to finding the solution of Brownian motion given by Einstein equation (Eq. 1.26). When site hopping does not involve any free energy barrier, we can write $D_s = D_s^0 = k_0a^2/6$ with the hopping rate $k_0 = 1/\delta t = v_0/a$. If we consider only collisions, we can define v_0 the thermal velocity and we get the same temperature dependence than for the Knudsen regime. However, when jumping between different sites involves a free energy barrier, there is an acceptance rate to diffuse from one site to another; the hopping rate can be written as an exponential form $k = k_0 \exp(-\Delta F/k_BT)$. By assuming that ΔF is independent of the temperature T, we get Arrhenius' law:

$$D_s = D_s^0 \exp\left(\frac{-\Delta F}{k_BT}\right) \tag{1.57}$$

The latter equation can be more formally demonstrated using the transition state theory [82, 83].

1.3.3 Fluid transport in zeolites

Reviewing all the literature on diffusion and transport in nanoporous materials is an enormous work that was done in several reviews [4, 5]. Indeed, the diffusion and transport mechanisms can be very different depending on pore size, network topology, chemical composition, etc. of the material under study. In this section, we will briefly focus on the state of the art of diffusion and transport in zeolites - more specifically in the MFI zeolite structure. We will try to highlight the general diffusive behavior observed for small gaseous molecules and its dependence on loading, temperature and pore shape in the light of previous published works. As seen before, zeolites possess good crystalline properties with different pore sizes and shapes. These properties make them interesting candidates for both fundamental and practical research. In their review article, Bukowski *et al.* [5] distinguished two special diffusive behaviors depending on the pore size of the host zeolite. We first consider diffusion in small pore zeolites (i.e. $<$ 8-ring openning) as we believe that understanding such phenomenon is relevant to our system. Small pores zeolites such as Chabazite (CHA), Rho zeolite (RHO), etc. [42] have a network of pores linked by "windows" whose opening size is equivalent to the size of a small gas molecule (such as methane considered in this thesis). This condition implies a very different behavior for the self diffusion coefficient D_s as a function of loading (compared to data for large pore zeolites). Indeed, several studies [78, 84, 85] have shown that the self diffusion coefficient increases with loading until reaching a maximum and then decreases drastically. On the other hand, this effect is not seen for large pore zeolites. The studies for small pore zeolites used simulation through a free energy approach such as the transition state theory (TST) to explain this behavior. They used the term "window effect" to describe this phenomenon: to jump from one pore to another, molecules have to cross the window which involves an important free energy barrier. At low loadings, molecules trapped in the pore do not overcome the free energy barrier as they remain trapped within the adsorption sites. When the loading increases, two mechanisms compete: collisions between the molecules promote hopping but steric repulsion between the confined molecules implies hampers diffusion. By computing the variation of the free energy barrier using simulation data, they have reached the conclusion that these two phenomena allow to explain the observations made.

We now consider diffusion in medium and large pore zeolites such as MFI or Faujasite. In this case, pore openings are larger than the molecular size of the confined fluid. In such zeolites, no "window effects" were observed so that increasing the loading only leads to steric repulsion and, thus, to a decrease in D_s. However, many parameters impact the observed diffusion. Without going into details (out of the scope of our study), we can cite the following elements:

- Influence of extra cation framework. Depending on the strength of the interaction between the fluid molecules and the cations, it can be observed an increase of D_s with loading. Indeed, at low loadings, molecules interact with cations. When more molecules are added (while the cationic sites are already filled), they interact with the zeolite part with which they have weaker interactions [86].

- Influence of gas mixtures. Snurr and Karger [87] studied a mixture of CH_4 and CF_4 using a combined simulation/experimental approach. By computing separately the diffusivity of both species, these authors found that increasing the adsorbed amount for the slowest gas makes the diffusivities of both species decrease.

- Influence of the hydrocarbon chain length (i.e. number of carbon atoms in the chain). Comparison between different techniques to assess D_s as a function of the number of carbon atoms can be found in Ref. [75, 88]. It can be seen that the increase in the chain length decreases the self diffusivity as expected.

We now focus on specific literature contributions dedicated to methane diffusion in silicalite-1 (pure silica of the MFI type). Several studies have compared the self diffusion coefficient obtained using experiments and molecular simulations and have showed a good agreement between methods [89, 90, 75]. One of the works by June, Bell and Theodorou [90] is particularly interesting to understand the behavior of methane in MFI zeolite. These authors used molecular dynamics simulations combined with a free energy approach (computational determination of the surface potentials, adsorption energies, activation energies and adsorbate density distributions) to study D_s in the different directions of the crystal x, y and z (one can refers to the Figure 1.8 for the corresponding channels). They also considered different temperatures in order to observe the effect of T on diffusion. For the 2 largest temperatures, D_s decreases when the loading increases. However, for 200 K, they observed that D_s reaches a maximum before decreasing. Using a free energy approach, the authors showed that the channel intersections are energetically less favorable than the channel segments for methane adsorption. In other words, these intersections present a highest potential barrier for diffusion. One explanation could be that, at the intersections, molecules that come from the zigzag channel and the straight channel collide with perpendicular velocities that deviate their trajectories. At low temperature and low loading, molecules are trapped in channel segments. Then two effects can be highlighted:

- Heating the system makes the molecule's energy increase, which promotes the hopping rate across the intersection and, thus, increases the diffusion.
- Increasing the loading increases the number of collisions between fluid molecules. As explained for the small pore zeolites, it has two effects: (1) help overcome the free energy barrier and (2) blocking diffusion because of steric hindrance.

The authors also highlighted the anisotropic nature of diffusion by computing the mean square displacements in the different directions of space. They also discussed the Fourier transform of the VACF. Diffusion along the x and y directions were found to be similar with both contributions being faster than along the z direction. Indeed, it can be explained because along z, there is no direct diffusion path for methane. Because of the collisions with the pore wall, the molecule velocity often changes its direction/sign – which prevents diffusion. Moreover, at low loadings, the differences between D_s^z and $D_s^{x,y}$ are important because of the effect of the channel geometry and the interactions with the wall (which prevail at low loadings). In contrast, at high loadings, collisions between molecules become predominant, which implies a reduction in the diffusion but also the appearance of anisotropic diffusion.

In order to close this brief literature review, we would like to cite and discuss the paper by Maginn *et al.* [91] on transport and collective diffusivity. Maginn, Bell and Theodorou studied the transport of methane in silicalite-1 using the Darken equation given in Eq. (1.48). These authors computed D_0 using a non equilibrium method which will be introduced in detail in Chapter 5. At infinite dilution, the self D_s and collective

D_0 diffusivities were found to be equal as expected. In contrast, at high loadings, D_s and D_0 are significantly different. Indeed, increasing the loading promotes fluid/fluid interactions which hinders to some extent individual motions corresponding to self diffusion. In contrast, due to the strong correlations in motion, D_0 is less affected so that it remains nearly constant. Maginn *et al.* also computed D_T using equilibrium and nonequilibrium methods and compared their results with Eq. (1.48) for the Darken factor. They showed a good agreement between the model and the results, which demonstrated that the Darken formulation is valid for this system (i.e. methane in MFI zeolite). They also found that the transport diffusivity increases when the loading increases. As the collective diffusivity remains constant, it is therefore the thermodynamic factor which increases with loading (i.e. for the Langmuir adsorption isotherm used, it can be shown that $\Gamma = 1/(1-\Theta)$ with Θ the loading fraction). Overall, these results are consistent with the findings by Skoulidas and Sholl [79].

This chapter provided a short summary of fundamental concepts that are going to be used in the following discussions: main characteristics of porous materials, principles of adsorption and models to predict it and fundamentals of diffusion and transport in porous media. However, even if these concepts have been developed for a long time, adsorption and transport in porous media still remain a topical subject as fluid behavior inside a porosity is not fully understood.

2 Methods

In a past decades, lot of work has been done in order to probe matter on smaller and smaller scales. In one hand the development of computer sciences allows to perform numerical experiences faster on increasingly large molecular systems. In an other hand, technological progress allows to improve experimental set up to get better resolution and to probe molecular motion on larger time and length scales. This chapter will focus on the fundamentals of computational and experimental methods that are going to be used in this thesis. In a first step, we will introduce the main concepts of the numerical simulations used to study adsorption and transport through Monte Carlo and Molecular Dynamic. In a second step, we will present the principles of neutron scattering experiments and the specific experimental set up used to probe gas diffusion in zeolite.

2.1 Computational methods

With the development of computers, macroscopic systems behavior and predictions of their properties became accessible realizing numerical experiences. From the knowledge of their microscopic composition, macroscopic properties can be computed. In this thesis numerical tools will be used to:

- simulate experiences of adsorption using Monte Carlo (MC) method.
- simulate experiences of self and collective diffusion using Molecular Dynamic (MD)

In this section, fundamental principles of statistic mechanics, Monte Carlo method and Molecular Dynamic will be presented. For the application of these methods to our system, the reader will refer to the Result part.

2.1.1 Fundamentals of Statistical Mechanics

Classical thermodynamics provides unified framework to describe the macroscopic properties of a substance (gas, liquid or solid). This formalism relies on a set of scalar variables to describe the system; these thermodynamic quantities can be extensive such as the volume V, the number of molecules N, the total energy E or intensive such as the temperature T, the pressure P. A macroscopic state corresponds to a set of thermodynamical values (E, V, N, T, etc.) describing the system. These quantities remain constant at equilibrium and can be measured. A microscopic state is the information (position, velocity, chemical nature, etc.) considering the arrangement of each atom or molecule in the system. It corresponds to a picture at a single instant of the macroscopic system. For any macroscopic state, there is in general a large number of microscopic states possible which lead to thermodynamic variables with the same values as those defining the macroscopic state. Even if the system is at thermodynamic (macroscopic) equilibrium, the continuous motion of molecules composing the system – as induced by thermal energy and collisions – leads to a continuous change in the microscopic state of the system. Statistical mechanics is the physical formalism which adopts a microscopic description of the system to describe its properties [92]. In this context, the understanding of the macroscopic, i.e. thermodynamic, behavior of substances can be derived from such a microscopic description. In order to introduce the fundamentals of statistical mechanics, let us consider the total energy of a system E which is defined as the sum of the energy of each molecule ϵ_i:

$$E = \sum_{i=1}^{N} \epsilon_i \tag{2.1}$$

Let us define the positions $\mathbf{r}_i(t) = [x_i(t),\ y_i(t),\ z_i(t)]$ and velocities $\mathbf{v}_i(t) = [v_i^x(t),\ v_i^y(t),\ v_i^z(t)]$ at time t of the N particles of the system ($i \in [1...N]$). Typically, this information is needed to describe the system's evolution in time using Newton's equation. In the framework of statistical mechanics, these $6N$ data describe a single microscopic configuration in the so-called phase space $[r^N,\ p^N]$ as illustrated in Figure 2.1. A specific configuration $[r^N,\ p^N]$ is referred to as a "microstate" l whose energy is E_l [93].

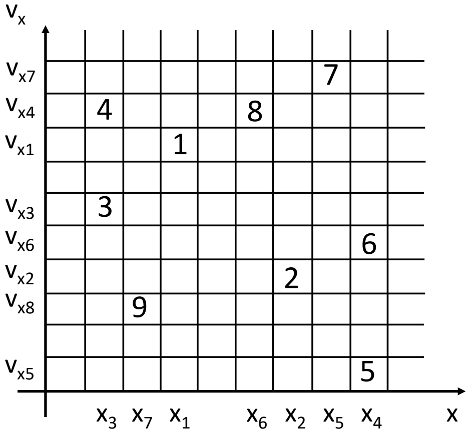

Figure 2.1: Phase space r^N,p^N discretized in the x direction for a system of 9 particles in a particular microstate l. In this example, the $2 \times 9 = 18$ values of positions/velocities allow to describe the space configuration: $x = [x_1, x_2, x_3, x_3, x_4, x_4, x_5, x_6, x_7]$ and $v_x = [v_{x1}, v_{x2}, v_{x3}, v_{x4}, v_{x5}, v_{x6}, v_{x7}, v_{x4}, v_{x8}]$.

Microstates in the microcanonical ensemble (constant energy)

Let us consider an isolated system so that the number of molecules N, the volume V and the energy E are constant. Because the total energy of the system E is constant, all possible microstates are not accessible as the condition $\sum_{i=1}^{N} \epsilon_i = E$ has to be reached. Let $\Omega(N, V, E)$ be the number of accessible microstates accessible to the system The fundamental postulate in statistical mechanics states that every microstate accessible to the system is equiprobable:

An isolated system (i.e. N,V,E constant) at equilibrium is equally likely to be found in any of the $\Omega(N, V, E)$ accessible microstates.

This postulate simply describes the fact that all accessible microstates are physical so that their probability distribution is homogeneous. With this fundamental property, the probability P_l for the system to be in the microstate l is:

$$P_l = \frac{1}{\Omega(N, V, E)} \tag{2.2}$$

From a macroscopic viewpoint, in the microcanonical ensemble (constant N, V, E), at equilibrium, the system will be in a macrostate corresponding to the largest number of microstates. As a result, the macrostate is defined from the largest subset of accessible microstates in $\Omega(N, V, E)$. In statistical mechanics, this allows defining the entropy S which is a measure of the system's degeneracy:

$$S = k_B \ln \Omega(N, V, E) \tag{2.3}$$

In fact, the maximization of entropy in the microcanonical ensemble corresponds to the second principle of thermodynamic: the entropy S is maximum at equilibrium. Finding the microcanonical entropy, which is performed by solving $\delta S/\delta E = 0$, provides all properties in the microcanonical ensemble (N, V, T).

Partition function and statistical ensembles

Except for small and/or very simple systems, the information needed to describe the system at the microscopic scale turns out to be impossible considering the large number of particles involved. In practice, such a description requires to determine and characterize all accessible microstates considering the external parameters imposed on the system. The exhaustive list of accessible microstates defines the partition function which contains all the microscopic information of the system. A partition function is function of one particular statistical ensemble. We mean by ensemble all the microscopic states that reach a macroscopic condition. As an example, without mentioning it, all what was explained before was in the microcanonical ensemble, where the volume, the number of molecules and the energy are constant. However, this fundamental ensemble is rarely suitable to describe physical experiments performed on adsorption and confinement of fluids in nanoporous materials. In this respect, another ensemble which proves to be very useful to consider is **the canonical ensemble** [94] where the number of particles N, the volume V and the temperature T of the system are constant. In other words, in this ensemble, all the microstates that correspond to constant N, V, and T form the canonical ensemble for a given system. In statistical mechanics, the probability to observe a particular microstate with an energy E_l is given by the corresponding Boltzmann factor:

$$P_l = \frac{exp(-E_l/k_\mathrm{B}T)}{\sum_{l'} \exp(-E_{l'}/k_\mathrm{B}T)} \tag{2.4}$$

The sum appearing in the denominator – the so-called partition function $Q_{N,V,T}$ (which also can be written $\mathcal{Z}$ in textbooks) in the canonical ensemble – is the function that ensures the normalization of the probability distribution:

$$\sum_l P_l = 1 \tag{2.5}$$

which leads to:

$$Q_{N,V,T} = \sum_l \exp(-E_l/k_B T) \tag{2.6}$$

In these expressions, the sum is performed over every microstate l accessible to the system considering the constraints imposed on the system (constant N, V, T). Most thermodynamic properties of the system treated in this ensemble can be derived from the partition function. This includes the total energy of the system:

$$\langle E \rangle = \sum_l P_l E_l = -\frac{\partial \ln Q_{N,V,T}}{\partial \beta} \tag{2.7}$$

with $\beta = 1/k_{\mathrm{B}}T$. As for the Helmholtz free energy, it is defined as:

$$F = -k_{\mathrm{B}}T \ln Q_{N,V,T} \tag{2.8}$$

Of particular interest in the context of the present thesis, **the Grand Canonical ensemble** [94] allows treating systems in which the system is at constant chemical potential μ (so that its conjugated thermodynamic variable N varies). Until now, we have considered the total number of particles N constant. However, for many systems such as those encountered when dealing with adsorption in porous materials, the total number of molecules N varies depending on the applied external conditions. The adequate ensemble to study the thermodynamics of these systems is the Grand Canonical ensemble in which the temperature T, the volume V and the chemical potential μ are kept constant. The probability P_l to find the system in a given microstate of energy E_l and with N_l particles is given by the corresponding Boltzmann factor:

$$P_l = \frac{\exp[-(E_l - \mu N_l)/k_{\mathrm{B}}T]}{Q_{\mu,V,T}} \tag{2.9}$$

where $Q_{\mu,V,T}$ (which can be written Ξ in textbooks) is the so-called partition function in the Grand Canonical ensemble. By definition $Q_{\mu,V,T}$ is written:

$$Q_{\mu,V,T} = \sum_l \exp[-(E_l - \mu N_l)/k_{\mathrm{B}}T] \tag{2.10}$$

In this ensemble, the average number of particles $\langle N \rangle$ is defined as:

$$\langle N \rangle = \frac{1}{\beta}\frac{\partial \ln(Q_{\mu,V,T})}{\partial \mu} \tag{2.11}$$

Similarly, the total energy $\langle E \rangle$ is:

$$\langle E \rangle = -\frac{\partial \ln Q_{\mu,V,T}}{\partial \beta} \tag{2.12}$$

Thermodynamic properties. In order to compute various thermophysical properties such as the density, viscosity and so on, statistical mechanics rely on the concept of ensemble average. As a simple example, let us take a single property corresponding to the observable $\mathcal{A}$. The ensemble average will be the average on all the N_s possible microscopic states l weighting by the probability P_l of having this particular state.

$$\langle \mathcal{A} \rangle = \frac{1}{N_s}\sum_{l=1}^{N_s} P_l \mathcal{A}_l \tag{2.13}$$

where $\mathcal{A}_l$ is the value of the computed observable in the microstate l. As can be seen from this expression, in ensemble averages, there is no explicit dependence on time t. However, in many experiments or molecular simulations, the system's properties are often realized using a time average – i.e. by probing the observable over a certain period of time – rather than using an ensemble average. The time average is expressed as the integral of the observable $\mathcal{A}(t)$ over time.

$$\overline{\mathcal{A}} = \lim_{\tau \to \infty} \frac{1}{\tau} \int_0^{\tau} A(t)dt \tag{2.14}$$

When the total sampling time τ is large enough, the time average $\overline{\mathcal{A}}$ is independent of the initial conditions. While ensemble and time averages rely on different expressions and underlying concepts, they are expected to be equal for a system at equilibrium. This is the essence of the fundamental principle known as ergodicity: for a system at equilibrium, considering the ensemble average of a given property over a large number of microscopic states at one time or the property averaged over a large period of time are equivalent:

$$\overline{\mathcal{A}} = \langle \mathcal{A} \rangle \tag{2.15}$$

2.1.2 Monte Carlo Methods

Monte Carlo (MC) method is a numerical method widely used to compute general properties of a system by computing ensemble average (Eq. (2.13)). It consists on sample the phase space randomly to get a set of representative microstates. In this thesis, this method was used to realise a numerical experiment of adsorption. We will detail the principle of the method and the reasons to use MC method rather than classical molecular dynamic. Then we will explain the Metropolis algorithm, first in the canonical ensemble (to simplify the understanding) and then in the Grand Canonical Ensemble (used in this thesis). Let us consider a system taken in the canonical ensemble (i.e. constant N, V, T). In a very large number of systems, the ensemble of microstates accessible cannot be considered explicitely as it involves a tremendous number of states, data, etc. In particular, for a system made up of particles that can occupy a continuum of positions and velocities, the number of microstates is infinite so that sums over microstates must be replaced by integrals. Let us consider a set of N particles whose positions and momenta are r^N and p^N. The corresponding density of probability to get particles in the configuration (r^N,p^N) in the canonical ensemble NVT is defined as [92, 94]:

$$\rho_{NVT}(r^N, p^N) = \frac{1}{Q_{N,V,T}} \frac{1}{h^{3N} N!} \exp(-\beta[U(r^N) + K(p^N)]) \tag{2.16}$$

where $U(r^N)$ and $K(p^N)$ are the potential and kinetic energies so that their sum is the system's total energy. h is Planck's constant which result from the continuous description while the term $N!$ accounts for the fact that the particles are indistinguishable [92]. The probability associated to $\rho_{NVT}(r^N, p^N)$ is directly: $p_{N,V,T}(r^N, p^N) = \rho_{NVT}(r^N, p^N)dr^N dp^N$. $Q_{N,V,T}$ is the partition function in the canonical ensemble. It can be define writing that the average of the probability $\rho_{NVT}(r^N, p^N)$ over all configuration must be equal to 1. It leads to:

$$Q_{N,V,T} = \frac{1}{h^{3N} N!} \int_{3N} \int_{3N} \exp(-\beta[U(r^N) + K(p^N)])dr^N dp^N \tag{2.17}$$

From the latter equation, it can be noticed that p^N is only involved in $K(p^N)$ and the two integrals can be separated. Using the theorem of equipartition, the kinetic energy can be written: $K(p^N) = p^2/2m$. The integral over p^N can be resolved using Gauss equation:

$$\int_{3N} \exp\left(-\beta K(p^N)\right) dp^N = \left[\int_{-\infty}^{+\infty} \exp(-\beta \frac{p^2}{2m})dp\right]^{3N} = \left(\sqrt{2\pi m k_B T}\right)^{3N} \tag{2.18}$$

Thus, replacing the integral over p^N in Eq. (2.17) using Eq. (2.18), we obtain a reduced form for $Q_{N,V,T}$:

$$Q_{N,V,T} = \frac{1}{\Lambda^{3N} N!} \int_{3N} \exp\left(-\beta U(r^N)\right) dr^N \tag{2.19}$$

where $\Lambda = h/\sqrt{2\pi m k_B T}$ is De Broglie's thermal wavelength. At constant temperature, Λ is fixed and so is the average value of the kinetic energy. As a result, considering that all molecular simulation methods used in this thesis were used at constant T, the rest of this brief introduction to the Monte Carlo methods in statistical mechanics will only consider the positions r^N [95].

Considering the complexity of this $3N$ dimension integral, the Monte Carlo methods in statistical mechanics were developed to compute this partition function. Let assume that we wish to compute a property as described earlier in this chapter. In a continuous description, the average property is given by:

$$\langle \mathcal{A} \rangle = \frac{\int \mathcal{A}(r^N) \exp[-\beta U(r^N)]}{Q_{N,V,T}} \mathrm{d}r^N \tag{2.20}$$

Computing $\langle \mathcal{A} \rangle$ can be done by sampling the phase space r^N to evaluate $\mathcal{A}(r^N)$ and $U(r^N)$ to estimate the ensemble average as defined in Eq. (2.20). However, even for small systems, it turns out to be very complex if not impossible as the number of evaluations scales as a power k^N. In this context, another sampling approach consists in targeting the sampling. Indeed, for systems such as a fluid, a large number of configurations occur with a very low probability distribution as they are unphysical: for example, strong steric repulsion forbids many configurations in the space phase (it would leads to a high potential energy $U(r^N)$ and thus the contribution of the integral will be quasi-zero). This is the spirit of Monte Carlo methods: targeted sampling is used to probe molecular configurations which correspond to those with the largest probability in the probability density distribution.

Metropolis method

The Metropolis algorithm was developed by Metropolis, Rosenbluth, Rosenbluth, Teller and Teller in 1953 [96, 97]. The principle proposed by these authors is to generate molecular configurations in the phase space following two rules:

1. A Markov chain is used to generate a large set of configurations. This implies that the configuration C_{i+1} in the chain only depends on the previous configuration C_i.
2. The generated configuration C_{i+1} is accepted or rejected according to a probability $\pi(i \to i+1)$.

Let us take a system under static equilibrium. As said previously, there is a large number of microstates which correspond to a given macrostate [95]. In order to maintain equilibrium , the probability that the system evolves from any microstate i to the microstate j must be equal to the probability that the system leaves the microstate j to reach any microstates i:

$$\sum_i p_i \pi_{i\to j} = \sum_i p_j \pi_{j\to i} \tag{2.21}$$

with p_i and p_j the probabilities to find the system in the state i or j, respectively, and $\pi_{i\to j}$ the probability for the system to evolve from the microstate i to the microstate j. As shown in Figure 2.2, in Monte Carlo simulations, evolution from a microstate to another can be achieved through molecule translation or rotation. In the Metropolis algorithm, an stricter rule is used: the concept of microreversibility. This fundamental principle states that the evolution from a particular microstate i to a particular microstate j is just as likely than the evolution from j to i:

$$p(r_i^N)\pi_{i\to j} = p(r_j^N)\pi_{j\to i} \tag{2.22}$$

The probability for the system to leave the i state to reach the j state $\pi_{i\to j}$ can be decomposed as:

$$\pi_{i\to j} = \alpha_{i\to j} \times P_{i\to j} \tag{2.23}$$

Indeed, as mentioned above, the evolution from a microstate to another depends on trial Monte Carlo moves. A trial move that drives the system from the microstate i to the microstate j should be attempted with a probability $\alpha_{i\to j}$ and accepted with a probability $P_{i\to j}$. In the case of translational and rotational moves in the canonical (N,V,T) ensemble, the matrix α is symmetrical with the condition $\alpha_{i\to j} = \alpha_{j\to i}$. Therefore, Eq. (2.22) can be written as:

$$\frac{P_{i\to j}}{P_{j\to i}} = \frac{p(r_j^N)}{p(r_i^N)} = \exp(-\beta[U(r_j^N) - U(r_i^N)]) \tag{2.24}$$

where r_i^N and r_j^N are the coordinates of the N particles in the microstates i and j, respectively. Similarly, $U(r_i^N)$ and $U(r_j^N)$ are the energies taken by the system in each of these two microstates. The solution chosen by Metropolis *et al.* for the acceptance probability – among other possibilities – is the following:

$$P_{i\to j} = min\left\{1, \Phi\right\} \text{ with } \Phi = \frac{p(r_j^N)}{p(r_i^N)} \tag{2.25}$$

As can be noted, this method bypasses the computation of the partition function $Q_{N,V,T}$ as already mentioned earlier. In practice, the Metropolis algorithm functions as follows:

- If the new microstate has a lower energy $U(r_j^N) < U(r_i^N)$, then $\Delta U = U(r_j^N) - U(r_i^N) < 0$ and $\exp(-\beta\Delta U) > 1$. The probability to accept the trial move is taken as $P_{i\to j} = 1$.
- If the new microstate has a lower energy $U(r_j^N) > U(r_i^N)$, then $\Delta U = U(r_j^N) - U(r_i^N) > 0$ and $\exp(-\beta\Delta U) < 1$. The probability to accept the trial move is taken as $P_{i\to j} = \exp(-\beta\Delta U)$.

To decide if the trial Monte Carlo move is accepted or not, considering the acceptance probability defined above in Eq. (2.25), the following approach is used. Let us take a trial move that drives the system from an energy state $U(r_i^N)$ to $U(r_j^N)$ with $U(r_j^N) > U(r_i^N)$. Then, $P_{i\to j} = \exp(-\beta[\Delta U])$. In order to reach a decision on acceptance/rejection, a random number ξ is generated uniformly in the interval [0,1]. If $\xi < P_{i\to j}$, the trial move is accepted, it is rejected otherwise. It can be shown that the probability of having $\xi < P_{i\to j}$ is directly $P_{i\to j}$. Let us now summarize the different steps of the Metropolis algorithm:

1. The system is taken with an initial configuration i. Its energy U_i is computed.
2. A particle is chosen at random and undergoes a trial move such as a translation or rotation.
3. The energy of the new configuration U_j is computed.
4. The trial move is accepted or rejected according to the probability $P_{i\to j} = min\left\{1, \exp[-\beta(U_j - U_i)]\right\}$

Monte Carlo technique in the Grand Canonical ensemble

In the Grand canonical ensemble, the number of molecules N in the system is not constant (in contrast, its conjugated variable – the chemical potential μ – is constant). Let us consider a system in equilibrium with a reservoir of particles which imposes its chemical potential μ and temperature T to the system. The system exchanges particles with the reservoir and, thus, the total energy of the system varies due to the variation of the number of particles. In practice, this implies that the total energy of the system includes a chemical potential contribution: $E = U + K + \mu N$ with U and K the potential and kinetic energies respectively, μ the chemical potential and N the number of particles. In order to give an expression for the partition function in the Grand Canonical ensemble, Frenkel and Smit considered an isolated system of volume V_0 composed of two subsystems, one of interacting particles of volume V exchanging particles with the reservoir of $V_0 - V$ volume. The complete demonstration can be found in Ref. [94]. In molecular simulation, particles are numbered and distinguishible. The term $1/N!$ will be then removed from the next equations. It can be shown that the density of probability to find the system in a configuration with N particles distributed according to the coordinate set r^N is given by:

$$\rho_{\mu,V,T}(N, r^N) = \frac{1}{Q_{\mu,V,T}} \frac{1}{\Lambda^{3N}} \exp[-\beta U(r^N)] \exp[\beta\mu N] \tag{2.26}$$

where we recall that Λ is De Broglie's thermal wavelength.
The partition function in the Grand Canonical ensemble $Q_{\mu,V,T}$ derives from the normalization of the probability defined in Eq. (2.26) over all the possible configurations. Thus, it includes a sum over the possible amount of particles, from 0 to $+\infty$. $Q_{\mu,V,T}$ is written as

$$Q_{\mu,V,T}(\mu, V, T) = \sum_{N=0}^{\infty} \int_{3N} \frac{1}{\Lambda^{3N}} \exp[-\beta U(r^N)] \exp[\beta\mu N] dr^N \tag{2.27}$$

We can also notice that the integral over p^N was reduced using the same equation than Eq. (2.18). The possible trial moves in the Grand Canonical ensemble are the displacement and rotation of a molecule like for the canonical ensemble. However, in this ensemble where the number of molecules N is not constant, the removal and addition of molecules – as illustrated in Figure 2.2 – are also acceptable trial moves as they respect the external constraints imposed on the system. In this section devoted to the Grand Canonical ensemble, we will not discuss the displacement or rotation of molecules as the procedure is the same as in the canonical ensemble. In contrast, we will focus on the insertion and deletion of molecules as they are specific to this ensemble. The microreversibility condition must also apply for these trial moves. Let us consider an initial configuration with N molecules and and proceed with the insertion of a molecule. The microreversibility rule can be written as:

$$\rho(r^N) dr^N \alpha_{N\to N+1} P_{N\to N+1} = \rho(r^{N+1}) dr^{N+1} \alpha_{N+1\to N} P_{N+1\to N} \tag{2.28}$$

We can write the probability $\alpha_{N\to N+1}$ to attempt the trial move as the product of the probability to chose an insertion over a deletion and the probability to insert the particle in the volume dr. In the case of non biased Monte Carlo, the probability of an insertion is the same than a deletion, thus:

$$\alpha_{N\to N+1} = \frac{1}{2} \frac{dr}{V} \tag{2.29}$$

with V the total volume. If we now consider $\alpha_{N\to N+1}$, we get:

$$\alpha_{N+1\to N} = \frac{1}{2}\frac{1}{N+1} \tag{2.30}$$

with the second term refers to the probability to choose one particle over $N+1$. From Eq. (2.28), we obtain:

$$\frac{P_{N\to N+1}}{P_{N+1\to N}} = \frac{\rho(r^{N+1})}{\rho(r^N)}\frac{dr^{N+1}\alpha_{N+1\to N}}{dr^N\alpha_{N\to N+1}} \tag{2.31}$$

$$= \frac{V}{(N+1)\Lambda^3}\exp(\beta\mu)\exp(-\beta[U(r^{N+1}) - U(r^N)]) \tag{2.32}$$

A possible solution for this condition, which is usually implemented in standard Grand Canonical Monte Carlo algorithm, is of the type:

$$P_{N\to N+1} = min\,\{1, \Phi\} \text{ with } \Phi = \frac{V}{(N+1)\Lambda^3}\exp(\beta\mu)\exp(-\beta[\Delta U]) \tag{2.33}$$

with $\Delta U = U(r^{N+1}) - U(r^N)$.
Similarly, it can be shown that the removal of a particle from the system should be accepted with the probability:

$$P_{N+1\to N} = min\,\{1, \Phi\} \text{ with } \Phi = \frac{\Lambda^3 N}{V}\exp(-\beta\mu)\exp(\beta[\Delta U]) \tag{2.34}$$

Then, in the spirit of the Metropolis algorithm for the canonical ensemble, the decision to accept or reject the trial move is made following the same procedure described earlier using random numbers.

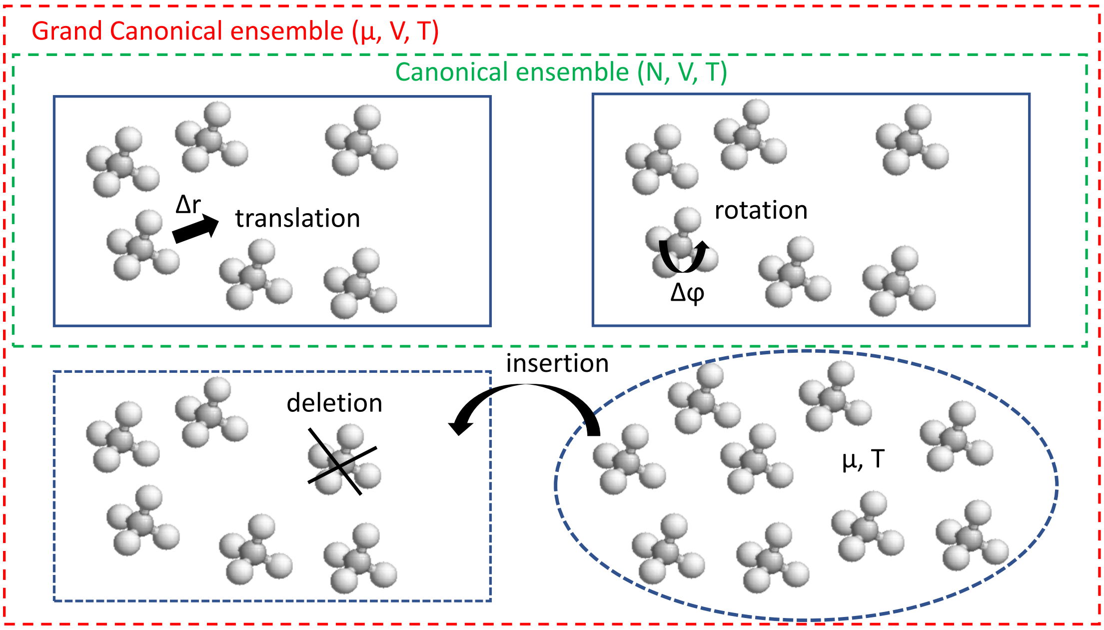

Figure 2.2: Monte Carlo trial moves. In the canonical ensemble (N, V, T) (green dashed lines), trial moves consist in translating or rotating a molecule. In the grand canonical ensemble (μ, V, T) (red dashed line), the system is in contact with a bulk reservoir (oval dashed line) which imposes its chemical potential μ and temperature T. The possible moves in this ensemble are translations and rotations as well as insertion or deletion of molecules.

2.1.3 Molecular dynamics

Molecular dynamics is the method of choice to investigate the dynamics of fluids confined in nanoporous materials. This well-known molecular simulation technique proceeds in a similar fashion as a typical experiment; the system evolution is monitored in time over a period of time [98]. Like for real experiments, the following aspects should be considered with caution:

- Sample initial preparation
- Thermodynamic conditions. For example, it must be ensured that the temperature remains constant during the 'numerical' experiment.
- Uncertainty issues which are sometimes important when the sampling time is insufficient for instance and/or the system size is too small.

In molecular dynamics, the time variable is discretized to solve in a discontinuous fashion Newton's equation:

$$\sum \mathbf{F}(t) = m\mathbf{a}(t) \tag{2.35}$$

where $\sum \mathbf{F}(t)$ are the sum of forces applied to a particle, m is the mass of the particle while $\mathbf{a}(t)$ is the acceleration of the particle. In practice, the following steps are followed:

- Define the force field that rule the intramolecular and intermolecular interactions between the molecules in the system. For the system used in this thesis, interactions are quite basics: a Lenard-Jones potential will be used to model zeolite/methane and methane/methane interactions while harmonic potential will be used for the flexibility of the matrix. This will be discussed in the Result part of the manuscript as this chapter is only focused on fundamentals of methods.
- Solve Newton's equation of motion by computing the position $\mathbf{r}$ and velocity $\mathbf{v}$ of each molecule at each time step.
- Monitor and record each molecule trajectory to compute thermodynamical and dynamical properties.

Verlet algorithm

Considering a set of N molecules, there are several algorithms that allow computing the equation of motions. Among the different strategies available, the Verlet algorithm is the most extensively used in the Physics and Physical Chemistry communities and even beyond [99]. Let us note Δt the discretized time step – the latter has to be small enough to apply the following Taylor expansion to express the position of a particle at time $t + \Delta t$.

$$\mathbf{r}(t+\Delta t) = \mathbf{r}(t) + \frac{d\mathbf{r}(t)}{dt}\Delta t + \frac{1}{2}\frac{d^2\mathbf{r}(t)}{dt^2}\Delta t^2 + \frac{1}{3!}\frac{d^3\mathbf{r}(t)}{dt^3}\Delta t^3 + O(\Delta t^4) \tag{2.36}$$

Similarly, we can write the same expansion for the particle position at time $t - \Delta t$.

$$\mathbf{r}(t-\Delta t) = \mathbf{r}(t) - \frac{d\mathbf{r}(t)}{dt}\Delta t + \frac{1}{2}\frac{d^2\mathbf{r}(t)}{dt^2}\Delta t^2 - \frac{1}{3!}\frac{d^3\mathbf{r}(t)}{dt^3}\Delta t^3 + O(\Delta t^4) \tag{2.37}$$

By adding Eqs. (2.36) and (2.37), we get:

$$\mathbf{r}(t+\Delta t) + \mathbf{r}(t-\Delta t) = 2\mathbf{r}(t) + \frac{d^2\mathbf{r}(t)}{dt^2}\Delta t^2 + O(\Delta t^4) \tag{2.38}$$

where Newton's equation motion imposes that $d^2\mathbf{r}(t)/dt^2 = \sum \mathbf{F}(t)/m$ ($\sum \mathbf{F}(t)$ is the sum of the forces applied to the molecule). From these equations, the position $\mathbf{r}(t)$ can be computed as:

$$\mathbf{r}(t+\Delta t) = 2\mathbf{r}(t) - r(t-\Delta t) + \frac{\sum \mathbf{F}(t)}{m}\Delta t^2 + O(\Delta t^4) \tag{2.39}$$

Interestingly, we notice here that the velocity $\mathbf{v}$ is not required to compute the position. Yet, the velocity can be computed using Eqs. (2.36) and (2.37) and omitting the third order term:

$$\mathbf{r}(t+\Delta t) - \mathbf{r}(t-\Delta t) = 2\frac{d\mathbf{r}(t)}{dt}\Delta t + O(\Delta t^3) \tag{2.40}$$

Finally, since $\mathbf{v}(t) = d\mathbf{r}(t)/dt$, we get:

$$\mathbf{v}(t) = \frac{\mathbf{r}(t+\Delta t) - \mathbf{r}(t-\Delta t)}{2} + O(\Delta t^3) \tag{2.41}$$

Thermostats

In molecular dynamics simulations, it is often needed to mimic physical conditions such as constant temperature environment. In particular, as the present PhD thesis aims at simulating systems in the canonical ensemble (i.e. at constant temperature T), we briefly discuss here thermostats employed in molecular dynamics simulatons (barostats can also be used in such numerical experiments but they will not be discussed here as this falls beyond the scope of the present manuscript) [98]. In molecular dynamics simulations, the temperature T is computed using the kinetic energy – i.e. from the particle velocities through the equipartition theorem in statistical mechanics:

$$\langle K \rangle = \frac{3}{2} N k_B T \tag{2.42}$$

The particle velocities fluctuate in time and so does the temperature. The idea of a thermostat in molecular dynamics is to find a physical algorithm that brings the average temperature of the system $\langle T \rangle$ around the desired temperature T_0.
The most intuitive method to apply a thermostat in molecular dynamics is to rescale the particle velocities. In that context, different thermostats can be highlighted.

Direct rescaling. Also called Gaussian thermostat, this method fixes the temperature and does not allow temperature fluctuations. Velocities are scaled at each time step according to:

$$v_i(t) = \sqrt{\frac{T_0}{T}} v_i(t-\Delta t) \tag{2.43}$$

with T_0 the desired temperature and T the computed temperature of the system at time t. The drawback of this method is that it introduces discontinuities in the phase space along p^N.

Andersen method. This method also rescales the particle velocities but using stochastic collisions [98]. The employed procedure is the following:

- Integrate the equations of motion until a characteristic time τ chosen to rescale the velocities.
- Select randomly a particle.
- Generate randomly its momentum from a Maxwell-Boltzmann distribution at the desired temperature T_0.

The main issue of this method is that it decorrelates velocities. Also, the dynamics of the system is necessarily biased so that the computing dynamical properties can be affected.

Berendsen thermostat. The Berendsen thermostat consists in weakly coupling the system with a heat bath at an imposed temperature [100, 101].The idea is to get a time evolution of the temperature proportional to the difference between the computed and desired temperatures:

$$\frac{dT}{dt} = \frac{(T_0 - T)}{\tau} \tag{2.44}$$

with τ the coupling time factor. If τ is large, the derivative of the temperature is small so that the system and thermostat are weakly coupled. On the other hand, if τ is small, the system and thermostat are strongly coupled. In general, τ has to be large enough to maintain the temperature constant but small enough to avoid strong perturbations of the system's dynamics. The drawback of this method is that the phase space distribution associated cannot be linked to the canonical ensemble.

Nosé Hoover thermostat. In contrast to direct rescaling or Andersen methods described above, the Nosé-Hoover thermostat described in Ref. [102, 103] does not rely on velocity rescaling but uses a heat bath at the desired temperature T_0. The main idea is to model the collisions between the heat bath particles and the system's particles by adding an external term to the forces applied to the system's particles. The approach is based on the use of an extended Lagrangian in which additional coordinates and velocities are involved [98]. Here, for the sake of simplicity, instead of deriving the whole problem, we will explain it using Newton's equation of motion [104]. In short, a friction term χ $[s^{-1}]$ which slows down or accelerates the particles in the system depending on the instantaneous temperature is added. This modified Newton's equation of motion can be written as:

$$m_i \frac{dv_i}{dt} = \sum f_i - \chi m_i v_i \tag{2.45}$$

where $\sum f_i$ is the sum of the physical forces applied to the particle i (i.e. all forces but the friction force that drives the system to the desired temperature). The derivative of the friction term is defined using the difference between the kinetic energy of the system and the thermal energy associated to the desired temperature T_0:

$$\frac{d\chi}{dt} = \frac{1}{Q}\left[\sum_{i=1}^{N} m_i \frac{v_i^2}{2} - \frac{3N+1}{2} k_B T_0\right] \tag{2.46}$$

where Q in J.s^2 refers to the speed of time response of the temperature fluctuation. The first term of the right side is the kinetic energy of the system provided by the actual temperature while the second term is the thermal energy imposed by the heat bath. The $N + 1$ factor counts the additional degree of freedom of the system. From the two latter equation, we notice that if the difference between the system's temperature and the desired one is large, the derivative of χ will be large and the system will reach faster the equilibrium temperature. And the other way around for $|T(t) - T_0|$ small. We notice that, in the steady state (i.e. $d\chi/dt = 0$), the kinetic energy writes as expected:

$$\langle K \rangle = \frac{3N+1}{2} k_B T_0 \tag{2.47}$$

The equation of motion in the Nosé-Hoover approach can be easily implemented in combination with the Verlet algorithm described above. In practice, within this PhD manuscript, the Nosé-Hoover thermostat was used to conduct the different molecular dynamics simulations.

2.2 Experimental methods

In this section, we will first detail principles of volumetric gas adsorption experiment that we used to load our system. In a second part, we will present fundamentals of neutron scattering and principles of use of the Time of Flight (TOF) experimental set up. Neutron experiments were used to determine dynamic properties of diffusion and transport of methane previously loaded in zeolite. The idea of this section is to give to the reader the main concepts and equations useful for the understanding of the results of this thesis.

2.2.1 Volumetric gas adsorption

Along with the gravimetric method, the volumetric (or manometric) adsorption measurement is a common method used to measure the adsorbed amount as a function of gas pressure. In our work, the experimental adsorption isotherms for methane in silicalite-1 were measured at different temperatures using a Hiden Isochema apparatus. Without being experts of this device, we provide the main principles about the volumetric adsorption measurement [105]. With this technique, the idea is to monitor the pressure in a system made up of a known calibration volume V_0, the sample holder V_1 and the sample (here a nanoporous material whose solid matrix volume will be called V_{skel}). The number of gas molecules which contribute to the pressure can be measured to estimate the adsorbed amount in the porous solid by comparing the pressure before and after adsorption. The exact procedure, which is detailed step by step below, is illustrated in Figure 2.3. For each step, the number of moles present in the system is accurately known from the pressure reading as the calibration volume V_0 is known. To do so, the volume V_0 is filled after closing the valve which links it to the sample holder. Assuming the adsorbing gas is ideal, the number of injected moles n_i is simply given by:

$$n_i = \frac{P_i V_0}{RT} \tag{2.48}$$

where P_i (in P_a) is the initial pressure, $R = 8.314$ J.mol^{-1}.K^{-1} the ideal gas constant and T the temperature in K. After this dosing step, the next step consists in measuring the sample holder volume V_1 without any solid sample using nitrogen gas. To do that, after having injected an initial number of moles n_i in V_0, the valve is opened and the final pressure P_f^{cal} obtained after equilibration is measured. The volume of the sample holder cell is directly computed as (Figure 2.3(a)):

$$V_1 = \frac{n_i RT}{P_f^{cal}} - V_0 \tag{2.49}$$

After this calibration step, the next step consists in measuring the dead volume by estimating the volume occupied by the solid skeleton of the nanoporous sample. In practice, this is achieved using He pycnometry. After having injected n_i moles of He in the calibration volume V_0, the valve is opened so that the He gas in the calibration volume flows towards the sample holder which contains the empty (i.e. non loaded) nanoporous sample. In this case, helium gas is used as it interacts very weakly with the porous material; as a result, it does not adsorb at room temperature. In other words, all He atoms injected in the system contribute to the pressure so that $n_f = n_i$ with n_f the final number of moles contributing to the pressure after equilibration. As the matrix skeleton occupies a certain volume in space, the corrected volume accessible to the gas is $V_0 + V_1'$ where V_1' can be inferred from the following ideal gas relationship as illustrated in Figure 2.3(b):

$$(V_0 + V_1') = \frac{RT n_i}{P_f^{pyc}} \tag{2.50}$$

with P_f^{pyc} the final pressure measured. The skeleton volume of the solid sample is directly obtained as $V_{skel} = V_1 - V_1'$ where we recall that V_1 is the known volume of the sample holder.

Finally, after all these calibration procedures, the adsorbed amount of methane in silicalite-1 as a function of the gas pressure can be measured as follows. An initial amount of moles n_i is injected in the calibration volume V_0. Then, the valve is opened and part of the injected molecules get adsorbed inside the zeolite porosity as illustrated in Figure 2.3(c). This adsorbed amount n_a does not contribute to the pressure measured in the set-up. In contrast, the amount of gas that contributes to the pressure n_f can be computed using the final pressure in the system P_f^{ads}:

$$n_f = \frac{P_f^{ads}(V_0 + V_1')}{RT} \tag{2.51}$$

The adsorbed amount is readily obtained as $n_a = n_i - n_f$. The adsorption isotherms measured in the framework of this thesis were realized at different temperature as discussed in more details in Chapter 3. The pressure measurement set up was coupled with a cryostat which allowed us to impose a temperature down to 225 K and up to 300 K.

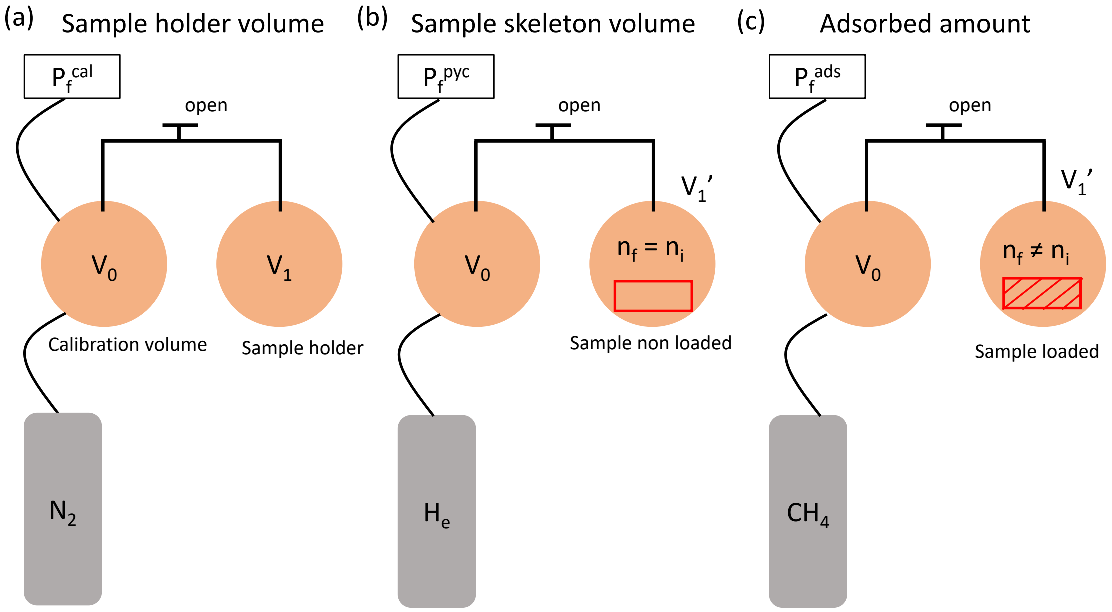

Figure 2.3: Volumetric adsorption technique. Several steps have to be taken into account: measuring the sample holder volume (a), measuring the sample skeleton volume (b) before measuring the the adsorbed amount (c).

2.2.2 Neutron scattering

In contrast with microscopy techniques which allow to study a localised area of a sample, neutron scattering technique as other radiation methods (for example X-ray or light) allow to involve an important number of atoms (as the radiation irradiate the whole sample). It allows to get an important statistic that is necessary to compute system's properties. As it will be explained in this section, neutrons are interesting over light or X-ray diffusion because they are probing both individual atoms motions but also collective behavior. In this section, we will first provide the fundamental framework for understanding neutron scattering and then we will describe the experimental set up used in this thesis. The detail of the experiments performed, the samples used and the models used for analysing neutron data will be presented in the Result part.

Neutron properties

Neutrons can be considered using the dual particle/wave framework [106]. They are particles without any charge, they possess a mass $m = 1.6610^{-27}$ kg, they have a kinetic energy, directly link to their velocities $E_{Kin} = 1/2mv^2$ and to the temperature in which they are thermalized $E_{Kin} = 3/2k_BT$ (with k_B the Boltzmann constant). They compose nucleus of atoms but they can also be separated from a nucleus by nuclear reaction in order to get a beam of "free" neutrons for scattering experiments. They also can be considered as a wave with a certain wavelength $\lambda = h/mv$ (with h the Planck constant) and a certain wave vector $\mathbf{k}$. As their wavelength is similar to molecular size, interatomic distances or crystal cell distances and energies similar to those involved in molecular displacements (phonon, diffusive relaxations...), they are a unique tool to probe the matter and its dynamic properties. According to the range of distances that ones want to probe during neutron experiment, neutrons are thermalized to reach the energy E involved in the molecular displacements: they are thermal if $E \sim 0.025$ eV, hot if $E \sim 0.2$ eV and cold if $510^{-5} < E < 0.025$ eV. In our case, we used a wavelength of $\lambda = 5.1$ Å. The associated average velocity is then:

$$v = \frac{h}{\lambda m} = 783m.s^{-1} \tag{2.52}$$

with $h = 6.62610^{-34}\mathrm{m}^2.\mathrm{kg}.\mathrm{s}^{-1}$ the Planck constant and m the mass. To reach this velocity, the neutron have to be thermalized at the temperature:

$$T = \frac{1}{3}\frac{mv^2}{k_B} = 25K \tag{2.53}$$

with k_B the Boltzmann constant. As it will be discussed later, neutrons have a particular sensitivity to H. Thus, in order to study methane diffusion in zeolite sample, we have used the cold neutron time of flight spectrometer (TOF) IN6/SHARP at the ILL. The following of this section will be about detailing principles of neutrons for studying diffusion and the TOF set up used.

Neutron/nucleus interaction. When a neutron interacts with a nucleus, two phenomena can happen, depending on the exciting level of the nucleus and the neutron energy:

- Absorption of the neutron and modification of the nucleus
- Scattering of the neutron with a modification of its momentum and velocity direction.

The interaction potential neutron/nucleus is short range. As neutrons do not have charges, they interact with nucleus through spins because of the strong interactions represented by the Fermi pseudo potential. When a neutron diffuses on a nucleus, the diffusion is isotropic and can be characterized by b, the scattering length which represents the strength of the interaction. This quantity depends on the spin of both the neutron and the scattered nucleus. From the scattering length, we can introduce the coherent and incoherent scattering:

- b_i^{coh}: coherent scattering length which is the average over all the diffusive nucleus. This would be the scattering length if the neutron would have evolved in a average interaction potential. This is intrinsically a collective property.

- b_i^{inc}: square deviation to the average. This term is added to b_i^{coh} and reports the fact that neutrons are not evolving in an average potential. It corresponds to the individual and non coordinated motion of molecules.

Because of the spin state differences, the scattering length varies for different chemical species but also between the different isotopes of a same species. From the scattering length, we can define the cross-section σ. σ_{scat} is defined as the scattering probability for a neutron to diffuse after a collision with a nucleus (similarly σ_{ads} is the probability of adsorption). σ_{scat} can be defined by the number of scattering process I_{scat} considering an incident beam I_0:

$$I_{scat} = I_0 \sigma_{scat} \tag{2.54}$$

The cross-section can also be seen as a geometric quantity as it is the surface that should have the nucleus to reproduce the probability of scattering during a collision. For this reason, the cross-section unity is the barn (1 b = 10^{-28} m^2). The cross section and the scattering length are linked:

$$\sigma_{scat} = 4\pi \langle b^2 \rangle \tag{2.55}$$

and can be separated in coherent and incoherent terms:

$$\sigma_{scat} = \sigma_{inc} + \sigma_{coh} = 4\pi b_{inc}^2 + 4\pi b_{coh}^2 \tag{2.56}$$

The relative part of coherent and incoherent cross section can vary a lot according the interacting particles. An interesting example is the hydrogen atom. In its common form, the hydrogen atom has 1 proton ^{1}H while the deuterium (i.e. hydrogen isotope) has 1 neutron and 1 proton ^{2}H. However, even if these two isotopes are the same chemical element with (nearly) similar properties, their cross sections are very different [106]. For the common hydrogen, we get:

$$\sigma_{inc}(^1\mathrm{H}) = 79.9 \text{ barns}$$

$$\sigma_{coh}(^1\mathrm{H}) = 1.8 \text{ barns}$$

$$\sigma_{scat}(^1\mathrm{H}) = 81.7 \text{ barns}$$

While for the deuterium, the reference values are:

$$\sigma_{inc}(^2\mathrm{H}) = 2.04 \text{ barns}$$

$$\sigma_{coh}(^2\mathrm{H}) = 5.6 \text{ barns}$$

$$\sigma_{scat}(^2\mathrm{H}) = 7.64 \text{ barns}$$

We can notice the large part of incoherent cross section of the hydrogen. It is because hydrogen spin is mainly incoherent. This property makes incoherent scattering a privileged method for studying individual motion and properties in hydrogenous compounds. On the other hand, we can notice that the coherent cross section of the deuterium is almost 3 times its incoherent cross section. Thus, to study collective properties by neutron coherent scattering, it is mandatory to use deuterated compounds.

Scattering experiment: important parameters

In a neutron scattering experiment, a sample is illuminated with an incident neutron beam where neutrons possess an initial energy E_0 and an initial wave vector $\mathbf{k}_0$. After interacting with the atoms of the sample, neutrons are scattered in all directions of space (as the scattering is isotropic). The scattering vector $\mathbf{q}$ (i.e. momentum transfer) is the vector difference between the scattered vector $\mathbf{k}$ and the initial one $\mathbf{k}_0$: $\mathbf{q} = \mathbf{k} - \mathbf{k}_0$. The energy gain or loss can be measured: $\Delta E = \hbar\omega = E - E_0$. In Time Of Flight (TOF) experiments, neutrons are then detected by detectors that record the time when neutrons reach detectors as well as the scattered angular position. Several specific cases can be notified:

- $E = E_0$ and $|\mathbf{k}| = |\mathbf{k}_0|$: there is no modification of the neutron energy; the collision in elastic (blue arrow in Figure 2.4(b)). Scattered neutrons will collide the detectors at the same time than non scattered neutrons.
- $E < E_0$ and $|\mathbf{k}| < |\mathbf{k}_0|$: there is a loss in the neutron energy; the collision is inelastic (green arrow in Figure 2.4(b)). Neutrons will collide the detectors later than elastic scattered neutrons.
- $E > E_0$ and $|\mathbf{k}| > |\mathbf{k}_0|$: there is a gain in the neutron energy; the collision is inelastic (red arrow in Figure 2.4(b)). Neutrons will collide the detectors earlier than elastic scattered neutrons.
- $E \sim E_0$ and $|\mathbf{k}| \sim |\mathbf{k}_0|$: the gain or loss of energy is weak; the collision is named quasi-elastic.

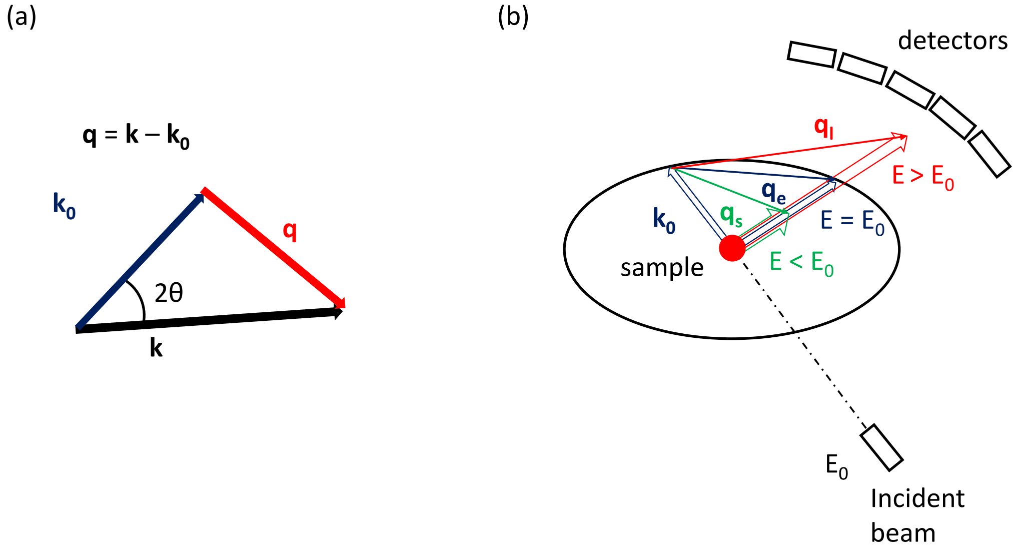

Figure 2.4: Principle of neutron scattering experiment. (a) The scattering vector $\mathbf{q}$ is the difference between the scattered wave vector $\mathbf{k}$ and the incident wave vector $\mathbf{k}_0$. The angle between the two vectors is 2θ. (b) [Adapted from Ref [106].] A neutron incident beam with an energy E_0 and a wave vector $\mathbf{k}_0$ interact with a sample. The scattering process can be elastic $E = E_0$ and $|\mathbf{k}| = |\mathbf{k}_0|$ (in blue) or inelastic with an energy loss $E < E_0$ and $|\mathbf{k}| < |\mathbf{k}_0|$ (in green) or inelastic with a gain in energy $E > E_0$ and $|\mathbf{k}| > |\mathbf{k}_0|$ (in red).

The several scattering regimes (elastic/inelastic/quasi-elastic) do not probe the same molecular motions as shown Figure 2.5(a). This will be discussed below after introducing the scattering functions.

Scattering functions

The classical formalism used for studying neutron scattering lies on the Van Hove functions $G(\mathbf{r},t)$ [107]. $G(\mathbf{r},t)$ is the probability, knowing the initial position **r'** of a particle at the initial time $t=0$, to find another particle at the position $\mathbf{r}$ at the time t. If we consider N diffusive particles, the correlation function $G(\mathbf{r},t)$ can be written:

$$G(\mathbf{r},t) = \frac{1}{N}\int \langle \rho(\mathbf{r'},0)\rho(\mathbf{r'}+\mathbf{r},t)\rangle d\mathbf{r'} \tag{2.57}$$

$\rho(\mathbf{r},t)$ is the density distribution of the system $\rho(\mathbf{r},t) = \sum_{i=1}^{N}\delta(\mathbf{r}(t)-\mathbf{r}_i(t))$ with $\mathbf{r}_i(t)$ the position of the particle i at the time t. $\langle ... \rangle$ denotes the time average. From the correlation function in the real space, several neutron scattering functions can be derived. They are all linked by Fourier transforms and reverse Fourier transforms. The intermediate scattering function $F(\mathbf{q},t)$ is the Fourier transform in space of $G(\mathbf{r},t)$:

$$F(\mathbf{q},t) = \int G(\mathbf{r},t)\exp(i\mathbf{q}\cdot\mathbf{r})d\mathbf{r} \tag{2.58}$$

By replacing $G(\mathbf{r},t)$ using Eq. (2.57), we get a double integral:

$$F(\mathbf{q},t) = \frac{1}{N}\int\int \langle \rho(\mathbf{r'},0)\rho(\mathbf{r'}+\mathbf{r},t)\exp(i\mathbf{q}\cdot\mathbf{r})d\mathbf{r'}d\mathbf{r} \tag{2.59}$$

If we replace the density distribution by its expression, we get:

$$F(\mathbf{q},t) = \frac{1}{N}\sum_{i=1}^{N}\sum_{j=1}^{N} I \tag{2.60}$$

with I the double integral:

$$I = \int\int \langle \delta(\mathbf{r'}-\mathbf{r}_i(0))\delta(\mathbf{r'}+\mathbf{r}(t)-\mathbf{r}_j(t))\rangle \exp(i\mathbf{q}\cdot\mathbf{r})d\mathbf{r'}d\mathbf{r} \tag{2.61}$$

Then, we can look for the conditions that I has to reach in order to be different than zero:

- If $\mathbf{r'}=\mathbf{r}_i(0)$, $\delta(\mathbf{r'}-\mathbf{r}_i(0))=1$ otherwise $\delta(\mathbf{r'}-\mathbf{r}_i(0))=0$.
- If $\mathbf{r'}+\mathbf{r}(t)=\mathbf{r}_j(t)$, $\delta(\mathbf{r'}+\mathbf{r}(t)-\mathbf{r}_j(t))=1$, otherwise $\delta(\mathbf{r'}+\mathbf{r}(t)-\mathbf{r}_j(t))=0$.

Then in order to get a non zero integral I, the two conditions have to be reached: $\mathbf{r'}=\mathbf{r}_i(0)$ and $\mathbf{r'}+\mathbf{r}(t)=\mathbf{r}_j(t)$. It leads to get $r(t)=\mathbf{r}_j(t)-\mathbf{r}_i(0)$. Then, $I = \langle \exp(i\mathbf{q}\cdot\mathbf{r}_j(t))\exp(-i\mathbf{q}\cdot\mathbf{r}_i(0))\rangle$ and we get the following expression:

$$F(\mathbf{q},t) = \frac{1}{N}\sum_{i=1}^{N}\sum_{j=1}^{N}\langle \exp(i\mathbf{q}\cdot\mathbf{r}_j(t))\exp(-i\mathbf{q}\cdot\mathbf{r}_i(0))\rangle \tag{2.62}$$

We can also derive the dynamic structure factor by taking the Fourier transform in space and time of $G(\mathbf{r},t)$:

$$S(\mathbf{q},\omega) = \frac{1}{2\pi}\int\int G(\mathbf{r},t)\exp(i(\mathbf{q}\cdot\mathbf{r}-\omega t)d\mathbf{r}dt \tag{2.63}$$

The static structure factor is defined as the integral over the whole energy range:

$$S(\mathbf{q}) = \int S(\mathbf{q}, \omega) d\omega \tag{2.64}$$

From these functions, we can define the self or incoherent correlation function $G_s(\mathbf{r}, t)$ which is the probability to find a particle at the position $\mathbf{r}$ at the time t knowing that the **same** particle was at the position **r'** at the initial time. With the correlation of position of an individual particle, we are looking at individual motion instead of looking at collective motion with $G(\mathbf{r}, t)$. In the same way, the incoherent intermediate scattering function $F_{inc}(\mathbf{q}, t)$ can be written using the average on all the particles:

$$F_{inc}(\mathbf{q}, t) = \frac{1}{N} \sum_i \langle \exp[-i\mathbf{q} \cdot (\mathbf{r}_i(t) - \mathbf{r}_i(0))] \rangle \tag{2.65}$$

We find the same expression for $F_{inc}(\mathbf{q}, t)$ than Eq. (1.30). We recall that the incoherent dynamic structure factor $S_{inc}(\mathbf{q}, \omega)$ is the time Fourier transform of $F_{inc}(\mathbf{q}, t)$ (Eq. (1.33)). However in neutron experiments, the sum of both coherent and incoherent contributions is measured in the scattered intensity. To separate the contributions and thus getting the separated dynamics, the coherent and incoherent terms have to be weighted. Thus, the intermediate scattering function is written:

$$F(\mathbf{q}, t) = \sum_{i,j} b_i^{coh} b_j^{coh} \langle \exp[-i\mathbf{q} \cdot (\mathbf{r}_i(t) - \mathbf{r}_i(0))] \rangle + \sum_i (b_i^{inc})^2 \exp[-i\mathbf{q} \cdot (\mathbf{r}_i(t) - \mathbf{r}_i(0))] \tag{2.66}$$

where b_i^{coh} and b_j^{coh} are the coherent scattering lengths of the atoms i and j respectively and b_i^{inc} the incoherent scattering length of the atom i. In this expression, the first term refers to the collective or coherent intermediate scattering function while the second term correspond to the self or incoherent intermediate scattering function.

Quasi elastic neutron experiments

As explained before, because of the similarity between neutron energy and energy involved in molecular motions, neutrons are suitable to probe the molecular dynamic. Indeed, several kind of motions can be distinguished. Figure 2.5(a) shows schematic representation of the scattering function $S(\mathbf{q}, \omega)$ and the molecular motions associated according the energy involved. At $E = 0$, there is no exchange of energy between the incident neutron and molecules. It physically means that the nuclei are immobile and the representative function is a dirac centred in $E = 0$. Near to the elastic peak, ~ 0.1 meV, neutrons are probing very slow motions as the energy exchange is low. It corresponds to molecular displacement (i.e. translations) and it leads to a broadening of the elastic peak. This regime is called quasi-elastic (it is going up to few meV). At higher energy range ~ 1 meV, molecular motions such as rotations are faster. It can still be probed by quasi-elastic scattering method as we are going to discuss in the Chapter 4. At even higher energy, other mechanisms can be observed such as phonon displacement or molecular vibrations. The regime above 1 meV is referred as spectroscopic and can be probed by inelastic scattering.
Molecular motions happen on separated energy and length scales. This is the reason why correlation functions can be taken separately for representing every different motion [106]. Thus, in order to describe the motion of an individual molecule, the total scattering function $S_{inc}^{tot}(\mathbf{q}, \omega)$ can be written as the convolution of each scattering functions describing a particular motion:

$$S_{inc}^{tot}(\mathbf{q}, \omega) = S_{inc}^{rot}(\mathbf{q}, \omega) * S_{inc}^{trans}(\mathbf{q}, \omega) * S_{inc}^{vib}(\mathbf{q}, \omega) \tag{2.67}$$

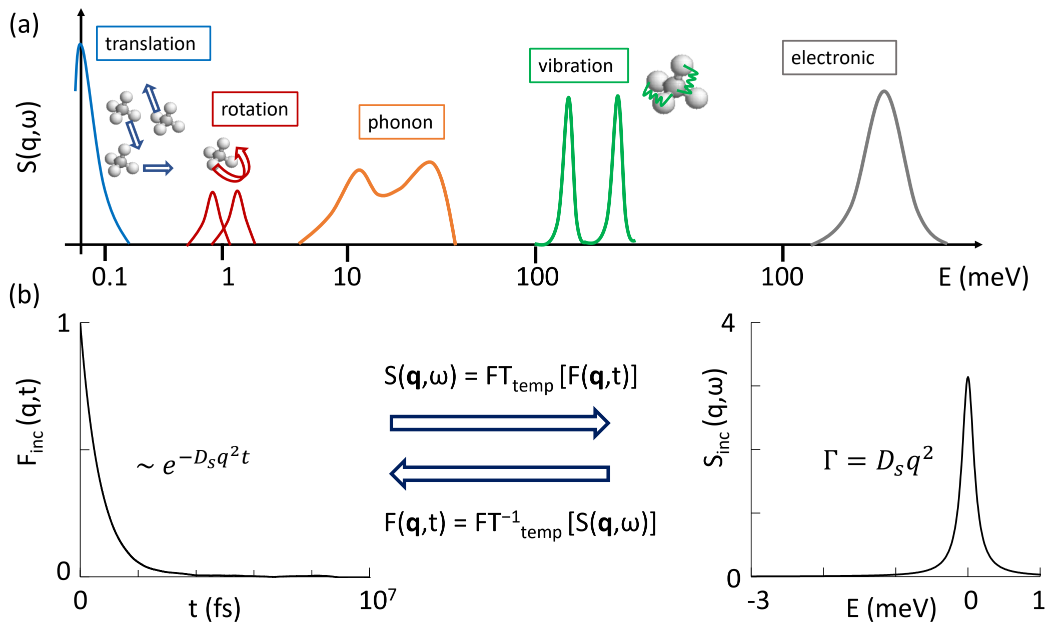

Figure 2.5: (a) [Adapted from Ref. [108].] Different molecular motions accessible according the energy range considered. Quasi elastic neutron scattering allows to look at the energy range up to few meV. (b) [Adapted from Ref. [109].] On the left side, the incoherent intermediate scattering function $F_{inc}(\mathbf{q},t) \sim \exp(-D_s q^2 t)$ for long range translational motion. The corresponding dynamic structure factor in the energy domain is a Lorentzian function whose Half Width at Half Maximum (HWHM) is equal to $D_s q^2$.

with $S^{rot}_{inc}(\mathbf{q},\omega)$, $S^{trans}_{inc}(\mathbf{q},\omega)$ and $S^{vib}_{inc}(\mathbf{q},\omega)$ the scattering functions associated to the rotation, translation and vibration respectively. In the following, we will give some description of these three components.

Diffusive molecular displacement. If we consider the displacement of a molecule over "large" time τ, the molecule is going to change its velocity and direction several times because of collisions with other molecules or even other events which can happen in the system. If the considered time is large enough for the molecule to have lost the information of the initial time, the regime reached is referred as Fickian and the incoherent correlation function $G_{inc}(\mathbf{r},t)$ is the solution of the equation:

$$\frac{\partial G_{inc}(\mathbf{r},t)}{\partial t} = D_s \nabla^2 G_{inc}(\mathbf{r},t) \tag{2.68}$$

This leads to the same solution than Eq. (1.25). Indeed, we are looking at the same phenomenon. In this regime, the Fourier transform in space of $G_{inc}(\mathbf{r},t)$ leads to an exponential form of the incoherent scattering function $F_{inc}(\mathbf{q},t) \sim \exp(-D_s q^2 t)$. Then, the Fourier transform in time of $F_{inc}(\mathbf{q},t)$ leads to the incoherent dynamic structure factor $S^{trans}_{inc}(\mathbf{q},t)$ with a Lorentzian form:

$$S_{inc}(\mathbf{q},\omega) = \frac{1}{\pi}\frac{D_s \mathbf{q}^2}{\omega^2 + (D_s \mathbf{q}^2)^2} \tag{2.69}$$

with a Half Width at Half Maximum (HWHM) equal to HWHM= $D_s q^2$ as shown in Figure 2.5(b). The self diffusion coefficient can be measured by plotting the HWHM in function of q^2. It will be detailed in the Results part.
However, if we look at smaller time scale, discrepancies to the Fickian regime are observed [74]. It is observed with large $\mathbf{q}$ scattering vectors (i.e. small distances). In this

case, the jump diffusion model (first developed by Chudley and Elliott in their paper [110]) assumes that a particle stays on a site for a certain time τ_0 before jumping to an other one separated by a distance $\mathbf{d}$. The particle has n jump possibilities. In this case, the dynamic structure factor writes as:

$$S(\mathbf{q},\omega)=\frac{1}{\pi}\frac{HWHM}{\omega^2+HWHM^2} \tag{2.70}$$

Here, the HWHM is not $D_s q^2$ anymore but has the following form:

$$HWHM=\frac{1}{n\tau_0}\sum_d[1-exp(-\mathbf{q}\cdot\mathbf{d})] \tag{2.71}$$

At small $\mathbf{q}$ values, the model join the Fick's law HWHM= $q^2d^2/6\tau = D_s q^2$. Other models for studying diffusion at small distances have been summarized by H.Jobic in Ref. [74].

Molecular rotation. If we consider a rotation of a molecule over a sphere in a confined media, the time Fourier transform of the solution of the differential equation on the orientational distribution is the rotational structure factor [111]:

$$S_{inc}^{rot}(\mathbf{q},\omega)=A_0(\mathbf{q})\delta(\omega)+\sum_{l=1}^{\infty}A_l(\mathbf{q})L_l^{rot}(\mathbf{q},\omega) \tag{2.72}$$

where $A_0(\mathbf{q})$ governs the intensity of the elastic term and $A_l(\mathbf{q})$ are the quasi-elastic structure factors which occur because of the quasi-elastic contributions. L_l^{rot} correspond to a Lorentzian function with a HWHM^{rot} directly proportional to the rotational coefficient D_r: HWHM^{rot} $=2D_r$. The rotational coefficient (in s^{-1}) is q independent.

Molecular vibration. Without going into too much details, in order to take into account vibrationnal dynamic of molecules, ones represents a system of N atoms represented by 3N harmonic oscillators. The vibrationnal scattering function is the sum of dirac functions centered on frequencies corresponding to vibrationnal modes:

$$S_{inc}^{vib}=\left[\sum_j \alpha_j\delta(\omega-\omega_j)+\delta(\omega)\right]\times DW(q) \tag{2.73}$$

with α_j inelastic terms and $DW(q)$ the Debye-Waller factor. The Debye-Waller factor will be used in the functions used to model our data as it weights the elastic intensity. For isotropic diffusion in three dimensions, the Debye-Waller factor can be written:

$$DW(\mathbf{q})=\exp(-q^2\langle u^2\rangle/3) \tag{2.74}$$

with $\langle u^2\rangle$ the mean square displacement of vibrating molecules.

EISF function If we consider the individual dynamic of a particle in a confined media through $F_{inc}(\mathbf{q},t)$: after a perturbation at $t=0$, the system is back to equilibrium at $t=+\infty$. Then, we can consider the Elastic Incoherent Structure Factor (EISF) is the elastic contribution of the elastic peak and relates the region of space accessible to the particle $F_{inc}(\mathbf{q},t=+\infty)$ at equilibrium. It can give information on confinement volume of a particle.

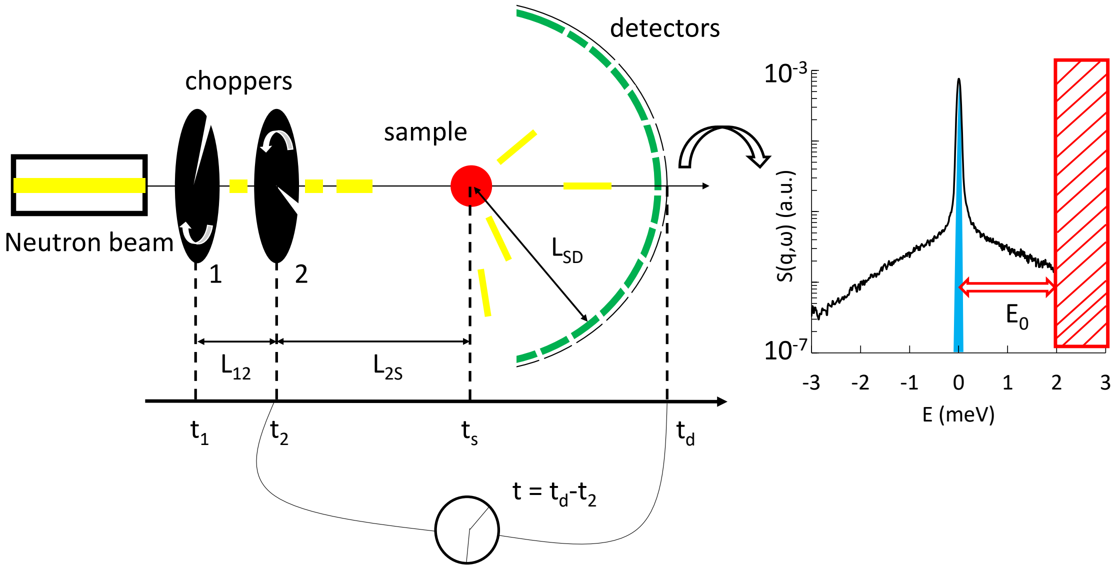

Figure 2.6: Schematic experimental set up and measurement principle. A neutron beam lighten a sample after passing through 2 choppers used for selecting the desired neutron wavelength. Neutrons are then scattered in all direction until reaching detectors which are placed all around the sample (at the same distance L_{SD}). The time t between the time when the neutron leaves the second chopper and reaches a detector is measured. The neutron is counted in the n^{th} channel using the time discretization $t = n\Delta\tau$. The data in the time domain is then transform into energy domain as explained in the core of the text. The spectrum at the right is the output of the experiment at a given angle. In blue the resolution of the spectrometer and in orange, the unavailable energy range.

Experimental set up

In order to realise neutron scattering experiments, we used the Time of Flight spectrometer IN6/SHARP at the Institute Laue Langevin (ILL). In the following, we will present the principle of the measurement and the limitation associated to the measure.

Neutron production. Neutrons are produced by the process of nuclear fission in the experimental nuclear reactor at the ILL. The fuel used in the core of the reactor is enriched uranium [112]. In a fission process, an uranium atom adsorbs a neutron after a collision. The nucleus produced is unstable and separates into two new nucleus. In this process, two neutrons are produced as well as thermal energy. The two neutrons are then going to create new fission processes with other uranium atoms: it is the nuclear chain reaction. In contrast with producing nuclear plant, at the ILL experimental reactor, the thermal energy is not used and is evacuated heating the Drac river in Grenoble. Moreover, neutrons produced in fission reactions are very fast (2×10^7 m.s^{-1}) while the experiments need slower neutrons (in our case, we estimated neutron velocity from Eq. (2.52) at 783 m.s^{-1}). In order to reach the desired velocities, neutron are slowed down using a cold source. It consists on liquid deuterium source with an imposed temperature chosen to reach the desired neutron energy. Once neutrons are thermalized, they are collected from the tank using neutron guides to experimental set up.

Time of flight set up. In such experiments, the main goal of the measurement is to count the number of neutrons scattered by the sample in function of the scattering angle

θ (related to the scattering vector $\mathbf{q}$) and the time for the neutron to travel up to each detector [109].

The first step is to select neutrons with the desired wavelength λ: the step is called monochromatization. There are several ways to realize the monochromatization. An elegant way used in TOF/TOF set up consists on two counter-rotating choppers positioned on the neutron beam axe (Figure 2.6). Choppers are neutrons absorbing disks except they possess a slit that allows a small amount of neutrons to pass through them. The second chopper is out of phase with a constant angle ϕ. The distance between the two choppers is also constant: L_{12}. Therefore, only neutrons with a specific speed and thus a specific wavelength will be allowed to pass through the two choppers. The other wavelengths are going to be adsorbed.

IN6/Sharp is a time focusing spectrometer where the monochromatization is realized using three composite pyrolytic graphite monochromators [113] and a Fermi chopper. The neutron beam is diffracted by the graphite monochromators, following Bragg conditions. As a result, four wavelengths close to each other (4.1 Å, 4.6 Å, 5.1 Å, 5.9 Å) are selected. A beryllium filter is positioned after the monochromators in the beam axe to cut the second order reflexion (i.e. in the Bragg law n$\lambda = 2d\sin(\theta)$ with λ the wavelength, d the lattice spacing and θ the scattering angle, the second order corresponds to n=2). The time focusing condition imposes that for all the four wavelength, neutrons reach detector at the same time for elastic scattering. To achieve this condition, the beam is pulsed by a Fermi chopper which possesses multiple slits. It allows to let neutrons pass at different time according their wavelength in a such way that the above condition is matched. Moreover, to avoid frame-overlap, an other chopper is placed before the Fermi one and rotates in phase with a speed n times slower (n integer).

Then the second important step is the detection of neutrons depending on the momentum transfer q and the energy E. The time space is discretized in n time channels of width $\Delta\tau$ which depends on the monochromatization. Thus, the time is $t = n\Delta\tau$. The neutron travel time t (i.e. the time for the neutron to browse the distance $L_{2S} + L_{SD}$) is measured and the neutron is counted in the n^{th} channel associated. We can notice that knowing the incident wavelength and neutron velocity, we can know the travel time t_0 of elastic scattered neutron (i.e. no energy modification). According to the angular position of the detector around the sample and the time/energy transfer, the scattering vector $\mathbf{q}$ is recovered. Now in order to get the dynamical structure factor from the measurement, we need to introduce more formal definitions. The measurement by unit of solid angle $d\Omega$ and arrival time dt of the neutrons onto a detector is link to the differential cross section by energy $d\omega$ and solid angle $d\Omega$ through:

$$\frac{d^2\sigma}{d\Omega dt} = \frac{d\omega}{dt}\frac{d^2\sigma}{d\Omega d\omega} \tag{2.75}$$

Moreover, $d^2\sigma/d\Omega d\omega$ is connected to the dynamic structure factor using:

$$\frac{d^2\sigma}{d\Omega d\omega} = N\frac{k_f}{k_0}\frac{\sigma}{4\pi}S(\mathbf{q},\omega) \tag{2.76}$$

$$= N\frac{k_f}{k_0}\frac{\sigma}{4\pi}[\sigma_{coh}S_{coh}(\mathbf{q},\omega) + \sigma_{inc}S_{inc}(\mathbf{q},\omega)] \tag{2.77}$$

with k_f and $\mathbf{k}_0$ the final and incident wave vectors respectively while $S_{coh}(\mathbf{q},\omega)$ and $S_{inc}(\mathbf{q},\omega)$ the coherent and incoherent structure factor. The associated energies are link using $k_{f,0} = \sqrt{E_{f,0}2m/\hbar^2}$ with m the mass of a neutron. We also have $\hbar\omega = E_f - E_0$ and $E_f = 1/2mv_f^2$. Moreover, using the experimental set up geometry (Figure 2.6), we know that:

$$v_f = \frac{L_{SD}}{t} \tag{2.78}$$

By using these different equations, we can link the dynamic structure factor to the direct measurement $d^2\sigma/d\Omega dt$.

Resolution and instrumental limitations. Figure 2.6 shows a typical scattering function $S(\mathbf{q},\omega)$ recorded by a TOF spectrometer. One of the limitation when it comes to observe molecular motions is the energy range. The accessible windows depends on the instrument (i.e. using cold, thermal or hot neutrons with different energy range associated) and the resolution depends on the chopper used. Then, if the observed motion is too fast, the energy transfer is large and the signal is lost in the background. On the other hand, if the molecular motion is too slow, the energy transfer can be lower than the instrumental resolution and the signal is indistinguishable from it. Indeed, the elastic peak is not a perfect dirac but has a certain width as represented by the blue peak in Figure 2.6. It is due to the uncertainty on the measured energy ΔE which leads to a broadening of the peak [109, 107]. The instrumental resolution is usually measured using a vanadium sample whose signal is only elastic. Neglecting other geometrical effects, the energy, time and wavelength resolutions are linked together using:

$$\frac{\Delta E}{E} = \frac{2\Delta\tau}{\tau} = \frac{2\Delta\lambda}{\lambda} \tag{2.79}$$

In order to get a better resolution in time and energy, the usual way is to reduce the uncertainty on λ by tightening the choppers' slits. However, the price to pay is the diminution of the neutron flux and therefore a weaker statistic.

In any case, the resolution function $R(\omega)$ of the spectrometer has to be deconvoluted from the experimental dynamic structure factor $S^{exp}(\mathbf{q},\omega)$ to get the theoretical dynamic structure factor $S^{theo}(\mathbf{q},\omega)$:

$$S^{exp}(\mathbf{q},\omega) = S^{theo}(\mathbf{q},\omega) * R(\omega) \tag{2.80}$$

Moreover, there are some physical limitations on the q and E range which are not due to the instrumental resolution.

Indeed, if the neutron can gain as much energy as the system can transmit, it can loose only the incident energy amount E_0. That is why the right part of the energy range is forbidden above $dE = E_0$ as shown by the red rectangle on the graph Figure 2.6. We have to notice here that the right part of the scattering function - positive energies - refers to a lost of the neutron energy and thus a gain of the sample energy. For the left part of the scattering function, it is the opposite.

Moreover the kinematic condition on the q range has to be highlighted. Indeed, by definition:

$$|\mathbf{q}| = |\mathbf{k}_f - \mathbf{k}_0| \tag{2.81}$$

which leads to:

$$|\mathbf{q}| = \sqrt{|\mathbf{k}_f|^2 + |\mathbf{k}_0|^2 - 2|\mathbf{k}_f||\mathbf{k}_0|cos(\theta)} \tag{2.82}$$

From the latter equation comes the condition that the term inside the square root is positive. It imposes forbidden values for θ and leads to a restriction on the accessible q range.

This chapter introduced the fundamentals of both numerical and experimental methods which are going to be used to probe adsorption, diffusion and transport of methane in zeolite. Thus, adsorption will be studied by simulation using Monte Carlo while it will be measured by experimental volumetric method. In an other hand, Molecular Dynamic will allow us to compute diffusion and transport properties that we will be able to compare with experimental data performing neutron scattering experiments.

3 Gas adsorption in zeolite and zeolite layers

This chapter reports the study realized within this thesis on methane physisorption on zeolite and zeolite layers. While the confinement of fluids in the core porosity of zeolites is rather well-understood, the design of novel zeolitic materials such as zeolite films [43], nanozeolites [44], hollow zeolites [45], hierachical zeolites [46, 114], dendritic zeolites [115], raises additional basic and practical questions related to adsorption in their complex architecture [116, 117, 118]. Indeed, a common point to nanozeolites, hollow zeolites and hierarchical zeolites is their large external surface through which different porosities connect in a more or less topologically ordered fashion (we note that even regular zeolite powders already possess a large external surface area but to a lesser extent compared to the sample types listed here). The impact of this external surface is already documented with striking examples in adsorption uptakes measurements [9, 10] as well as in separation/chromatography where it plays a key role in the balance between intra-particle diffusion and hydraulic transport [11, 12] (see also Ref. [20] for a discussion on the adsorption of xylene isomers at the external surface of zeolites). In catalysis, the effect of the external surface remains to be fully established but many papers report pore mouth catalysis mechanisms [119, 120]. In this context, the geometry and defects at the external surface was shown to affect both the catalysis of reacting molecules (e.g. Refs. [121, 122]) and the adsorption/dynamics of fluids (e.g. Refs. [123, 117]) in nanoporous solids.

Despite the acknowledged impact of the external surface, a detailed picture of adsorption and transport across nanoporous materials displaying large external surface areas is still missing. In particular, very practical questions remain unanswered such as the influence on gas adsorption of the surface geometry (orientation, flexibility, etc.). Moreover, while theoretical frameworks are available to describe gas adsorption in zeolites, a unified formalism to model in a consistent fashion adsorption in the zeolite core and at its external surface is lacking. To gain fundamental insights into these issues, this chapter reports a joint experimental and molecular simulation study on gas adsorption in zeolite materials. In more detail, using a prototypical system consisting of methane confined in silicalite-1 [42], we investigate gas adsorption at different temperatures in the zeolite core porosity as well as at the external surface of zeolite thin layers with different crystallographic orientations. Using our simulated and experimental data, we first extend the adsorption potential theory - originally developed by Polanyi to describe adsorption of condensable vapor onto surfaces [59, 60, 61] - for fluids under supercritical conditions. Then, we show that this powerful adsorption theory can be used to predict adsorption at different temperatures both at the external surface and in the core porosity of zeolites.

The remainder of this chapter is arranged as follows. In Section 3.1, we describe the numerical tools used to investigate adsorption. We first report how we build both "infinite" zeolite and zeolite layers before detailing the application of Monte Carlo methods to study adsorption. In Section 3.2, the experimental samples employed in our experiments using adsorption volumetry are described. Then, in Section 3.3, both the simulated and experimental adsorption isotherms are presented. We first discuss methane adsorption at different temperatures in a bulk zeolite. We also assess the influence of different parameters such as the lattice parameter and flexibility. Then, using our simple model of zeolite layers, we discuss the role of the external surface on the overall adsorption phenomenon. Indeed, using results from the bulk zeolite, we can separate the contributions from the external surface and from the zeolite core. In Section 3.4, using our experimental and simulated adsorption data, the adsorption potential theory is invoked to provide a formalism which allows predicting adsorption in the core of zeolites and at their external surface.

3.1 Computational methods

This section is dedicated to the description of the zeolite numerical system and computational tools used to simulate adsorption isotherms. We first describe both the "infinite" zeolite crystal and the zeolite layers with the intermolecular potentials associated. Then, we present the Monte Carlo algorithm emmployed in Lammps to compute adsorption isotherms.

3.1.1 Zeolite systems: infinite crystal and layers

The two structures used for our molecular simulations will be presented in this section. The first zeolite structure is an infinite zeolite crystal, which corresponds in molecular simulation to crystal used with periodic boundary conditions. The second numerical structure is the zeolite layer which is oriented along an axis and which present external surfaces.

Zeolite crystal. The zeolite structure used as input for the molecular simulations was taken from the International Zeolite Association database (IZA) [42]. Silicalite-1, which possesses a crystalline network known as MFI, is a pure silica structure – i.e. only composed of silicon and oxygen atoms as explained in Section 1.1.4 (other MFI structures, which also include Al atoms with compensation cations such as Na, are not referred to as silicalite). The experimental unit cell parameters for silicalite-1 are a = 20.09 Å, b = 19.738 Å and c = 13.142 Å (Figure 3.1 (a)). We chose to work in this thesis with the orthorhombic version of the MFI structure. Indeed, at the T and P ambient, the structure is slightly monoclinic. Moreover, under the adsorption, the silicalite goes to an orthorhombic structure. It is a reasonable approximation.
A MFI crystal supercell, consisting of 2 × 2 × 2 cells along the x, y and z axes, was obtained by duplicating the crystallographic unit cell. The dimensions were chosen to optimize the computational time while minimizing finite size effects. Thus, the dimensions of the duplicated crystal are 40.18 Å along x, 39.476 Å along y, and 26.284 Å along z (Figure 3.1(b)). In practice, the system is made up of a total of 2304 atoms of the matrix (768 Si and 1536 O).

Zeolite layer. In our molecular simulations, a zeolite layer corresponds to a structure where periodic boundary conditions are applied in two directions of space (as the zeolite crystal defined above) while the third direction is considered as the layer axis. Along this axis, the layer presents external surfaces. However, these surfaces are in contact with bulk volume at each side of the layer which are subject to periodic boundary conditions. Three layers were built from the MFI unit cell crystal by considering different

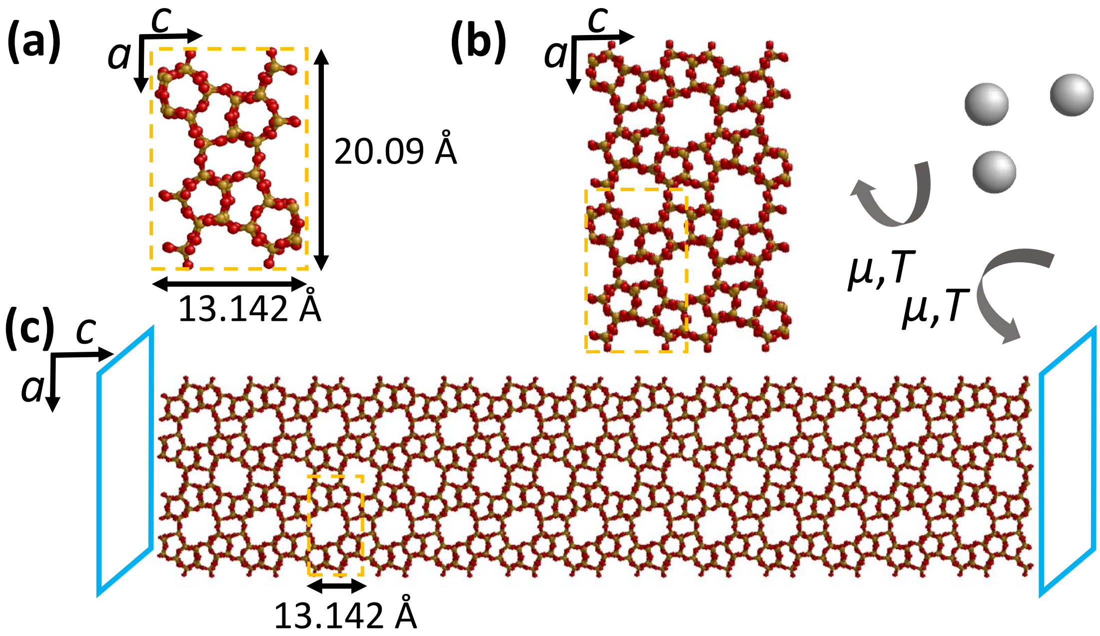

Figure 3.1: (color online) Silicalite-1 zeolite crystal. The Si and O atoms are represented as yellow and red spheres, respectively. a, b, c denote the crystallographic axes which are aligned with the x, y and z axes of the Cartesian reference frame. A single unit cell is represented in (a) while a $2 \times 2 \times 2$ crystal is shown in (b). Periodic boundary conditions (PBC) are applied in each direction to mimic an infinitely large system and, hence, avoid finite size effects. (c) The MFI unit cell was duplicated 10 times along the chosen direction (the layer axis, here z) and 2 times along the other directions (perpendicular to the layer axis, here x and y) to form a zeolite layer with an external surface. Methane adsorption is simulated by setting the system in contact with a fictive bulk reservoir which imposes its temperature T and chemical potential μ.

crystallographic orientations for the external surface. In practice, each of the three layers corresponds to a system in which the external surface is perpendicular to one of the crystallographic axis: a, b, c (i.e. the crystallographic axes which are aligned with the x, y and z axes of the Cartesian reference frame). To do so, the MFI unit cell was duplicated 10 times along the chosen direction (the layer axis) and 2 times long the other directions (perpendicular to the layer axis). The Figure 3.1(c) shows an example provided for the zeolite layer c.

These layers were cut at well-defined positions along the chosen perpendicular axis (i.e. a, b or c); these positions were used to ensure that the two opposite layer external surfaces are equivalent in the sense that they possess the same silicon density (to do this, the silicon and oxygen density profiles were plotted along the layer axis). In so doing, the two opposite surfaces have similar properties towards gas adsorption, diffusion, and transport. Finally, whenever the surface has a terminating Si atom, an oxygen atom was added to build surfaces that are oxygen terminated. The use of an oxygen terminated external surface corresponds to a simplified version of real materials which are expected to display surfaces terminated with silanols (OH groups). Surface termination is expected to affect the behavior of many adsorbates at the zeolite external surface – especially polar molecules or molecules with complex chemical structure. On the other hand, with simple molecules such as methane considered here, the details of surface termination is assumed to be of limited impact (in particular, considering the very small polarizability of hydrogen atoms, the absence of H atoms at the external surface is believed to be a reasonable approximation).

Table 3.1: Lennard-Jones parameters σ and ϵ for the fluid/fluid and fluid/zeolite interaction potentials.

type	σ (Å)	$\epsilon/k_B(K)$
CH_4-CH_4	3.73	147.92
CH_4-O	3.214	133.27

To account for zeolite flexibility while maintaining the same overall crystalline structure, two different models were considered. In the rest of this article, "surface oxygen" denotes an oxygen atom which is only bonded to a silicon atom while "bulk oxygen" denotes an oxygen atom which is bonded to two silicon atoms. For the first surface flexibility model (s1), "surface oxygens" were maintained to their original position so that the surface is frozen while all other atoms are allowed to move. For the second surface flexibility model (s2), the "surface oxygens" were allowed to move during the simulation but their motion was restricted to the plane perpendicular to the layer axis.

Intermolecular interactions. The fluid/fluid and fluid/zeolite intermolecular interaction potential used in this work correspond to Lennard-Jones potentials. This generic interaction potential corresponds to the sum of long-range attractive and short-range repulsive contributions as described in Section 1.2.1.We recall that the potential energy E_p can be written as:

$$E_p(r) = 4\epsilon\left[\left(\frac{\sigma}{r}\right)^{12} - \left(\frac{\sigma}{r}\right)^{6}\right]$$

A cut-off $r_c \sim 13$ Å was used in our molecular simulations to speed up the computational times; beyond this distance ($r > r_c$) the potential energy $E_p = 0$. To avoid any non-physical behavior, the box dimension in each Cartesian direction is always larger than $2r_c$. The Lennard-Jones potential was used to model the fluid/fluid interactions between CH_4 molecules but also the fluid/solid interactions between CH_4 and O groups. Parameters used can be found in Table 3.1. The United Atom model (UA) was used for CH_4 in which the methane molecule is treated as a single Lennard-Jones sphere. As a result, no intramolecular interactions have to be taken into account. This is known to be a good approximation for methane provided the temperature is high enough (like in the present work in which the minimum temperature considered is about 200 K). As for the fluid/zeolite contribution, following previous works [124, 125], no Lennard-Jones potential between CH_4 and Si atoms were considered as it can be reasonably neglected. Indeed, Si atoms have a small polarizability while O atoms have a large polarizability. Moreover, the Coulomb interaction between zeolite atoms and CH_4 molecules is not taken into account within the united atom model hypothesis (as there is no partial charge on the CH_4 molecule).

Zeolite intramolecular interactions. We use the model by Vlugt and Schenk [125] to take into account the flexibility of the zeolite matrix. With this model, simple harmonic potentials are used to describe the bonds between Si-O and O-O atoms connected to the same Si atom:

$$E_{\mathrm{SiO}} = k_{\mathrm{SiO}}(r - r^0_{\mathrm{SiO}})^2$$

$$E_{\mathrm{OO}} = k_{\mathrm{OO}}(r - r^0_{\mathrm{OO}})^2$$

For each bond type, the corresponding potential energy is E while k is the spring constant and r^0 the equilibrium bond length. The O-O potential does not correspond to a real chemical bond but allows to model the matrix flexibility in an effective fashion. The particularity of this model is that the Si-O and O-O equilibrium bond lengths are

Table 3.2: Root mean square displacement (RMS) $\langle \delta r^2 \rangle$ for the three zeolite layers. As explained in the text, two approximations were considered to describe the mobility of surface atoms. The first number is the RMS computed in the core of the layer (i.e. calculated at the center of the layers in a 2×2×2 region). The second number is the RMS of the "surface oxygen" i.e. computed at the external surface. In the last column, for comparison is the RMS for the MFI "infinite" crystal.

type	Layer a	Layer b	Layer c	MFI crystal
s1	0.149/2.45 10^{-24} Å^2		0.155/0.12 10^{-24} Å^2	0.15 Å^2
s2	0.148/0.248 Å^2		0.149/0.547 Å^2	0.15 Å^2

not unique but depend on the bond length distribution of the initial zeolite structure. Indeed, using flexibility, the average position of zeolite atoms can deviate from the rigid crystal. Using a unique value to describe the distribution of the bond length induces a model not very accurate. For this reason, the equilibrium bond length distribution in the initial zeolite structure (experimental data) was calculated. Both the data for Si-O and O-O bonds were estimated. The equilibrium bond lengths were discretized with a very fine step of 0.01 Å. In practice, considering this discretization level, 5 values for the Si-O bond lengths and 12 values for the O-O bond length were considered. As proposed by Vlugt and Schenk, to reduce the number of variables, we have chosen $k = k_{\mathrm{OO}} = 0.2k_{\mathrm{SiO}}$ [125]. Figure 3.2 shows the root mean square fluctuation $\sqrt{\langle \delta r^2 \rangle}$ of the oxygen atoms around their average position as a function of k_{OO}/k_B with k_B the Boltzmann constant. As expected, the oxygen displacement decreases with increasing the spring constant k. In the rest of this manuscript, the spring constant k will be set equal to $k_{\mathrm{OO}}/k_B = 2.6 \times 10^4$ K.Å^{-2} as initially proposed in Ref. [125].

Before investigating adsorption in the zeolite layer, we first performed test to verify that the core of each zeolite layer behaves in a similar fashion as the silicalite-1 crystal. To do so, the root mean square displacement (RMS) of the "bulk oxygens" were calculated and compared for each layer. In these calculations, the two surface models – flexible and rigid – were considered. These data can be found in Table 3.2. The RMS for the "bulk oxygens" in the layers are in good agreement with those found for the oxygen atoms in the zeolite crystal. This result indicates that, as expected, the core of the zeolite layer and the zeolite crystal behave similarly. Moreover, the RMS for "surface oxygens" from s1 is zero as the "surface oxygens" are maintained to their original position. In contrast, the RMS for "surface oxygens" with the flexible surface is larger than the RMS for "bulk oxygens". This result suggests that these flexible surface atoms are more mobile as they are linked to a silicon atom only. Therefore, even if their motion is restricted to a plane parallel to the layer surface, their average displacement is larger than that for bulk oxygen atoms.

3.1.2 Grand Canonical Monte Carlo simulations

The methane adsorption isotherms at different temperatures in silicalite-1 were calculated using Grand Canonical Monte Carlo (GCMC) simulations. General principles of this method were explained in Section 2.1.2. All Monte Carlo simulations were performed using the simulation package LAMMPS (version openmpi 1.8.1) [126]. For both the zeolite crystal and the zeolite layers, the zeolite system is set in contact with a fictive bulk reservoir of methane imposing its temperature T and chemical potential μ. In Lammps μ and T are defined by the following lines:

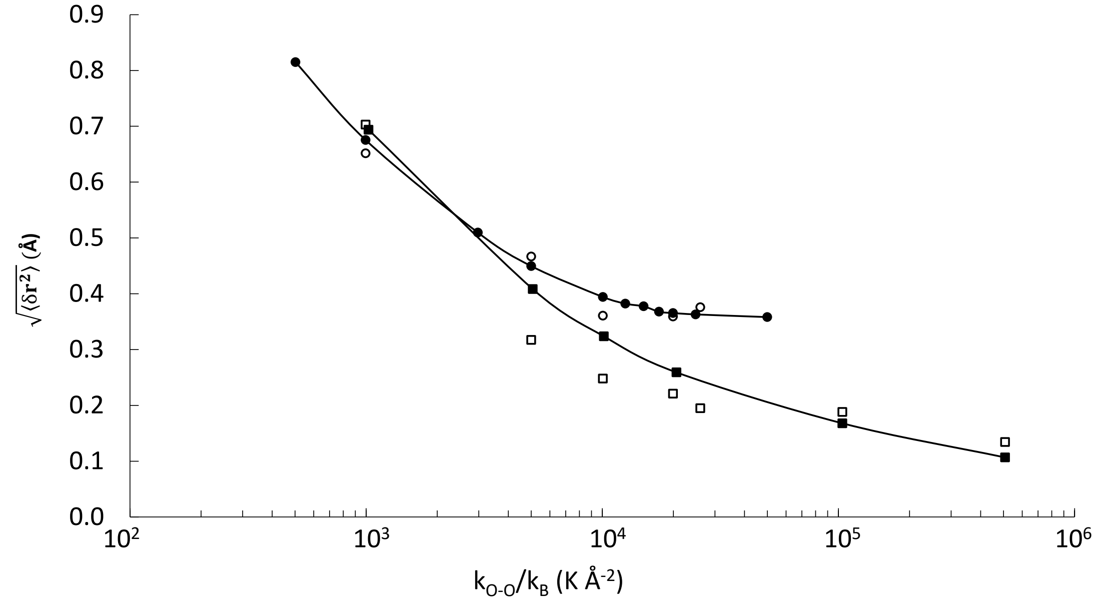

Figure 3.2: Root mean square fluctuation $\sqrt{\langle \delta r^2 \rangle}$ of the oxygen atoms around their average position. Lines with symbol correspond to the results from the literature [125]: Vlugt and Schenk (■), Demontis *et al.* (●). Open symbols correspond to the results from this work: simulation based on Vlugt and Schenk model (□), simulation based on the model by Demontis *et al.* (○)

```
variable mu index -11.4522
variable temp index 300
```

As an example, μ and T are fixed at -11.4522 kcal.mol^{-1} and 300 K respectively. μ can be directly converted into a pressure P through the equation of state as there is a unique relation between P and μ at constant T. Assuming an ideal gas, we can write (see "Transport and thermodynamic (Darken) factor" in Section 1.3.1):

$$\mu = k_B T \ln \left(\frac{P\Lambda^3}{k_B T} \right) \tag{3.1}$$

We recall that Λ is the thermal de Broglie wavelength. At equilibrium, the methane adsorbed amount n_a is calculated from the number of molecules N in the system that fluctuates around its equilibrium value $\langle N \rangle$. In practice, to reach equilibrium, methane molecules are translated, inserted or removed randomly (Monte Carlo moves) with an acceptance probability defined using the Boltzmann factor in the Grand Canonical ensemble. In order to perform Monte Carlo moves, the following line is added:

```
fix mygcmc fluid gcmc 10 10 10 1 29494 $temp $mu $disp
```

Grand Canonical Monte Carlo ("gcmc") is applied to methane atoms ("fluid") at temperature defined by $temp and chemical potential $mu every 10 (first number) time steps. The number of inserting/deleting methane atoms (fourth number "1") attempts is given by the second number (10) while the number of translation attempts is given by the third number (10). The maximum distance for translation attempts is fixed by $disp which was set at 3.48 Å. The fifth number is an initialization parameter for the random generator used in Metropolis method.

Finally, the time of the run has to be determined in function of the time needed for reaching equilibrium. The number of Monte Carlo moves needed to reach equilibrium

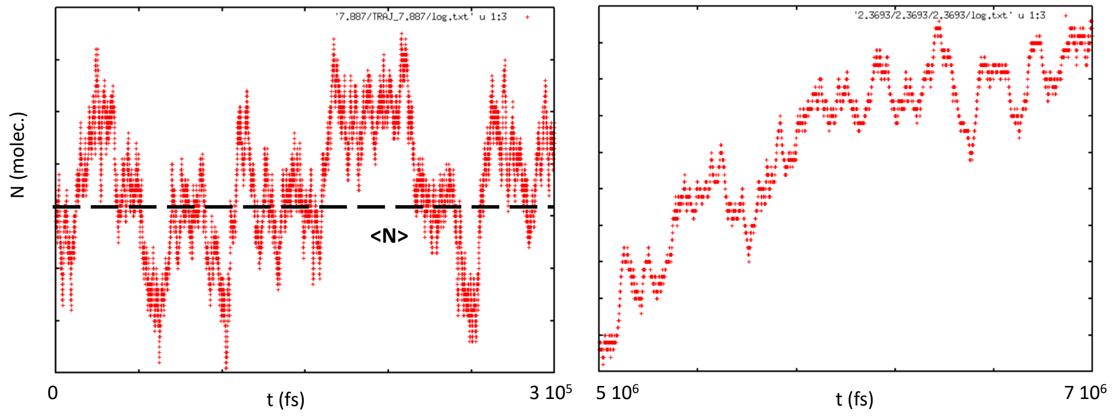

Figure 3.3: Methane amount in the zeolite crystal at 300 K in function of the time for pressures corresponding to 4.7 bars (left data) and 4.8 10^4 bars (right data).

depends on both T and P. Indeed, the higher the pressure is, the more MC moves are needed while the higher the temperature is, the faster the thermalization is and less MC moves are needed to reach equilibrium. Figure 3.3 shows one MC simulation that reached equilibrium (at the left) in 3×10^5 fs and another one which is still out of equilibrium after 7×10^6 fs (at the right).

3.2 Adsorption experiments

This section is dedicated to the presentation of the zeolite powder samples and the experimental protocol used to measure adsorption isotherms. First, we present the zeolite sample characterization. This characterization was done by Martin Drobek and Anne Julbe in Montpellier who synthesized the samples according to the procedure described elsewhere [127]. Even if it is not my own work, the characterization is important for the readability of the manuscript. On the contrary, I did the experimental adsorption measurements with the help of Simon Baudoin at Institut Laue Langevin and my supervisors.

3.2.1 Zeolite samples

There are four powder samples with different crystallite sizes (diameter) D_g: 1 μm, 350 nm, 200 nm and 80 nm. The scanning electron microscope (SEM) images of the silicalite-1 powder samples are shown in Figure 3.4. For each sample, powder X-ray diffraction (XRD) and N_2 adsorption isotherm at 77 K were determined (see Figure 3.5 and Figure 3.6 respectively). XRD analysis corroborates the presence of silicalite-1 diffraction lines at $2\theta = 7.9°$, $8.7°$, $23.1°$, and $24.4°$, corresponding to the reflections of (101), (020), (501) and (303) crystallographic planes. Nitrogen sorption experiments reveal comparable microporous characteristics for the four prepared zeolite samples (typical for MFI zeolites), reaching all a specific surface area of $S_{BET} \sim 400$ m^2/g. This measured specific surface area is mainly attributed to the internal zeolite network.

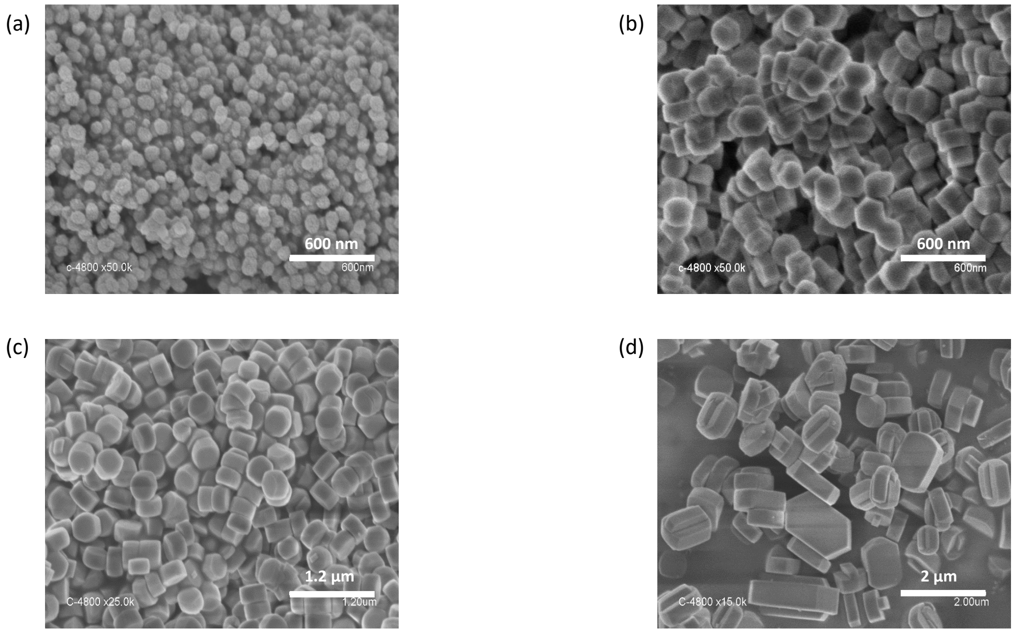

Figure 3.4: FESEM images of silicalite-1 powder samples with different grain sizes: (a) D_g: ∼80 nm ; (b) D_g: ∼200 nm ; (c) D_g: ∼350 nm ; (d) D_g: ∼1 μm. (Field Emission Scanning Electron Microscope, Hitachi 4800)

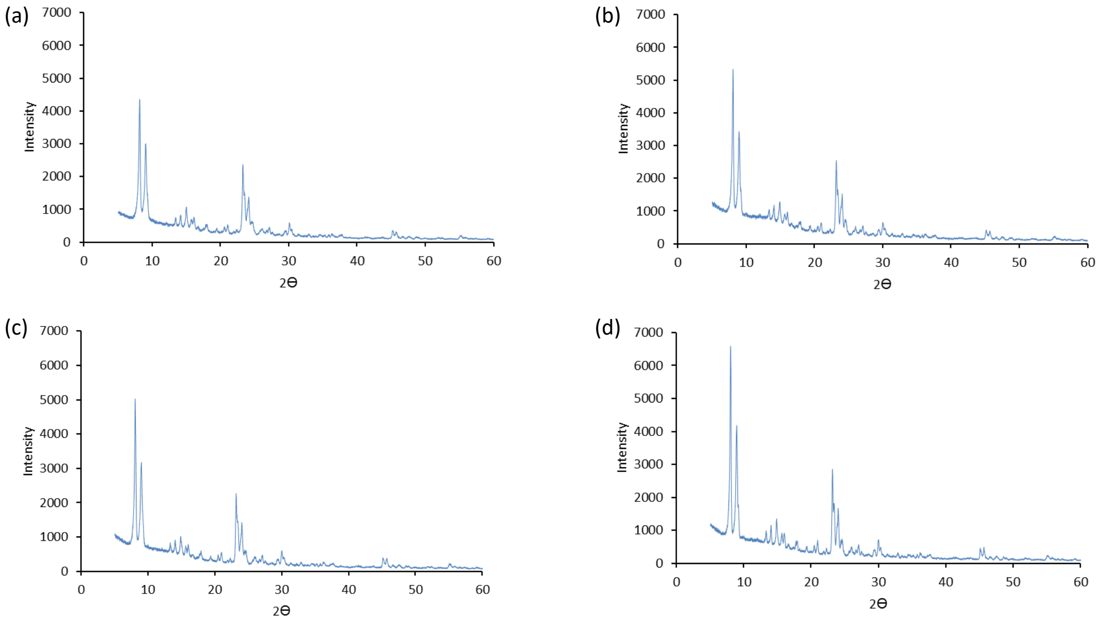

Figure 3.5: XRD patterns for the silicalite-1 powder samples with different grain sizes: (a) Dg: ∼80 nm ; (b) Dg: ∼200 nm ; (c) Dg: ∼350 nm ; (d) Dg: ∼1 μm. (Philips X'Pert X-ray diffractometer, CuKα, 40kV, 20mA)

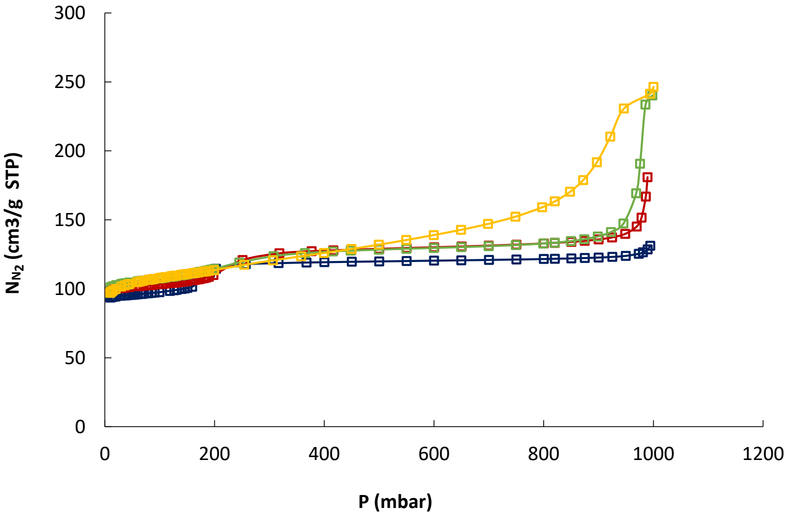

Figure 3.6: Experimental adsorption isotherms for N_2 at 77 K in silicalite-1 samples as determined by Drobek and Julbe (courtesy from IEM). Different colors correspond to different samples: (🟦) $D_g = 1\ \mu$m, (🟥) $D_g = 350$ nm, (🟩) $D_g = 200$ nm, (🟨) $D_g = 80$ nm.

3.2.2 Experimental protocol

Experimentally, methane adsorption in the zeolite samples was measured at the Institute Laue Langevin (ILL) in Grenoble, France. These experiments were carried out using a Hiden Isochema apparatus which relies on a volumetric method to measure adsorption at equilibrium. The principles of this method were developed in Section 2.2.1. In short, methane is injected in a dosing cell prior to connection to the sample holder containing the zeolite matrix. The number of adsorbed molecules is determined from the difference between the number of injected molecules and the number of molecules left in the gas phase once equilibrium is reached (the latter being assessed from the final pressure and the cell volume corrected for the volume occupied by the zeolite sample). The sample is put in a cryostat which regulates the temperature. These experiments last between 10 minutes and few hours depending on the injected amount of methane and imposed temperature. Considering the experimental setup employed in this study, the adsorption data were recorded at low temperatures for which the operating conditions allowed us to obtain reliable data. As will be discussed later, these data were found to be consistent with data obtained by other groups at larger temperatures. Data at higher temperatures were also recorded but, as will be explained later, their reliability can be questioned.

3.3 Adsorption in zeolitic systems

This section presents first experimental and simulation results on adsorption in "bulk" zeolite and second simulated adsorption isotherms for zeolite layers. In order to study the impact of the external surface, layers were described using three regions : the core, the external surface and the external phase. Adsorption in "bulk" zeolite was compared to adsorption in zeolite layers in order to separate the external surfaces contribution.

3.3.1 Bulk zeolite

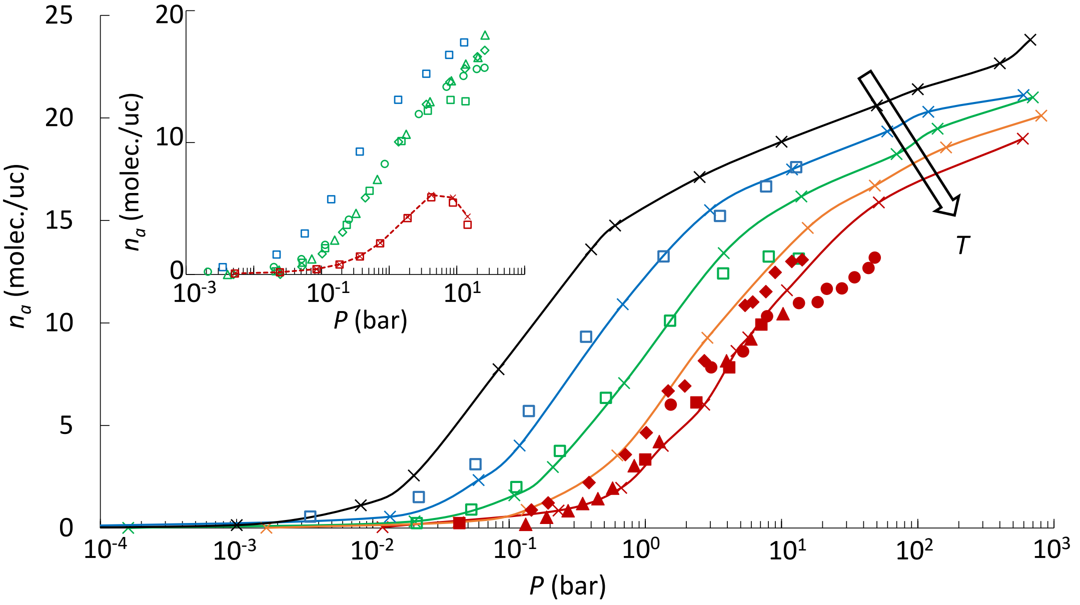

Figure 3.7: (color online) Experimental and simulated adsorption isotherms $n_a(P)$ for methane at different temperatures in silicalite-1 zeolite. The different colors correspond to the following temperatures: 200 K (black), 225 K (blue), 250 K (green), 275 K (orange), 300 K (red). The lines with crosses correspond to the results from our molecular simulations. The symbols without lines correspond to experimental data. The open symbols correspond to our experimental data. The closed symbols correspond to experimental data at 300 K from other groups: Abdul-Rehman *et al.* (diamonds), Ding *et al.* (circles), Golden and Sircar (squares), Richard and Rees (triangles). All these experimental data were reproduced from Smit *et al.* [124]. The adsorbed amount n_a is expressed in number of methane molecules per zeolite unit cell. The arrow indicates data obtained for increasing temperatures. The insert shows our experimental data obtained at 250 K for powder samples with different grain sizes: $D_g = 1$ µm (squares), 350 nm (diamonds), 200 nm (circles), 80 nm (triangles). It also shows experimental data at 225 K (blue) and 300 K (red) for $D_g = 1$ µm.

Figure 3.7 shows the methane adsorption isotherms obtained at $T = 300$ K (red), 275 K (orange), 250 K (green), 225 K (blue), 200 K (black). The lines with crosses correspond to the simulation data while the symbols denote the experimental data. As expected for fluids confined in the very narrow pores of zeolites, adsorption is a reversible and continuous process which does not display any sharp increase in the adsorbed amount or hysteresis loop [128, 117]. While the methane adsorbed amount n_a increases upon increasing the pressure P at a given T, it increases upon decreasing T at a given P. For each T, the different regions of the adsorption isotherm correspond to different phenomena. Typically, at $T = 300$ K, the data in the pressure range between $\sim$ 0.4 and 11 bar corresponds to pore filling while the data in the pressure range from 11 to 10^3 bar corresponds to pore saturation. In the latter range, the zeolite pore volume is already filled so that the slope in the adsorption isotherm arises from the compressibility of confined methane which allows the insertion of additional methane molecules upon further increasing the pressure. Such a scenario (pore filling followed by saturation) was verified by careful inspection of the molecular configurations generated along the Grand Canonical Monte Carlo simulations at different chemical potentials. The effective methane compressibility inside the zeolite once pores are saturated was estimated from the slope of the adsorption isotherm in this pressure range: $\chi_T = 1/\rho \times \partial\rho/\partial P$. For example, at 300 K and P = 1200 bar, the compressibility from our simulating data is 3.52 Pa^{-1} for confined methane and 4.68 Pa^{-1} for bulk methane. The fact that the compressibility of confined methane is lower than that of bulk methane under similar thermodynamic conditions is in agreement with previous studies on nanoconfined fluids [129]. In addition, Figure 3.7 shows the experimental adsorption isotherms for methane obtained at different temperatures for the four powder samples (open symbols). We also show experimental data obtained at 300 K from other groups taken from Ref. [124] (Abdul-Rehman *et al.* [130], Ding *et al.* [131], Golden and Sircar [132], Richard and Rees [133]).

Experimentally, the trend observed in our molecular simulation is also seen as adsorption increases upon decreasing the temperature (owing to the reduced thermal energy which promotes adsorption). The grain size D_g in the zeolite powders does not strongly impact adsorption as can be observed from the data obtained at T = 250 K in the insert. This result was expected as the external surface area in the zeolite samples is small compared to the internal surface in the zeolite porous structure. The simulation data at 300 K are found to be in reasonable agreement with the experimental data. However, Abdul-Rehman *et al.* [130] found larger adsorbed amounts compared to our simulation data but also with respect to other experimental data. Such discrepancies may stem from different material parameters including the type of silicalite-1 used by these authors; in particular, as explained in Ref. [124], Linde S-115 sample corresponds to silicalite-1 mixed with a clay binder to form pellets so that its porosity and, hence, adsorption properties may differ from other (more conventional) samples. The insert also shows experimental data measured at 300 K (open red squares). When the pressure increases, the adsorbed amount reaches a maximum ($\sim$ 4.2 bars) and start to decrease. We applied a correction (red dashed line with crosses) which is based on the difference excess/absolute adsorption (see Section 1.2.1). Indeed, volumetric set up measures the excess amount of molecules as adsorbed molecules do not contribute to pressure. However, the methane amount inside the zeolite (also given by MC) is: $n^{abs} = n^{exc} + V_p \times \rho^g$ with V_p and ρ^g the porous volume and the gas phase density respectively. The right side of the equation gets more and more importance with an increasing temperature (as the density increases with temperature). However, by comparing the excess and absolute data, we concluded that the decrease observed at the highest pressures is not only the result of excess/absolute correction but corresponds to measurements out of the regular regime of the device.

Influence of lattice parameters. The effect of the specific zeolite microscopic structure was also studied by considering 3 different zeolite unit cells. The first structure, which corresponds to the standard model discussed in Section 3.1.1, is built from the IZA database [42]. The structure referred to as “A” corresponds also to an orthorombic structure but with the following lattice parameters: a = 20.072 Å, b = 19.9517 Å and c = 13.4262 Å. These parameters were provided by F. Porcher from LLB, Saclay, France, who performed diffraction experiments for a silicalite-1 structure. The structure referred to as “B” corresponds to an orthorombic structure but with the following lattice parameters: a = 20.022 Å, b = 19.899 Å and c = 13.383 Å. “B” was obtain using the crystallographic structure from the IZA database after relaxation with the forcefield developed by Catlow *et al.* Figure 3.8 (b) shows the methane adsorption isotherms obtained by means of GCMC simulations for the different zeolite structures presented above: ○ IZA database, □ model “A”, △ model “B”. The structure does not have much effect on the adsorption isotherms. As the IZA structure is the most referenced, we will used this structure in the rest of the study.

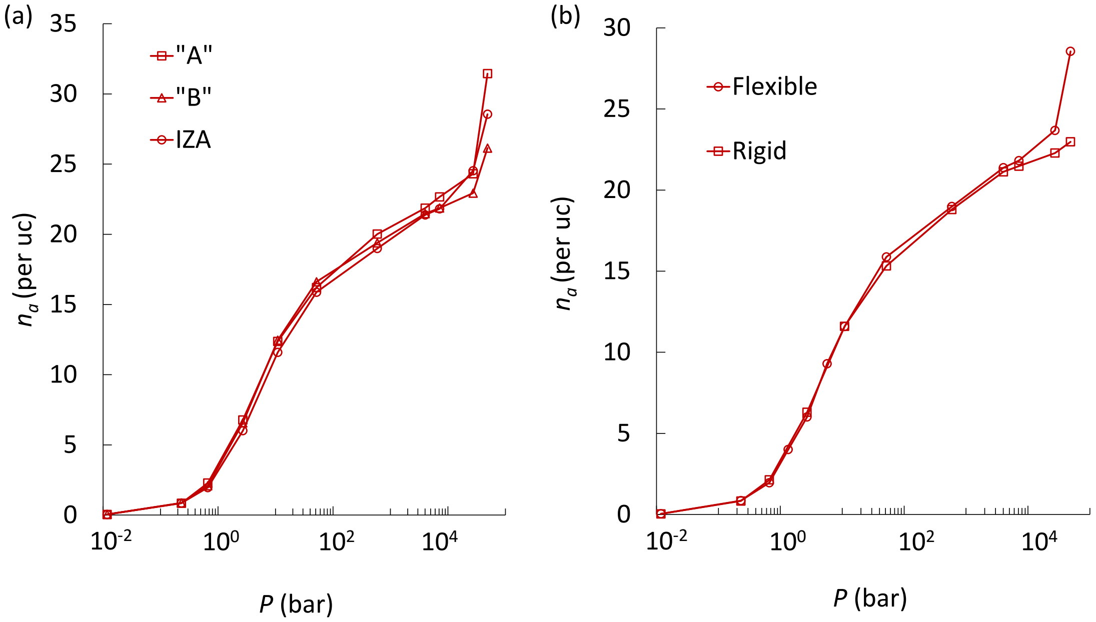

Figure 3.8: (a) Comparison of methane adsorption isotherms at 300K for different unit cell parameters. “A” refers to an orthorhombic structure with the following lattice parameter: a = 20.072 Å, b = 19.9517 Å, c = 13.4262 Å. “B” refers to IZA database structure after relaxation with the force field developed by Catlow *et al.* and corresponds to the following lattice parameter: a = 20.022 Å, b = 19.899 Å, c = 13.383 Å. (b) Simulated adsorption isotherms for methane at 300 K using a rigid or a flexible framework.

Influence of the zeolite flexibility. Figure 3.8 (b) shows simulated adsorption isotherms for methane at 300 K using a rigid or a flexible zeolite framework. The flexibility of the zeolite matrix does not impact significantly the adsorption at low and intermediate pressures (pressures up to 2000 bars). However, beyond this pressure, in the flexible matrix, the zeolite structure distorts as more CH_4 molecules get adsorbed inside the small cages. Such additional adsorption at high pressures is responsible for the adsorbed amount increase around 10^4 bars. In contrast, the rigid zeolite cannot distort by construction so that the adsorbed amount reaches and stays at a plateau at high pressures. Despite the small impact of flexibility, in the rest of this manuscript, the flexible structure will be used to describe the zeolite structure as flexibility might have a stronger impact on methane diffusion and transport.

3.3.2 Zeolite layers

Using molecular simulation, the adsorption isotherms were computed at $T = 300$ K, 275 K, 250 K, 225 K, and 200 K for the three layers aligned along the a, b and c directions, respectively. As explained in the Section 3.1.1, for each layer, the adsorption isotherms were computed for two surface flexibility models (s1 and s2). As will be discussed later, the adsorption isotherms for these two surface models were found to lead to similar adsorption isotherms so that only data for the model s1 will be discussed extensively. Moreover, for the sake of clarity, we will present adsorption isotherms for the layer a (data for the layers b and c at $T = 300$ K will be discussed later).

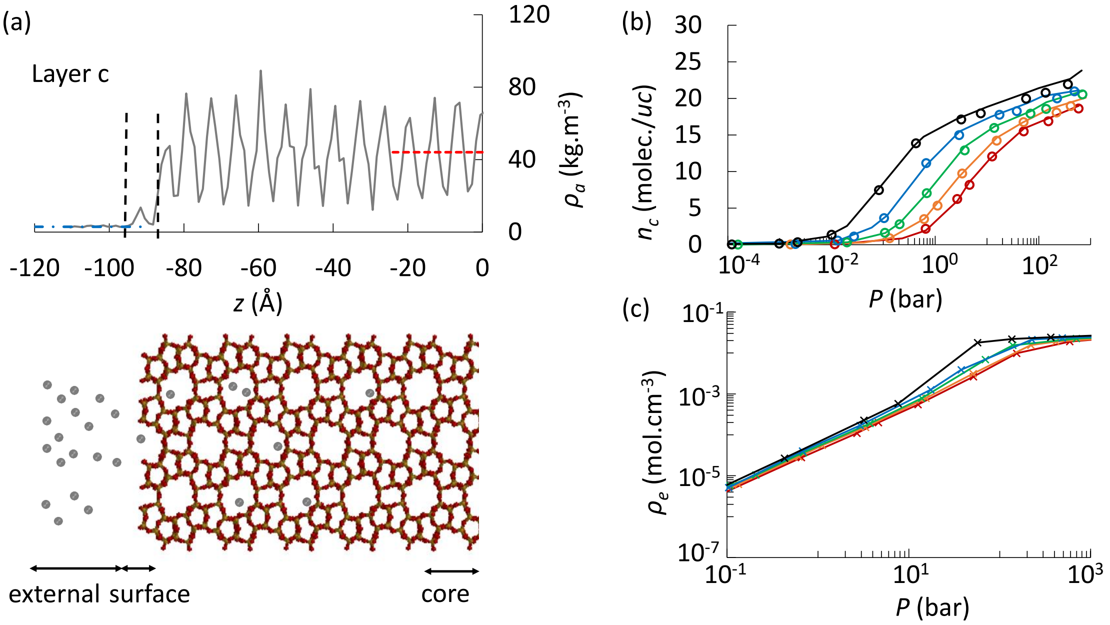

Figure 3.9: (color online) (a) Methane density for the silicalite-1 layer aligned along the c crystallographic axis. For visualization purpose, only the left side of the layer is shown (the system is symmetrical with respect to the position $z = 0$). The cavity size is about 1/3 of the Lennard-Jones size parameter for the methane molecule. (b) and (c) show the adsorption isotherms in the core of the zeolite layer and density in the external fluid phase, respectively. Different colors correspond to different temperatures T: 300 K (red), 275 K (orange), 250 K (green), 225 K (blue), 200 K (black). In (b), the lines show the adsorbed amounts obtained for the infinite zeolite while the open circles show the adsorbed amounts obtained by counting methane molecules adsorbed in the core of the layers.

To determine the impact of the zeolite external surface, the methane density profile was first computed at different methane pressures for each zeolite layer. An example obtained for the layer aligned along the c axis at $T = 300$ K and $P = 4.6$ bar is provided in Figure 3.9(a). The gray line corresponds to the local methane density in the system at a given position z – where z can lie in the bulk phase, at the external surface or in the core of the zeolite layer. These three regions are delimited by the two vertical black dashed lines. The first region, which is located on the left Figure 3.9(a), corresponds to the methane density in the external gaseous phase. The simulated density in this region was found to be close to the experimental density available from NIST [134] for bulk methane under the same thermodynamic conditions [see the blue horizontal dashed line in Figure 3.9(a)]. The second region, which is located between the two black vertical dashed lines in Figure 3.9(a), corresponds to the methane density at the external surface of the zeolite layer. Finally, the third region corresponds to methane adsorbed in the core of the zeolite layer as illustrated in Figure 3.9(a). The adsorbed density peaks in this region show marked variations corresponding to the varying methane concentration in the zeolite channels/cages. The average adsorbed methane density computed in this region - which does not include any contribution from the gaseous phase or methane adsorbed at external surface – was compared with the average adsorbed methane density estimated from the calculations for the infinite zeolite crystal [indicated by the horizontal red dashed line in Figure 3.9(a)]. The two values are found to be close to each other; while the mean adsorbed methane density for the zeolite crystal is $\rho_{inf} = 44.14$ kg.m^{-3}, the average methane density in the core of the zeolite layer is $\rho_c = 45.65$ kg.m^{-3}. An important remark is in order here. Different choices can be made to define the boundaries used to estimate the methane density in the zeolite core, at the external surface, and in the bulk phase (leading to different excess quantities once volume boundaries and interfaces have been selected). However, to ensure consistency between volume and surface amounts, we made sure that our boundary definition in Figure 3.9 leads to bulk densities and adsorbed amounts in the zeolite core that match those obtained for bulk methane and the zeolite crystal without external surface (further discussion will be provided later when excess data for adsorption at the external surface are commented). In the same context, we highlight that Barrer and Robbins [135] developed a general approach that provides an equation of state for adsorbed films. In our case, while such a strategy could be used to define adsorption at the external surface, there is additional complexity as the surface on which adsorption occurs is nanoporous (zeolite layer beneath the external surface). Therefore, this raises the question of the boundary used to define surface adsorption versus adsorption in the core of the zeolite layer. Figure 3.9(b) shows the methane adsorbed amount as a function of pressure for the core of the zeolite layer a at different temperatures ranging from $T = 200$ K to 300 K. These data, which were extracted from the simulation data for the zeolite layer, correspond to the adsorbed amount in the innermost region of the zeolite layer (to avoid any surface effects from the zeolite external surface). In more detail, such data in molecules per unit cell correspond to the number of molecules adsorbed in a 2×2×2 supercell located at the center of the layer. As can be seen in Figure 3.9(b), these adsorption isotherms (open circles) match those obtained for the infinite zeolite crystal (full lines which correspond to data from Figure 3.7). Figure 3.9(c) shows the density of the bulk methane phase as assessed from the number of molecules in the region outside the zeolite layer. As expected, for all temperatures, methane behaves as an ideal gas (i.e. $\rho_e = P/RT$) provided the pressure does not exceed ~ 100 bar. The density of bulk methane at $P = 10^3$ b and $T = 300$ K in our simulation ($\rho_e = 2.11 \times 10^{-2}$ mol.cm^{-3}) is in good agreement with the experimental value from NIST ($\rho_{NIST} = 2.13 \times 10^{-2}$ mol.cm^{-3}).

Adsorption at the external surfaces. Figure 3.10 shows the adsorption isotherms obtained at different temperatures for methane at the external surface of the zeolite layer oriented with a normal vector along the crystallographic axis a. These data correspond to the absolute adsorbed amount obtained in the region between the two vertical dashed lines in Figure 3(a). As expected, the methane adsorbed amount ρ_s in mol per unit of surface area increases upon increasing pressure but decreases upon increasing the temperature. Figure 3.10 also shows the data obtained for the different surface flexibility models (s1 or s2) and layer orientations (a, b or c) at 300 K. Considering the different layer orientations, in the lower pressure range [< 200 bar], the methane adsorbed amounts for a, b and c are found to be very similar. On the other hand, above 200 bar, at a given pressure, the methane adsorbed amount can be ranked as $c > a > b$. This result can be explained as follows. While the external surface in layers a and b possesses the same surface oxygen density, surface oxygens in layer b are distributed heterogeneously because of the large porosity corresponding to the MFI straight channels along the y-axis; layer a is thus believed to display a larger number of adsorption sites which, in turn, leads to larger adsorbed amounts. On the other hand, the layer c presents a larger oxygen surface density than the layers a and b, therefore leading to larger methane adsorbed amounts for c. As far as the effect of surface flexibility is concerned, the methane adsorbed amounts for the s1 and s2 models are found to be very close to each other over the entire pressure range. The insert in Figure 3.10 shows the contributions of the external phase, the adsorbed amount at the external surface and in the zeolite core to the adsorption isotherm for the zeolite layer a at $T = 300$ K. In more detail, for the different pressures considered in our study, these data show the ratios $r = N_e/N$, N_s/N, and N_c/N – expressed in % – where N_e, N_s and N_c are the number of methane molecules in the external phase, at the zeolite external surface and in the zeolite core while N is the total number of methane molecules. At low pressures (< 10 bar), due to strong confinement in the zeolite pores, the fraction of methane molecules in the zeolite core is the main contribution to the adsorption isotherm. For pressures larger than 10 bar, the zeolite pores are saturated with methane while the number of molecules at the external surface and in the gas phase keeps increasing. As a result, the contribution from these two regions increase while that from the zeolite core decreases.

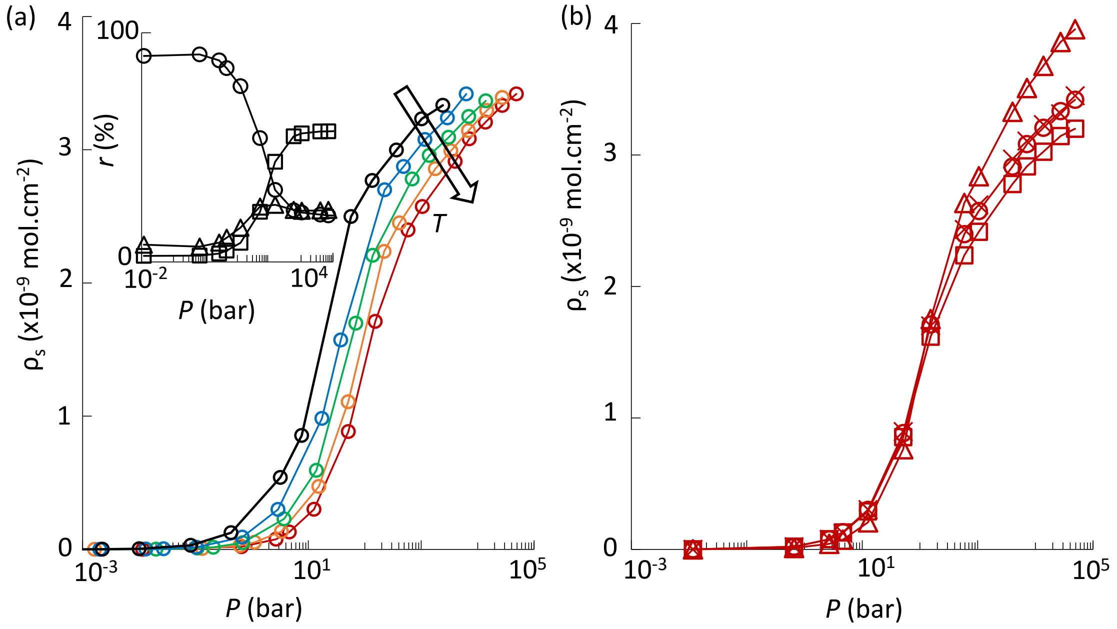

Figure 3.10: (color online) (a) Adsorption isotherms for methane at the external surface of the zeolite layer a (these data are obtained for the surface model s1 in which surface atoms are frozen). Different colors correspond to the following temperatures: 300 K (red), 275 K (orange), 250 K (green), 225 K (blue), 200 K (black). The methane adsorbed amounts are expressed as surface densities ρ_s in mol.cm^{-2}. The insert shows the following ratios at 300 K where N is the total number of methane in the system: methane at the surface N_s/N (line with open triangles), methane inside the core N_c/N (line with open circles), methane in the external phase N_e/N (line with open squares). (b) Adsorption isotherms for methane at the external surface for layers a, b, c which correspond to the lines with open circles, open squares, and open triangles, respectively. The symbols are obtained for the surface model s1 in which surface atoms are frozen (s1 model). The crosses correspond to data for the layer a with the flexible surface model (s2 model). Note that the data for the s1 and s2 models are nearly identical.

Following the work by Do *et al.* [136] on methane adsorption on surfaces at temperatures T > T$_c$, we have also calculated surface excess density for the layer orientation a which is illustrated in Figure 3.11. Surface excess densities were estimated by subtracting the methane density of the external phase density from the methane surface density. As expected, in the low pressure range, the excess surface density is close to the absolute density as the external phase density is small (below 10 bar, the external phase and the surface both contribute to adsorption with the same amount). Around 15 bar, a peak is observed corresponding to a higher contribution from the surface. It happens when the core of the zeolite is saturated with methane and surface adsorption takes over. Then surface is saturated and methane stays in the bulk phase. Then, in the large

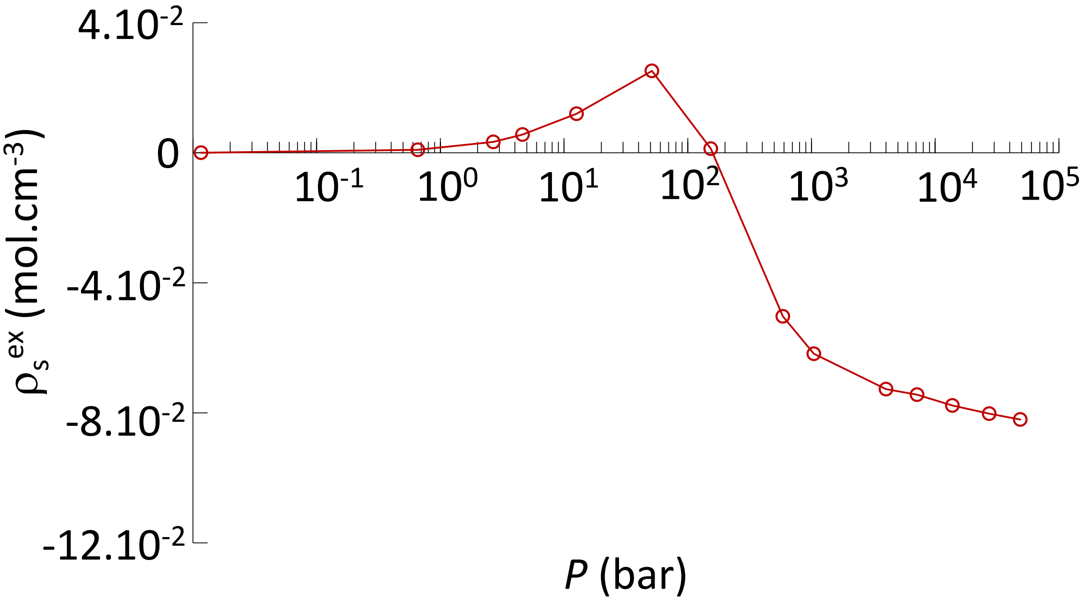

Figure 3.11: Surface excess density (in mol.cm^{-3}) at 300K for the surface model s1 and for the layer orientation *a*.

pressure range, the external phase density is large so that the excess density becomes very small and even negative. These results are consistent with previous work by Vlugt and coworkers [137] who showed that surface excess concentrations for pure ethane and propane increase and become positive when the adsorption isotherm reaches a plateau (therefore also supporting favorable adsorption at the surface). Similarly, using free energy considerations, Inzoli *et al.* [138] proposed that surface adsorption becomes more favorable as pores get saturated due to the increasing contribution from steric interactions inside the zeolite cages.

3.4 Polanyi's adsorption potential theory

In this section, we discuss a rational thermodynamic framework that allows describing in a consistent fashion adsorption in the zeolite core and at its external surface. With this goal, we invoke the adsorption potential theory which was introduced in his seminal work by Polanyi [59, 60, 61]. Despite its theoretical nature, this model is mostly used in an empirical way with very practical applications through characterization equations such as the Dubinin–Radushkevich relation for instance [139]. In contrast, in the following section, we derive the adsorption potential theory by starting from the Hill's adsorption scheme which corresponds to a perturbation treatment of molecular adsorption [140, 141, 142].

3.4.1 Frenkel-Halsey-Hill approximation

Polanyi's adsorption potential theory can be derived by starting from a simple approximation which provides a physical model for gas adsorption on a solid surface. Let us consider a fluid phase adsorbed (a) at a temperature T on a flat surface in equilibrium with a bulk fluid phase (g) so that their chemical potential are equal $\mu_a = \mu_g$ (Figure 3.12). Assuming the fluid phase behaves as an ideal gas, its chemical potential μ_g can be written as $\mu_g - \mu_0 = RT\ln[P/P_0]$ where μ_0 is the chemical potential at the saturating vapor pressure $P_0(T)$ (we note that the same expression can be used for a non-ideal phase but the pressure has to be replaced by the fugacity). Within this approximation, the chemical potential μ_a of the adsorbed phase is described using a simple perturbation treatment by assuming that it corresponds to the chemical potential μ_0 of the bulk liquid at saturation corrected for the interaction $U(z)$ with the solid surface:

$$\mu_a - \mu_0 = U(z) \tag{3.2}$$

This is the essence of this simple approximation which assumes that a molecule gets adsorbed at a position z from the surface when the interaction with the solid surface counterbalances the difference between the chemical potential of the fluid phase and that of the dense, cohesive liquid. In other words, at the chemical potential μ, the bulk liquid phase is not stable but the solid/fluid interaction stabilizes the adsorbed liquid. At very small z, the surface interaction potential $U(z)$ is positive due to the repulsive interactions with the solid surface (hard core-like, repulsive part of the solid/fluid interaction). In contrast, at larger z, $U(z)$ becomes negative with a minimum observed at a distance corresponding approximately to the position of the first adsorbed layer. At even larger z, $U(z)$ goes to zero as interactions with the solid surface become vanishingly small. Note that Eq. (3.2) does not assume that the pressure or chemical potential depends on the position z; this would be unphysical from a thermodynamic viewpoint as chemical potential and pressure must be homogeneous because of chemical and mechanical equilibrium, respectively. In practice, the statistical film thickness t and surface potential $U(z)$ can be related to the position z of the outermost adsorbed molecules as follows: t can be converted from the adsorbed volume Nv as $t = Nv/S$ where N is the number of adsorbed molecules, v the molar volume assumed to correspond to that of the bulk liquid and S the surface area of the solid phase (Figure 3.12). For a given molecular configuration of adsorbed molecules, there is a unique function that links t and z; $t = z + \sigma/2$ where σ is the kinetic diameter of the adsorbate molecule. In other words, the surface interaction potential can be written as $U(z)$ or equivalently $U(t)$ – therefore offering a mean to relate the film thickness and surface potential using the perturbation treatment described in Eq. (3.2).

While the treatment above shares similarities with the well-known Frenkel-Halsey-Hill approximation, it differs from this seminal treatment for the following reasons.

First, in the Frenkel-Halsey-Hill approximation, the adsorption film is assumed to be a homogeneous phase whose properties are close to those of the bulk liquid. In contrast, considering that we treat the case of a highly heterogeneous adsorbed phase (above the bulk critical point and in a pressure range where the adsorbed phase is heterogeneous), our system departs from the conditions considered in the Frenkel-Halsey-Hill approximation.

Second, within this approximation, one considers that the free energy difference between the adsorbed film and the bulk liquid simplifies to the potential energy difference corresponding to the adsorbate/solid interactions (in other words, entropy terms and fluid/fluid contributions cancel out as the bulk and adsorbed phase are assumed identical). Here, despite the important differences between the adsorbed and bulk phase, we assume that the free energy difference can still be approximated as the interaction energy of an adsorbed methane molecule with the MFI zeolite channel or external surface. For these different reasons, our treatment should be considered only related to the Frenkel-Halsey-Hill approximation. In fact, in this respect, considering the treatment made and system conditions under study, this approach is closer to that introduced by Barrer and Robbins [135] and Hill [142, 141, 140] who proposed extension to non homogeneous adsorbed films (with local densities dependent on the distance from the surface).

3.4.2 Polanyi's model

Polanyi's adsorption potential theory states that adsorption equilibrium is governed by a simple bijective function f such as:

$$Nv = f[\mu - \mu_0] \tag{3.3}$$

where N is the adsorbed amount in moles and v is the molar volume of the adsorbed phase. This function, which is unique for a given fluid/solid couple, has no explicit temperature dependence but we note that v, μ and μ_0 are temperature dependent. This equation is most often used as an empirical relation but its physical meaning can be understood as follows. Polanyi's model simply states that adsorption in sites having an adsorption energy E occurs as the chemical potential difference $\mu - \mu_0$ is such that $\mu - \mu_0 = E$. With this formalism, considering that intermolecular interactions are temperature independent since they derive from a Hamiltonian, it can be assumed that the latter condition is temperature independent and so is the function f. The characteristic function f does not have to be temperature independent. However, to allow practical use (i.e. to determine adsorbed amounts at a given temperature from available adsorption data at a reference temperature), it is often assumed that f is temperature independent – at least on the temperature range covering the reference temperature and that at which the data will be extrapolated. In particular, as will be shown below, Polanyi's model is found to be relatively accurate by offering at least a semi-quantitative description of adsorption in zeolite materials.

At equilibrium, the gas and adsorbed phase possess the same chemical potential, i.e. $\mu_g = \mu_a = \mu$. Using the FHH approximation, we can write that molecules get adsorbed at a position z when the chemical potential of the adsorbed molecules is such that $\mu - \mu_0 = U(z)$. Considering that $U(z)$ is a bijective function of z in the range of z values where adsorption occurs, we can write $z = U^{-1}(\mu - \mu_0)$ (where U^{-1} is the inverse function that transforms the chemical potential into the z position of the adsorbed molecule). By noting that $t = Nv/S \sim z$, this equation is equivalent to Polanyi's equation with this analogy leading to $f \sim U^{-1}$. In practice, Polanyi's equation relies on the knowledge of an adsorption isotherm at a given temperature T to predict any adsorption isotherm at a different temperature. To illustrate Polanyi's model application, let us assume that the adsorbed amount at a state P, T is known.

The chemical potential is also known through the appropriate equation of state at such pressure/temperature conditions (here, for the sake of simplicity, we assume that the ideal gas equation applies as it is relevant to the conditions considered in our study). Using the chemical potential/pressure relation for an ideal gas [i.e. $\mu - \mu_0 \sim k_{\mathrm{B}}T \ln P/P_0$], we can predict the pressure P' at which the same chemical potential condition will be reached when the temperature is T' :

$$k_{\mathrm{B}}T' \frac{\ln P'}{P'_0} = k_{\mathrm{B}}T \frac{\ln P}{P_0} \tag{3.4}$$

where P_0 and P'_0 are the saturating vapor pressure at T and T', respectively.

Using Polanyi's model, i.e. $Nv \sim$ constant, we obtain :

$$N'v' = Nv \tag{3.5}$$

when the same chemical potential conditions are met. In practice, with such a model, to predict data at a given temperature, one needs to shift the adsorbed amount along the y axis by considering that the molar volume v of the adsorbed film is identical to that of the bulk phase at the same temperature. Upon considering a different temperature, the data must also be shifted along the x axis to account for the shift in chemical potential (or equivalently in pressure) since Polanyi's model assumes that data can be described consistently through Eq. (3.3) where μ_0 describes the saturating chemical potential.

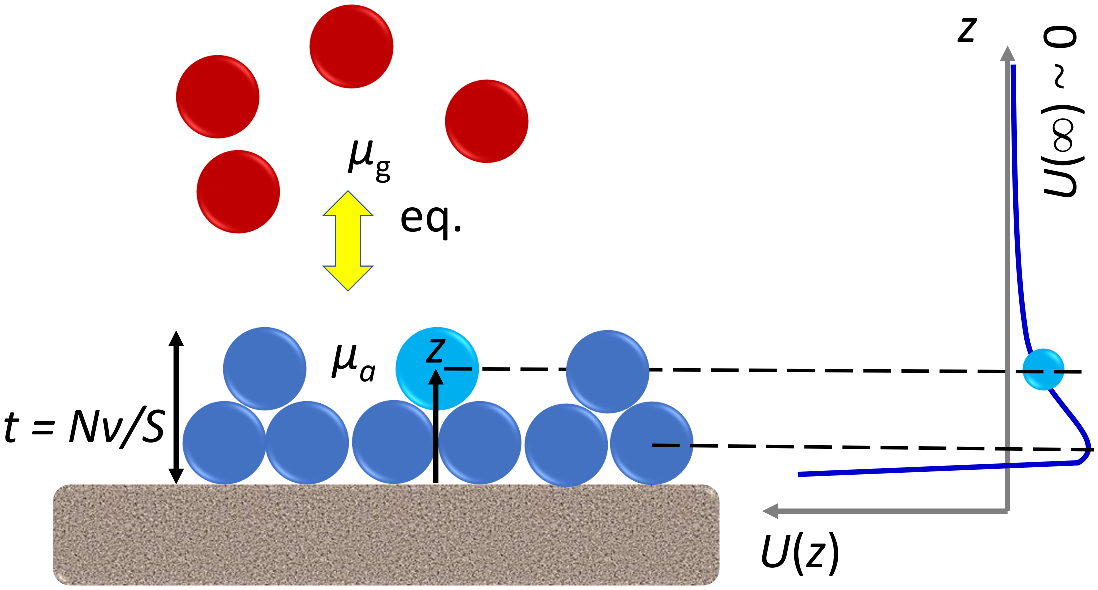

Figure 3.12: (color online) Schematic representation of the adsorption potential theory. The chemical potential of the fluid phase (red spheres) is μ_g. The adsorbed phase (blue spheres) has a statistical film thickness t which can be converted from the adsorbed volume Nv as $t = Nv/S$ where N is the number of adsorbed molecules, v the molar volume and S the surface area of the solid phase. For the adsorbed phase, the chemical potential μ_a is described using a perturbation term by assuming that it corresponds to the chemical potential μ_0 of the bulk liquid at saturation corrected for the interaction $U(z)$ with the solid surface: $\mu_a - \mu_0 = U(z)$. At very small z, the surface interaction potential $U(z)$ is positive due to repulsive interactions with the solid surface. At larger z, $U(z)$ becomes negative with a minimum located at a distance corresponding approximately to the position of the first adsorbed layer. At larger z, $U(z)$ goes to zero as interactions with the solid surface become vanishingly small.

3.4.3 Predictions of Polanyi's model

Figure 3.13 compares the predictions from Polanyi's model with our simulated methane adsorption isotherms obtained at different temperatures. Both the theoretical and simulated data for adsorption at the external surface (a) and in the zeolite pores (b) are shown. For both adsorption types, the adsorption isotherm obtained at $T = 250$ K (green data) was used as reference data to predict the adsorption isotherms obtained at other temperatures T'. Within the frame of the adsorption potential theory, we note that the accuracy of the inferred adsorption data from available data depends on the chosen reference temperature. In the present work, we chose to use data at 250 K as this temperature is intermediate between all temperatures under study (+/- 50 K). While we think that this is the best option available, we checked that the absolute error bar remains of the same order – typically $\sim$ 1-2 molecules per unit cell – when choosing an extremum temperature (i.e. 200 K or 300 K). The reference data were smoothed using a nearest neighbor moving average (full green lines). In more details, data were first interpolated using splines and then 15 points were considered for the nearest neighbor

smoothing – it was checked that, within numerical errors, the detailed treatment does not affect our conclusions below. Considering that all data shown in Figure 3.13 are obtained at temperatures above the critical point of methane ($T_c \sim 190$ K), Polanyi's model must be extended under such conditions. Indeed, for such temperatures, there is no saturating vapor pressure P_0 and, hence, no chemical potential at saturation μ_0. Similarly, for a fluid phase under such supercritical conditions, one cannot define the liquid molar volume v as involved in the adsorption potential theory. To extend the validity of Polanyi's approach, we invoke the two following hypotheses to define pseudo-quantities equivalent to $v(T)$ and $P_0(T)$ for $T > T_c$.
(1) $P_0(T)$ is obtained by extrapolating Antoine's Law at temperatures above T_c. Antoine law parameters were taken from NIST [134].
(2) v is obtained by fitting our simulated adsorption isotherms at the external surface once saturation is reached (Figure 3.10). In more detail, for each temperature T, the high pressure range of the adsorption isotherm at the external surface was fitted using the following function: $\rho_s(P,T) = \rho_{s,0}(T) + b\exp[-cP]$ where $\rho_{s,0}(T) = 1/v(T)$ is the surface density at saturation while b and c are fitting parameters. Considering that the molar volume v of methane adsorbed at saturation (or equivalently its density since $\rho \sim 1/v$) is not defined above the critical temperature T_c, one has to estimate its extrapolated value from the saturation value observed in the adsorption isotherms. To do so, several functions were considered to fit the simulated adsorbed amounts obtained for the external surface. In practice, the simple mathematical function above was found to accurately describe the change in the methane adsorbed amount upon increasing the pressure. While purely mathematical, we note that this function does predict the right evolution of the methane adsorbed amount upon increasing the pressure, so that it can be used to predict the extrapolated molar volume at saturation as $1/\rho_{s,0}(T)$ (we note that the parameters b and c were determined using the fit of the isotherm at 250 K and then were kept constant for the other temperatures as they relate to the same fluid/solid couple). The insert in Figure 3.13(a) shows the evolution of the ratio $v(T')/v(T)$ where, as mentioned above, $T = 250$ K is the reference temperature considered when applying Polanyi's model.
Before discussing the predictions from the adsorption potential theory, we mention that the extrapolation of the concepts of the saturating vapor pressure and molar volume of the adsorbed phase is far from trivial. Such approximations assume that the adsorbed phase at temperatures above the critical point is reminiscent of the liquid phase under subcritical conditions. This is justified by the fact that, even under critical conditions, the dense adsorbed phase displays a density that is close to the random close packing density inherent to the liquid phase. Similarly, while the concept of saturating vapor pressure does not apply to fluids above their critical point, its extension at temperatures beyond T_c characterizes the pressure (or chemical potential) at which surface adsorption increases sharply with pressure.

As shown in Figure 3.13, for both adsorption in the zeolite pores and at its external surface, the predictions from the adsorption potential theory are in good agreement with the simulated data. To further test the validity of the adsorption potential theory, it was also applied to our experimental adsorption isotherms obtained for methane adsorption at different temperatures (two powder samples with grain sizes $D_g = 350$ nm and $D_g = 1$ µm were considered but as mentioned above the grain size was found to make almost no difference). Like with the simulated data, the experimental adsorption isotherm at 250 K for the powder with grain size $D_g = 350$ nm was used as reference data to predict adsorption at a lower temperature for the other powder. The extrapolated values for P_0 and molar volumes at saturation $v(T)$ were taken identical to those obtained from the simulated data. As shown in Figure 3.13(c), a good agreement is observed between the predictions from the adsorption potential theory and the experimental data. This finding further confirms the applicability of Polanyi's theory to predict adsorption as a function of temperature from available reference data – even at conditions above the fluid critical temperature.

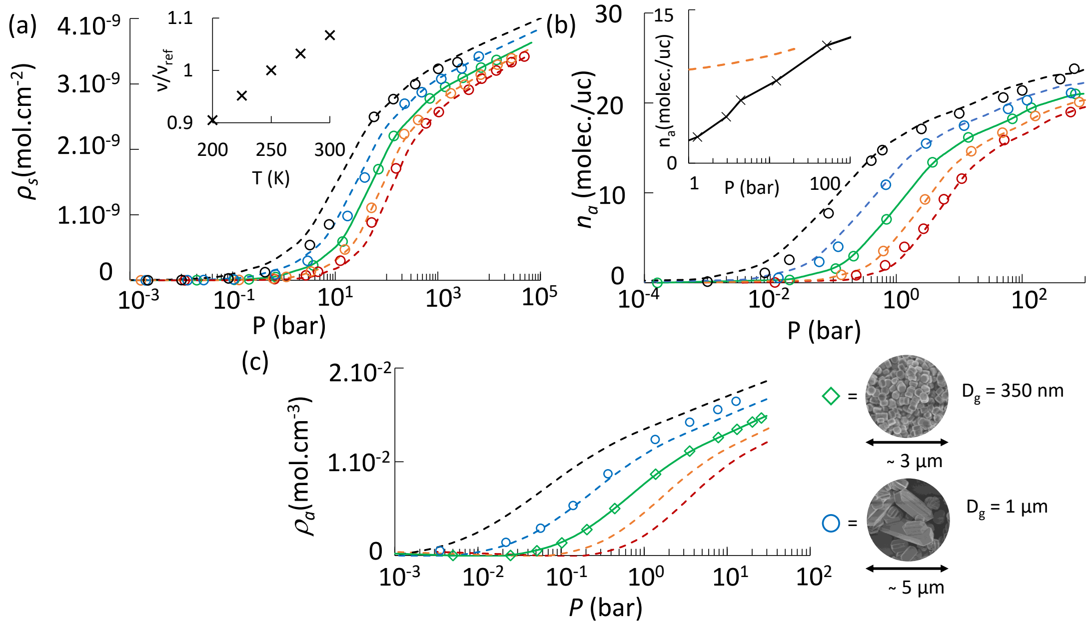

Figure 3.13: (color online) Polanyi's adsorption potential theory applied to simulated methane adsorption isotherms in zeolite layer a (a) and in a zeolite crystal (b) at different temperatures T. In (c), Polanyi's model is applied to our experimental data. Different colors correspond to the following temperatures: 300 K (red), 275 K (orange), 250 K (green), 225 K (blue), 200 K (black). The open symbols correspond to the simulated/experimental adsorbed amounts as obtained using Monte Carlo simulations in the Grand Canonical ensemble/adsorption volumetric technique. For the three figures, the adsorption isotherm obtained at $T = 250$ K (green data) was used as reference data to predict the adsorption isotherms obtained at other temperatures. The dashed lines correspond to the predictions from Polanyi's model at different temperatures T'. In (c) the adsorption isotherm for the powder of $D_g = 350$ nm at 250 K was used as the reference to predict the adsorption of the powder of $D_g = 1$ µm at 225 K. The adsorbed amount n_a is expressed in mol.cm^{-2} (a), number of methane molecules per zeolite unit cell (b) and mol.cm^{-3} (c). The insert in figure (a) corresponds to the ratio of the molar volume at T over the molar volume at the reference temperature $T = 250$ K. The insert in figure (b) corresponds to the adsorption data predicted using the FHH approximation in combination with the interaction potential by Peterson *et al.*. These data correspond to the adsorbed amount in the straight channels of silicalite-1 in the pressure range from 1 to 100 bar. The black line corresponds to the adsorption isotherm for the zeolite channels obtained by means of molecular simulation. The dashed orange line corresponds to the adsorption isotherm calculated using the attractive part of the interaction potential by Peterson *et al.* [143].

To assess the quantitative validity of perturbation treatment, we now consider explicitly the fluid/solid interaction potential $U(z)$ to describe methane adsorption in the cylindrical channels aligned along the b-axis in silicalite-1. To do so, considering the cylindrical geometry of these channels and the Lennard-Jones potential employed in our molecular simulation to describe the methane/zeolite interactions, we use the interaction potential by Peterson *et al.* [143] which corresponds to an integrated version of the 12-6 Lennard-Jones interaction energy:

$$V(s_1) = 16\epsilon_1\rho_z\pi \times \left(\frac{7\sigma_1^{12}}{512}K_9(s_1) - \frac{\sigma_1^6}{16}K_3(s_1)\right) \tag{3.6}$$

where $K_9(s_1)$ and $K_3(s_1)$ are two mathematical functions that only depend on the distance of a methane molecule from the channel center s_1. ρ_z is the atom density of the cylindrical pore considered as homogeneous in this continuum-level equation while ϵ_1 and σ_1 are the fluid/solid Lennard-Jones parameters (for detailed calculations, the reader is referred to Ref. [143]). Here, we use the same Lennard-Jones parameters as those used in the GCMC simulations for the CH_4/zeolite interactions. However, while the solid/fluid interaction for an adsorbed molecule in GCMC simulations is given by a discrete sum over each O atom in the zeolite, the interaction potential by Peterson *et al.* assumes that the zeolite can be described as a continuum medium. By inserting such an integrated potential into the FHH approximation, we can predict the adsorption isotherm at 300 K for methane restricted to the straight channels in silicalite-1. For a straight cylindrical channel having a radius R and a length L, the radial position of the outermost adsorbed molecules z is related to the adsorbed amount $N(z)$ as $N(z) = \pi\rho L[R^2 - (R-z)^2]$ where ρ is the density of the adsorbed phase. The insert in Figure 3.13(b) compares the simulated adsorption isotherm for the straight channels (black line with crosses) with the predictions from the perturbation treatment based on the interaction potential by Peterson *et al.* (orange lines). The methane density ρ used to compute the methane adsorbed amount was adjusted to match the simulated adsorbed amount at saturation. The orange dashed line corresponds to data obtained using the perturbation treatment in combination with the attractive contribution of the interaction potential by Peterson *et al.* The data are plotted up to 20 bars only where the pore gets filled $z = R$ (the FHH approximation model assumes the adsorbed phase to be incompressible so that adsorbed amount remains constant beyond pore filling). As can be seen from these data, the perturbation treatment used here in combination with the interaction potential by Peterson *et al* is not quantitatively accurate. We emphasize that this is not due to an intrinsic failure of the Frenkel–Halsey–Hill approximation but to the following points.
(1) As already discussed, while the Frenkel–Halsey–Hill hypothesis relies on the free energy rather than the interaction energy, here we only consider the interaction energy of a single methane molecule so that it neglects the role of entropy contributions as well as of fluid/fluid contributions to the adsorbed phase free energy.
(2) In our estimate of the interaction energy, we use Peterson's potential which relies on a continuum description of the Lennard-Jones interaction potential while the interaction energy landscape – even for a single molecule – can be more complex.

3.5 Partial conclusion

Using a combined experimental and molecular simulation study, we provide microscopic insights into the adsorption of simple gases in silicalite-1 zeolite crystals and thin layers. By considering both adsorption in the zeolite pores and at the external surface of zeolite layers with different crystalline orientations, we investigate the impact of the zeolite external surface on the overall thermodynamic behavior of the gas/solid couple. Due to strong confinement effects in the zeolite pores, we observe that methane first adsorbs inside the zeolite porous structure and then adsorbs at the external surface once the core porous volume gets filled. In an attempt to provide a simple thermodynamic framework for adsorption in such zeolite samples, we employ the formalism of the adsorption potential theory to rationalize adsorption data at different temperatures. Considering that methane adsorption in our study occurs at temperatures above its critical point, we extend the adsorption potential theory for such supercritical conditions. Both our experimental and simulated data suggest that the adsorption potential theory is a robust thermodynamic modeling approach to capture adsorption at different temperatures in zeolite materials. We believe that this general framework can be applied to any zeolite pore geometries (channels and/or cages). In particular, considering that the MFI zeolite displays a rather complex network structure compared to many other zeolites, we feel that such an extension should apply successfully. Moreover, our simulated data for the adsorption in the zeolite core porous volume and at its external surface suggest that the same parameters can be used to rationalize adsorbed amounts in these different regions. These findings provide a step toward the development of a consistent thermodynamic formalism to predict surface/volume adsorption in nanoporous materials with non-negligible external surface areas.

4 Methane self-diffusion in zeolite

Diffusion in nanoporous materials can be studied using both experimental and theoretical approaches (for details, the reader is referred to the recent review paper by Bukowski *et al.* [5]). Experimentally, microscopic methods such as quasi-elastic neutron scattering, nuclear magnetic resonance relaxometry and pulse field gradient nuclear magnetic resonance allow probing diffusion on length scales varying from nm to μm. Macroscopic methods such as the zero length column approach and the different chromatography techniques allow assessing diffusion on larger lengthscales. However, due to intrinsic free energy barriers and/or surface barriers in nanoporous solids, the transport coefficients obtained by means of macroscopic approaches are usually smaller than those estimated by means of microscopic methods [144, 145, 146]. As for the theoretical methods, molecular dynamics simulations are considered the method of choice to estimate self diffusivity in nanoporous materials as the typical system size accessible in these calculations are of the order of a few times the representative elementary volume of the host solid [32, 147, 148]. With this class of methods, diffusion is probed over length scales of the order of nm so that it is directly comparable to quasi-elastic neutron scattering experiments. This has lead several studies to couple neutron experiments and molecular simulation in order to probe fluid diffusion inside the porosity of various porous materials [149, 150, 151]. Among nanoporous materials, the dynamics of fluids confined in zeolites have received significant attention with an abundant literature reporting both experimental and molecular simulation approaches [32, 66, 152, 5]. While confinement and surface forces lead to fluid dynamics that is smaller than that of the bulk fluid under the same thermodynamic conditions, a rich behavior is often reported. Typically, the loading dependence of diffusivity is expected to be non-monotonous [5, 153]. Many pioneering works were reported as mentioned in Section 1.3.3 however several questions remain unanswered regarding the dynamics of fluids in the porosity of zeolite (even when simple probes are considered). In particular, despite the numerous studies on the dynamics of fluids confined in zeolite with different adsorbed amounts, the loading dependence of the observed self diffusivity remains to be fully rationalized.

This chapter is dedicated to present an approach to predict the loading-dependence of self diffusivity in zeolites. Using a combined experimental/theoretical approach involving quasi-elastic neutron scattering and molecular dynamics simulations, we show that the free volume theory – which was initially derived to describe diffusion in liquids and glasses [154] – provides a simple thermodynamic framework to predict the impact of loading on self diffusion. In more detail, using the system consisting of methane loaded in silicalite-1 zeolite as described in the precedent chapter, the self diffusion of the confined fluid is studied at different temperatures and pressures. First, using quasi-elastic neutron scattering experiments, we investigate the scattering vector q-dependence of the dynamic structure factor $S(q, \omega)$ to identify the translational and rotational diffusion modes. After validation of our molecular simulation approach against the experimental data, we investigate by means of molecular dynamics the microscopic mechanisms for diffusion in the zeolite including its matrix components along both the straight channels and the zigzag channels. Using our molecular simulation data, we check the ability of the free volume theory to accurately capture the impact of loading on the self diffusivity of confined methane. We further assess its validity by verifying its predictions for the diffusion in the different directions of space as well as when the zeolite/fluid interaction is varied. The remainder of this chapter is organized as follows. Section 4.1 presents the details about the experimental and simulation methods used to conduct our study. Section 4.2 presents the experimental and simulated data obtained for methane diffusion in silicalite-1 as a function of temperature and pressure. In the molecular simulation part, we also discuss the diffusivity anisotropy by considering diffusion in the straight and zigzag channels. In Section 4.3, we present the free volume theory and discuss its applicability to anisotropic diffusion in zeolite materials.

4.1 Experimental and computational methods

This section is dedicated to the presentation of the experimental and numerical approaches used to measure diffusivities. The first part describes the sample used and the protocol to analyse neutron data while the second part will be dedicated to the application of molecular dynamic using LAMMPS to study methane diffusion in zeolite.

4.1.1 Neutron scattering and zeolite samples

The quasi-elastic neutron scattering (QENS) experiments were performed at the Institut Laue-Langevin (ILL) in Grenoble, France, using the Time of Flight (TOF) IN6/Sharp spectrometer. This instrument was recently upgraded to achieve higher neutron flux. The incident wavelength was taken at 5.1 Å. The energy resolution of 40 μeV at the half width at half maximum (HWHM) was measured using a vanadium reference sample. The software used to process the data and perform the fits is Lamp which was developed at the Institut Laue Langevin. The scattering vector q range used in our analysis is 0.14 Å$^{-1} < q < 0.9$ Å^{-1}.

Sample preparation. The zeolite sample used in our study was silicalite-1 (pure silica MFI) synthesized in Montpellier at the Institut Européen des Membranes. The sample grain size used for all the experiments is $D_g = 1\mu$m (Figure 3.4(d)). The characterization of this sample was described in Section 3.2.1. Prior to the experiments, in order to remove all the likely adsorbed molecules inside the zeolite porosity, the sample powder was first heated up to 473 K for 60 hours in an oven under vacuum. The powder was then carefully transferred into a cylindrical sample holder to perform the neutron scattering experiments. Even if silicalite-1 is known to be hydrophobic, we tried to avoid as much as possible contact with air. All neutron scattering experiments were performed using a cryostat and a pressure set up to monitor the temperature and pressure in the sample holder.

Neutron data analysis. As described in Section 2.2.2, IN6 spectrometer records the intensity of neutrons arriving on detectors in function of the time. Figure 4.1 shows the analysis performed on these data. The steps are detailed in the following:

1. We select the files with data to analyse.
2. The incident intensity is not constant as it depends on the reactor flux. Then the recorded intensity is normalized by the incident intensity.
3. As some detectors are not functional, we remove them.

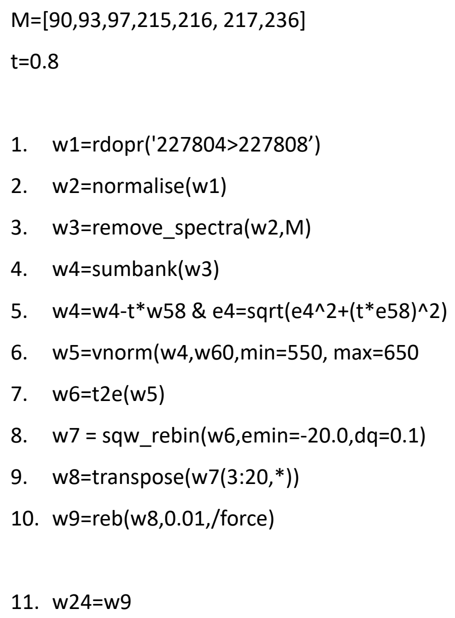

```
M=[90,93,97,215,216, 217,236]
t=0.8

1.  w1=rdopr('227804>227808')
2.  w2=normalise(w1)
3.  w3=remove_spectra(w2,M)
4.  w4=sumbank(w3)
5.  w4=w4-t*w58 & e4=sqrt(e4^2+(t*e58)^2)
6.  w5=vnorm(w4,w60,min=550, max=650
7.  w6=t2e(w5)
8.  w7 = sqw_rebin(w6,emin=-20.0,dq=0.1)
9.  w8=transpose(w7(3:20,*))
10. w9=reb(w8,0.01,/force)

11. w24=w9
```

Figure 4.1: Lamp script used to analyse our data. The detail of each command line is given in the core of the text.

4. We sum the intensities coming from detectors which have the same angle θ but different height.
5. The intensity from the sample holder is subtracted to the intensity from the sample. The elastic diffusion coming from the sample holder is more intense than the one from the sample. We took it into account by using a factor 0.8.
6. We normalize the intensity by the one from the vanadium which is q dependent.
7. Time bin are converted into energy bin as explained in Section 2.2.2.
8. Angular range is converted into q range using Eq. (2.82). The q discretization was taken $dq = 0.1\text{Å}^{-1}$.
9. Matrices are transposed to represent the energy on the x-axis.
10. As explained in chapter II, there is no linear relation between E and t as $E \sim 1/t^2$. Energy channels are rebin with a constant width of $dE = 0.01$ meV.

4.1.2 Molecular dynamics simulations

Molecular dynamic simulations were performed using LAMMPS package (version Open-MPI 1.8.1) [126]. Numerical samples used for this study are "infinite" flexible zeolite crystals defined in Section 3.1.1. The intermolecular interactions are also defined in Section 3.1.1. In this chapter, molecular dynamic simulations are performed at constant methane adsorbed amount. Initial configurations with a fixed number of molecules N were taken after having performed adsorption using Monte Carlo simulation as explained in Chapter 3. All MD simulations were performed in the canonical ensemble (i.e. constant number of molecules N, volume V and temperature T) using a Nosé hoover thermostat. The LAMMPS command line which allows to perform MD simulation is :

```
fix mynvt all nvt temp $temp $temp $(100.0*dt)
```

with a constant temperature at the start and end of the run (= 300 K) and a dumping parameter (i.e. it controls how fast the temperature is relaxed) 100 times the timestep dt.
When one perform molecular dynamic simulations on small systems, some precautions have to be taken. One side effect of MD is the shift of the center of mass.

Center of mass displacement. The shift of the center of mass of the zeolite matrix has an impact on the computation of properties. This issue arises from the small system size considered in a typical molecular simulation ($\sim$ nm). Indeed, as discussed before, the flexible zeolite model involves harmonic bonds between the Si and O atoms, which are therefore allowed to move during the simulation. This movement leads to a fluctuating shift in the center of mass together with an instantaneous momentum to the mass center. However, for a large system, the center of mass displacement will be vanishingly small because of the statistics. In a finite system, this phenomenon has to be corrected because it biases properties we want to observe. To avoid that, we consider two corrections: we calculate the mass center, the vector between the new mass center and the initial zeolite mass center and substract to all atoms this vector, we also calculate the mass center velocity and substract it to all atoms as shown in Figure 4.2. The procedure is repeated at each time step. It does not bias the velocity of each atom but removes the contribution of the mass center displacement.

Three other parameters are important: the total simulation time, Newton's equation integration time and the frequency at which positions and velocities are recorded. In this chapter, simulations were performed for at least 10 ns – this simulation time was found to be large enough to allow molecules to explore distances larger than 10 nm and, more importantly, to reach the Fickian regime. The time step used to integrate Newton's equation of motion is 1 fs and the molecular configurations were stored every 1 ps along the trajectory. We notice that a compromise has to be made between a frequent recording (i.e. more statistic) and the weight of the produced trajectories files.

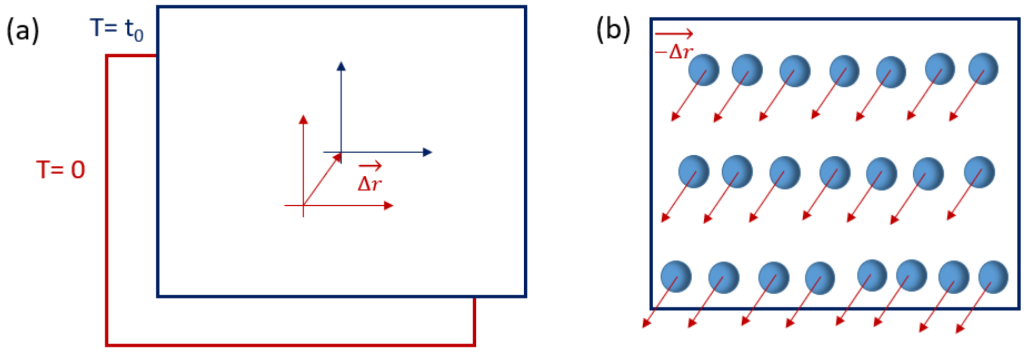

Figure 4.2: Mass center displacement phenomenon and applied correction. (a) During the simulation, due to the use of a zeolite flexible model, the center of mass drifts (from the red frame to the blue frame). (b) To correct this non physical contribution, which becomes be vanishingly small as the system size increases, vectors of the direction and speed of the mass center is subtracted for all atoms.

4.2 Self diffusion in zeolite crystals

This section reports experimental and numerical results of methane self diffusion in zeolite crystal. Molecular simulation and quasi-elastic neutron scattering are combined to study the effect of the loading, the temperature and the crystal orientation on the self diffusivity. The first and second parts present experimental and simulation results, respectively. The last part compares and discusses the self diffusion coefficients obtained using experimental and simulation approaches.

4.2.1 Experimental results

Dynamic structure factor. The QENS experiments were performed at four temperatures T: 210 K, 225 K, 250 K and 275 K. For each temperature, several methane loadings n_a were considered by imposing different pressures P using the equation given in Eq. (3.1). Figure 4.3(a) shows the experimental and simulated adsorption isotherms at $T = 250$ K (correspond to green ones in Figure 3.7). The color circles referring to the methane adsorbed amounts n_a considered in the neutron experiments. During the experiments, because of intrinsic inaccuracies in the pressure set up and in the pressure monitoring within the sample holder, it was realized that the error bar on the imposed loading is quite large especially for the lowest loadings. As a result, the exact methane adsorbed amounts considered were cross-checked and refined – as discussed later in this section – using the overall scattered amplitudes.
Figure 4.3(b) shows the dynamic structure factors $S(q, \omega)$ as measured using QENS experiments. For hydrogenated molecules such as methane, neutron scattering is mostly incoherent owing to the large incoherent cross-section of hydrogen atoms. For all loadings/temperatures, the dynamic structure factor presents a narrow and a broader contribution over a few tenth of meV. While the first peak corresponds to the elastic contribution from the host zeolite, the second peak corresponds to the quasi-elastic component due to methane diffusive motions. In the quasi-elastic contribution, two components can be identified: a first contribution corresponding to methane rotation and a second contribution corresponding to methane translation. The top panel in Figure 4.3(b) shows $S(q, \omega)$ obtained for $T = 250$ K and $n_a = 6$ molec./uc (i.e. molecules per unit cell) with different scattering vectors q. As expected, due to diffusion, a broadening of the quasi-elastic peak is observed upon increasing q (see more quantitative discussion below). The bottom panel in Figure 4.3(b) shows $S(q, \omega)$ obtained at $T = 250$ K and a scattering vector $q = 0.5$ Å^{-1} for different loadings n_a. A narrowing of the quasi-elastic peak is observed upon increasing n_a, which suggests that diffusion becomes slower upon increasing the methane adsorbed amount.

Fitting and data analysis

Even under equilibrium conditions, diffusion occurs as molecules explore their environment through thermal motion and collisions. As a result, even when no thermodynamic gradient is applied to the system, diffusion remains an important transport mechanism that prevails in many situations (such as in extreme confinement where advection is usually of very limited amplitude). We recall the expression of the functions that are going to be used for studying self diffusivity. The development of these functions can be found in the Section 1.3.1. The equation for the incoherent scattering function is given :

$$F_{\text{inc}}(\mathbf{q}, t) \sim \langle \rho(\mathbf{q}, t) \rho^*(\mathbf{q}, 0) \rangle \sim \exp[-D_s q^2 t] \tag{4.1}$$

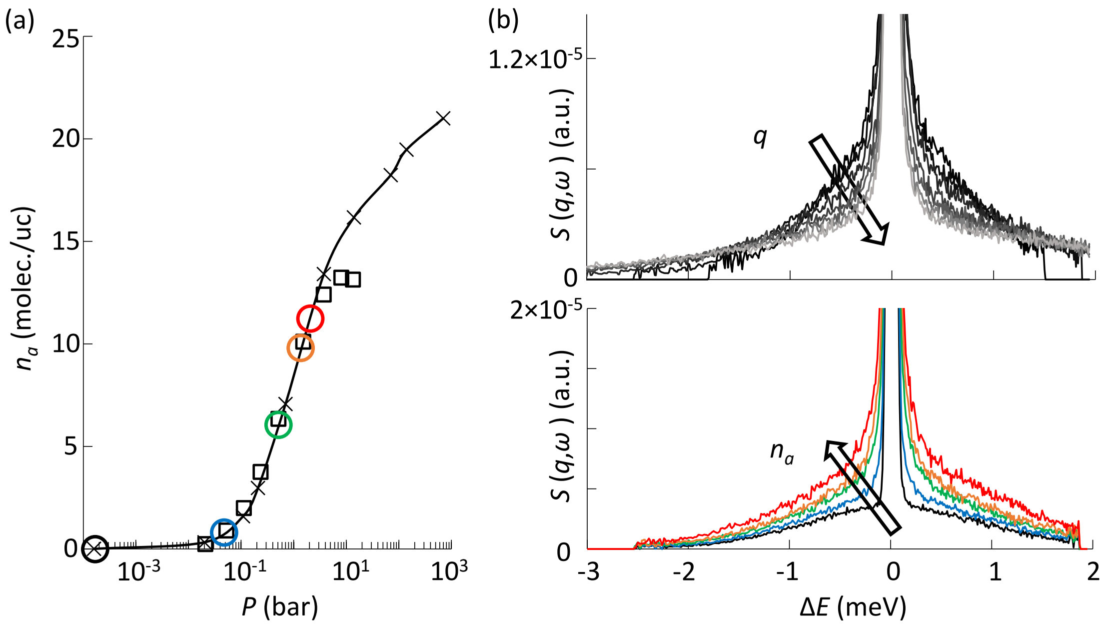

Figure 4.3: (a) Adsorption isotherm n_a(P) for methane in silicalite-1 zeolite at 250 K as obtained using Grand Canonical Monte Carlo simulations (full line with crosses) and adsorption experiments (open squares) [Adapted from Ref. [13]]. The experiments were realized for a powder sample with a grain size of $D_g = 1$ µm. Open colored circles correspond to the values (P, n_a) considered in the neutron scattering experiments. (b) dynamic structure factors $S(q,\omega)$ measured by QENS experiments. The upper figure corresponds to $S(q,\omega)$ measured at a fixed temperature T and loading n_a but different scattering vectors q. The Lorentzian function width increases as q increases. The bottom figure corresponds to $S(q,\omega)$ measured at a fixed temperature T and scattering vector q but different loadings n_a (corresponding to those represented in (a)). The Lorentzian function width decreases as n_a increases.

The incoherent dynamic structure factor $S(\mathbf{q},\omega)$ is the time Fourier transform of the intermediate incoherent scattering function $F_{inc}(\mathbf{q},t)$. Using Eq. (4.1), $S(\mathbf{q},\omega)$ can be written as a Lorentzian function:

$$S(\mathbf{q},\omega) = \frac{1}{\pi}\frac{D_s q^2}{\omega^2 + (D_s q^2)^2} \tag{4.2}$$

whose half width at half maximum is given by HWHM $= D_s q^2$. In the Fickian regime (i.e., in the long time regime), the self diffusion coefficient D_s is homogeneous, i.e. q-independent, so that HWHM is a linear function of q^2. In contrast, at short times, the HWHM is not linear in q^2 as diffusion is not homogeneous on short time scales/small length scales.

Translational/rotational diffusion. The dynamic structure factors $S(q,\omega)$ in Figure 4.3(b) were fitted using a sum of three contributions: two Lorentzian functions [to account for translational diffusion $L_T(q,\omega)$ and for rotational diffusion $L_R(q,\omega)$, respectively] and a delta function $\delta(q)$ [to account for the elastic peak].

$$S(q,\omega) = f_{DW}(q) \times [L_T(q,\omega) + L_R(q,\omega) + \delta(q)] \tag{4.3}$$

In this phenomenological equation, $f_{DW}(q)$ refers to the Debye-Waller factor where the mean square displacement $\langle u^2\rangle$ was taken constant at 1.5 Å^2 in every fit (i.e. regardless of T, n_a and q). The function defined in Eq. (4.3) was also convoluted with the instrumental resolution and a flat background (for the sake of clarity, it is omitted here).

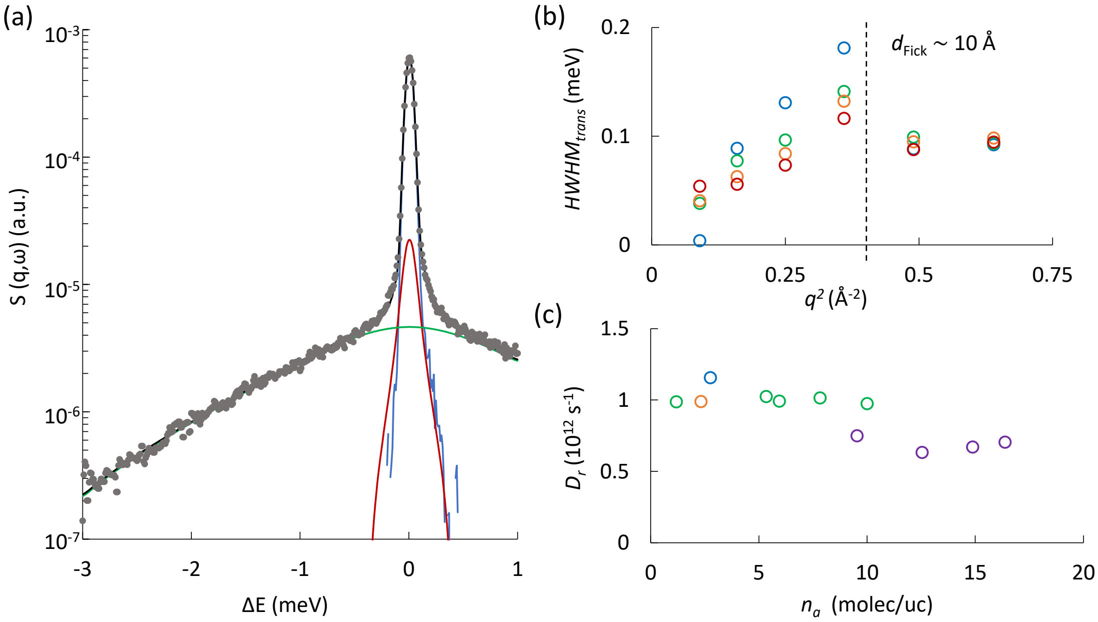

Figure 4.4: (a) Typical dynamic structure factor $S(q,\omega)$ (grey closed circles) for the silicalite-1 powder with grain sizes D_g =1 μm filled with methane at 250 K and $P = 485$ mbar. The scattering vector is $q = 0.6$ Å^{-1}. The data are fitted against a three component model as described in the core of the text. The blue line is made up of a delta function which corresponds to the elastic peak (no energy transfer between the neutron and the zeolite) while the red and green curves correspond to a Lorentzian functions which describe translational and rotational diffusion respectively. Finally the black line correspond to the fitting function which is the sum of the three mentioned functions. A flat background was taken into account. (b) Half width at half maximum (HWHM) for the translational Lorentzian component as a function of q^2 for different loadings (as indicated in Figure 4.3(a)). The black dashed line indicates the Fickian regime limit in the low q range where the self diffusion coefficient D_s can be extracted from a linear fit $D_s \sim q^{-2}$. d_{Fick} indicates the typical size beyond which Fickian diffusion is observed. (c) The rotational diffusion coefficient D_r as a function of loading n_a for different temperatures T: 210 K (purple), 225 K (blue), 250 K (green), 275 K (orange).

Figure 4.4(a) shows the experimental $S(q,\omega)$ (grey closed circles) measured at $T = 250$ K for the adsorbed amount $n_a = 6$ molec./uc (the scattering vector is $q = 0.6$ Å^{-1} in this specific example). In this figure, the solid lines correspond to the different contributions to the fitting function given in Eq. (4.3). In more detail, the blue line corresponds to the delta function - which describes the elastic peak arising from the zeolite - while the red curve refers to the Lorentzian function corresponding to translational diffusion. The green line corresponds to the Lorentzian function describing rotational diffusion.

Figure 4.4(b) shows the width of the translational Lorentzian as a function of q^2 for different loadings n_a (the color code for loadings is indicated in Figure 4.3(a); it increases from blue, green, orange and red). HWHM increases linearly with q^2 until reaching q^2=0.4 Å^{-2} (we notice that the HWHM at the lowest q falls within the resolution range of the instrument). The maximum q at which HWHM $= D_s q^2$ is observed ($q^2 \sim 0.4$) allows probing the minimum distance needed to observe Fickian diffusion; we find $d \sim 2\pi/q \sim 10$ Å. The highest q values are not fitted as they do not fall within the

Fickian range (the signal remains flat and does not evolve anymore). The linear regime HWHM $= D_s q^2$ was fitted to extract the self diffusivity D_s as a function of loading n_a and temperature T. Self diffusion coefficients will be presented later in this chapter when comparison with the simulation data will be made. However, we already see in Figure 4.4(b) that D_s decreases with loading (see the decreasing slope in HWHM $\sim D_s q^2$), which suggests that steric repulsion hinders diffusion upon increasing the loading n_a. This behavior, which will be analyzed more quantitatively below, is well-known in the field of nanoporous materials such as zeolites [66, 152].

Before discussing all results together, we analyze in Figure 4.4(c) the rotational coefficient D_r as a function of loading n_a for different temperatures: 210 K (purple), 225 K (blue), 250 K (green), 275 K (orange). The rotational diffusion is measured using the HWHM of the rotational compound as: HWHM $= 2D_r$. Because D_r is expected to be independent of the scattering vector q, for each couple (T, n_a), it was decided to keep D_r constant for all q in the fitting procedure. As shown in Figure 4.4(c), the rotational coefficient D_r remains constant upon varying the loading n_a and tends to increase with temperature T. These values for D_r are 20 times larger than those reported by Jobic *et al.* [155]; such a discrepancy can be explained by the fact that these authors used an aluminosilicate zeolite with a large number of compensation cations which hinder diffusion through steric repulsion and additional interactions. Interestingly, Theodorou and coworkers [90], who computed the rotational coefficient D_r for methane in the same silicalite-1 zeolite, reported values of the same order of magnitude as those found in the present study (on the other hand, they also reported an increase in D_r with loading which does not seem to be observed in our experimental data).

4.2.2 Molecular dynamics simulations

Mean square displacements and incoherent scattering. Like in experimental approaches, there are several frameworks that can be used to assess theoretically the self diffusion coefficient D_s. In molecular dynamics simulations, the classical strategy consists of measuring the mean square displacement (MSD) $\langle \Delta \mathbf{r}^2(t) \rangle$ as a function of time t to extract D_s in the Fickian regime:

$$\langle \Delta \mathbf{r}^2(t) \rangle = \langle |\mathbf{r}(t) - \mathbf{r}(0)|^2 \rangle = 6 D_s t \tag{4.4}$$

In practice, considering the limited statistics available in a typical molecular simulation run, data accuracy can be increased by considering time shift averages (using the system's stationary property):

$$\langle \Delta \mathbf{r}(\tau)^2 \rangle = 1/N \times 1/[t_{max} - \tau] \times \sum_{i=1}^{N} \sum_{t'=\tau}^{t_{max}} |\mathbf{r}_i(t') - \mathbf{r}_i(t' - \tau)|^2 \tag{4.5}$$

where the first sum runs over the N molecules in the system and the time origin goes from $t = 0$ to t_{max}. In the long time limit, the molecules obey the Fickian regime as described in Eq. (4.4). Formally, we checked that extracting the self diffusivity D_s from the MSD is equivalent to its determination from the time integral of the velocity auto-correlation function $D_s \sim 1/3 \int_0^\infty \langle \mathbf{v}(0) \cdot \mathbf{v}(t) \rangle \mathrm{d}t$ (see Figure 4.6 and the associated discussion in the part 4.2.2). In the present work, the anisotropic diffusion was also studied by considering the MSD restricted to the x, y and z directions. To compute the corresponding anisotropic self diffusion coefficients D_s^α with $\alpha = x$, y and z, the MSD in a single direction was determined using molecular dynamics simulations. Figure

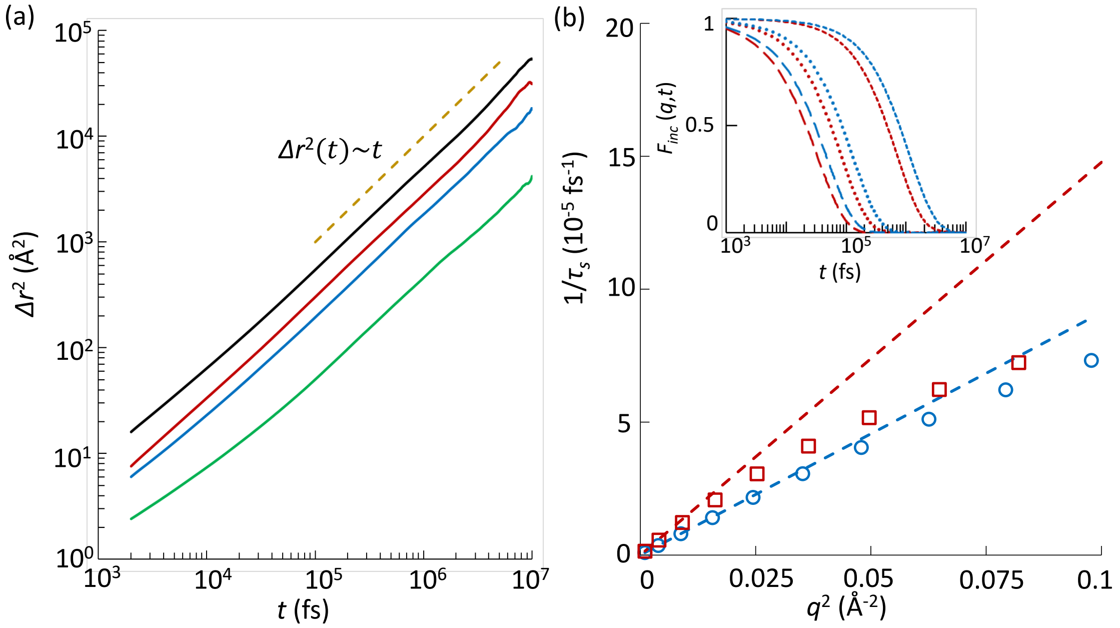

Figure 4.5: (a) Mean square displacement (MSD) as a function of time in log-log scale. The MSD is shown in each direction of space x (blue), y (red), z (green) and averaged over the three directions (black). In the Fickian regime, $\Delta r^2 \sim t$ with the slope yielding the self diffusion coefficient D_s^{3D} and its three components D_s^x, D_s^y, and D_s^z. (b) Inverse relaxation time $1/\tau_s(q)$ as a function of the squared scattering vector q^2 for the direction x and y. The open symbols correspond to data obtained from the simulated intermediate incoherent scattering function $F_{inc}(q,t)$; $F_{inc}(q,t)$ is fitted using an exponential function $F_{inc}(q,t) \sim \exp[-t/\tau_s(q)]$. The open blue circles correspond to the simulated data in the x direction while the open red squares correspond to the y direction. The lines indicate the expected behavior at small q (large distances) where the dynamics is expected to be Fickian: $1/\tau_s(q) = D_s(0)q^2$ with $D_s(q \to 0)$ estimated from the MSD obtained in molecular dynamics. The red line corresponds to the data for the y direction while the bluoe line corresponds to the x direction. The insert shows the 1D intermediate incoherent scattering function $F_{inc}^{x,y}(q,t)$ for $q \sim 0.031$ Å^{-1} (dashed), $q \sim 0.09$ Å^{-1} (dotted), $q \sim 0.15$ Å^{-1} (long dashed).

4.5(a) shows the 3D and anisotropic MSD for a methane loading of $n_a = 6$ molec./uc in silicalite-1 at 300 K. As expected, in the Fickian regime limit, the MSD in each direction is proportional to time with the anisotropic self diffusion coefficient given by:

$$\Delta r_\alpha^2 = 2D_s^\alpha t \tag{4.6}$$

where $\alpha = x$, y or z. One recovers the 3D self diffusion coefficient by computing:

$$D_s = [D_s^x + D_s^y + D_s^z]/3 \tag{4.7}$$

Looking at the MSD obtained using molecular dynamics, we find that the Fickian regime is reached for distances larger than $\Delta r^2 \sim 100$ Å^2. This value implies that the minimum distance that must be traveled by molecules to reach the Fickian regime is of the order of $d_{Fick} \sim 10$ Å – a value in very good agreement with that estimated from our experimental data (Figure 4.4).

The self diffusion coefficients derived from the MSD were cross-checked by determining the intermediate incoherent scattering functions from the MD trajectories:

$$F_{\mathrm{inc}}(\mathbf{q},t) = 1/N \sum_i \exp\left[-i\mathbf{q}\cdot(\mathbf{r}_i(t)-\mathbf{r}_i(0))\right] \tag{4.8}$$

We should warn the reader that these functions were computed on large zeolite crystals oriented along x, y and z. The description of these systems are reported on Section 5.3.1. Indeed, as it is going to be described in Section 5.2.1, the periodic boundary conditions used in molecular simulation impose that the scattering vectors $\mathbf{q} = (q_x, q_y, q_z)$ have to be chosen of the type $(2\pi n_x/L_x,\ 2\pi n_y/L_y,\ 2\pi n_z/L_z)$ where $n_{x,y,z}$ are integers and L_x, L_y, L_z are the box sizes in the three directions of space. Thus, we had to build a larger zeolite system to consider lowest q range (i.e. larger distances). The insert in Figure 4.5(b) shows $F_{inc}(q,t)$ computed for different scattering vectors q values chosen along the x and y directions. As expected, these data show that the decay time in $F_{inc}(q,t)$ increases with decreasing q; this is due to the fact that the relaxation of density fluctuations over large distances (small q) occurs over longer times. Moreover, for a given q vector, we find that the relaxation time in the y direction is faster than in the x direction. This indicates that diffusion in the large straight channels is faster than in the narrow zigzag channels. For small q, the Fickian regime is reached so that the exponential form $F_{inc}(q,t) \sim \exp[-D_s q^2 t]$ can be used to fit the data.

Figure 4.5(b) shows the reciprocal of the relaxation time $1/\tau_s(q) = D_s(q)q^2$ as a function of q^2. The circles and squares correspond to data obtained from the simulated intermediate incoherent scattering function $F_{inc}(q,t)$ along the x and y directions, respectively. The lines indicate the Fickian behavior $1/\tau_s(q) = D_s(q)q^2$ with D_s obtained from the MSD. The dashed and dotted lines correspond to the data for the x and y directions, respectively. As can be seen from this comparison, there is very good agreement between the self diffusivity obtained from the MSD and $F_{inc}(q,t)$ at small q. Interestingly, the Fickian regime seems to hold to larger q for the x direction than for the y direction. This result suggests that, owing to the smaller pore size in the zigzag channels (enhanced confinement effects), more collisions with other fluid molecules and the zeolite atoms allow reaching the Fickian regime on shorter length scales.

In order to check the numerical model that we used, we looked at the influence of different parameters on the self diffusion coefficient. We will first discuss the method of both MSD versus VACF, then the effect of the matrix flexibility and finally, the influence of the correction of the center of mass displacement.

Comparison of the Green Kubo and Einstein formalisms. Simulations using VACF method lasted 10 ps saving molecules trajectories each 1 fs. Figure 4.6 shows important differences between the integration of the VACF and the MSD methods (30 % for 16 molecules per uc). Such large difference could be explained by the simulating time in VACF analysis which is too small to reach equilibrium (insert in Figure 4.6). Indeed, a dilemma has to be faced: trajectories files generated during the simulations reach an important size which make the data analysis complicated. Indeed, a small discretization of the trajectories is necessary to take into account the first peak at the beginning of simulations. The minimal delta calculated for discretization was 1 fs. However, with a 10 ps simulating time, the file sizes started to increase. The analysis becomes too complicated for such data files to allow increasing the simulating time. For this reason, we chose to use the mean square displacement method (the MSD) to compute self diffusion coefficients.

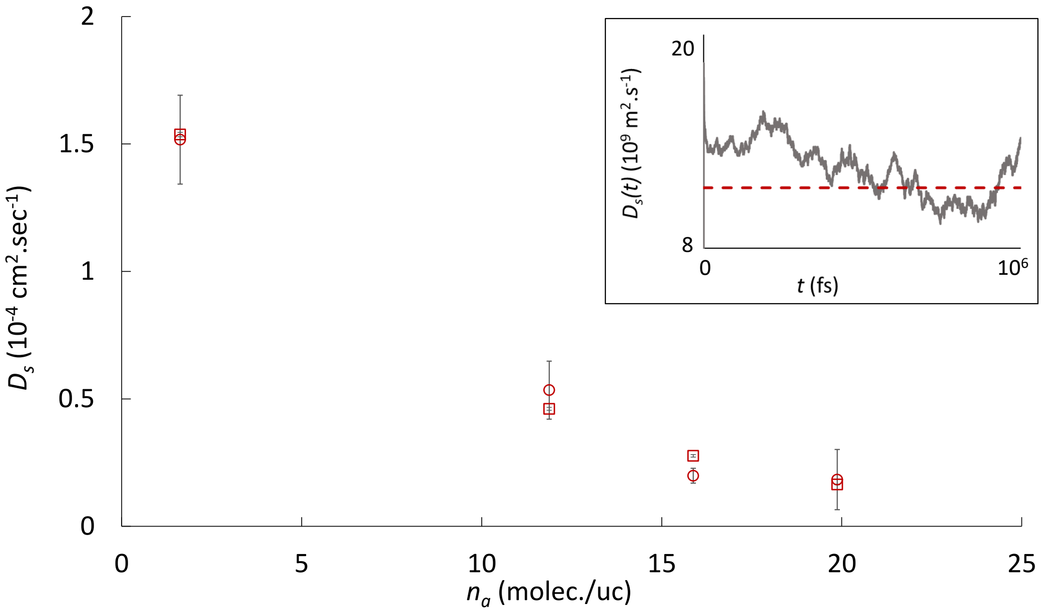

Figure 4.6: Simulated self diffusion coefficients D_s in function of the loading computed using the integral of the VACF (open circles) and the MSD method (open squares). The difference between the results from the both methods are quite important, up to 30 % on our simulating points. It can be explained by the insert showing the integral of VACF simulation on 2 ns. A long time has to be simulated to reach a convergence of the integral (not obtained here). Because of that, errors bars in VACF points are very important.

Influence of the matrix flexibility. The influence of flexibility was studied by comparing our system to a rigid one (i.e. same crystal without zeolite/zeolite interactions). Even if the simulation points were made with a varying loading between the curve corresponding to flexible matrix and the curve corresponding to rigid matrix, a trend can be observed. Indeed, the self diffusion coefficient is higher for flexible matrix than for rigid matrix as it is shown in Figure 4.7 (a). For the lowest loading the difference is around 25 %. The vibration of the frame, represented as an harmonic oscillator, in case of flexible matrix, helps methane molecules to diffuse inside the zeolite pores as it can be expected.

4.2.3 Self diffusivity in silicalite-1

Correction of the loading. Figure 4.8(a) compares the self diffusion coefficients obtained by molecular dynamics and neutron scattering experiments for the different methane adsorbed amounts considered in our study. The open circles correspond to the experimental data D_s extracted from HWHM $\sim D_s q^2$ (see Section 3.1). As explained earlier, the experimental loadings n_a suffer from significant uncertainties so that the corresponding error bar is large. To provide more accurate values for n_a and estimate the error bars associated, we computed the scattered amplitude by integrating the Lorentzian function associated to diffusion L_T. The insert of Figure 4.9 shows the scattered amplitude I_{tot} as a function of the adsorbed amount n_a^* estimated from the imposed gas pressure in QENS experiments using the adsorption isotherm data at the three temperatures considered. The total scattered amplitude I_{tot} is the sum on the whole q range considered of the amplitudes of the Lorentzian functions associated to the translational diffusion. The total scattered amplitude should be proportional to the

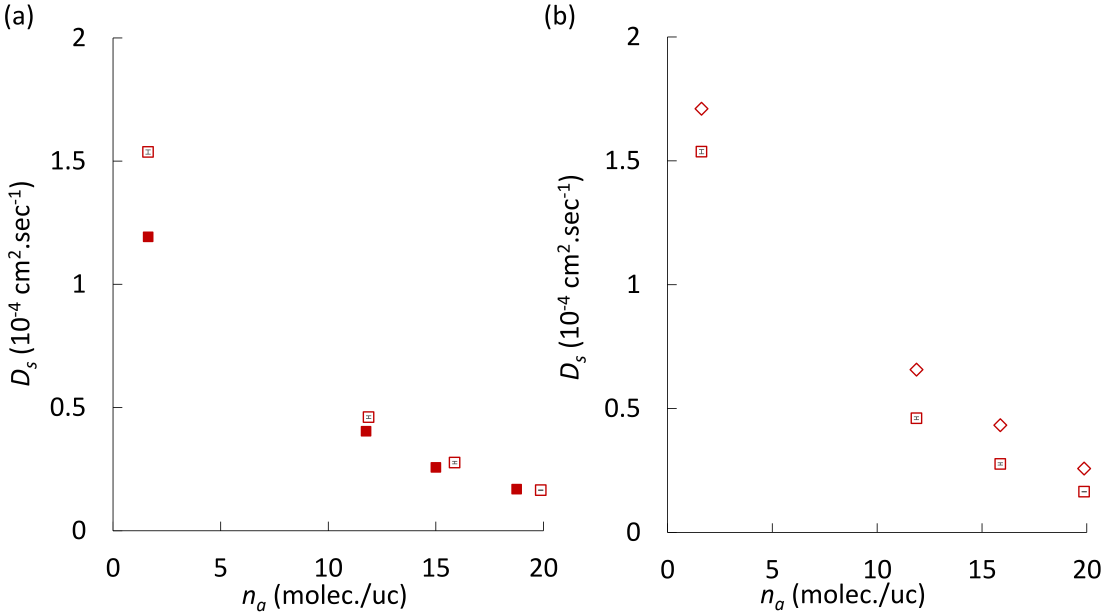

Figure 4.7: Effect of different parameters on the self diffusion coefficient D_s. (a) Self diffusion coefficient computed for a flexible (open squares) and a rigid (close squares) matrix. D_s is larger for the flexible matrix. It is due to the capacity of the structure to distort helping methane molecules to diffuse inside the matrix. (b) Self diffusion coefficient computed before the correction of the center of mass deviation (open squares) and without the correction (open diamonds). For the explanation of the correction procedure, see the core of the text. D_s is lower when the bias is corrected. Indeed, the mass center displacement adds a contribution.

methane adsorbed amount. The linear fit (black dashed line) is used to correct the methane loading : $n_a = n_a^*/\alpha$ (with α=0.556) the slope of the linear fit). This method allows to estimate more accurately the real adsorbed amount n_a in the sample during the experiment and its error bar which raises from $|n_a - n_a^*|$. Indeed, the inaccuracy on the loading measurement comes from several factors such as the pressure set up precision and an outgassing too quick. In this context, the high loading values are more reliable and thus are used to interpolate the low loading values.
Moreover, it was checked that consistent results are obtained when considering the amplitude of the rotational Lorentzian $L_R(q, \omega)$. While this approach allowed us to estimate the corrected adsorbed amount (i.e. using the scattered amplitude I_{tot}), we decided to leave in Figure 4.8(a) the error bars which arise from the discrepancy between the corrected and nominal adsorbed amounts. As for the y axis, the error bars correspond to the uncertainty in the linear fit used to extract D_s from HWHM $\sim D_s q^2$.

Self diffusion coefficients

As shown in Figure 4.8(a), a reasonable agreement is obtained between the simulated and experimental self diffusivities at different loadings. Both the experimental and simulated data show that D_s decreases upon increasing the loading n_a. This result suggests that increasing the density in the dense adsorbed phase necessarily leads to a decrease in diffusion like in bulk liquids. This interpretation is supported by our analysis performed in the final section in which a simple free volume theory was found to fully capture the dependence of D_s on the adsorbed amount n_a. Overall, as shown in Figure 4.9, our data are in good agreement with previous simulation data on methane in silicalite-1.

Experimentally, Jobic *et al.* [155] found self diffusion coefficients of the same order of magnitude; the measured self diffusivities are lower than those found in our work but, as already mentioned, these authors considered an aluminosilicate sample with a small Si/Al ratio (and, hence, with a large number of compensation cations which slow down diffusion of confined fluids in the zeolite porosity).

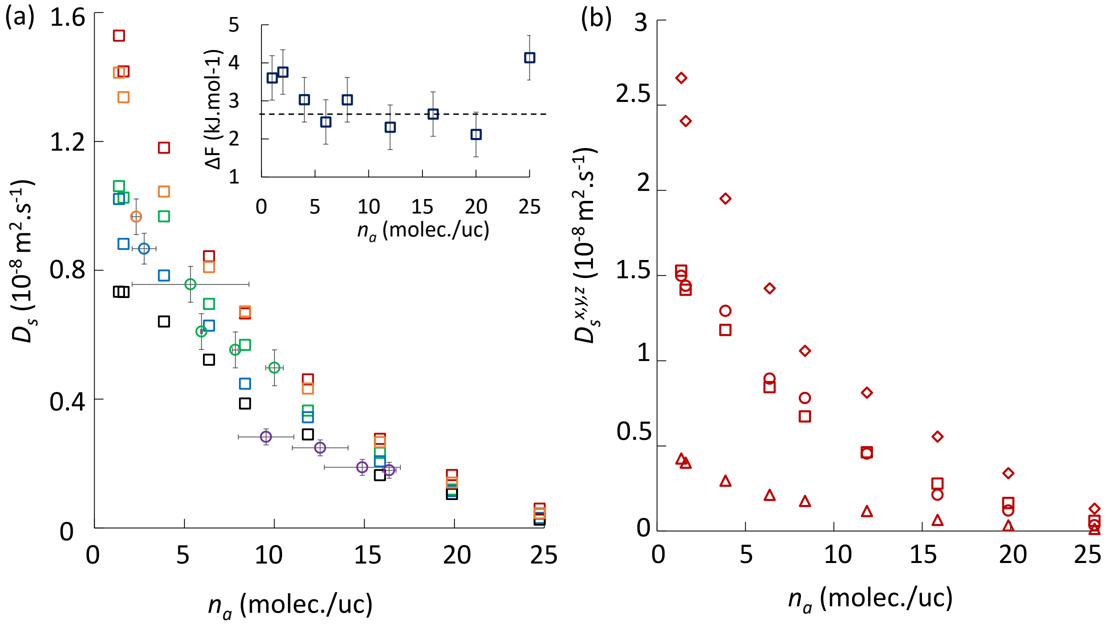

Figure 4.8: (a) Self diffusion coefficient D_s as a function of methane adsorbed amount n_a. Different colors corresponds to different temperatures: 300 K (red), 275 K (orange), 250 K (green), 225 K (blue), 210 K (purple), 200 K (black). The open squares correspond to data derived from the MSD obtained by molecular dynamics simulation while the open circles correspond to experimental data measured by QENS. The insert shows the free energy as a function of the methane adsorbed amount as estimated from an Arrhenius plot of D_s versus $1/T$. The dashed line corresponds to the thermal energy at 300 K, $RT \sim 2.5$ kJ.mol^{-1}. (b) Self diffusivity as a function of loading n_a obtained by molecular simulation at 300 K. The open symbols correspond to D_s^z (triangles), D_s^x (circles), D_s^y (diamonds), D_s^{3D} (squares).

As shown in Figure 4.8(a), D_s increases with increasing the temperature T as thermal energy promotes diffusion. The simulation data were used to estimate the free energy barrier ΔF for diffusion from a simple Arrhenius law:

$$D_s = D_s^0 \exp\left[-\Delta F/k_B T\right] \tag{4.9}$$

where D_s^0 is the self diffusion coefficient at high temperature. As shown in the insert of Figure 4.8(a), ΔF decreases with increasing the loading n_a. This result can be explained by the fact that fluid/fluid interactions become more significant upon increasing the loading. On the one hand, at low loading, the free energy barrier is mostly driven by the fluid/solid interaction energy (adsorption site free energy). On the other hand, upon increasing n_a, the free energy barrier evolves towards the bulk free energy barrier which is driven by the fluid/fluid interactions. Overall, the data in Figure 4.8(a) show that the steric repulsion between adsorbed molecules leads to a decrease in D_s with increasing n_a but with a free energy barrier that decreases with n_a. This dual impact of loading and temperature on diffusion of methane in zeolite is in agreement with the findings by June *et al.* [90]. Considering that the free energy barriers assessed in our molecular simulations are close to the thermal energy at room temperature ~ 2.5 kJ.mol^{-1}, we do not expect strong diffusion barriers for methane in silicalite-1 – a result which is also supported by the fact that the MSD were found to reach the Fickian regime on very short timescales ($\sim 1-10$ ns). However, we note that diffusion barrier effects are expected if the temperature is decreased or if bulkier and/or more complex molecules are considered (so that the free energy barrier becomes larger than the thermal energy $k_{\mathrm{B}}T$).

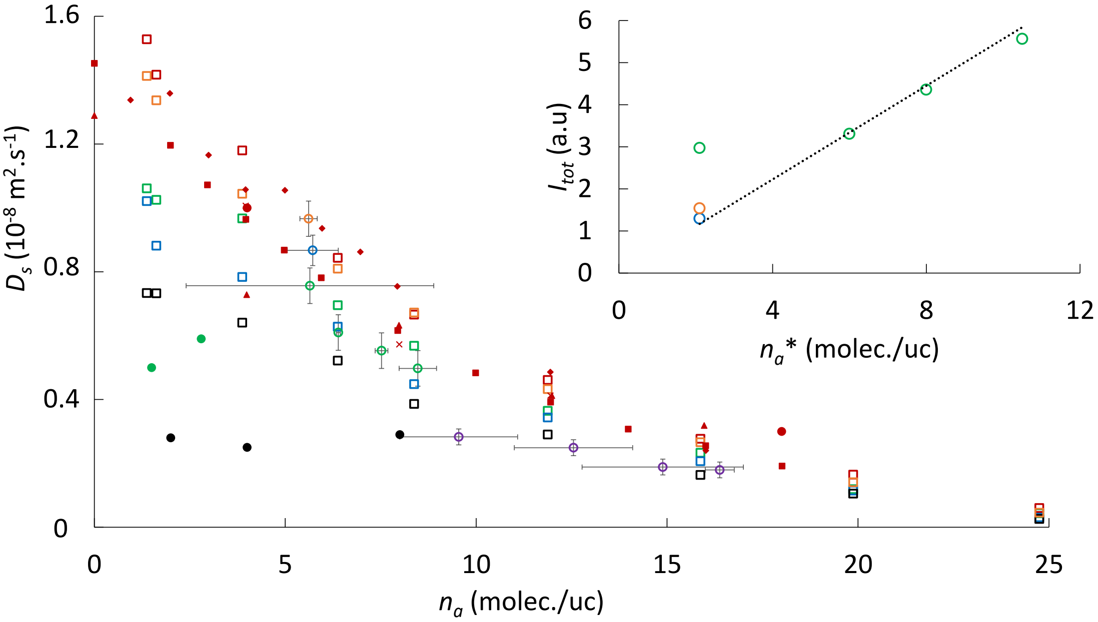

Figure 4.9: Self diffusion coefficient D_s as a function of the methane adsorbed amount n_a for methane confined in silicalite-1. Different colors correspond to various temperatures: 300 K (red), 275 K (orange), 250 K (green), 225 K (blue), 210 K (purple), 200 K (black). The open symbols correspond to the results of our molecular simulations (squares) and experiments (circles) while the closed symbols correspond to experimental data from Jobic *et al.* (close circles) and simulation data from several groups [taken from Skoulidas *et al.* [79]] (close squares : Skoulidas *et al.* [156] / triangles : June *et al.* [157] / diamond : Goodbody *et al.* [158] / cross : Jost *et al.* [159]). The insert shows the total scattered amplitude I_{tot} measured by QENS neutron experiments as a function of methane adsorbed amount n_a^* : 275 K (orange), 250 K (green) and 225 K (blue). n_a^* is estimated from the imposed gas pressure in QENS experiments using the adsorption isotherm data.

Anisotropic self diffusion. Figure 4.8(b) shows the self diffusivity D_s as a function of loading n_a as obtained by molecular simulation along the x, y and z directions (for comparison, we also report the 3D self diffusivity). Like for the 3D self diffusion coefficient, D_s^x, D_s^y and D_s^z decrease when the loading increases. For all n_a, the self diffusion coefficients follow the order: $D_s^z < D_s^x < D_s^y$. This logical order is due to the channel geometries and sizes in which molecules diffuse along these directions. While the channels in the y direction are straight and of a large diameter (~ 5.5 Å), the zigzag channels oriented along the x direction are smaller and tortuous (with a diameter ~ 5.3 Å). As for the z direction, there is no direct diffusion path so that the corresponding diffusion component is even weaker. Figure 4.10 shows that the ratio D_s^y/D_s^x evolves from 1.8 to 1.4 and D_s^y/D_s^z from 6.2 to 6.0 as n_a increases from 1 to 8 molec./uc. At low loadings, the impact of the channel geometry and of the solid/fluid interactions prevail with important differences between D_s^z, D_s^y, D_s^z. On the other hand, at high loadings, collisions between fluid molecules become more important which leads to a reduction in the diffusion as already discussed but also to smaller anisotropy effects in diffusion. Such evolution is consistent with the analysis performed by June *et al.* [90]. In contrast to the analysis above, for $n_a > 10$ molec./uc, anisotropy increases with $D_s^y/D_s^x \sim 3.8$ and $D_s^y/D_s^z \sim 9.9$; this is due to the fact that the free volume available for diffusion per unit volume – which necessarily decreases with increasing the number of confined molecules – is smaller in small channels than in large channels.

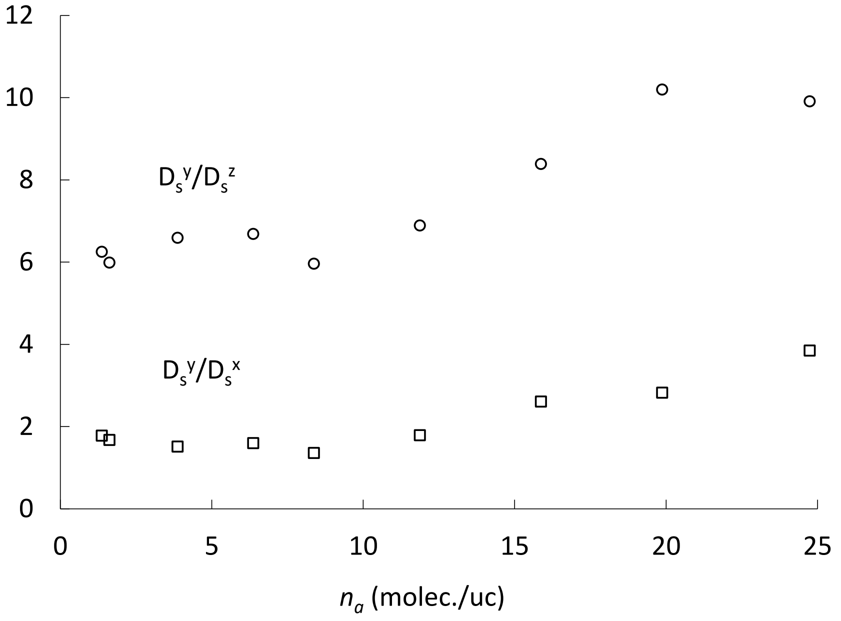

Figure 4.10: Self diffusivity ratio D_s^y/D_s^x (open squares) and D_s^y/D_s^z (open circles) as a function of the methane loading n_a. All these data were obtained by means of molecular dynamics simulations for methane confined in silicalite-1 at 300 K.

4.3 Free volume theory

In this section, we consider the free volume theory – which was initially introduced by Cohen and Turnbull [154] for molecular transport in liquids and glasses – to rationalize the self diffusivity of fluids nanoconfined in zeolite porosity. This molecular model, which accounts for the free volume left in the cavity when fluid molecules are adsorbed in their porosity, allows describing the impact of the fluid adsorbed amount and, hence, the pressure dependence of the self diffusivity D_s. This model, applied in bulk fluid systems [160, 161] was also probed on confined media [162, 163]. We describe in a first part the principles of the model. Then, we consider the numerical calculation of the free volume for our zeolite system. Finally, in the last part, we apply this model to 3D and anisotropic diffusivities.

4.3.1 Principles

In order to introduce this seminal model, we consider a zeolite filled with N fluid molecules. Within the free volume theory, we write that the self diffusion coefficient corresponding to diffusion through a cavity of volume v can be written as $D_s(v) = f_g a(v) u$. In this formula, f_g is the structure factor which takes into account the cavity geometry,

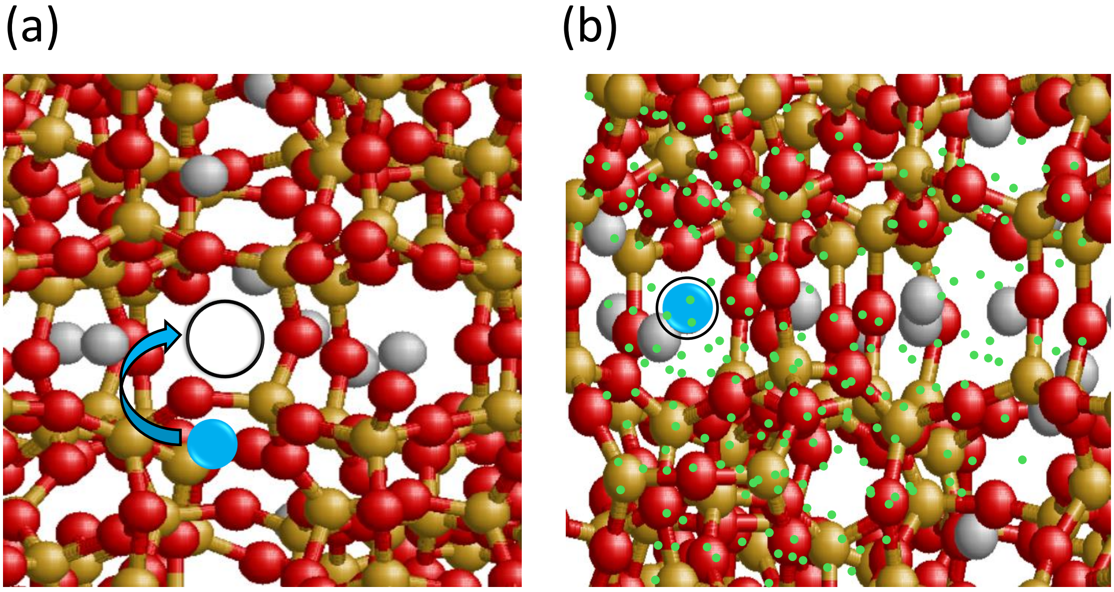

Figure 4.11: (a) Schematic representation of the free volume theory: a methane molecule (in blue) diffuses provided a free cavity is available around it. As explained in the text, a free cavity is defined as a void which does not overlap with any other methane molecules (grey spheres) or Si/O atoms of the zeolite structure. (b) Schematic principle of the free volume calculations $V_f(N)$. Many mathematical points (in green) are selected randomly in the zeolite structure. The distance d_i to every atom/molecule i in the system (zeolite atoms + methane molecules) is calculated for each mathematical point. If $d_i < \sigma_i/2$ with σ_i corresponding to the excluded diameter around the atom/molecule i, the point does not contribute to the free volume $V_f(N)$. Otherwise, it contributes to the free volume. In the end, the free volume is derived from the ratio between the number of mathematical points which contribute to the free volume and the total number of mathematical points picked in the zeolite structure.

$a(v)$ is the cavity diameter and u is the fluid velocity. Without any net flow (i.e. without any thermodynamic gradient imposing transport), u corresponds to the thermal velocity $u = \sqrt{3kT/m}$. With this simple model, introducing the normalized probability $p(v, N)$ to find a cavity with a free volume v in the zeolite filled with N fluid molecules, the average self diffusivity $D_s(N)$ is simply given by integrating $D_s(v)$ over the whole free volume available:

$$D_s(N) = \int_{v_0}^{\infty} p(v, N) D_s(v) dv \tag{4.10}$$

where v_0 is the smallest cavity volume accessible to the diffusing molecule. Using $p(v, N)$, one can define the free volume $V_f(N)$ available for diffusion of the N molecules as:

$$V_f(N) = \int_{0}^{\infty} \gamma v p(v, N) dv \tag{4.11}$$

where γ is a numerical factor that depends on the molecule shape/size. In more detail, γ takes into account the fact that several of the N fluid molecules inside the system can share the same free volume. By assuming an exponential cavity size distribution as proposed by Cohen and Turnbull [154]:

$$p(v, N) = \gamma N / V_f(N) \exp[-\gamma v / V_f(N)] \tag{4.12}$$

and that $D_s(v) = D_s(v_0)$ for all v, it is straightforward to show that the solution of Eq. (4.10) is:

$$D_s(N) = D_s(0)\exp\left[-\frac{\gamma N v_0}{V_f(N)}\right] \tag{4.13}$$

$$= D_s(0)\exp\left[-\gamma\left(\frac{V_f^0}{V_f}-1\right)\right] \tag{4.14}$$

where $D_s(0)$ is the self diffusion coefficient at infinite dilution ($N \to 0$) (the latter takes implicitly into account the fluid velocity u). To obtain the second equality, we simply use that $V_f(N) = V_f^0 - N v_0$ where V_f^0 is the free volume in the absence of any adsorbed molecules (porous volume). As shown in Refs. [162, 163], the free volume $V_f(N)$ can be expressed as a function of the adsorbed amount:

$$V_f(N) = V_f^0(1-\beta\Gamma) \tag{4.15}$$

where Γ is the ratio between the adsorbed amount N and the maximum adsorbed amount N^∞ and β is the packing fraction that takes into account the geometry of the molecules. In practice, this free volume versus adsorbed amount relationship is very useful as it allows expressing the self diffusivity as a function of loading/adsorbed amount instead of the free volume; $D_s = D_s(0)\exp[-\gamma\beta\Gamma/(1-\beta\Gamma)]$. In the present work, as shown in Figure 4.12, using Eq. (4.15), we found $\beta = 0.24$. This value is lower but similar to the one found in previous work [163]. The numerical method to compute the free volume is given in the next section.

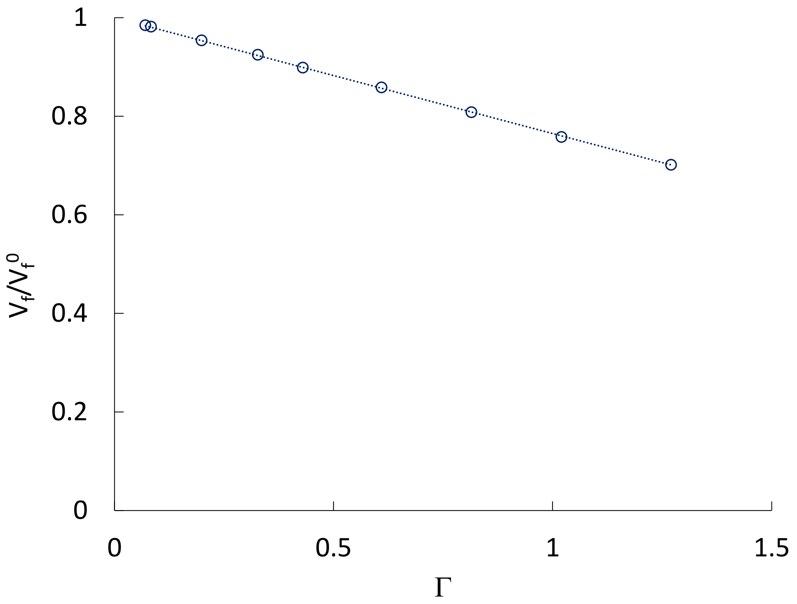

Figure 4.12: V_f/V_f^0 as a function of $\Gamma = n/n_{inf}$ using the simulation data (see manuscript). n_{inf} was obtained by fitting the simulated adsorption isotherm with the function $n_a = n_{inf} \times [1 - \exp(-cP)]$ with n_{inf} and c the fitting parameters. The slope of the linear fit is β which corresponds to the packing fraction (the value is reported in the main text).

4.3.2 Free volume assessment

To verify the validity of the free volume theory to describe the impact of adsorption on methane diffusion in silicalite-1, we estimated the free volume V_f as a function of the loading n_a. As illustrated in Figure 4.11, for each loading, using configurations generated along the MD simulations, we estimated V_f using a simple Monte Carlo sampling procedure. A total of N_p^T mathematical points are selected randomly in the zeolite volume. For each point, the distance d_i to every atom/molecule i in the system (zeolite atoms and methane molecules) is calculated and compared to the exclusion diameter σ_i around this atom (for a given atom/molecule type, this exclusion diameter is taken equal to the Lennard-Jones parameter between this species and the methane molecule). On the one hand, if any of the measured d_i is such that $d_i \leq \sigma_i/2$, the mathematical point overlaps with the zeolite and/or methane phase so that it does not contribute to V_f(N). On the other hand, if $d_i > \sigma_i/2$ for all i, the mathematical point is accessible so that it contributes to $V_f(N)$. The total number N_p of mathematical points which verifies the second condition allows computing the free volume as $V_f/V = N_p/N_p^T$ where V is the system's entire volume.

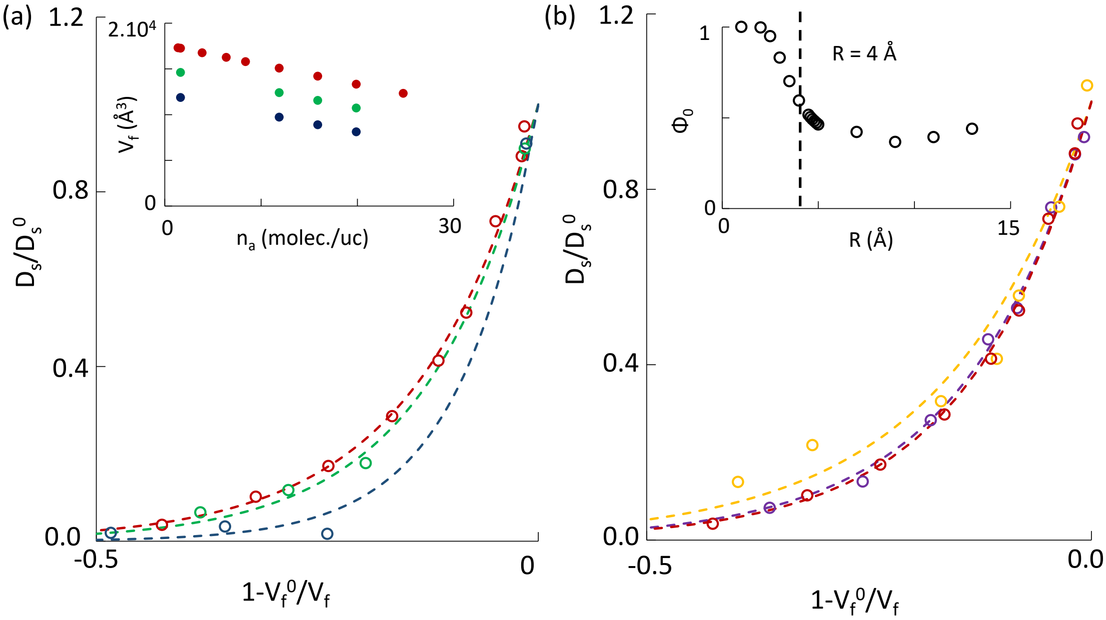

Figure 4.13: Comparison between the free volume model and the molecular dynamics results for the self diffusion coefficient D_s. The symbols correspond to D_s as obtained by molecular dynamics while the dashed lines correspond to the free volume model (with D_s^0 and γ fitted against the simulation data as explained in the main text). (a) The different data sets were obtained by varying the Lennard-Jones parameter of the methane molecule interaction with the oxygen atoms of the zeolite: $\sigma = 3.214$ Å (red), $\sigma = 3.5354$ Å (green) and $\sigma = 3.8568$ Å (blue). The insert shows the variation of the free volume V_f as a function of the methane adsorbed amount n_a. (b) Same as in (a) but for the self diffusivity along the y direction D_s^y (yellow) and in the xz plane D_s^{xz} (purple). Like in (a), we also show in red the 3D self diffusivity D_s. To estimate V_f along the y axis, we define a channel radius R; the insert shows the ratio $\phi_0 = V_f(R)/V$ along y as a function of R. The vertical dashed line indicates $R = 4$ Å which was chosen to estimate $V_f(y)$ as explained in the main text.

4.3.3 Loading dependence

Figure 4.13(a) compares our simulation results (open circles) with the free volume theory (dashed lines). We also show in the insert the estimated free volume V_f as a function of the loading n_a. As can be seen from the red data in the main figure, this simple model describes accurately the change in self diffusivity $D_s(n_a)$ upon increasing the loading n_a with only the shape factor γ and the self diffusivity at infinite dilution $D_s(0)$ as fitting parameters. To further assess the robustness of the free volume theory in describing the impact of adsorption on diffusivity, the following additional molecular simulations were performed. The Lennard-Jones parameter σ describing the interaction between the methane molecule and the zeolite oxygen atoms was artificially increased. As expected, such modifications induce a drastic change both in the free volume V_f available for diffusion and in the associated self diffusion coefficient D_s. In practice, at every loading n_a, the self diffusion coefficients $D_s(n_a)$ and free volumes $V_f(n_a)$ were calculated for $\sigma = 3.8568$ Å, $\sigma = 3.5354$ Å, $\sigma = 3.214$ Å (the latter value is the nominal value which has been discussed at the beginning of this paragraph). As can be seen in Figure 4.13(a), for all data sets, even when σ gets large, the free volume model reasonably captures the decrease observed in $D_s(n_a)$ upon increasing n_a. The parameters γ and D_s^0 obtained by fitting the free volume model against the simulated data for different σ are presented in Table 4.1. As expected, $D_s(0)$ decreases when σ increases as larger excluded volumes in the methane/oxygen interaction leads to reduced volumes for diffusion – even under infinite dilution conditions. Moreover, our data suggest that increasing σ leads to more free volume overlap between different confined molecules as γ increases.

Table 4.1: Free volume parameters γ and D_s^0 as obtained when varying the Lennard-Jones parameter σ for the interaction between the methane molecule and the oxygen atoms in the zeolite (see text).

σ(Å)	γ	$D_s^0(m^2.s^{-1})$
3.214	7.43	$1.61\ 10^{-8}$
3.5354	8.13	$1.58\ 10^{-8}$
3.8568	11.49	$1.56\ 10^{-8}$

4.3.4 Diffusion anisotropy

To further assess the validity of the free volume model, we checked its ability to probe anisotropic diffusion as observed in our molecular simulations for methane confined in silicalite-1. As already discussed, the methane molecules exhibit different diffusivities inside the straight channels (i.e. along the y direction) and inside the zigzag channels (i.e. in the xz plane). To apply the free volume model in different directions/planes, we computed the free volume along the y direction and in the xz plane. The same methodology as that described in Figure 4.11 was used but we restricted the mathematical sampling to the straight channels or to the zigzag channels. To illustrate our free volume approach restricted to a channel type, let us consider the straight channels in the y direction. Considering such channels without any adsorbed molecules, we first need to define its radius. To do so, as shown in the insert in Figure 4.13(b), we measured the void fraction $\phi_0 = V_f/V$ by sampling randomly the pore volume in a region of radius R. As expected, $\phi_0 = 1$ when R is smaller than the channel radius as only the void region is probed ($R < R_{channel}$). On the other hand, as $R \sim R_{channel}$, the void fraction drops as sampling lead to selected mathematical points that overlap with the zeolite atoms. Finally, when $R >> R_{channel}$, ϕ_0 converges to the average porosity in silicalite-1 (0.4–0.5) as sampling is homogeneous within the unit cell. From such data, we define the straight channel radius $R_{channel} \sim 4$ Å as it corresponds to the intermediate ϕ_0 value between the two asymptotic regimes described above. While this value is somewhat arbitrary, the data in Figure 4.13(b) shows that it leads to a good agreement between the free volume theory and the molecular simulation data. A similar treatment was used to predict the free volume in the zigzag channels – i.e. in the xz plane. As can be seen in Figure 4.13(b), the free volume model describes also reasonably the self diffusivity in the zigzag channels at different loadings n_a.

4.4 Partial conclusion

In this chapter, we used a combined experimental/theoretical approach to investigate the dynamics in confinement of a simple fluid inside the nanoscale porosity of zeolites. By using QENS experiments and MD simulations, we considered the effect of temperature and loading on self diffusivity with the aim to identify the molecular mechanisms responsible for diffusion. In particular, by analyzing in detail the experimental dynamic structure factor, we showed that the obtained data can be rationalized using a combination of q-independent rotational modes and q-dependent translational modes (the latter providing a means to derive the self diffusivity). To further identify the microscopic mechanisms leading to diffusion in confinement, we complemented our QENS approach using MD simulations (the latter are first validated against our experiments and data from previous works [155, 79, 159, 157, 158, 156]). By considering data at different P and T conditions, we showed that the self diffusivity of the confined fluid can be rationalized using a simple free volume theory in which the free volume is directly related to the adsorbed amount. The robustness of this approach is assessed by verifying that it captures both the 3D self diffusivity and its anisotropic components in the y direction and in the xz plane. We also checked that it describes consistently the self diffusivity as a function of loading when the fluid/zeolite interaction is varied. The following chapter will be dedicated to the study of the collective and transport diffusivities - properties which take account of, not only individual motion of molecules, but also correlations between different molecules.

5 Collective diffusion and transport in zeolite

In this chapter, we present our main results about gas transport in zeolite. In this context, transport through the nanoporous material is induced using a concentration, density or pressure gradient applied to the fluid. Transport diffusivity of molecules in such confined environment depends on the length and time scales on which it is observed. This dependence has been already related to the microscopic structure of the confined geometry with correlation between dynamic and structural properties [7, 8]. In order to study these correlations, wave vector dependent diffusion coefficients can be computed using intermediate scattering functions (as described in Section 1.3) as shown by several studies [164, 165]. As an important aspect in this chapter, the concept of De Gennes narrowing is used to rationalize the wave vector dependent collective diffusivity $D_0(q)$ using the structure factor $S(q)$. In order to check ability of De Gennes narrowing to describe transport at the nanoscale, we first consider a simple model consisting of a simulation box filled with methane above its critical temperature. Then, in a second step, we assess the ability of De Gennes narrowing model to describe the collective diffusion of methane in an "infinite" zeolite crystal. Finally, at the end of this chapter, as a preliminary step, we also report neutron scattering data for deuterated methane, which allow us to probe microscopically the transport of nanoconfined methane in the zeolite porosity.

5.1 Generalities and principles

This section presents generalities concerning collective diffusion that is going to be used for probing De Gennes narrowing model. First, we will present the gradient method which is a numerical method for computing homogeneous collective diffusion coefficients. The loading dependence of global and anisotropic collective diffusion coefficients will be discussed. Then, we will present the main principles of De Gennes narrowing model.

5.1.1 Collective diffusion

Non equilibrium MD: the gradient method

Equilibrium molecular dynamics techniques are commonly used to compute the collective diffusion coefficient D_0 using the Green-Kubo formalism or from the mean square displacement of the center of mass of the fluid. However, unlike computing the self diffusion coefficient D_s, for which the statistics is greatly improved by considering all the molecules in the system, a very large number of configurations has to be considered to get sufficient statistics when computing D_0. In this context, non equilibrium molecular dynamics, in which the fluid response to a thermodynamic gradient is probed, is an important method (typically, D_0 is the response to a chemical gradient $\nabla\mu$ imposed on each molecule in the system). In the linear response regime (i.e. for sufficiently small gradients as will be discussed later), a flux J proportional to $\nabla\mu$ is induced:

$$J_N = -D_{eff}\nabla\mu \tag{5.1}$$

with D_{eff} an effective coefficient which describes the system's response to $\nabla\mu$. Considering Eq. (1.45) in Section 1.3, we have :

$$D_{eff} = \frac{\rho D_0}{k_B T} \tag{5.2}$$

with D_0 the so-called collective diffusion coefficient, ρ the density of the fluid and T the temperature. In practice, by definition, the induced flux can be written as the sum of the molecular velocities over every molecule i:

$$J_N = \rho\frac{1}{N}\sum_{i=1}^{N} v_i \tag{5.3}$$

As explained in Section 2.1.3, molecular dynamics provides every molecule's coordinates and velocities at each time step. The principle of the non-equilibrium method is to apply a constant force (i.e. constant chemical potential) to each molecule to set the system in motion. In other words, the system responds to this external solicitation by flowing. We can compute the velocity of the center of mass $v_c = 1/N\sum_i v_i$ as a function of the applied force $\nabla\mu$. In the linear response regime, we have:

$$v_c = -\alpha\nabla\mu \tag{5.4}$$

with α the proportionality coefficient. By multiplying this last equation by the density, we get:

$$J = -\alpha\rho\nabla\mu \tag{5.5}$$

Comparison between Eqs. (5.1) and (5.5) shows that D_0 is readily obtained as:

$$D_0 = \alpha k_B T \tag{5.6}$$

Implementation. In practice, the non equilibiurm method introduced above can be performed using the Molecular Dynamics software LAMMPS [126]. Let us consider a typical LAMMPS molecular dynamics script. First, we define the driving force (chemical potential gradient) as:

```
variable F index 6.0
variable forcefac equal 0.01439
variable extforce equal $(v_F*v_forcefac)
```

Here, we apply a driving force $F = \nabla\mu = 6$ pN that is applied to each molecule. However, in LAMMPS, forces have to be input in kcal.mol^{-1}.Å^{-1}. The conversion coefficient is then defined as "forcefac" variable (second line). Finally, "extforce" is the force variable in the right unit that is applied to each molecule:

```
fix pressure fluid addforce $extforce 0 0
```

This command is adding "extforce" defined above on the x component of the forces applied to a methane molecule (ie "fluid") in Newton's equation of motion. No additional forces are applied along the y and z directions (i.e. 0 0 at the end of the line). As explained in the "Thermostat" section, the temperature is computed using molecular velocities. Without any other modifications in the script here, the temperature would be computed using the modified v_x wich could lead to a wrong estimation of the temperature for large $\nabla\mu$. To avoid such errors, we add the next two lines in the LAMMPS script :

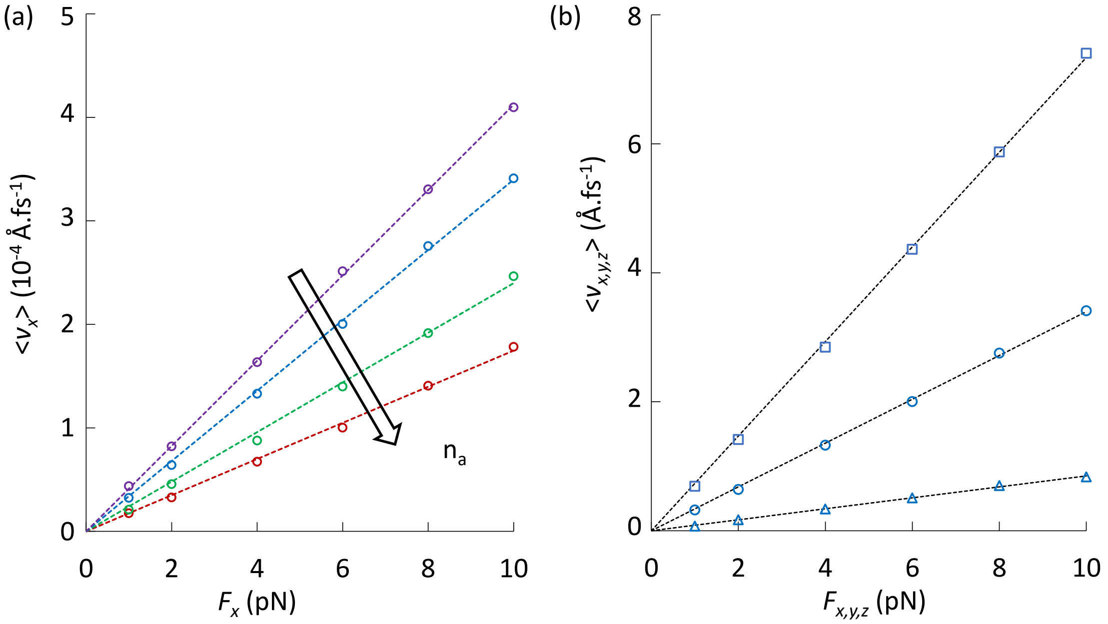

Figure 5.1: (a) Velocity of the fluid center of mass along the x direction as a function of the driving force F_x (i.e. chemical potential gradient applied along the x direction) for different methane loadings in silicalite-1 (6 molec/uc: purple, 12 molec/uc: blue, 16 molec/uc: green, 20 molec/uc: red). (b) Velocity of the fluid center of mass along the x (open circles), y (open rectangles), z (open triangles) directions for methane in silicalite-1 at a fixed loading of 12 molec/uc.

```
compute yztemp all temp/partial 0 1 1
fix_modify mynvt temp yztemp
```

The first line allows us to compute the partial temperature using v_y and v_z velocities. The second line modifies the MD parameters to take into account the new partial temperature.
Figure 5.1(a) shows the velocity of the fluid center of mass along the x direction as a function of F_x (i.e. force applied along the x direction) for different methane loadings in silicalite-1. Upon increasing the loading, the proportionality coefficient α decreases. This indicates that the anisotropic collective diffusion coefficient D_0^x decreases with loading. In order to compute the collective diffusion D_0, the anisotropic diffusion coefficients were computed by plotting the fluid center of mass velocity as a function of the force applied along the three directions x, y, z [Figure 5.1(b)]. Then, the 3D average collective diffusivity is given by $D_0 = [D_0^x + D_0^y + D_0^z]/3$.

Linear response regime. The linear response regime is a necessary condition to write a linear relation between the flux and the force as defined in Eq. (5.1). In order to verify the application range of the linear regime hypothesis, we ran several simulations with applied forces up to 30 pN. We compared the square of the thermal velocity v_{th} at 300 K (kinetic energy) and the average of the square of the center of mass velocity during the simulation time (in each space direction). The thermal velocity in one direction was computing using the energy equipartition: $\langle v_{th}^2 \rangle = k_B T/m$ with m the molecular mass of the fluid molecule. The average square of the center of mass velocity for each directions was computed as $\langle v^2 \rangle = \sum_{i=1}^{N} v_i^2$ where N is the number of molecules. Figure 5.2(a) shows that for a 2 pN force applied to each molecule the squared velocity reaches the expected value at 300 K (in each direction of space). On the other hand, Figure

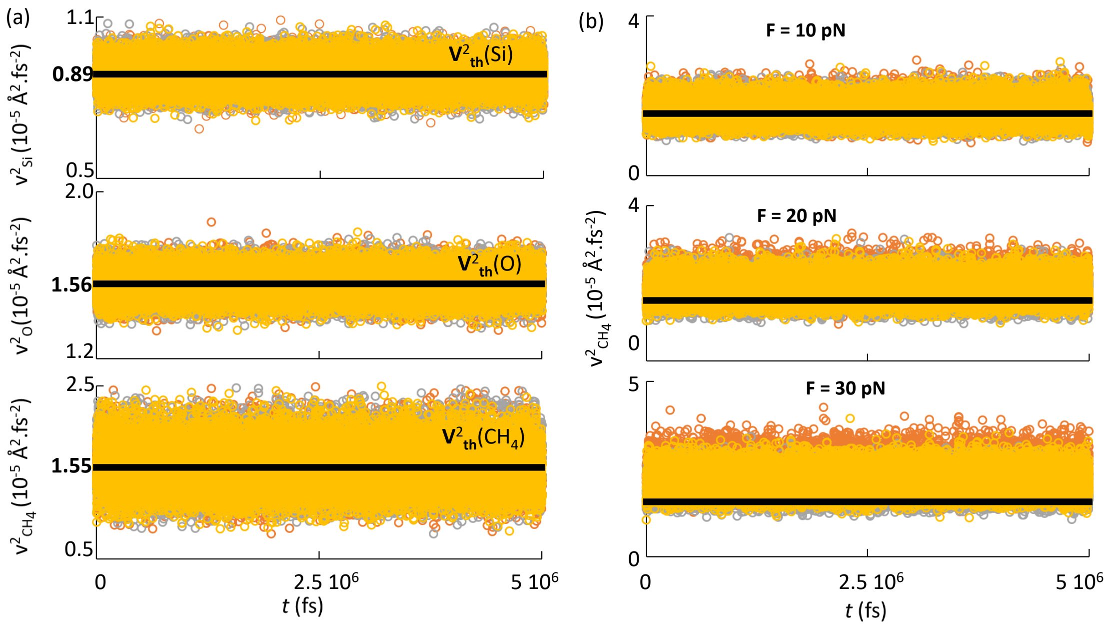

Figure 5.2: (a) Squared velocity at 300 K (black line) and squared velocity components v_x^2 (orange circles), v_y^2 (grey circles) and v_z^2 (yellow circles) for Si atoms (top), oxygen atoms (middle) and methane molecules (bottom). Velocities were computed while methane molecules were subjected to a 2 pN force in the x direction. (b) Comparison of the squared thermal velocity at 300 K and methane squared velocity components v_x^2, v_y^2 and v_z^2 for different forces applied to methane molecules in the x direction [from 10 pN to 30 pN, the color code is the same as in panel (a)].

5.2(b) shows that for an increasing force, a discrepancy appears between the computed and expected kinetic energy. This discrepancy is more pronounced on the x direction (orange circles). Indeed, it is the direction of the applied force so that the velocity increase in this direction is more pronounced. Moreover, we can notice that the y and z components of the velocities are also affected in this case even if no force is applied in these directions.

3D and anisotropic collective diffusion coefficients

Figure 5.3(a) shows the collective diffusion coefficients computed using non equilibrium molecular dynamics along x (open circles), y (open squares), z (open triangles) and total (open diamonds) as a function of methane loading in silicalite-1. The anisotropic diffusion coefficients can be ranked as $D_0^z < D_0^x < D_0^y$. The effect of channels geometry explains this ranking as channels in the y direction are larger than the zigzag channels in the x direction (on the other hand, we recall that there is no direct path in the z direction). Moreover, with increasing the loading, two regimes can be observed. First, a plateau is observed in D_0 until the loading reaches a value which depends on the orientation: 6 molec./uc for D_0^x and D_0^z and 16 molec./uc for D_0^y. Then, upon further increasing the plateau, the collective diffusion coefficients decrease with loading. This result is in good agreement with the work by Maginn *et al.* [91]. The collective diffusion coefficient is the sum of a self-contribution (correlations of a molecule's velocity at different times) and a cross-contribution (cross-correlations between molecule velocities at different times) as described by Eq. (1.42). Figure 5.3(b) shows the decrease in the ratio D_s/D_0 as the methane loading in silicalite-1 increases. As the loading tends to zero, D_s/D_0 tends to 1 as methane-methane cross-interactions become negligible. In contrast,

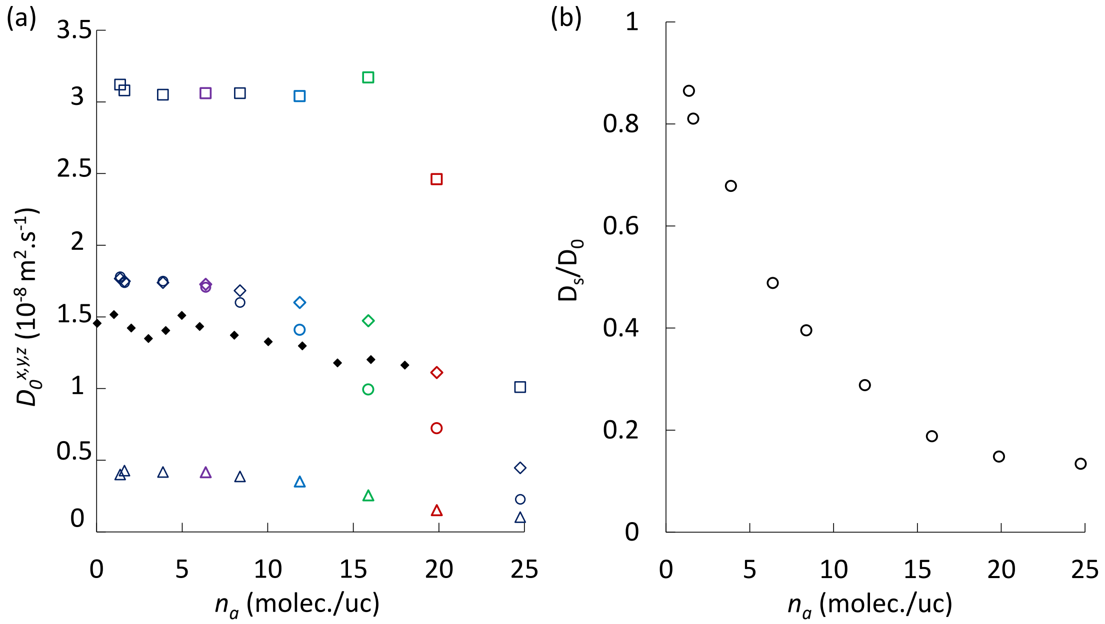

Figure 5.3: (a) Collective diffusion coefficients computed using the gradient method along x (open circles), y (open squares), z (open triangles) and total (open diamonds) in function of the loading. Collective diffusion coefficient values from Skoulidas *et al.* are reported by the closed diamonds. Loading corresponding to different colors (6 molec/uc: purple, 12 molec/uc: blue, 16 molec/uc: green, 20 molec/uc: red) are the same than Fig5.1 and will be used to probe De Gennes narrowing in the last section. (b) Ratio D_s/D_0 in function of the loading. As the loading increases, the ratio is decreasing as expected. Indeed, at low loading D_0 is driven by individual motions as collective effects is negligible.

as the loading increases, the packing density increases and methane-methane interactions become significant. As already discussed with Figure 4.8, steric repulsion becomes more important as density/loading increases so that D_s decreases in a monotonous fashion with loading. Moreover, as cross-correlations from methane-methane interactions increase with loading, the self diffusion contribution to the collective diffusion coefficients decreases. We can conclude that the collective interactions in D_0 increases with increasing loading, therefore compensating to some extent the decrease due to steric repulsion (in fact, D_0 remains nearly constant upon changing the loading). At larger loadings, the density increase leads to more pronounced steric repulsion which make D_0 decrease with loading.

5.1.2 De Gennes narrowing

In 1959, the French physicist De Gennes proposed a model to describe and predict the collective diffusivity $D_0(q)$ [166]. This model, known as De Gennes narrowing, relates the structural ordering through the structure factor $S(q)$ to wave vector-dependent collective diffusivity $D_0(q)$. As discussed in Section 1.3, the limit at vanishingly small wave vector $q \to 0$ of this collective diffusivity is the macroscopic value as defined in Onsager's theory of transport. As already discussed, the latter is directly related to the permeability k measured in macroscopic experiments on transport in porous media. Here, we present the general principles of De Gennes narrowing. This simple model describes the collective response of the system to a deviation from the equilibrium position of the system. As will be introduced in a more quantitative and formal way below, the structure factor $S(q)$ describes the distribution of molecules at thermodynamical equilibrium. Typically, this structure factor describes density correlations in the system at a characteristic lengthscale $l \sim 1/q$. Near the main correlation peak observed at $q \sim q_{max}$ in the structure factor, density correlations are frequent as they correspond to low free energy models. On other hand, far from the $S(q)$ peak, density correlations are less frequent because the associated free energy cost is large so that $S(q)$ is small. The concept of De Gennes narrowing can be understood as follows: a density perturbation involving a wave vector $q \sim q_{max}$ relaxes slowly to equilibrium as the density correlations at $\sim 1/q_{max}$ are frequent (i.e. thermodynamically favorable) and the free energy cost is low. Therefore, in this case, the associated collective diffusion coefficient $D_0(q)$ is small. On the other hand, for density perturbations with a wave vector q such that $S(q)$ is small, the system relaxes fast to equilibrium as the associated free energy cost is large. Therefore, in this case, the corresponding collective diffusion coefficient $D_0(q)$ is large.

To introduce more formally the concept of De Gennes narrowing, let us consider a system whose local density distribution at time t is $\rho(r,t)$ [77]. We can define the local chemical potential $\mu(r,t)$ from the local free energy $F(r,t)$ as:

$$\mu(r,t) = \frac{\delta F(r,t)}{\delta \rho(r,t)} \tag{5.7}$$

The conservation of the number of particles imposes that:

$$\frac{\delta \rho}{\delta t} + \nabla J = 0 \tag{5.8}$$

where J is the particle flux which is assumed to follow the linear response theory:

$$J_N = -\alpha \nabla \mu \tag{5.9}$$

By replacing J and μ in Eq. (5.8), we obtain:

$$\frac{\delta \rho(r,t)}{\delta t} - \alpha \triangle \frac{\delta F(r,t)}{\delta \rho(r,t)} = 0 \tag{5.10}$$

Using Fourier transforms, we can convert Eq. (5.10) into:

$$\frac{\delta \rho(q,t)}{\delta t} - \alpha q^2 \frac{\delta F(q,t)}{\delta \rho(q,t)} = 0 \tag{5.11}$$

At this stage, we express the free energy as a sum of uncoupled modes having an amplitude $A(q)$:

$$F(q,t) = \sum_q \frac{1}{2} A(q) \rho(q,t) \rho^*(q,t) \tag{5.12}$$

where the * indicates the conjugated complex quantity. For a given mode q, $F(q,t)$ can be identified as the potential energy of a harmonic oscillator that brings the system back to its equilibrium state (in this expression, $A(q)$ is the force constant). Inserting Eq. (5.12) in Eq. (5.10) leads to :

$$\frac{\delta \rho(q,t)}{\delta t} + \alpha q^2 A(q) \rho(q,t) = 0 \tag{5.13}$$

The solution to this equation is given by:

$$\rho(q,t) = \rho(q,0) \exp[-D_0(q) q^2 t] \tag{5.14}$$

with $D_0(q) = \alpha A(q)$ the wave vector dependent collective diffusivity. The energy equipartition theorem implies that each mode is populated by the thermal energy so that $A(q)\rho(q)^2 \sim k_B T$. As a result, the structure factor can be written as:

$$S(q) =< \rho(q)\rho^*(q) >= \frac{k_B T}{A(q)} \tag{5.15}$$

Replacing $A(q)$ in the expression for $D_0(q)$ leads to:

$$D_0(q) = \frac{\alpha k_B T}{S(q)} \tag{5.16}$$

This correlation between structural and dynamical properties has been probed for diverse bulk systems such as glasses [167], colloidal dispersion [168] or supercooled liquid [169]. However, studies structure/diffusivity relations on confined fluid are still missing. On this topic, Nygard *et al.* showed -using photon spectroscopy- the wave dependence of the collective diffusion coefficient following the structure factor oscillations around the $S(q)$ peak. This qualitative agreement with the model was shown to stand when considering anisotropic $S(q)$ and $D_0(q)$.
In the next two sections, we present the calculations for the collective diffusion coefficient $D_0(q)$ and structure factor $S(q)$ to discuss the applicability of Eq. (5.16) in the case of a bulk fluid phase and the zeolite filled with confined methane molecules.

5.2 Bulk fluid

This section is dedicated to De Gennes narrowing applied to a bulk fluid phase. In practice, this simple system is used to develop our computational tools and illustrate the application of De Gennes' model.

5.2.1 Structure factor

Computational aspects. The system is made up of 8586 methane molecules within a box of a size L_x = 120.54 Å, L_y = 118.428 Å, L_z = 78.858 Å. The intermolecular pair potential used is the Lennard-Jones potential (see section 3.1.1) between CH_4 molecules. All molecular Simulations were done at 300 K. The static structure factor $S(q)$ was computed from a molecular dynamics simulation using the two following conventional methods. The first method consists of using the radial distribution function $g(r)$ which is linked to the Fourier transform of the $S(q)$. The second method, which is a direct method, relies on computing the structure factor $S(q)$ directly in Fourier space.

Indirect calculation ($g(r)$ method). The radial distribution function $g(r)$ describes the distribution of molecules at a distance between r and $r + dr$ of another molecule. For an isotropic medium, it is linked to the static structure factor $S(q)$ by the following Fourier transform:

$$S(q) = 1 + \rho \int_0^\infty [g(r) - 1] \times \frac{sin(q.r)}{q.r} \times 4\pi r^2 dr \tag{5.17}$$

with ρ the fluid number density. In practice, $g(r)$ was computed in this work by counting for each methane molecule the number of methane molecules at a distance between r and $r + dr$: $\mathrm{d}n(r) = N/V g(r)\mathrm{d}r$ with N the total number of methane molecules and V the volume of the system.

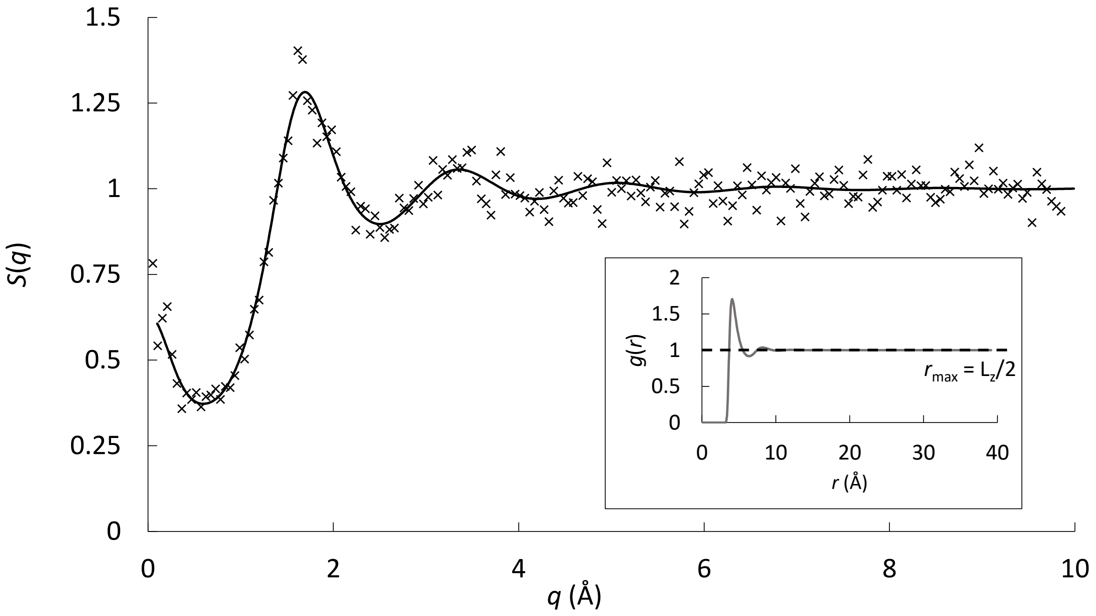

Figure 5.4: Static structure factor using both the direct method (crosses) and the radial distribution function integration (full line). The insert shows the radial distribution function $g(r)$ plotted up to the maximum distance $r_{max} = L_z/2$

Direct calculation in Fourier space. $S(q)$ can also be computed directly as:

$$S(q) = \frac{1}{N} < \rho(q)\rho^*(q) > \tag{5.18}$$

with $\rho(q) = \int \rho(r)e^{-i\mathbf{q}\cdot\mathbf{r}}\mathrm{d}\mathbf{r}$ the Fourier component of the density ($\rho^*(q)$ is its complex conjugate as already introduced) and N the total number of molecules. The density can be expressed as a sum of Dirac on each atom position at the time t, $\mathrm{r}_i(\mathrm{t})$:

$$\rho(r,t) = \sum_{i=1}^{N} \delta(\mathbf{r} - \mathbf{r}_i(t)) \tag{5.19}$$

Upon replacing $\rho(r)$ in Eq. (5.19), the Dirac sum selects r in the Fourier transform as:

$$\rho(q) = \sum_{i=1}^{N} e^{-i\mathbf{q}\cdot\mathbf{r}_i(t)} \tag{5.20}$$

The structure factor $S(q)$ can then be computed as:

$$S(q) = \left\langle \frac{1}{N} \sum_i \sum_j e^{-i\mathbf{q}(\mathbf{r}_i - \mathbf{r}_j)} \right\rangle \tag{5.21}$$

where the bracket <> denotes ensemble or temporal average. Because of the use of periodic boundary conditions, only some particular, quantified scattering vectors q can be considered. Indeed, periodic boundary conditions induce an infinite number of molecules images with the coordinates $(x + n_xL_x,\ y + n_yL_y,\ z + n_zL_z)$, $n_{x,y,z}$ integers so that in general the structure factor $S(q)$ will be dependent on the origin of the system. Indeed, if we do not take into account this specificity linked to the use of periodic boundary conditions, we will add the terms of the unphysical images correlations at infinity in the structure factor $S(q)$. To overcome this difficulty, we use quantified scattering vectors

q as $q = n_{x,y,z} 2\pi/L_{x,y,z}$ so that the calculated structure factor is corrected for such artefacts:

$$S(q) = \left\langle \frac{1}{N} \sum_i \sum_j e^{-i\mathbf{q}\cdot(\mathbf{r}_i - \mathbf{r}_j + L_x\mathbf{x} + L_y\mathbf{y} + L_z\mathbf{z})} \right\rangle \tag{5.22}$$

$$= \left\langle \frac{1}{N} \sum_i \sum_j e^{-i\mathbf{q}(\mathbf{r}_i - \mathbf{r}_j)} e^{-i\mathbf{q}\cdot(L_x\mathbf{x} + L_y\mathbf{y} + L_z\mathbf{z})} \right\rangle \tag{5.23}$$

$$= \left\langle \frac{1}{N} \sum_i \sum_j e^{-i\mathbf{q}\cdot(\mathbf{r}_i - \mathbf{r}_j)} e^{-i(2\pi n_x\mathbf{x} + 2\pi n_y\mathbf{y} + 2\pi n_z\mathbf{z})} \right\rangle \tag{5.24}$$

$$= \left\langle \frac{1}{N} \sum_i \sum_j e^{-i\mathbf{q}\cdot(\mathbf{r}_i - \mathbf{r}_j)} \right\rangle \tag{5.25}$$

Figure 5.4 shows the static structure factor $S(q)$ computed by the direct method (crosses) and the radial distribution function integration (full line). Both methods give similar results. The smallest q value computed using the direct method is given by the box length $q = 2\pi/L_z$. On the other hand the limiting distance below which the radial distribution function (in the insert) is integrated is $r_{max} = L_z/2$.

5.2.2 Collective diffusivity

To test the concept of De Gennes narrowing, the wave vector collective diffusion coefficient $D_0(q)$ has to be computed. To do so, we rely on intermediate scattering functions $F(q,t)$ which characterize correlations between molecules taken at different times. Two $F(q,t)$ functions can be defined. On the one hand, $F_{\text{inc}}(q,t)$ characterizes self-correlations as it corresponds to correlations for the same molecule at different times t:

$$F_{\text{inc}}(q,t) = 1/N \sum_{i=0}^{N} < \rho_i(q,0)\rho_i^*(q,t) >$$

with $\rho_i(q,t)$ the Fourier transform of the single molecule density. On the other hand, $F_{\text{coh}}(q,t)$ corresponds to collective correlations as it characterizes correlations between molecules at different times t:

$$F_{\text{coh}}(q,t) =< \rho(q,0)\rho^*(q,t) >$$

In this context, we note that the structure factor is given by the intermediate coherent scattering function at $t = 0$: $S(q) = F_{\text{coh}}(q,0)$

Self diffusivity. We recall that $F_{\text{inc}}(q,t)$ is related to the self diffusion coefficient D_s as determined in Fick's regime (see Section 1.3.1):

$$F_{\text{inc}}(q,t) = \exp[-D_s q^2 t] \tag{5.26}$$

However, even if the Fickian regime is not reached (typically, for large q vectors), a relaxation time $\tau_s(q)$ can be associated with an underlying wave vector self diffusivity $D_s(q)$: $\tau_s(q) = 1/D_s(q)q^2$ is the relaxation time over a characteristic length $\sim 1/q$. In the present thesis, the functions $F_{\text{inc}}(q,t)$ were computed by the direct method (see Section 5.2.1) with an average performed over all the molecules in the system:

$$F_{\text{inc}}(q,t) = 1/N \sum_i < \rho_i(q,0)\rho_i^*(q,t) >= 1/N \sum_i \exp\left[-i\mathbf{q}(\mathbf{r}_i(t) - \mathbf{r}_i(0))\right]$$

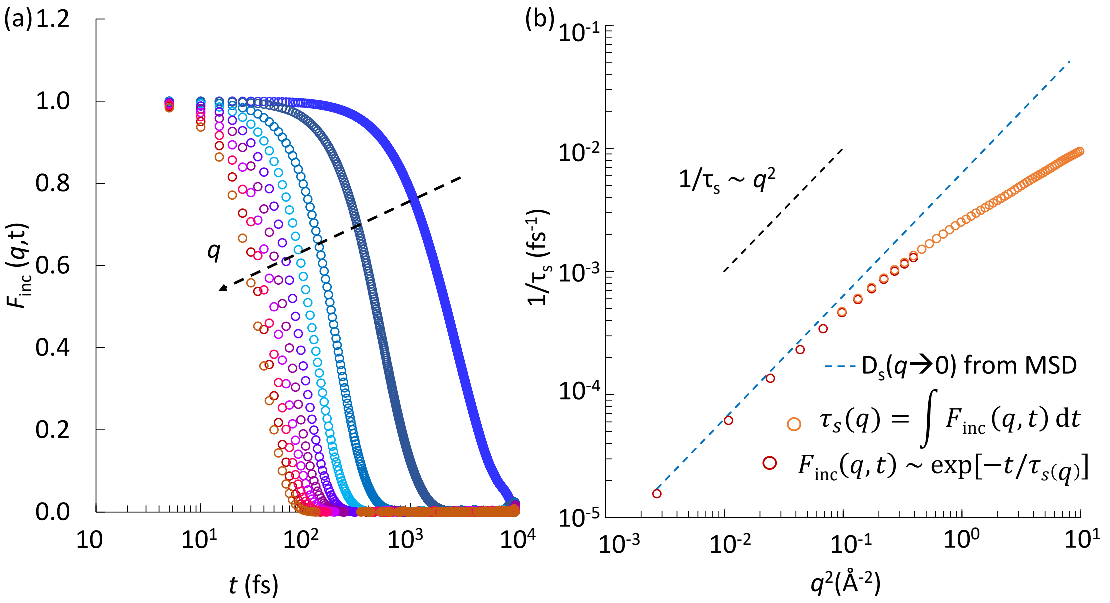

Figure 5.5: (a) Intermediate incoherent scattering function $F_{inc}(q,t)$. The open symbols correspond to the simulated data $F_{inc}(q,t)$ as obtained from molecular dynamics. The different colors correspond to increasing wave vectors q as indicated by the dashed arrow: $q = 0.261$, 0.782, 1.824, 2.867, 3.909, 4.952, 5.994, 7.037, 8.079 and 9.122 Å^{-1}. (b) Inverse relaxation time $1/\tau_s(q)$ a function of the squared wave vector q^2. The open symbols correspond to data obtained from the simulated intermediate incoherent scattering function $F_{inc}(q,t)$ the orange circles correspond to $1/\tau_s(q)$ as obtained by integrating $F_{inc}(q,t)$. The red circles were obtained by fitting $F_{inc}(q,t)$ using a simple exponential function $F_{inc}(q,t) \sim exp[-t/\tau_s(q)]$. The blue dashed line indicates the expected behavior at small q (large distances) where the dynamics is expected to be Fickian $1/\tau_s(q) = D_s(0)q^2$ where $D_s(0)$ was estimated from the mean square displacement obtained in molecular dynamics.

with $r_i(t)$ and $r_i(0)$ the positions of molecule i at time t and 0, respectively. Figure 5.5 (a) shows the simulated intermediate incoherent scattering functions $F_{\mathrm{inc}}(q,t)$. As expected, upon increasing q, the relaxation time becomes shorter because molecules are displaced over shorter distances.

To extract $1/\tau_s(q)$ from $F_{\mathrm{inc}}(q,t)$, two methods were used. The first method corresponds to the time average as defined from $F_{\mathrm{inc}}(q,t)$:

$$\tau_s(q) = \int F_{\mathrm{inc}}(q,t)\mathrm{d}t \tag{5.27}$$

However, for small q, integrals as defined in this equation do not converge because the simulation time was not large enough. In this case, we chose to fit $F_{\mathrm{inc}}(q,t) \sim \exp[-t/\tau_s(q)]$ with $\tau_s(q)$ the characteristic relaxation time. This fitting method relies on the fact that $F_{\mathrm{inc}}(q,t)$ can be written as an exponential in the small q range (i.e. Fickian regime). The results from the two methods are presented in Figure 5.5(b) where data from the integral method are represented by orange circles while data from the fitting method correspond to red circles. The two methods converge in the interval $q \sim 0.08 - 0.3$ Å^{-1}. The blue dashed line indicates the expected behavior at small q (large distances) where the dynamics is expected to be Fickian. Thus, in this range, the characteristic time is $1/\tau_s(q) = D_s(0)q^2$ where $D_s(0)$ was estimated from the mean square displacement obtained in real space from molecular dynamics trajectories.

Collective diffusivity. $F_{\mathrm{coh}}(q,t)$ and $D_0(q)$ are related thanks to Eq. (5.14). Indeed, if we multiply Eq. (5.14) by $\rho^*(q,0)$, we obtain:

$$F_{coh}(q,t) = S(q)\exp[-D_0(q)q^2 t] \tag{5.28}$$

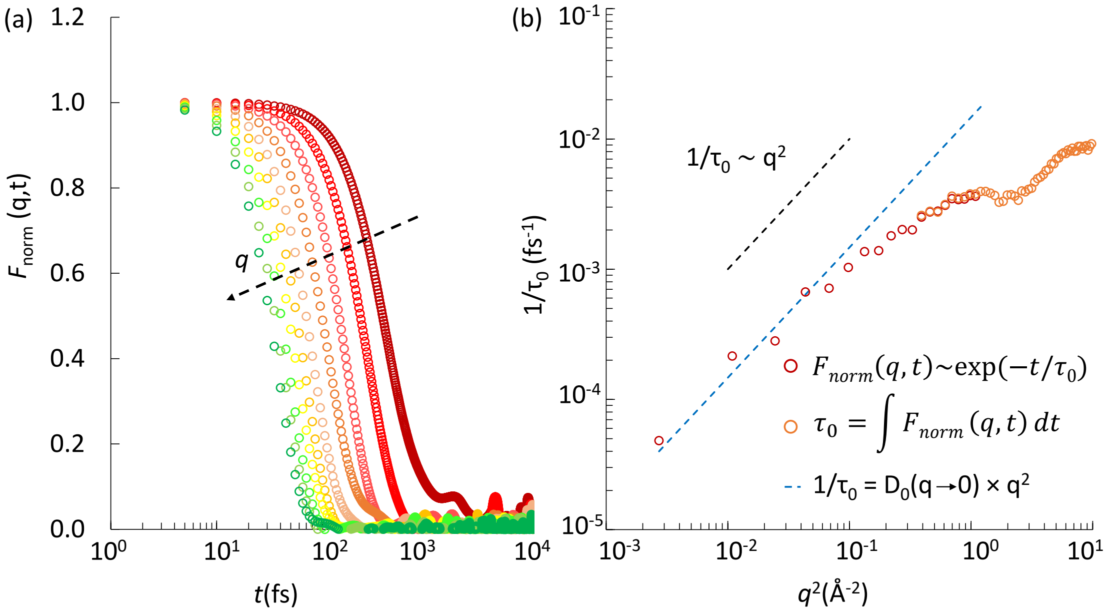

Figure 5.6: (a) Intermediate coherent scattering function $F_{coh}(q,t)$ normalized to $F_{coh}(q,0)$. The open symbols correspond to the simulated data $F_{norm}(q,t) = F_{coh}(q,t)/F_{coh}(q,0)$ as obtained from molecular dynamics. The different colors correspond to increasing wave vectors q as indicated by the dashed arrow: $q = 0.573$, 1.095, 2.137, 3.180, 4.222, 5.265, 6.307, 7.350, 8.392 and 9.435 Å^{-1}. (b) Inverse relaxation time $1/\tau_0(q)$ as a function of the squared wave vector q^2. The open symbols correspond to data obtained from the simulated intermediate coherent scattering function $F_{coh}(q,t)$. While the orange circles correspond to $1/\tau_0(q)$ as obtained by integrating $F_{coh}(q,t)$ after normalization by $F_{coh}(q,0)$, the red circles were obtained by fitting $F_{coh}(q,t)$ using a simple exponential function $F_{coh}(q,t) \sim exp[-t/\tau_0(q)]$. The blue dashed line indicates the expected behavior at small q (large distances) where the dynamics is expected to be Fickian $1/\tau_0(q) = D_0 q^2$ with D_0 the macroscopic collective diffusivity.

The functions $F_{coh}(q,t)$ were computed by means of the direct method: $F_{coh}(q,t) =< \rho(q,0)\rho^*(q,t) >= 1/N\sum_i\sum_j \exp\left[-i\mathbf{q}(\mathbf{r}_i(t)-\mathbf{r}_j(0))\right]$ with $r_i(t)$ and $r_j(0)$ the positions of molecule i at time t and molecule j at time $t=0$, respectively.
Figure 5.6(a) shows the intermediate coherent scattering function $F_{coh}(q,t)$ normalized by $F_{coh}(q,0) = S(q)$. When q increases, the characteristic time $\tau_0(q)$ decreases. In practice, data at large time t suffer from poor statistics as they are coherent functions (so that statistics is much less than for the incoherent functions). Therefore, to extract $\tau_0(q)$ by the integral method (see above), the coherent functions were fitted at large times using a function of the form : $f = a\exp[-(t-t_0)/\tau_{fit}]$ with t_0 the time where the coherent function is equal to 0.2 (this value was taken arbitrarily but it was checked that the following conclusions remain valid) and a the value of the function at the cut $F_{\mathrm{coh}}(q,t_0)$. Figure 5.6(b) shows $1/\tau_0(q)$ as a function of q^2. The orange circle correspond to $1/\tau_0(q)$ as computed by the integral method after smoothing the data.

The red circles correspond to the fitting method against $F_{coh}(q,t) \sim \exp[-t/\tau_0(q)]$ with $\tau_0(q)$ the characteristic relaxation time. The two methods provide similar results in the range $q \sim 0.3 - 0.8$ Å^{-1}. At small q, $1/\tau_0(q) = D_0(0)q^2$ and $D_0(q)$ is independent of q because molecules follow the Fickian regime.

5.2.3 De Gennes narrowing

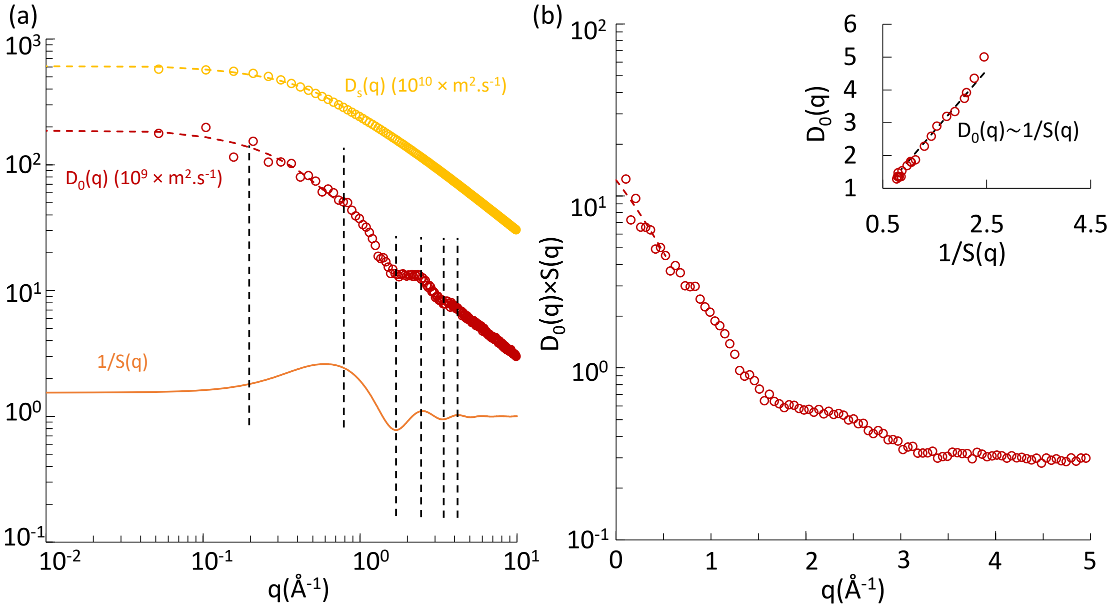

Figure 5.7: (a) Reciprocal static structure factor $1/S(q)$ (orange line), collective diffusion coefficient $D_0(q)$ (red symbols) and self diffusion coefficient $D_s(q)$ (yellow symbols) as a function of the wave vector q. For q <0.3 Å^{-1}, as expected, $D_0(q)$ is q-independent. The red dashed line was obtained by smoothing the data $D_0(q)$ (see text).The yellow dashed curve was obtained by smoothing the data $D_s(q)$. The vertical black dashed lines indicate q vectors where changes in the structure factor and in $D_0(q)$ are observed. (b) Product of the static structure factor $S(q)$ and collective diffusion coefficient $D_0(q)$. The symbols are obtained using the data in (a) while the dashed line was obtained by replacing the data points $D_0(q)$ by the smoothed line in (a). The insert shows $D_0(q)$ as a function of $1/S(q)$ for wave vectors corresponding to the second plateau of $D_0(q) \times S(q)$ (i.e. $q \sim 0.8 - 1.9$ Å^{-1}).

For each scattering vector q, the wave vector dependent collective coefficient $D_0(q)$ was calculated from the relaxation time $D_0(q) = 1/\tau_0(q)q^2$. Similarly, the self diffusion coefficient was calculated as $D_s(q) = 1/\tau_s(q)q^2$. Figure 5.7(a) shows the structure factor $S(q)$ represented by the orange line, the collective diffusion coefficient $D_0(q)$ (red data) and the self diffusion coefficient $D_s(q)$ (yellow symbols). Data at small q were fitted by a polynomial curve to smooth $D_0(q)$ as q tends to zero (this fit, which corresponds to the red dashed line, is only intended for visualization purpose but it does not impact the following discussion). As expected, $D_0(q)$ is constant as q tends to zero. More importantly, in qualitative agreement with the concept of De Gennes narrowing, the collective diffusion $D_0(q)$ follows oscillations that correspond to those observed in the structure factor $S(q)$. For the sake of visualization, the vertical black dashed line in the figure indicates q vectors where changes/oscillations in $D_0(q)$ and $S(q)$ are observed. In contrast, as expected, no correlation is observed between the self diffusivity $D_s(q)$ and the structure factor $S(q)$ since static structure ordering only involves correlations

between different molecules.
Figure 5.7(b) shows the product of the structure factor $S(q)$ and the collective diffusion coefficient $D_0(q)$ as a function of q. The red dashed line corresponds to the fit of the curve by a polynomial. These data indicate that $D_0(q) \times S(q)$ is q-independent when q tends to zero as expected. It is also observed that $D_0(q) \times S(q)$ is constant in the range $q \sim 0.8 - 1.9$ Å^{-1}. This range corresponds to the region around the main peak in the $S(q)$ data. This correlation between $D_0(q)$ and $1/S(q)$ is illustrated in the insert in Figure 5.7(b) which shows a direct correlation. This correlation shows that De Gennes narrowing applies in the region around the main correlation peak observed in the structure factor $S(q)$. In contrast, at larger q, very small distances are considered so that the mesoscopic equations used to define transport coefficients do not apply. As a result, in this range of high q vectors, we do not expect the concept of De Gennes narrowing to apply.

5.3 Nanoconfined fluid

This section is dedicated to De Gennes narrowing applied to a nanoconfined fluid. First, we introduce the system used for this study and discuss the static structure factor and the effect of loading. Then, we present the self diffusion and collective diffusion as obtained for this system. Finally, we discuss the applicability of De Gennes narrowing to a severely confined fluid.

5.3.1 Structure factor

In what follows, 3 elongated zeolite crystals were built to allow investigating correlations at small q in the directions x, y and z. Indeed, as explained in Section 5.2, quantified q values have to be used to compute properties such as the static structure factor or intermediate scattering functions. However, the smallest q that can be considered depends on the crystal size as $q_{min} = 2\pi/L$. Therefore, to reach small q values and thus large distances, we increased as much as possible the size of the system in a given direction (x, y or z). In practice, as shown in Figure 5.8 an elongated zeolite crystal consists of a structure where the unit cell was duplicated 10 times along the chosen direction and 2 times along the other directions. Three large zeolite crystals were built considering the different crystal orientations x, y and z. Like throughout this thesis, the interaction potentials used to model zeolite/zeolite, zeolite/methane and methane/methane interactions are the same as those described in Chapter 3. The next step consisted of filling the large zeolite crystals with methane by duplicating the configurations obtained for smallest zeolite crystals. To investigate the dynamics in these systems, we ran three molecular dynamics simulations: "Large" (L) trajectories of 80 ns with configurations saved every 1000 fs; "Middle" (M) trajectories of 40 ns with configurations saved every 100 fs and "Small" (S) trajectories of 2 ns with configurations saved every 5 fs. Figure 5.8(c) shows the adsorption isotherm at 300 K as described in Section 3.3 for the small zeolite crystal. The different colors correspond to the different loadings considered in this study: 20 molec./uc (red), 16 molec./uc (green), 12 molec./uc (blue), 6 molec./uc (purple). All simulations were performed at 300 K.

Like for the bulk fluid, direct calculation methods were used to compute the static structure factors $S(q)$ for methane for different loadings and crystal orientations. We recall the main equation used to compute $S(q)$:

$$S(q) = \left\langle \frac{1}{N} \sum_i \sum_j e^{-i\mathbf{q}(\mathbf{r}_i - \mathbf{r}_j)} \right\rangle \tag{5.29}$$

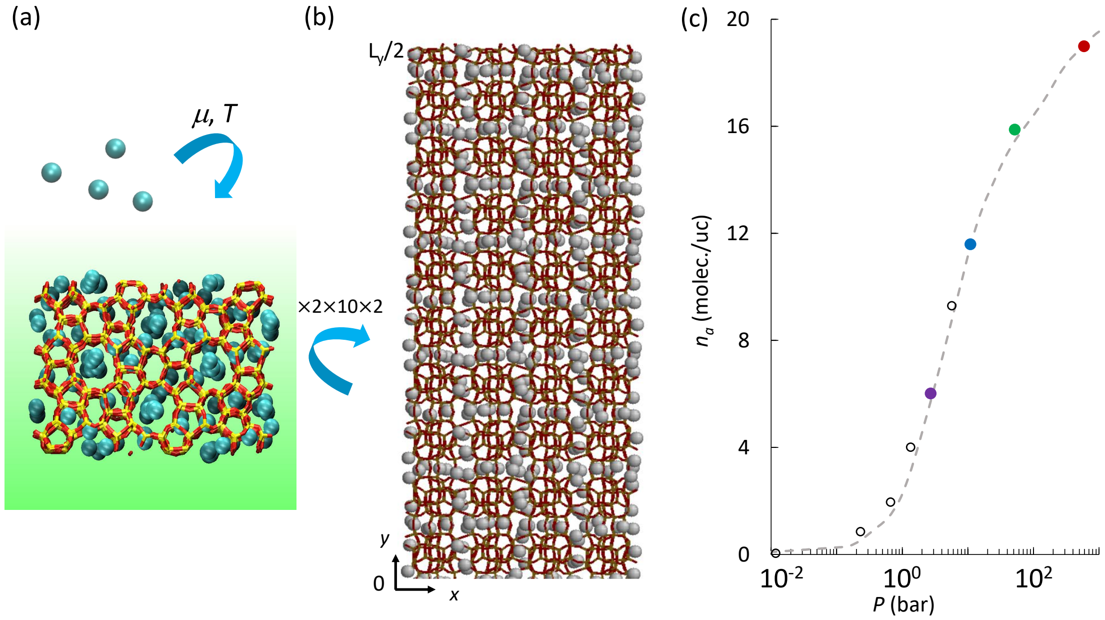

Figure 5.8: (a) Schematic representation of a small zeolite crystal filled with methane using GCMC method. (b) Large zeolite crystal oriented in the y direction filled with methane. (c) Adsorption isotherm at 300 K as described in Section 3.3. Colors correspond to different loadings: 20 molec./uc (red), 16 molec./uc (green), 12 molec./uc (blue), 6 molec./uc (purple).

with N the number of molecules, $\mathbf{r}_i$ and $\mathbf{r}_j$ the positions of molecules i and j, respectively. The rest of this chapter will mainly present results obtained for the large zeolite crystal oriented along the x axis. Some results for the large zeolite crystal oriented along the y axis will also be discussed.

Bragg peaks. Figure 5.9(a) shows the static structure factor $S(q)$ for methane confined in large zeolite crystal along x for different loadings. The static structure factor shows very narrow and intense peaks at some specific q values. These values, which depend on the loading and crystal orientation as shown in Figure 5.9(a) and (b), correspond to multiples of the lattice parameter. The black dashed lines indicate the three first peaks which are centered exactly at $q_x = n \times 2\pi/a$ with $n \in$ [2,4,6]. n has to be even because the system is periodic on a distance of twice the lattice parameter (see Figure 3.1). While the data for the bulk fluid does not show such Bragg peaks (bottom of Figure 5.9(a)), the zeolite crystal imposes its periodicity for nanoconfined methane (a sort of fingerprint from the host matrix). As an example, along the x direction, the Bragg peaks arise from methane molecules within the straight channels which are centered with a periodicity of $2 \times a$ (with a the lattice parameter along the x crystallographic axis). It is also interesting to notice the effect of loading. Figure 5.9(a) shows a variation of the peak intensity depending on the loading (see also experimental results Figure 5.17). More interesting, some peaks decrease upon increasing the loading.

Correlation peaks. Omitting such Bragg peaks, the first peak in the static structure factor (indicated by a red dashed line in Figure 5.9(a) for the bulk phase and the loaded zeolite at 20 molec./uc) provides information on the fluid structure. The position of this peak, i.e. q_{peak}, corresponds to the reciprocal of the typical distance between nearest methane molecules. Interestingly, this distance is the same for bulk and confined methane. This can be rationalized by comparing the zeolite straight channel size and the distance corresponding to $q_{peak} = 1.72$ Å^{-1}. Indeed, the first methane neighbour is at a distance of $l = 2\pi/q_{peak} = 3.65$ Å which is 3 times smaller than the straight channel opening. Therefore, the zeolite structure does not have severe impact on the peak position. Figure 5.9(a) also shows that the peak in the $S(q)$ data is shifted to a lower q value as the loading decreases. Indeed, as the methane amount decreases, the equilibrium distance for the first neighbor is larger (i.e. smaller q). Figure 5.9(b) shows the effect of the orientation as $q^x_{peak} > q^y_{peak}$. In contrast to the data for the x axis, the zeolite matrix has a strong effect on the first neighbor distance in the y direction. Indeed, the zigzag channel opening is smaller than that of the straight channels so that the zigzag channel morphology imposes a larger equilibrium distance between neighbour molecules. Finally, Figure 5.9(c) shows the static structure factor for flexible (red) and rigid (back dashed line) zeolites filled with a loading 20 molec./uc. These data show that there is not noticeable effect of the matrix flexibility on the static structure factor.

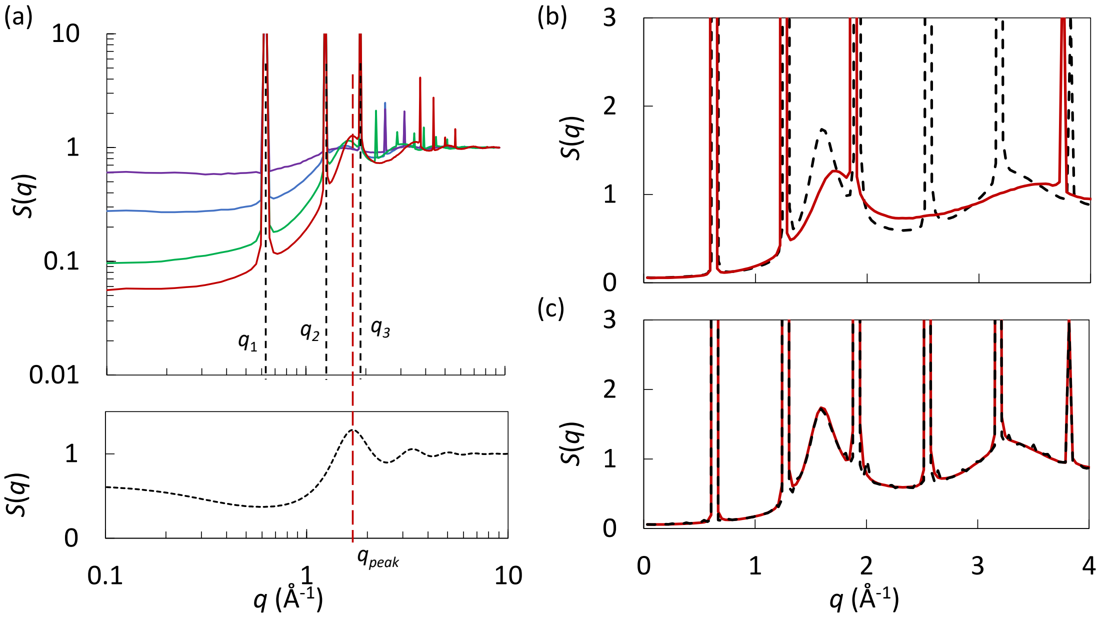

Figure 5.9: (a) The top panel shows the static structure factor $S(q)$ for methane confined in the elongated zeolite crystal in the x direction for different loadings (the color legend is the same as in Figure 5.8(c)). The bottom panel shows the static structure factor $S(q)$ for the bulk system described in section 5.2. Black dashed lines refer to the four first Bragg peaks while the red dashed line corresponds to the $S(q)$ peak at 20 molec/uc. (b) Comparison of $S(q)$ for the elongated zeolite crystals in the x (red line) and y (black dashed line) directions taken at the same loading 20 molec./uc. (c) Static structure factor for flexible (red) and rigid (back dashed line) zeolites.

5.3.2 Wave vector dependent diffusion

As mentioned in Section 5.1.2, De Gennes narrowing allows relating the wave vector dependent collective diffusivity to the static structure factor. This section considers the transport and collective diffusion coefficients as a function of the wave vector q. As explained in Section 1.3, D_0 is the sum of the self diffusion coefficient D_s and a term which corresponds to collective interactions (see Eq. (1.42)). Thus, the first part of this section will present the results for $D_s(q)$ i.e. the wave vector dependent self diffusion coefficient. In practice, for both $D_s(q)$ and $D_0(q)$, we can write:

$$D_s(q) \xrightarrow[q\to 0]{} D_s \tag{5.30}$$

$$D_0(q) \xrightarrow[q\to 0]{} D_0 \tag{5.31}$$

where D_s and D_0 are the homogeneous diffusion coefficients studied in Chapter 4 and Section 5.1 respectively.

Self diffusion coefficient $D_s(q)$.

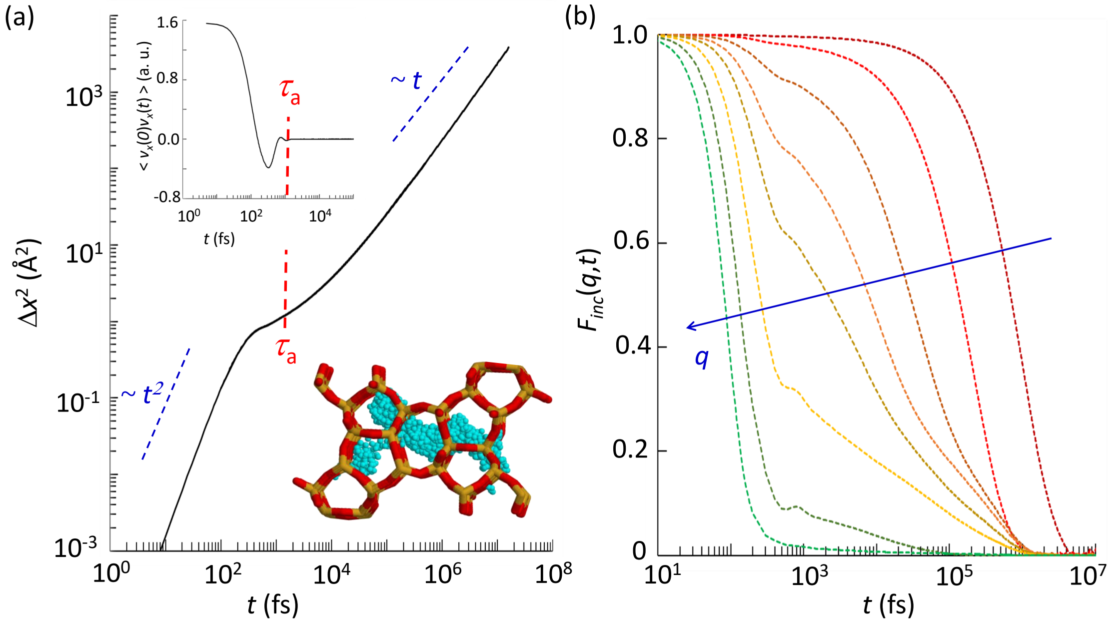

Figure 5.10: (a) Mean square displacement for an elongated crystal along the x axis loaded at 20 molec./uc. The insert shows the VACF for the same loaded zeolite. Between the ballistic regime ($\Delta x^2 \sim t^2$) and the Fickian regime ($\Delta x^2 \sim t$), a plateau can be observed in the MSD at a characteristic time of $\tau_a = 1000fs$. It also corresponds to the time of the second minimum in the VACF. (b) Incoherent intermediate scattering function $F_{inc}(q,t)$ for the elongated crystal along the x axis with a loading of 20 molec./uc. Different colors correspond to different q values. From the right to the left (in Å^{-1}) : 0.09, 0.2, 0.4, 0.7, 1.0, 1.7, 2.6, 3.9.

As explained in Chapter 4, several methods can be used to compute the self diffusion coefficient.

The mean square displacement along a given direction is computed as:

$$\langle \Delta\alpha(\tau)^2 \rangle = 1/N \times 1/[t_{max} - \tau] \times \sum_{i=1}^{N} \sum_{t'=\tau}^{t_{max}} |\alpha_i(t') - \alpha_i(t' - \tau)|^2 \tag{5.32}$$

where $\alpha = x$, y or z.

The velocity autocorrelation function along a given direction is computed using:

$$VACF =< \mathbf{v}_\alpha(0) \cdot \mathbf{v}_\alpha(t) >= 1/N \times 1/[t_{max} - \tau] \times \sum_{i=1}^{N} \sum_{t'=\tau}^{t_{max}} \mathbf{v}_\alpha^i(t') \cdot \mathbf{v}_\alpha^i(t' - \tau) \tag{5.33}$$

The incoherent scattering function along a given direction is computed using:

$$F_{\text{inc}}^{\alpha}(q_\alpha, t) = 1/N \sum_i \exp\left[-iq_\alpha \cdot (\alpha_i(t) - \alpha_i(0))\right] \tag{5.34}$$

These functions were computed for the elongated crystal along the x and y axes for different loadings. Figure 5.10 shows the self diffusivity of methane loaded at 20 molec./uc inside the large crystal oriented along x. Using the three functions presented above (i.e. MSD, VACF, F_{inc}), we can assess the self diffusivity on different time and length scales.

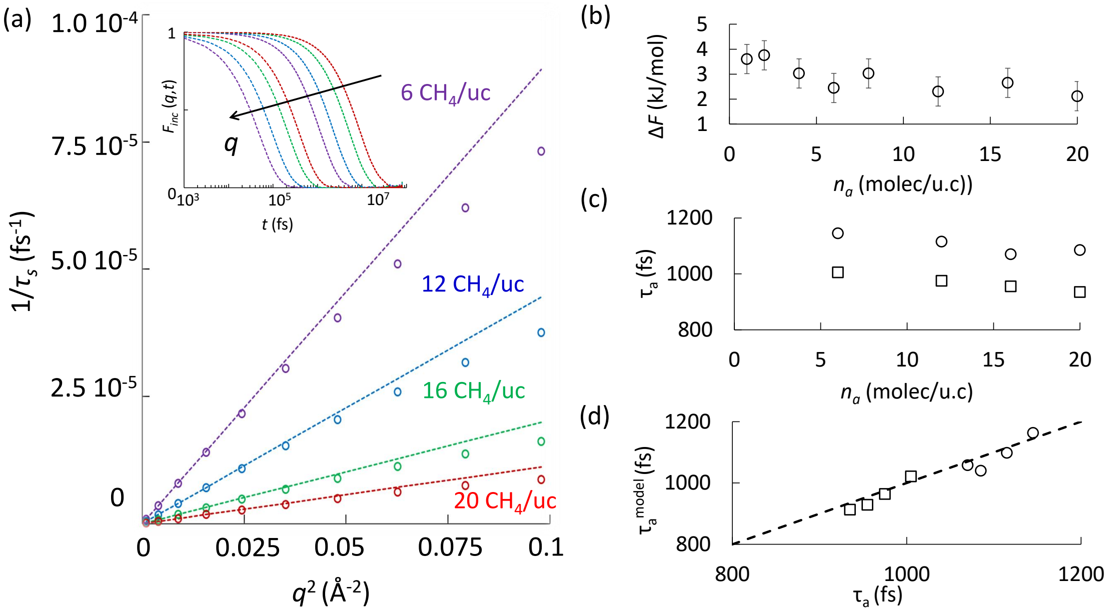

Figure 5.11: (a) Inverse relaxation time $1/\tau_s(q)$ as a function of the squared scattering vector q^2 for the elongated crystal along x. The open symbols correspond to data obtained from the fits of simulated intermediate incoherent scattering functions $F_{inc}(q,t)$. Different colors correspond to different loadings with the same color code as in Figure 5.8(c). The lines indicate the expected behavior at small q (large distances) where the dynamics is Fickian: $1/\tau_s(q) = D_s(0)q^2$ with $D_s(q \to 0)$ estimated from the MSD obtained in molecular dynamics. The insert shows the 1D intermediate incoherent scattering function $F^x_{inc}(q,t)$ for four loadings and two q (from right to left: $q \sim 0.031$ Å^{-1} and $q \sim 0.16$ Å^{-1}). (b) Characteristic time of the second minimum in the VACF τ_a as a function of methane loading. (c) Characteristic time of the model (see text) as a function of τ_a presented in (b) for x data (open circles) and y data (open squares). The dashed line corresponds to $\tau_a = t_{model}$.

The results presented in this paragraph are similar to those in Chapter 4 which deals with the self diffusivity in the long time limit. However, as this stage, it seems important to us to show the good agreement between the D_s values obtained from the MSD and the F_{inc} functions. As explained in Chapter 4, the homogeneous self diffusion coefficient can be computed using MSD in the Fickian regime (see Eq. (4.6)). It corresponds to large times in Figure 5.10(a) (t > 10^6 fs). D_s can also be extracted from incoherent scattering functions at large distances (i.e. small q values). These functions have an exponential form, as shown by the red curves in the right side of Figure 5.10(b) and in the insert of Figure 5.11(a). Therefore, they can be fitted using $F_{inc}(q,t) \sim \exp[-D_s q^2 t]$. Figure 5.11(a) shows the inverse relaxation time $1/\tau_s(q) = D_s(q)q^2$ as a function of the squared vector q^2 for the elongated crystal along x for different loadings. For small q, $1/\tau_s(q)$ (open symbols) is proportional to q^2 so that $D_s(q)$ is q independent and reaches the value inferred from the MSD (dashed lines). At larger q, $D_s(q)$ diverges from the macroscopic value D_s ($q > 0.05$ Å^{-1} for 16 molec./uc) as the typical displacements are too small to reach the Fickian regime. In all cases, we verified that the self diffusivities D_s inferred from the MSD for the elongated zeolite crystals are the same as those obtained for the small zeolite crystal presented in Chapter 4. Figure 5.12(b) shows similar MSD for large zeolite crystals (full lines) and the small zeolite crystal (dashed lines).

Large wave vectors. At intermediate q values, a "bump"' can be observed in the incoherent scattering functions (see Figure 5.10(b) for the brown to the green F_{inc} functions). The characteristic time at which this feature is observed is approximately $\tau_a = 1000$ fs. Such a typical time corresponds to both the end of the plateau in the MSD and the position of the second minimum in the VACF [see red dashed line in Figure 5.10(a)]. This characteristic time correspond to the time during which methane molecules remain trapped in adsorption sites. These molecules collide with a sign change in their velocity (corresponding to an extremum in the VACF) before leaving the site. Thus, this characteristic time τ_a can be seen as the residence time of the molecule in the adsorption sites. Figure 5.11(c) shows τ_a as measured from the position of the second minimum in the VACF as a function of methane loading. Upon increasing the loading, τ_a slightly decreases until 15 molec./uc. Indeed, increasing the amount of methane molecules leads to a larger number of collisions which, in turn, increases the probability to leave an adsorption site. To verify this interpretation, the characteristic time τ_a was modeled using a simple activation energy barrier in Figure 5.11(b). We write that τ_a depend on the energy barrier ΔF (the higher the free energy barrier, the longer the residence time in the adsorption site):

$$\tau_a(n_a) = \tau_c(n_a)\exp[\Delta F(n_a)/k_{\mathrm{B}}T] \tag{5.35}$$

with τ_c the crossing time, i.e. the time between two attempts to escape from the site, and n_a the loading. In this work, this time was estimated as the time difference between the second maximum t_2 and the first minimum t_1 in the VACF: $\tau_c = t_2 - t_1$. ΔF is the energy barrier fitted from the data shown in Figure 5.11(b). An exponential form was used to fit the data: $\Delta F = a + b \times \exp(-n_a/x_0)$. The fitting parameters are $a = 2.28$ kJ.mol^{-1}, b=1.77 kJ.mol^{-1}, and $x_0 = 5.1$ molec./uc. Figure 5.11(d) shows the predicted value for τ_a plotted as a function of τ_a obtained from the VACF. Open circles and squares correspond to data for the elongated zeolite crystals along the x and y axes, respectively. The agreement between the model and the measured characteristic time is very good, therefore suggesting that our interpretation is relevant.

5.3.3 Collective diffusivity

As described in the beginning of this chapter, the macroscopic collective diffusion coefficient D_0 was computed using two methods: the integration of the collective VACF and the non equilibrium molecular dynamics approach. Moreover, we also used the coherent scattering functions as described when discussing the transport properties of a bulk fluid. Figure 5.13 shows the results obtained by the three methods to compute D_0. Figure 5.13(a) shows a comparison between the integration of the VACF and D_0 obtain by the gradient method for a loading of 6 molec./uc. While the integration becomes very noisy at long times t, the inferred value is qualitatively consistent with $D_0(t)$ around 20 ps. Figure 5.13(b) shows the coherent scattering functions at a small wave vector $q = 0.0313$ Å^{-1} normalized by $S(q)$ for each loading considered. The relaxation time $\tau_0(q)$ is defined from the coherent scattering functions. At small q, we can assume that the Fickian regime is reached as the coherent scattering functions have a clear exponential form:

$$F_{coh}(q,t) = S(q)\exp[-D_T(q)q^2t] \tag{5.36}$$

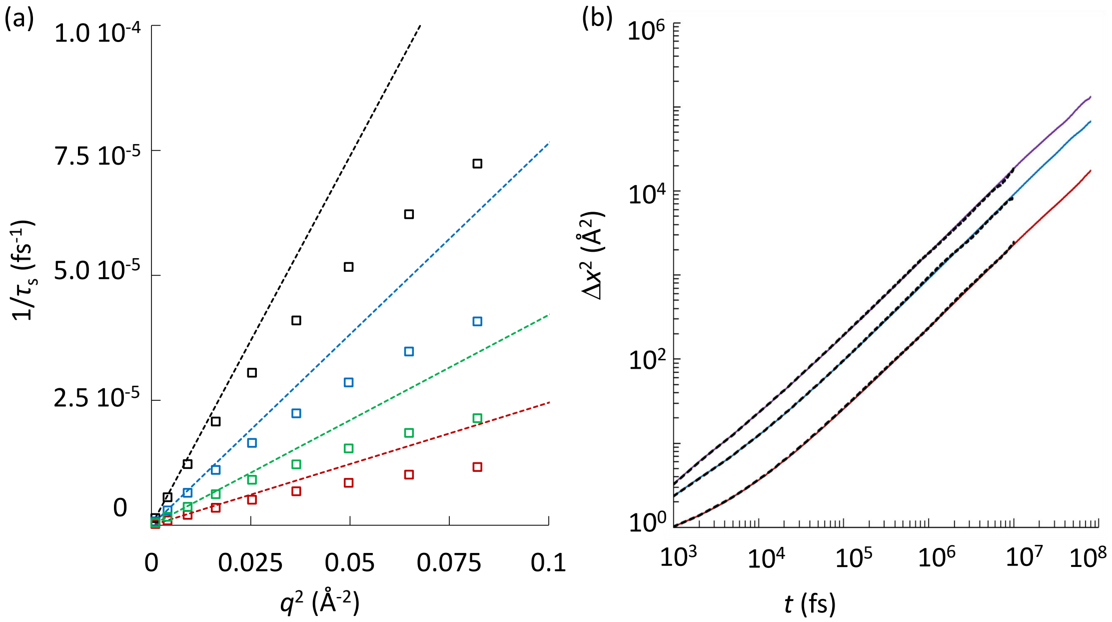

Figure 5.12: (a) Inverse relaxation time $1/\tau_s(q)$ as a function of the squared wave vector q^2 for the elongated crystal along y. The legend is the same as for Figure 5.11(a). (b) Comparison of the MSD along x at different loadings (see color code in Figure 5.8(c)) for the elongated crystal along x (full lines) and the small crystal as described in Chapter 3 (dashed black lines).

where $1/\tau_0(q) = D_T(q)q^2$. As will be seen in the next paragraph, the assumption of an exponential form does not hold anymore when larger q values are considered. In the rest of the manuscript, the coherent scattering functions F_{coh} will be plotted after normalization by $S(q)$. Figure 5.13(c) shows the inverse relaxation time $1/\tau_0(q)$ as a function of q^2 for the elongated crystal along x and for different loadings. In Figure 5.13(c), the open circles correspond to data from the fitted F_{coh} functions while the dashed lines are plotted using the non equilibrium method $1/\tau_0(q) = D_T^{NEMD}q^2$. The simple quantitative difference between D_0 and D_T will be clarified in the next paragraph.

Transport versus collective diffusion. We recall the connection between D_T and D_0 as given in Section 1.3 :

$$D_T = D_0 \frac{\partial \ln f}{\partial \ln \rho}\Big|_T \tag{5.37}$$

where $\Gamma = \partial \ln f / \partial \ln \rho$ is known as the thermodynamic factor. Γ can be linked to the structure factor $S(q)$ in the limit $q \to 0$ using the isothermal compressibility χ_T. Let us start from definitions provided in standard textbooks [73]. The isothermal compressibility is linked to the fluctuation of the number of molecules N through the following equation:

$$\rho k_B T \chi_T = \frac{< N^2 > - < N >^2}{< N >} \tag{5.38}$$

with ρ the density of molecules in the system. In the small q limit, the structure factor can be written as:

$$\lim_{q \to 0} S(q) = \rho k_B T \chi_T \tag{5.39}$$

Together, Eqs. (5.38) and (5.39) lead to:

$$\lim_{q \to 0} S(q) = \frac{\langle N^2 \rangle - \langle N \rangle^2}{\langle N \rangle} \tag{5.40}$$

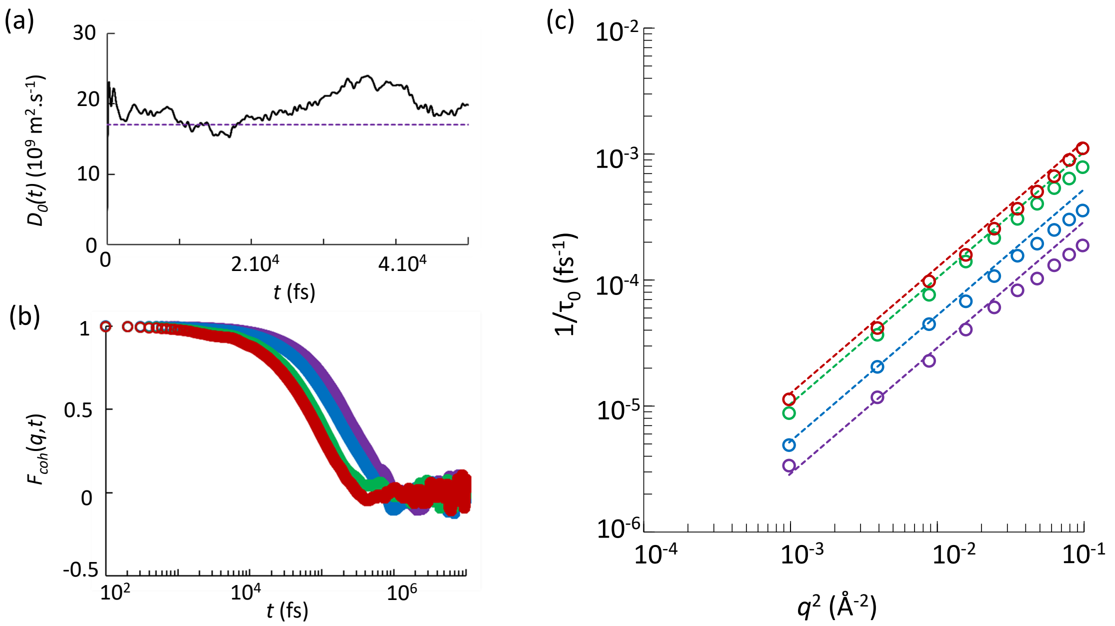

Figure 5.13: [The color code remains the same as the one defined Figure 5.8(c)] (a) The black line corresponds to $D_0(t)$ which is computed by integrating the collective VACF for 6 molec./uc. The dashed purple line refers to D_0 obtained by non equilibrium molecular dynamics. (b) The coherent scattering functions at $q = 0.0313$ Å^{-1} normalized by $S(q)$ for each loading. (c) Inverse relaxation time $1/\tau_0(q)$ as a function of q^2 for the elongated crystal along x and for different loadings.

$S(0)$ is therefore a measure of the fluctuation in the number of molecules in the system [170]. Eqs. (5.39) and (5.40) allow us to go further into the interpretation of the following result $S_6(0) > S_{12}(0) > S_{16}(0) > S_{20}(0)$ shown in Figure 5.9. At small loadings, the methane molecules are more compressible than at high loadings where $S(0)$ tends to 0. Furthermore, methane in confined zeolite is less compressible than in the bulk zeolite as $S_{Bulk}(0) > S_{zeo}(0)$ [129]. This result is in good agreement with the compressibilities compared in Section 3.3.1 of Chapter 3.

To link the isothermal compressibility to the thermodynamic structure factor, we start from the definition of the thermodynamic structure factor : $\Gamma = \partial ln(P)/\partial ln(\rho)$ with P the pressure and ρ the density.
Considering a constant number of molecules $\partial N = 0$, we use $\partial ln(\rho) = \partial\rho/\rho$ to get $\partial ln(\rho) = N/\rho \times \partial V/V^2$. Then, the thermodynamic structure factor can be written :

$$\Gamma = -\frac{\partial P}{\partial V} \times \frac{V}{P} \tag{5.41}$$

By definition, the isothermal compressibility χ_T is given by :

$$\chi_T = -\frac{1}{V} \times \frac{\partial V}{\partial P}\Big|_{T,N} \tag{5.42}$$

Combining Eq. (5.41) and Eq. (5.42) leads to :

$$\Gamma = \frac{1}{\chi_T} \times \frac{1}{P} \tag{5.43}$$

Replacing χ_T in Eq. (5.43) by Eq. (5.39) and using the ideal gas law leads to:

$$\Gamma = \frac{1}{S(0)} \tag{5.44}$$

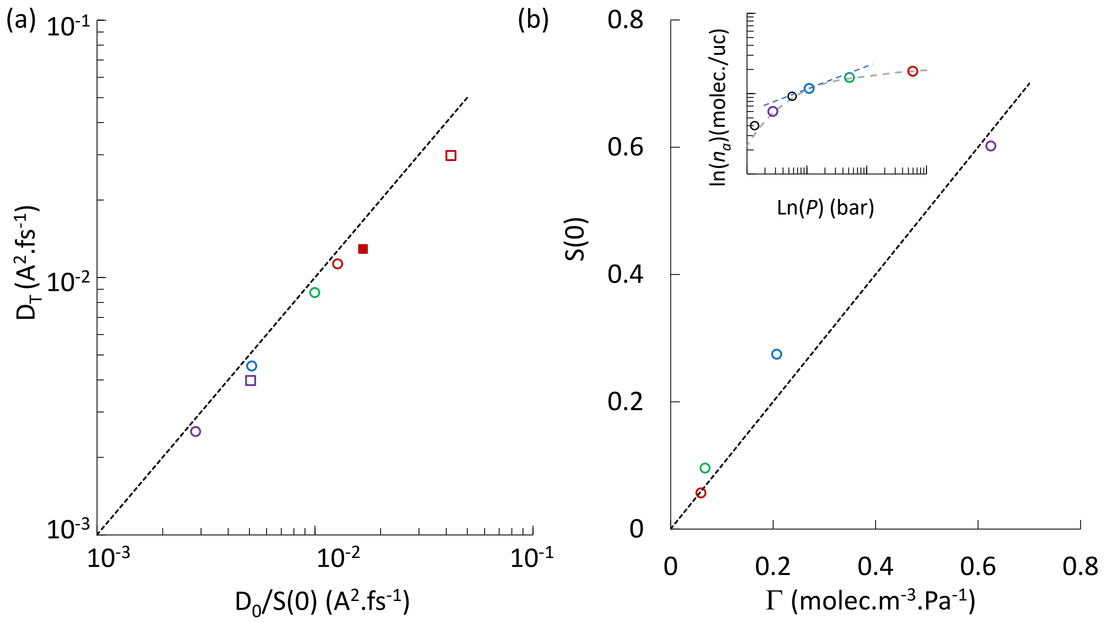

Figure 5.14: (a) Transport diffusivity D_T obtained by fitting the coherent scattering functions at low q values (see text) as a function of $D_0/S(0)$. The color code is the same as in Figure 5.8(c). The open circles correspond to the data for the elongated crystal in the x direction while the squares refer to the data for the elongated crystal along y. The data for the flexible matrix (open) or rigid (closed) matrices are shown. The D_0 data were obtained from the non equilibrium method while $S(0)$ correspond to the extrapolation of $S(q)$ shown in Figure 5.9(a). (b) Static structure factor at $q \to 0$ $S(0)$ as a function of the thermodynamic factor $\Gamma = \partial P/\partial \rho$. The insert shows Γ which corresponds to the slope of the adsorption isotherm at given loadings (as an example, the dashed blue line is the derivative of the isotherm at 12 molec./uc).

Figure 5.14(a) shows the transport diffusivity D_T – as assessed by fitting the coherent scattering functions at small q values – as a function of $D_0/S(0)$. D_T, D_0 and $S(0)$ were measured for different loadings and crystal directions. $S(0)$ was extrapolated from a linear fit of the smallest q values in the $S(q)$. Comparison between Eqs. (5.44) and (5.37) leads to:

$$D_T = \frac{D_0}{S(0)} \tag{5.45}$$

As can be seen in Figure 5.14(a), there is a good agreement between D_T and $D_0/S(0)$ as expected from Eq. (5.45). However, we can notice that data are always below the black dashed line indicating $D_T = D_0/S(0)$. This is due to the fact that D_T is measured from the slope of the linear curve given by the slowest q values ($1/\tau_0 = D_T q^2$). Unfortunately, this slope depends on the number of q values available; It is therefore probable that we do not have enough small q values to ensure that the Fickian regime is fully reached. Further investigation is needed to clarify this issue. Figure 5.14(b) shows the static structure factor at $q \to 0$ extrapolated from a linear fit mentioned above as a function of the thermodynamic factor $\Gamma = \partial P/\partial \rho$. In practice, Γ was measured directly from the adsorption isotherm computed in Chapter 3 (see insert Figure 5.14(b)). The agreement is very good between the two measurement methods, which confirms that Eq. (5.44) is verified in our computational study.

Microscopic/molecular scale. As coherent scattering functions do not have an exponential form on the whole q range, several methods were considered to assess the relaxation time τ_0 associated to diffusion.

Simple exponential form. We fitted F_{coh} at small q using a simple exponential function:

$$f(q,t) = \exp[-t/\tau_0(q,t)] \tag{5.46}$$

Stretched exponential form. We fitted F_{coh} using a stretched exponential:

$$f(q,t) = \exp[-(t/\tau^*(q))^{\beta}] \tag{5.47}$$

with β the stretching factor ($\beta > 1$). With a stretched exponential, the characteristic relaxation time is given by $\tau_0(q) = \tau^*(q,t)\beta^{-1}\Gamma^*(\beta^{-1})$ with Γ^* the gamma function.

Characteristic time at 1/e decay. We also measured $\tau_0(q)$ by determining the time at which the coherent scattering functions reaches the value of $F_{coh} = 1/e = 0.368$. The main advantage of this method is that it does not depend on the time range used to fit functions using the two other methods.

As shown in Figure 5.15(a), F_{coh} always display the "bump" around 1000 fs (see discussion above on incoherent scattering). Indeed, as the coherent scattering functions characterize the correlations between molecules, it also includes a self term which takes into account correlations between the same molecule at different times. Thus, the residence time, which was discussed in the previous section, is also found in the coherent functions. In practice, as we focus only on the diffusive behavior of confined methane, we fitted F_{coh} with a stretched exponential on the time range before τ_B, i.e. the characteristic time corresponding to molecule residence in adsorption sites. Figure 5.15(a) shows the comparison between the three methods. At low q values, the agreement is good between the simple exponential and the $1/e$ method. We notice that, as we increase q, the exponential form is no longer valid as the Fickian regime does not apply in this range. At larger q values, the stretched exponential and the $1/e$ method lead to a very similar behavior with very close $1/\tau_0(q)$ values. Because the $1/e$ method is not time range dependent, we will use this method to probe the applicability of De Gennes narrowing in the rest of this chapter.

Bragg peaks. The data presented in Figure 5.15(a) were corrected at q values corresponding to Bragg peaks. Indeed, as shown in the insert of Figure 5.15(b), the coherent functions obtained at q corresponding to Bragg peaks do not converge to zero at very large times; in fact, they decrease to a non zero value as the structural order imposed by the matrix make the confined molecules relax towards a well-defined structure. Yet, F_{coh} at q corresponding to the Bragg peaks display a relaxation time so that we shifted and renormalized these F_{coh} so that they converge to zero in the long time limit. The result of this correction is shown as the black curve in Figure 5.15(b). Figure 5.15(b) shows also F_{coh} around the first Bragg peak. We can notice that the closest curves from the peak have an oscillatory behavior. From this figure, we can rank the relaxation times as: $\tau_0(q_{peak}) < \tau_0(q_{peak+2}) < \tau_0(q_{peak-2}) < \tau_0(q_{peak+/-1})$. It means that, regardless of the method used to determine the characteristic time τ, the relaxation time at the Bragg peak is lower than those in the neighboring q values. Moreover, the relaxation time for the two closest F_{coh} from the Bragg peak are the largest. At the time this manuscript is being finalized, we are still in the process of fully understanding these data. However, as will be shown in the next paragraph, we are already in a position to discuss – at least to some extent – the ability of De Gennes narrowing to describe the wave vector dependent collective diffusivity.

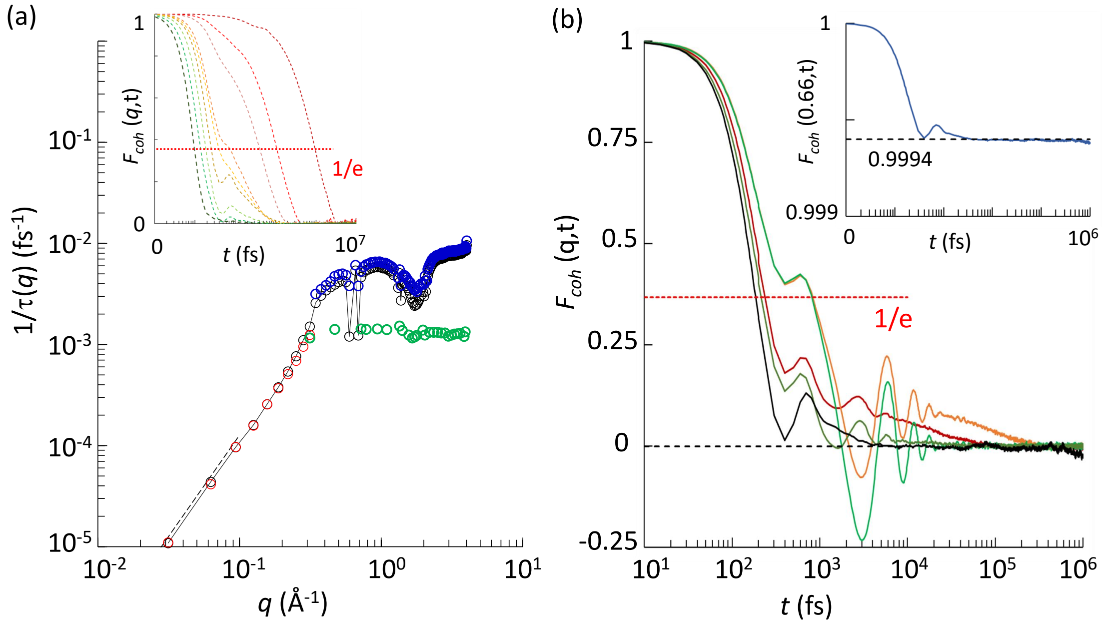

Figure 5.15: (a) Inverse relaxation time $1/\tau$ as a function of q. Open green circles correspond to $1/\tau_B$ with τ_B the characteristic time of the bump observed in F_{coh}. This residence time does not depend on q and remains around 10^3 fs. Other colors refer to the three methods employed to determine the characteristic time for collective diffusion from F_{coh}: a simple exponential (red circles), a stretched exponential (blue circles) and the time at which $F_{coh} = 1/e$ (black circles). These data are corrected when q corresponding to the Bragg peaks are considered (see main text). The insert shows F_{coh} for different q values. From right to left (in Å^{-1} : 0.031, 0.094, 0.156, 0.313, 0.469, 1.72, 2.03, 2.658, 3.909). (b) Coherent scattering functions F_{coh} around the first Bragg peak (q_{peak-2}=0.563 Å^{-1} [peak-2] dark red, q_{peak-1}=0.594 Å^{-1} [peak-1] orange, q_{peak+1}=0.657 Å^{-1} [peak+1] light green, q_{peak+2}=0.688 Å^{-1} [peak+2] dark green) and at the Bragg peak after correction (q=0.626 Å^{-1} black curve). The black dashed line indicates the zero while the red one indicates the value of $1/e$. In insert, F_{coh} at the Bragg peak without the correction.

5.3.4 De Gennes narrowing in a nanoconfined fluid

Figure 5.16(a) shows the inverse static structure factor $1/S(q)$ after corrections for Bragg peaks as well as the transport diffusion coefficient $D_T(q)$ and self diffusion coefficient $D_s(q)$. These data are shown as a function of the wave vector q for $q < 4$ Å^{-1}. The transport and self diffusion coefficients were obtained using the relaxation time measured by the $1/e$ method [see Figure 5.15(a)] as $D_T(q) = 1/(\tau_0(q) \times q^2)$ and $D_s(q) = 1/(\tau_s(q) \times q^2)$. The static structure factor was corrected from the Bragg peaks. First, we removed the $S(q)$ values at the Bragg peaks. Then, we used a Bessel Spline function as an interpolation method to smooth the data. The result is shown in the insert of Figure 5.16(b): the red curve corresponds to the corrected structure factor and the black line with open squares corresponds to the raw data. From Figure 5.16(a), we see that the transport diffusion coefficient follows the variation in $1/S(q)$ as expected from De Gennes narrowing. The vertical black dashed lines indicate oscillations with a change in $D_T(q)$ and $1/S(q)$. In contrast, as expected, $D_s(q)$ does not correlate with the structure factor

$S(q)$. At small q, both $D_T(q)$ and $D_s(q)$ are constant as expected in the macroscopic Fickian regime. Figure 5.16(b) shows the product of the structure factor and the transport diffusion coefficient $D_T(q) \times S(q)$ for the bulk supercritical fluid (black circles) and the zeolite (red circles which come from data in (a)). It is interesting to notice that around q_{peak} (i.e. the value at which the fluid correlation peak is observed in $S(q)$), the q range where $D_T(q) \times S(q)$ is constant is much larger for the zeolite system than for the bulk fluid (0.7 $Å^{-1}$ < q < 2.15 $Å^{-1}$ for the zeolite against 0.8 $Å^{-1}$ < q < 1.9 $Å^{-1}$ for the bulk phase). In contrast, while the concept of De Gennes narrowing seems to apply to extremely confined nanofluids – such as methane in zeolite nanoporosity – the behavior for q values near the Bragg peaks requires more work to be fully understood.

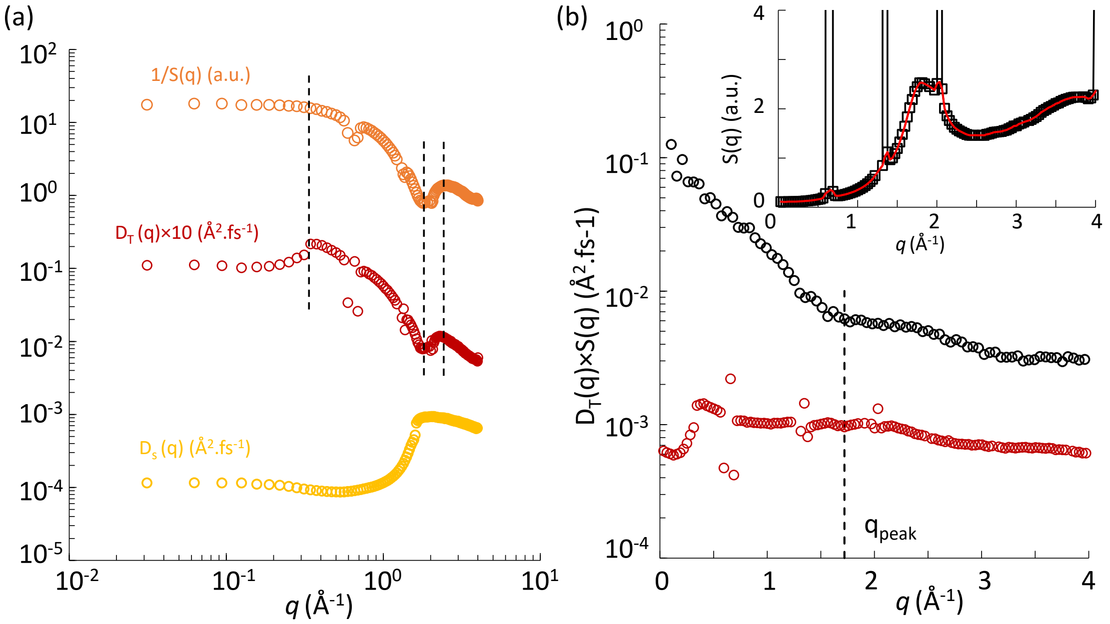

Figure 5.16: (a) Inverse static structure factor $1/S(q)$ (orange open circles) after corrections for Bragg peaks, transport diffusion coefficient $D_T(q)$ (red symbols) and self diffusion coefficient $D_s(q)$ (yellow symbols) as a function of the wave vector q. The vertical black dashed lines indicate changes in the structure factor that correspond at the same time to changes in $D_T(q)$. (b) Product of the static structure factor $S(q)$ and transport diffusion coefficient $D_T(q)$. Red symbols are obtained using the data in (a) while black symbols correspond to the $D_T(q) \times S(q)$ rescaled for the bulk supercritical fluid obtained in Section 5.2. The insert shows the static structure factor before (open squares and black line) and after (red line) corrections as discussed in the main text.

5.4 Experimental investigation : QENS experiment and preliminary analysis.

The experimental investigation of De Gennes narrowing was performed by quasi-elastic neutron scattering, which indeed provides a method of choice in probing the collective diffusive dynamics at the microscopic scale. This QENS experiment was performed - similarly to the one presented in the previous chapter to characterize the individual diffusion - by using CD_4 as a substitution of the CH_4. Indeed, as explained in Section 2.2.2, deuterium possesses a large coherent cross section compared to its incoherent one at the difference of CH_4. We recall that $\sigma_{coh}(^2\mathrm{H}) = 5.6$ barns while $\sigma_{inc}(^2\mathrm{H}) = 2.04$ barns.

This implies that using deuterated methane, we are able to track the collective diffusion behavior of the gas. The experiments were performed at the Institut Laue-Langevin (ILL) in Grenoble, France, using the Time of Flight (TOF) IN6/Sharp spectrometer in similar conditions to the CH_4 one. The instrument was, in between our two experiments, upgraded to achieve higher neutron flux. The incident wavelength was taken at 5.1 Å, the energy resolution was 40 μeV at the half width at half maximum (HWHM) and measured using a vanadium reference sample. The data were recorded up to q values of ~ 2.1 Å^{-1}. They were reduced using the MANTID program and the software Lamp was used for data fitting. The range of scattering vector q useful in our analysis, for reasons explained below, was reduced to 0.14 Å$^{-1} < q < 1$ Å^{-1}.
The powder sample used for these experiments has a grain size of $D_g = 1\mu$m (the description of the sample can be found section 3.2.1). The measurements were performed at two temperatures : 210 K and 250 K. For each temperature, different loadings were considered by imposing different pressures. The loading n_a was estimated from the monitored pressure P, based on the computed adsorption isotherms (see Figure 3.7).

5.4.1 Structure factor : effect of the methane adsorption.

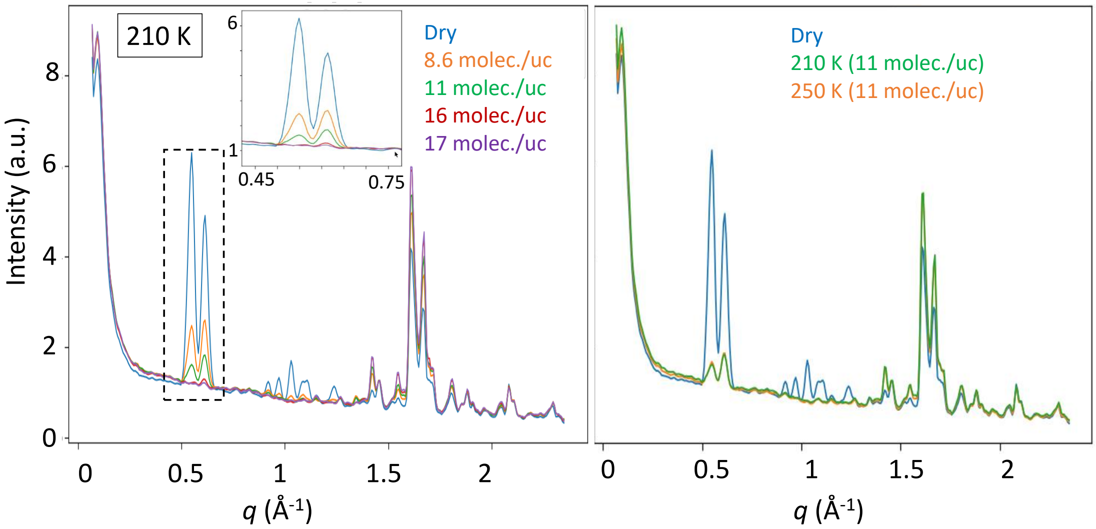

Figure 5.17: Experimental structure factor $S(q)$ as function of q. On the left side, comparison of the $S(q)$ at 210 K for different loadings : dry (blue), 8.6 molec./uc (orange), 11 molec./uc (green), 16 molec./uc (red) and 17 molec./uc (purple). The insert is a zoom on the second and third Bragg peaks. The two curves corresponding to loadings 16 molec./uc and 17 molec./uc are almost indistinguishable. Right side, a comparison between the dry sample (blue) and the sample loaded at 11 molec./uc at 210 K (green) and 250 K (orange). The curves at 250 K and 210 K are very well overlapped.

Figure 5.17 shows the experimental static structure factor $S(q)$ as function of q, obtained by integrating the spectra over the energy range. The intense peaks, already present in the dry sample, are the Bragg peaks of the zeolite matrix. For example, the two peaks centered at $q_1 = 0.55$ Å^{-1} and $q_2 = 0.62$ Å^{-1} correspond to distances between 12 and 10 Å respectively, which are the characteristic distances between two straight or zigzag channels. The left side of Figure 5.17 shows a comparison of the $S(q)$ at 210 K for different loadings. We observe a clear variation of the peaks intensity with the loading.

We note that this variation can be a decrease or an increase of intensity when the loading increases: for example, the two peaks centered in q_1 and q_2 exhibit a decrease of intensity with I(dry) $>$ I(8.6 molec./uc) $>$ I(11 molec./uc) $>$ I(16 molec./uc) $>$ I(17 molec./uc); on the contrary, the peaks centered around $q = 1.6$ Å^{-1} increase their intensity with methane adsorption and I(dry) $<$ I(8.6 molec./uc) $<$ I(11 molec./uc) $<$ I(16 molec./uc) $<$ I(17 molec./uc). Similar effects have been reported on different matrices by X-ray or neutron scattering experiments [171, 172]. In particular, in their paper [171] on methane adsorption in MFI zeolites, Llewellyn *et al.* shows a decrease of the Bragg peak centered at $q = 0.6$ Å^{-1} that they associated to pore filling process. Indeed, this effect is related to additional scattering length involved in the Bragg peaks intensities when CD_4 is adsorbed. At small values of q (0-5-0.6Å^{-1}), the contrast between the zeolite matrix and void/CD_4 is at play, decreasing with methane adsorption thus reducing the intensities. Indeed, zeolite atoms have coherent cross sections of $\sigma_{coh}(\mathrm{Si}) = 2.2$ barns and $\sigma_{coh}(\mathrm{O}) =$ 4.2 barns which lead to a contrast between empty voids and the matrix at the origin of a coherent signal (dry sample in blue). When the loading increases and CD_4 molecules enter inside the porosity, the contrast decreases and we can observe a reduction of the peaks. We notice that as CH_4 has a very low coherent cross section, this loading effect is not visible. At higher values of q, Bragg peaks related to smaller distances are affected because of variation of the unit cell content, inducing here in the observed peaks an increase of the intensities. This effect could be, in the future, quantitatively exploited to precisely deduce the loading and methane organization within the zeolite. The right side of Figure 5.17 shows the $S(q)$ at [P,T = 300 mb, 210 K] and [P,T = 2 b, 250 K]. According to the adsorption isotherms, these two experimental conditions provide the same loading in the matrix. We indeed observe that the curves are overlaid, meaning that the loading is quite similar in both conditions. Moreover, it has already been shown that the structure factor is not modified with the temperature (this result was observed for a temperature up to 80 K) for the same loading [171].

5.4.2 QENS analysis

For each loading and temperature, the raw data were reduced according to standard procedures and normalized to the vanadium reference sample. Figure 5.18(a - top left) shows $S(q, \omega)$ measured by QENS experiments at a fixed temperature (T = 210 K) and fixed loading ($n_a = 16$ molec./uc) but for different scattering vectors. We can observe an increase of the Lorentzian width with the increase of q on the first q values. This signal broadening with q indicates a diffusive process. The signal become apparently flat after the fourth first q values indicating a dynamic too fast for the energy window available. The fitting model considers three components: first, the dry sample is used as a background with a scaling factor. We check that the scaling factor was close to the sample transmission, although the presence of Bragg peaks alters this assumption. Second, an additional elastic contribution was added, accounting for potential mismatch in the dry matrix intensity, and/or localised dynamics giving rise to an elastic contribution. Third, a Lorentzian function accounts for diffusional dynamics. Note that in a first approximation in which both translational and rotational dynamics give rise to Lorentzian signal, which are moreover convoluted since they apply on the same molecules, the resulting function is a Lorentzian of width equal to the sum of the rotational and translational components.

Once the matrix intensity is removed, the given dynamic structure factor can therefore be written :

$$S(q, \omega) = f_{DW}(q) \times [L_T(q, \omega) + \delta(q)] \tag{5.48}$$

$f_{DW}(q)$ refers to the Debye-Waller factor (see analysis of the CH_4 experiment in Section

4.2.1) where the mean square displacement $\langle u^2 \rangle$ was taken constant at 1.5 Å^2 in every fit (i.e. regardless of T, n_a and q). The function defined in Eq. (5.48) was also convoluted with the instrumental resolution and summed with the background (scaled dry sample) as previously stated.

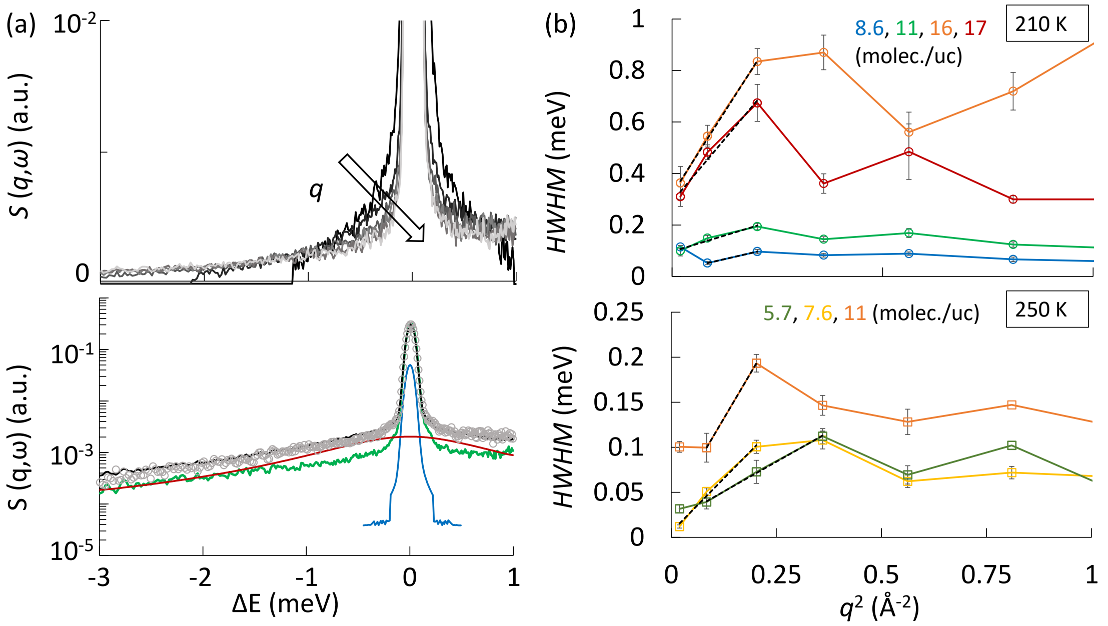

Figure 5.18: (a - top) Dynamic structure factor $S(q, \omega)$ measured by QENS experiments at a fixed temperature (T = 210 K) and fixed loading (n_a = 16 molec./uc) but for different scattering vectors. The signal broadens with q on the firsts q values but remain constant quickly. (a - bottom) Typical fit of the dynamic structure factor $S(q, \omega)$ (grey open circles) under the same conditions than the upper figure but for one scattering vector $q = 0.45$ Å^{-1}. The data are fitted with a three components model as described in the text. The green line corresponds to the dry sample, the blue line is made up of a delta function which corresponds to the elastic peak while the red curve corresponds to a Lorentzian function which describes diffusional motions. The black curve is the total fitting function. (b) Half width at half maximum (HWHM) as a function of q^2 for two temperatures : 210 K (above) and 250 K (below). Colors correspond to different loading. For 210 K : 17 molec./uc (red), 16 molec./uc (orange), 11 molec./uc (green) and 8.6 molec./uc (blue). For 250 K : 11 molec./uc (orange), 7.6 molec./uc (yellow) and 5.7 molec./uc (dark green). Black dashed lines correspond to the fit of the firsts q value with a function of a form $f(x) = ax + b$.

Figure 5.18(a - bottom) shows a typical fit of the dynamic structure factor $S(q, \omega)$ (grey open circles, $T = 210$ K and $n_a = 16$ molec./uc, $q = 0.45$ Å^{-1}). In the figure, the green line corresponds to the dry sample used for the background, the blue line is made up of a delta function which corresponds to the additional elastic peak while the red curve corresponds to a Lorentzian function which describes diffusional motions. The black curve is the total fitting function. Figure 5.18(b) shows the half width at half maximum (HWHM) as a function of q^2 for different loadings (the color code is indicated in the figure caption) at two temperatures : 210 K (top panel) and 250 K (bottom panel).
We notice first that the highest q value in this analysis is 1 Å^{-1}. Beyond this value, the quasi-elastic component is too large and not distinguishable anymore from the background.
Considering Eq. (1.54), for transport diffusivity in the Fickian regime, the HWHM is expected to be proportional to q^2 as HWHM= $D_T q^2$. We emphasize that the trans-

port diffusion coefficient D_T is involved - and not the collective one D_0 - even if we will further show that both are related. In the Figure 5.18(b), we can see that for the firsts values of q (ie below $q = 0.45$ Å^{-1}), the HWHMs can be fitted by a straight line crossing or not zero. In order to measure this transport diffusion coefficient, we chose to fit the HWHM in the linear regime by an equation of the form f(x)=$a \times q^2 + b$. The linear fits are shown by the dotted lines in Figure 5.17(b). By using this equation, we assume that the observed HWHM is the sum of two contributions: one is q-independent and could be associated to the rotational diffusion (as assumed in Chapter 4) and the other is linear with q^2 and corresponds to the translational diffusion ($a = D_T$). The slope of this curve, a, increases when the loading increases - except at 210 K for n_a=16 molec./uc and n_a=17 molec./uc. It implies that the transport coefficient is increasing with the loading.

We observe that for the lowest loadings at 210 K and at the temperature of T = 250 K, the HWHM vs q^2 crosses 0 (b $\sim$ 0). This trend occurs for the fastest dynamics, when the rotation is faster and the associated signal broader (see results and discussions of Figure 4.4(c)). The associated Lorentzian is then too large to be distinguishable from the background, in agreement with the hypothesis of a rotational compound.

We also specify that the HWHM corresponding to the first q value ($q \sim 0.14$ Å^{-1}) has not been used when the value was too far from the linear fit, as can be seen in the Figure 5.17(b). The lowest q range is indeed more sensitive to various artefacts (direct beam pollution, small energy range...) and less reliable.

5.4.3 Transport diffusivity in silicalite-1 : experimental results

Figure 5.19 shows the experimental transport diffusion coefficient (open circles) measured as previously described as a function of the loading for 210 K (purple) and 250 K (green). We want to notice that for the y axis, error bars are probably underestimated as they correspond to the uncertainty in the linear fit used to extract D_s which strongly depend on the number of q values considered. In Figure 5.19, we first observe for both temperatures an increases of D_T when the loading increases, as expected from previous work [91, 79]. The only discrepancy is at 210 K for data at 17 molec./uc and 16 molec./uc, that may however be assigned to the error bars on the loading, as already observed in the static structure factors (see Figure 5.18), almost overlapped for 16 and 17 molec./uc.

Second, the transport diffusion coefficients increase when the temperature increases, as expected because of the thermal agitation.

The transport diffusion coefficients D_T computed at 300 K are shown in the same figure for comparison (black filled circles). Transport diffusion coefficients were computed using $D_T = D_0/S(0)$ (see Eq. (5.45)) with D_0 computed using the gradient method (the data are presented in Section 5.1.1 and figure 5.3) while $S(0)$ was obtained by extrapolating the simulated $S(q)$ at low q values (data are presented in Figure 5.14(b)). The experimental results are in qualitative agreement with the numerical ones, being of the same order of magnitude and showing the same trends as a function of the loading. Both simulated and experimental data are also coherent with the temperature as $D_T(300K) > D_T(250K) > D_T(210K)$. These results are also in good agreement with the simulated ones founded by Maginn *et al.* [91].

Figure 5.19 also presents the experimental self diffusion coefficients D_s presented Figure 4.8 in the previous Chapter. Data are consistent with transport diffusion coefficients at 210 K, less at 250 K. Indeed, at 210 K, we can see $D_T > D_s$ at constant loading. The transport coefficient indeed corresponds to correlation between molecules, it also includes the self part and should therefore be larger. In addition, at low loading, the measured D_T and D_s seem to converge which is expected according to the relation

$D_T = D_s$ in the limit of infinite dilution [91]. However, at 250 K, D_T and D_s cross each other at low loading. The error bars may be underestimated in this region.

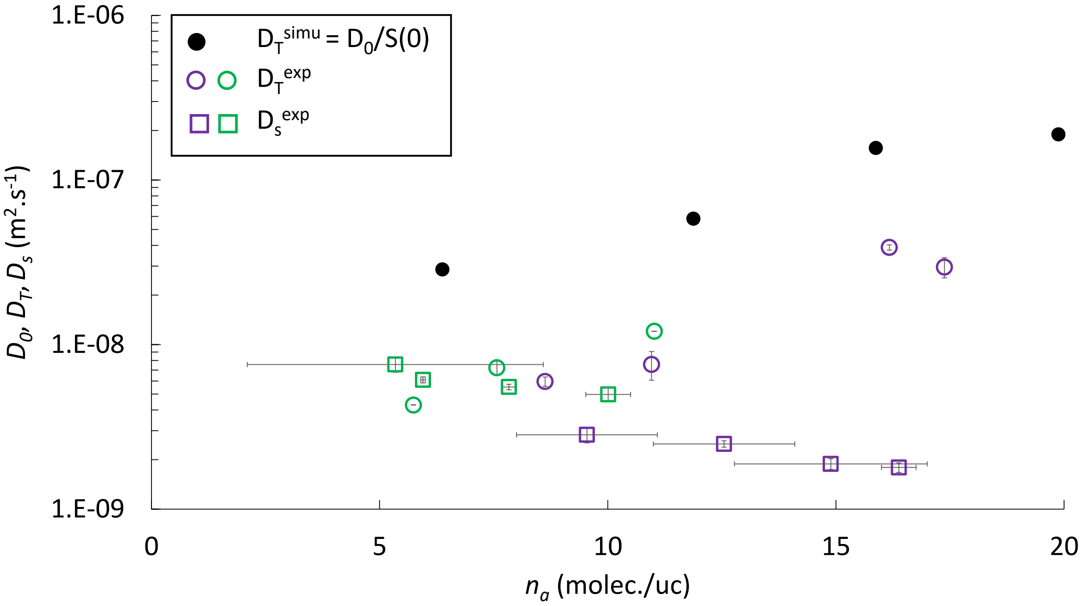

Figure 5.19: Transport and self diffusion coefficients (D_T and D_s respectively) as function of the loading. Black filled circles correspond to transport diffusion coefficient computed at 300 K $D_T = D_0/S(0)$. Open symbols refer to experimental diffusion coefficients measured for different temperatures. Circles correspond to transport diffusion coefficients while self diffusion coefficients correspond to squares. The color code refers to temperatures : 210 K (purple), 250 K (green).

This section has presented an original QENS experiment for measuring transport diffusivity in zeolite. The results presented at this first stage of analysis are quite encouraging. However, some points of the analysis need be be deepened. First, a procedure to measure the CD_4 amount inside the zeolite from the Bragg peaks variations will bring an improvement on the accuracy of the loading measurement. Then, as explained, the fitting model will be improved in taking explicitly into account the rotational diffusion. Moreover, we believe that with slowest diffusive motions (by lowering the temperature for example), we could get access to more accurate data on a larger q range. A complementary perspective is to use different neutron spectroscopy instruments to increase available energy resolution, i.e. getting access to smaller or higher diffusion coefficients. These are a valuable perspectives in order to experimentally probe De Gennes narrowing model around $q \sim 1.7$ Å^{-1}.

5.5 Partial conclusion

In this chapter, using molecular simulations, we were able to compute the macroscopic collective diffusion coefficients by means of the non equilibrium method and the coherent scattering functions obtained at small wave vectors (large correlation distances). These results were used to check the consistency of the definitions for D_0 and $D_0(q)$ when $q \to 0$ (the latter is a measure of the collective diffusivity on different length scales). Coherent and incoherent scattering functions were computed on a large q range ~ 0.03 Å^{-1} to ~ 4 Å^{-1} to estimate $D_s(q)$ and $D_0(q)$. The structure factor was also computed and plotted against the diffusion coefficients $D_s(q)$ and $D_0(q)$ to assess the ability of the concept of De Gennes narrowing to rationalize the transport of a severely nanoconfined fluid. We found a good agreement between our results and De Gennes prediction around the $S(q)$ peak. Considering that MFI zeolites posses a rather complex pores architecture, we believe that De Gennes narrowing model can be extended to any zeolite geometries. However, some questions remain to be addressed as the behavior of the system around Bragg peaks is not fully understood as this manuscript is being written. In addition, the first stage of an original neutron experiment for probing collective diffusivity was presented.

General Conclusion

Adsorption and transport of fluid in nanoporous media display a complex interplay due to specific interactions with the porous architecture that imposes surface forces and geometrical confinement. Despite the abundant literature on the topic, the comprehensive description of some of these rich phenomena is still missing. Yet, these nanoporous materials are at the heart of important developments impacting our economy and environment with diverse applications in our everyday life (gas storage and separation, energy conversion/storage, etc). Indeed, these nanoporous solids possess a large internal surface that promotes interactions between the host porous material and the guest fluid. In this thesis, we chose to work on zeolites, which are prototypical nanoporous materials. These materials are crystalline, inorganic, silica-based porous compounds. They are already well-known for their permeability properties to fluids and are used in numerous applications from oil industry to cat litter. By using such model systems, we aim to study adsorption/transport coupling with the idea that the results found could be extended to more complex systems. The MFI zeolite structure was chosen as it displays different pore types such as channels and small cages and an underlying anisotropic architecture. Pores and channels for which the opening size varies between 5 and 8 Å lead to marked confinement effects on the behavior of the confined fluid.

A specific feature of this thesis is to use a dual approach by combining results obtained using experiments and molecular simulations to study methane behavior inside the zeolite porosity. By using this hybrid approach, we were able to produce a set of data that allowed us to interpret adsorption, diffusion and transport mechanisms of methane in zeolite but also to probe available theoretical models to predict these mechanisms. On the one hand, among experiments, volumetric adsorption was used to measure adsorption isotherms while quasi elastic neutron scattering was used to probe molecular motion of methane over a distance range up to few Å. On the other hand, molecular simulations were set up to investigate the adsorption and transport of the same fluid – methane – in the zeolite nanoporosity. In particular, the Grand Canonical Monte Carlo method was used to compute adsorption isotherms at different temperatures and pressures (up to pressures not accessible by most experimental set ups). Molecular dynamics simulations were used to track molecules trajectories that provide a means to assess structural and dynamical properties. We tried to check as much as possible the validity of our model and our computation methods by studying the impact of different parameters such as the matrix flexibility.

A first objective of this thesis was to study methane adsorption in two zeolite systems: a bulk zeolite and a thin zeolite layer. By comparing the data for these two systems, we were able to evaluate the contributions of the adsorption contributions from the bulk zeolite and the external surface, respectively. As a first step, we studied the methane adsorption in the bulk zeolite. Both experimental and simulation results showed that adsorption increases with pressure until reaching a plateau corresponding to porosity saturation. As expected for physisorption phenomena, our results also show that temperature promotes desorption. In order to cross check our results, the experimental and simulated results were compared between them and with results from the literature. As a second step, we showed that adsorption at the external surface follows the same trend as adsorption in bulk zeolite when varying the pressure and temperature. It was also shown that, upon increasing the pressure, methane first adsorbs in zeolite porosity and then - once the core porosity saturation is reached - adsorbs at the external surface. The effect of the layer orientation was shown to be linked to the amount of adsorption sites and their distribution on the external surface. Considering a formalism combining Frenkel-Halsey-Hill approximations and Polanyi's model, we extended the adsorption potential theory to supercritical gas conditions. This framework was validated by comparing the model predictions and the set of experimental and simulation results in the bulk zeolite and at the external surfaces of zeolite layers. The good agreement between the theoretical predictions and our results suggests that this model is a robust thermodynamic framework to describe adsorption at different temperatures and pressures. Moreover, this model predicts at the same time bulk and external surface adsorption which is a step forward to the understanding of the effect of external surface on adsorption mechanisms. Considering that the MFI structure has a rather complex architecture as it possesses different channels along different orientations, we think that this thermodynamic framework could be extended to different zeolite materials.

In a second step, methane self diffusivity was probed in the bulk zeolite. One interesting aspect of the study reported here was to couple quasi elastic neutron scattering experiments and molecular simulations to unravel the molecular mechanisms at play. Using neutrons experiments, we were able to decipher both translational and rotational diffusion. However, using molecular simulation, as methane is treated as a single sphere (United Atom model), no rotation was considered but only translational motion. Using molecules positions given by molecular dynamics, the mean square displacement and incoherent scattering functions were computed in order to assess the self diffusion coefficient for different loadings and along different crystallographic directions. Using experimental and simulation data, we showed that the diffusivity decreases when the loading increases due to steric effects. By probing the diffusivity at different temperatures, we estimated the free energy barrier using an Arrhenius law. This barrier close to thermal energy at room temperature decreases when the loading increases, therefore indicating that collisions between molecules promote desorption from adsorption sites. Anisotropic diffusivities were also found to be strongly dependent of the porosity architecture as larger diffusion coefficients were computed along larger channels (i.e. straight channels). A simple free volume theory was invoked to rationalize our simulated diffusion data. The robustness of this approach was checked by comparing simulated 3D and anisotropic diffusion coefficients against predictions of this model. Considering the good agreement between the theoretical predictions and the data, we believe that the free volume theory is a powerful model to predict diffusivity in porous media.

Finally, in a last step, the collective and transport diffusivities were studied in bulk zeolites (these two quantities are directly related to the engineering concept of permeability as shown in this thesis). First, we computed the self and collective diffusion coefficients dependent on the length scale considered. In the limit of vanishing wave vector ($q \to 0$), these self and transport coefficients reach the macroscopic limits D_s and D_0. In parallel, to cross check our data, we also determine D_0 using the non equilibrium molecular dynamics in which a chemical potential gradient is applied. The resulting collective diffusion coefficients were obtained as a function of the loading for each crystallographic direction. Then, we relied on the concept of De Gennes narrowing to relate the structure factor $S(q)$ to the collective diffusion coefficient $D_0(q)$. This model considers the collective diffusivity as a response to density fluctuations over a distance of characteristic length scale $1/q$. For both bulk supercritical methane and methane nanoconfined in zeolite, we showed that De Gennes narrowing provides a reasonable description of the wave vector dependent collective diffusivity. For the zeolite system, the collective diffusion coefficients also include the signature of the Bragg peaks imposed in the structure factor by the host zeolite (crystalline) matrix. Indeed, through its periodic architecture, the zeolite matrix imposes strong structural ordering on the distribution of methane molecules inside the porosity. The consequences of this crystalline, periodic fingerprint for the collective diffusion are discussed in this thesis by scrutinizing the coherent scattering functions. In this chapter, some issues remain to be clarified such as the behavior of coherent scattering functions around Bragg peaks. Finally, in this chapter, we also reported a preliminary analysis of a complete set of experimental data using deuterated methane. While this contribution deserves to be further investigated, we think that it is an important source of information to better understand collective diffusivity and, hence, permeability in nanoconfined fluids. In particular, it provides direct microscopic information on fluid permeability and flow at the nanoscale that perfectly complements available molecular simulation approaches and nanofluidic experiments.

Bibliography

[1] Sabine Brueske, Caroline Kramer, and Aaron Fisher. Bandwidth study on energy use and potential energy saving opportunities in u.s. petroleum refining. Technical report, U.S. Department of Energy, 2015.

[2] David S. Sholl and Ryan P. Lively. Seven chemical separations to change the world. *Nature*, 532(7600):435–437, 2016.

[3] Pascal Van Der Voort, Karen Leus, and Els De Canck. *Introduction to Porous Materials*. Wiley, 2019.

[4] Pierfranco Demontis and Giuseppe B. Suffritti. Structure and dynamics of zeolites investigated by molecular dynamics. *Chemical Reviews*, 97(8):2845–2878, 1997.

[5] Brandon C. Bukowski, Frerich J. Keil, Peter I. Ravikovitch, German Sastre, Randall Q. Snurr, and Marc-Olivier Coppens. Connecting theory and simulation with experiment for the study of diffusion in nanoporous solids. *Adsorption*, 27(5):683–760, 2021.

[6] David A Reed and Gert Ehrlich. Surface diffusion, atomic jump rates and thermodynamics. *Surface Sciences*, 102:588–609, 1981.

[7] Jeetain Mittal, Jeffrey R. Errington, and Thomas M. Truskett. Thermodynamics predicts how confinement modifies the dynamics of the equilibrium hard-sphere fluid. *Phys. Rev. Lett.*, 96:177804, May 2006.

[8] Trond S. Ingebrigtsen, Jeffrey R. Errington, Thomas M. Truskett, and Jeppe C. Dyre. Predicting how nanoconfinement changes the relaxation time of a supercooled liquid. *Phys. Rev. Lett.*, 111:235901, Dec 2013.

[9] Julien Cousin Saint Remi, Alexander Lauerer, Christian Chmelik, Isabelle Vandendael, Herman Terryn, Gino V. Baron, Joeri F. M. Denayer, and Jörg Kärger. The role of crystal diversity in understanding mass transfer in nanoporous materials. *Nature Materials*, 15(4):401–406, 2016.

[10] Libor Brabec and Milan Kocirik. Silicalite-1 crystals etched with hydrofluoric acid dissolved in water or acetone. *The Journal of Physical Chemistry C*, 114(32):13685–13694, 2010.

[11] Julia Rybka, Alexandra Höltzel, Andreas Steinhoff, and Ulrich Tallarek. Molecular dynamics study of the relation between analyte retention and surface diffusion in reversed-phase liquid chromatography. *The Journal of Physical Chemistry C*, 123(6):3672–3681, 2019.

[12] Sergey M. Melnikov, Alexandra Höltzel, Andreas Seidel-Morgenstern, and Ulrich Tallarek. A molecular dynamics study on the partitioning mechanism in hydrophilic interaction chromatography. *Angewandte Chemie International Edition*, 51(25):6251–6254, 2012.

[13] Wanda Kellouai, Patrick Judeinstein, Marie Plazanet, Simon Baudoin, Martin Drobek, Anne Julbe, and Benoit Coasne. Gas adsorption in zeolite and thin zeolite layers: Molecular simulation, experiment, and adsorption potential theory. *Langmuir*, 38(18):5428–5438, 2022.

[14] Catherine P. Raptopoulou. Metal-organic frameworks: Synthetic methods and potential applications. *Materials*, 14(2):310, 2021.

[15] Maria Letizia Terranova, Silvia Orlanducci, and Marco Rossi. *Carbon Nanomaterials for Gas Adsorption.* Jenny Stanford Publishing, 2012.

[16] Susana Valencia and Fernando Rey. *New Developments in Adsorption/Separation of Small Molecules by Zeolites.* Springer, Cham, 2021.

[17] Mark E. Davis. Design for sieving. *Nature*, 382(6592):583–585, 1996.

[18] Valentin Valtchev, Gerardo Majano, Svetlana Mintova, and Javier Pérez-Ramírez. Tailored crystalline microporous materials by post-synthesis modification. *Chemical Society Reviews*, 42(1):263–290, 2013.

[19] Bert M. Weckhuysen and Jihong Yu. Recent advances in zeolite chemistry and catalysis. *Chemical Society Reviews*, 44(20):7022–7024, 2015.

[20] Jean-Pierre Bellat, Emmanuelle Pilverdier, Marie-Hélène Simonot-Grange, and Sophie Jullian. Microporous volume and external surface of y zeolites accessible to p-xylene and m-xylene. *Microporous Materials*, 9(5):213–220, 1997.

[21] J. Rouquerol, D. Avnir, C. W. Fairbridge, D. H. Everett, J. M. Haynes, N. Pernicone, J. D. F. Ramsay, K. S. W. Sing, and K. K. Unger. Recommendations for the characterization of porous solids (technical report). *Pure and Applied Chemistry*, 66(8):1739–1758, 1994. Publisher: De Gruyter.

[22] Claire Bernardon. *Les zéolithes comme catalyseurs "verts" pour la synthèse organique: de leur synthèse à façon à leurs applications en chimie organique.* PhD thesis, Université de Strasbourg, 2017.

[23] IUPAC. International union of pure and applied chemistry. https://goldbook.iupac.org/terms/view/A00155, Data last update in February 24, 2014.

[24] Wilfried Louisfrema. *Caractérisation des oxydes nanoporeux contenant des ions lourds en milieu aqueux.* PhD thesis, Université Paris Science Lettres, 2016.

[25] David Bousquet. *Modélisation de l'adsorption dans les matériaux nanoporeux flexibles.* PhD thesis, Université Pierre et Marie Curie, 2013.

[26] Renato Campesi. *Synthèse, caractérisation et étude des propriétés thermodynamiques d'hydrogénation de nanocomposites matériaux poreux / métaux-alliages.* PhD thesis, Université Paris Est, 2008.

[27] Arne Thomas. Much ado about nothing – a decade of porous materials research. *Nature Communications*, 11(1):4985, 2020.

[28] Behzad Ghanbarian, Allen G. Hunt, Robert P. Ewing, and Muhammad Sahimi. Tortuosity in porous media: A critical review. *Soil Science Society of America Journal*, 77(5):1461–1477, 2013. _eprint: https://onlinelibrary.wiley.com/doi/pdf/10.2136/sssaj2012.0435.

[29] Laura Scalfi, Benoît Coasne, and Benjamin Rotenberg. On the gibbs–thomson equation for the crystallization of confined fluids. *The Journal of Chemical Physics*, 154(11):114711, 2021.

[30] Abderrahmane Rhardane, Sara Al Haj Sleiman, Syed Yasir Alam, and Frédéric Grondin. A quantitative assessment of the parameters involved in the freeze–thaw damage of cement-based materials through numerical modelling. *Construction and Building Materials*, 272:121838, 2021.

[31] Benoit Coasne, Anne Galarneau, Roland J. M. Pellenq, and Francesco Di Renzo. Adsorption, intrusion and freezing in porous silica: the view from the nanoscale. *Chemical Society Reviews*, 42(9):4141, 2013.

[32] Berend Smit and Theo L. M. Maesen. Molecular simulations of zeolites: Adsorption, diffusion, and shape selectivity. *Chemical Reviews*, 108(10):4125–4184, 2008.

[33] Subhash Bhatia. *Zeolite Catalysis: Principles and Applications: Principles and Applications*. CRC Press, 2020.

[34] J Weitkamp. Zeolites and catalysis. *Solid State Ionics*, 131(1):175–188, 2000.

[35] Yi Li and Jihong Yu. Emerging applications of zeolites in catalysis, separation and host–guest assembly. *Nature Reviews Materials*, 6(12):1156–1174, 2021.

[36] Jie Li, Yingluo He, Li Tan, Peipei Zhang, Xiaobo Peng, Anjaneyulu Oruganti, Guohui Yang, Hideki Abe, Ye Wang, and Noritatsu Tsubaki. Integrated tuneable synthesis of liquid fuels via fischer–tropsch technology. *Nature Catalysis*, 1(10):787–793, 2018.

[37] Vyacheslav N. Romanov, Terry E. Ackman, Yee Soong, and Robert L. Kleinman. CO $_2$ storage in shallow underground and surface coal mines: Challenges and opportunities. *Environmental Science & Technology*, 43(3):561–564, 2009.

[38] Stéphanie Hongois, Frédéric Kuznik, Philippe Stevens, and Jean-Jacques Roux. Development and characterisation of a new $MgSO_4$-zeolite composite for long-term thermal energy storage. *Solar Energy Materials and Solar Cells*, 95(7):1831–1837, 2011.

[39] Beata Michalkiewicz and Zvi C. Koren. Zeolite membranes for hydrogen production from natural gas: state of the art. *Journal of Porous Materials*, 22(3):635–646, 2015.

[40] A.R. Loiola, J.C.R.A. Andrade, J.M. Sasaki, and L.R.D. da Silva. Structural analysis of zeolite NaA synthesized by a cost-effective hydrothermal method using kaolin and its use as water softener. *Journal of Colloid and Interface Science*, 367(1):34–39, 2012.

[41] Omar Falyouna, Osama Eljamal, Ibrahim Maamoun, Atsushi Tahara, and Yuji Sugihara. Magnetic zeolite synthesis for efficient removal of cesium in a lab-scale continuous treatment system. *Journal of Colloid and Interface Science*, 571:66–79, 20.

[42] IZA. Database of zeolite structure - mfi. https://europe.iza-structure.org/IZA-SC/framework.php?STC=MFI, Data last update in July 1, 2007.

[43] M.P. Pina, R. Mallada, M. Arruebo, M. Urbiztondo, N. Navascués, O. de la Iglesia, and J. Santamaria. Zeolite films and membranes. emerging applications. *Microporous and Mesoporous Materials*, 144(1):19–27, 2011.

[44] Svetlana Mintova, Jean-Pierre Gilson, and Valentin Valtchev. Advances in nanosized zeolites. *Nanoscale*, 5(15):6693, 2013.

[45] Céline Pagis, Ana Rita Morgado Prates, David Farrusseng, Nicolas Bats, and Alain Tuel. Hollow zeolite structures: An overview of synthesis methods. *Chemistry of Materials*, 28(15):5205–5223, 2016.

[46] Valentin Valtchev and Svetlana Mintova. Hierarchical zeolites. *MRS Bulletin*, 41(9):689–693, 2016.

[47] IZA. Explanatory notes - structures. https://europe.iza-structure.org/IZA-SC/DatabaseHelp$_()$Structures.html, Data last update in August 21, 2021.

[48] Walter Loewenstein. The distribution of aluminum in the tetrahedra of silicates and aluminates. *American Mineralogist*, 39(1):92–96, 1954.

[49] S. Tarling, Paul Barnes, and Jacek Klinowski. The structure and si,al distribution of the ultramarines. *Acta Crystallographica Section B-structural Science - ACTA CRYSTALLOGR B-STRUCT SCI*, 44:128–135, 1988.

[50] Christopher J. Gump, Vu A. Tuan, Richard D. Noble, and John L. Falconer. Aromatic permeation through crystalline molecular sieve membranes. *Industrial & Engineering Chemistry Research*, 40(2):565–577, 2001.

[51] A. Dąbrowski. Adsorption — from theory to practice. *Advances in Colloid and Interface Science*, 93(1):135–224, 2001.

[52] Pierre Desre and Fiqiri Hodaj. *Thermodynamique des matériaux: Équilibres de phases et métastabilité*. EDP Sciences, 2021.

[53] Ibach Harald. Adsorption. In *Physics of Surfaces and Interfaces*, pages 245–308. Springer Berlin Heidelberg, 2006.

[54] Ondřej Kadlec. The History and Present State of Dubinin's Theory of Adsorption of Vapours and Gases on Microporous Solids. *Adsorption Science & Technology*, 19(1):1–24, February 2001.

[55] Irving Langmuir. The adsorption of gases on plane surfaces of glass, mica and platinum. *Journal of the American Chemical Society*, 40(9):1361–1403, 1918.

[56] Stephen Brunauer, P. H. Emmett, and Edward Teller. Adsorption of gases in multimolecular layers. *Journal of the American Chemical Society*, 60(2):309–319, 1938.

[57] Stephen Brunauer and P. H. Emmett. THE USE OF VAN DER WAALS ADSORPTION ISOTHERMS IN DETERMINING THE SURFACE AREA OF IRON SYNTHETIC AMMONIA CATALYSTS. *Journal of the American Chemical Society*, 57(9):1754–1755, 1935.

[58] Stephen Brunauer and P. H. Emmett. The use of low temperature van der waals adsorption isotherms in determining the surface areas of various adsorbents. *Journal of the American Chemical Society*, 59:2682–2689, 1937.

[59] M. Polanyi. Adsorption from the point of view of the third law of thermodynamics. *Verhandlungen der Deutschen Physikalischen, Gesellschaft*, 16:1012–1016, 1914.

[60] Michael Polanyi. The potential theory of adsorption. *Science, New Series*, 141(3585):1010–1013, 1963.

[61] Alexander V. Neimark and Ivan Grenev. Adsorption-Induced Deformation of Microporous Solids: A New Insight from a Century-Old Theory. *The Journal of Physical Chemistry C*, 124(1):749–755, January 2020.

[62] Zeid Alothman. A review: Fundamental aspects of silicate mesoporous materials. *Materials*, 5:2874–2902, 12 2012.

[63] R. Byron Bird, Warren E. Stewart, and Edwin N. Lightfoot. *Transport Phenomena, Revised 2nd Edition.* Wiley, 2006.

[64] Noelle Pottier. *Nonequilibrium Statistical Physics.* Oxford press, 2014.

[65] Jean-Louis Barrat and Jean-Pierre Hansen. *Basic Concepts for Simple and Complex Liquids.* Cambridge University Press, 2003.

[66] Jörg Kärger. Transport phenomena in nanoporous materials. *ChemPhysChem*, 16(1):24–51, 2015.

[67] Ryogo Kubo. Statistical-mechanical theory of irreversible processes. i. general theory and simple applications to magnetic and conduction problems. *Journal of Physical Society of Japan*, page 16, 1957.

[68] Melville S. Green. Markoff random processes and the statistical mechanics of time-dependent phenomena. II. irreversible processes in fluids. *The Journal of Chemical Physics*, 22(3):398–413, 1954.

[69] N. Bernstein, J. L. Feldman, and D. J. Singh. Calculations of dynamical properties of skutterudites: Thermal conductivity, thermal expansivity, and atomic mean-square displacement. *Physical Review B*, 81(13):134301, 2010.

[70] Suranjan Sarkar and R. Panneer Selvam. Molecular dynamics simulation of effective thermal conductivity and study of enhanced thermal transport mechanism in nanofluids. *Journal of Applied Physics*, 102(7):074302, 2007.

[71] Haruki Oga. Theoretical framework for the atomistic modeling of frequency-dependent liquid-solid friction. *Physical Review Research*, page 6, 2021.

[72] A. Zaragoza, M. A. Gonzalez, L. Joly, I. López-Montero, M. A. Canales, A. L. Benavides, and C. Valeriani. Molecular dynamics study of nanoconfined TIP4p/2005 water: how confinement and temperature affect diffusion and viscosity. *Physical Chemistry Chemical Physics*, 21(25):13653–13667, 2019.

[73] Jean-Pierre Hansen and Ian R. McDonald. *Theory of Simple Liquids.* Academic Press, 2013.

[74] H. Jobic. Diffusion à longue distance. *Le Journal de Physique IV*, 10:Pr1–77–Pr1–104, 2000.

[75] H. Jobic and A. Méthivier. Intracrystalline diffusion in zeolites studied by neutron scattering techniques. *Oil & Gas Science and Technology*, 60(5):815–830, 2005.

[76] Ryogo Kubo, Morikazu Toda, and Natsuki Hashitsume. *Statistical Physics II Chapter 4*, volume 31 of *Springer Series in Solid-State Sciences*. Springer Berlin Heidelberg, 1991.

[77] Alexender Schlaich, Jean-louis Barrat, and Benoit Coasne. Transport in nanoporous materials: From microscopic to coarse-grained descriptions. To be published.

[78] Anastasios I. Skoulidas and David S. Sholl. Molecular dynamics simulations of self-diffusivities, corrected diffusivities, and transport diffusivities of light gases in four silica zeolites to assess influences of pore shape and connectivity. *The Journal of Physical Chemistry A*, 107(47):10132–10141, 2003.

[79] Anastasios I. Skoulidas and David S. Sholl. Transport diffusivities of CH_4 , CF_4 , He, Ne, Ar, Xe, and SF_6 in silicalite from atomistic simulations. *The Journal of Physical Chemistry B*, 106(19):5058–5067, 2002.

[80] Catherine O'Sullivan, Chloé Arson, and Benoit Coasne. A perspective on darcy's law across the scales: From physical foundations to particulate mechanics. *Journal of Engineering Mechanics*, 2022.

[81] Kouichi Miura, Junichi Hayashi, and Kenji Hashimoto. PREPARATION OF MOLECULAR SIEVING CARBON FROM COAL MODIFIED BY ORGANIC COMPOUNDS. In International Energy Agency Coal Research Ltd, editor, *1991 International Conference on Coal Science Proceedings*, pages 560–563. Butterworth-Heinemann, 1991.

[82] Arthur F. Voter and Jimmie D. Doll. Transition state theory description of surface self-diffusion: Comparison with classical trajectory results. *The Journal of Chemical Physics*, 80(11):5832–5838, 1984. Publisher: American Institute of Physics.

[83] Jeffrey S. Camp and David S. Sholl. Transition state theory methods to measure diffusion in flexible nanoporous materials: Application to a porous organic cage crystal. *The Journal of Physical Chemistry C*, 120(2):1110–1120, 2016. Publisher: American Chemical Society.

[84] D. Dubbeldam, E. Beerdsen, S. Calero, and B. Smit. Dynamically corrected transition state theory calculations of self-diffusion in anisotropic nanoporous materials. *The Journal of Physical Chemistry B*, 110(7):3164–3172, 2006. Publisher: American Chemical Society.

[85] Shushu Gao, Zhiqiang Liu, Shutao Xu, Anmin Zheng, Pengfei Wu, Bing Li, Xiaoshuai Yuan, Yingxu Wei, and Zhongmin Liu. Cavity-controlled diffusion in 8-membered ring molecular sieve catalysts for shape selective strategy. *Journal of Catalysis*, 377:51–62, 2019.

[86] David A. Newsome and Marc-Olivier Coppens. Molecular dynamics as a tool to study heterogeneity in zeolites - effect of na cations on diffusion of co and n in na-zsm-5. In *Chemical Engineering Science*, 2015.

[87] Randall Q. Snurr and Jörg Kärger. Molecular simulations and NMR measurements of binary diffusion in zeolites. *The Journal of Physical Chemistry B*, 101(33):6469–6473, 1997. Publisher: American Chemical Society.

[88] Edward J. Maginn, Alexis T. Bell, and Doros N. Theodorou. Dynamics of long n -alkanes in silicalite: A hierarchical simulation approach. *The Journal of Physical Chemistry*, 100(17):7155–7173, 1996.

[89] Vadim V. Guliants and Anthony J. Huth. Force fields for classical atomistic simulations of small gas molecules in silicalite-1 for energy-related gas separations at high temperatures. *Journal of Porous Materials*, 20(4):741–751, 2013.

[90] R. Larry. June, Alexis T. Bell, and Doros N. Theodorou. Molecular dynamics study of methane and xenon in silicalite. *The Journal of Physical Chemistry*, 94(21):8232–8240, 1990.

[91] Edward J. Maginn, Alexis T. Bell, and Doros N. Theodorou. Transport diffusivity of methane in silicalite from equilibrium and nonequilibrium simulations. *The Journal of Physical Chemistry*, 97(16):4173–4181, 1993.

[92] Donald A.McQuarrie. Statistical mechanics. In Donald A.McQuarrie, editor, *Statistical Mechanics*. University Science Books, 2000.

[93] Daan Frenkel and Berend Smit. Chapter 2 - statistical mechanics. In Daan Frenkel and Berend Smit, editors, *Understanding Molecular Simulation (Second Edition)*, pages 9–22. Academic Press, San Diego, second edition edition, 2002.

[94] Daan Frenkel and Berend Smit. Chapter 5 - monte carlo simulations in various ensembles. In Daan Frenkel and Berend Smit, editors, *Understanding Molecular Simulation (Second Edition)*, pages 111–137. Academic Press, San Diego, second edition edition, 2002.

[95] Daan Frenkel and Berend Smit. Chapter 3 - monte carlo simulations. In Daan Frenkel and Berend Smit, editors, *Understanding Molecular Simulation (Second Edition)*, pages 23–61. Academic Press, San Diego, second edition edition, 2002.

[96] Nicholas Metropolis and S. Ulam. The monte carlo method. *Journal of the American Statistical Association*, 44(247):335–341, 1949. Publisher: Taylor & Francis _eprint: https://www.tandfonline.com/doi/pdf/10.1080/01621459.1949.10483310.

[97] Nicholas Metropolis, Arianna W. Rosenbluth, Marshall N. Rosenbluth, Augusta H. Teller, and Edward Teller. Equation of state calculations by fast computing machines. *The Journal of Chemical Physics*, 21(6):1087–1092, 1953. Publisher: American Institute of Physics.

[98] Daan Frenkel and Berend Smit. Chapter 6 - molecular dynamics in various ensembles. In Daan Frenkel and Berend Smit, editors, *Understanding Molecular Simulation (Second Edition)*, pages 139–163. Academic Press, San Diego, second edition edition, 2002.

[99] Loup Verlet. Computer ”experiments” on classical fluids. i. thermodynamical properties of lennard-jones molecules. *Phys. Rev.*, 159:98–103, Jul 1967.

[100] Victor Ruhle. Berendsen and nose-hoover thermostats. *American Journal of Physics*, page 4, 2007.

[101] Philippe H. Hünenberger. Thermostat algorithms for molecular dynamics simulations. In Christian Dr. Holm and Kurt Prof. Dr. Kremer, editors, *Advanced Computer Simulation*, volume 173, pages 105–149. Springer Berlin Heidelberg, 2005. Series Title: Advances in Polymer Science.

[102] Shuichi Nosé. A unified formulation of the constant temperature molecular dynamics methods. *The Journal of Chemical Physics*, 81(1):511–519, 1984. Publisher: American Institute of Physics.

[103] William G. Hoover. Canonical dynamics: Equilibrium phase-space distributions. *Phys. Rev. A*, 31:1695–1697, Mar 1985.

[104] The university of Edinburgh. The nose-hoover thermostat. https://www2.ph.ed.ac.uk/ dmarendu/MVP/MVP03.pdf, Data last update in ?

[105] Alejandro ORSIKOWSKY SANCHEZ. *Propriétés d'adsorption de differents substrats microporeux appliques a la separation de gaz : caracterisation, modelisation et methodologie de selection.* PhD thesis, Université de Pau et des pays de l'Adour, 2020.

[106] M. Bée. La diffusion quasiélastique des neutrons ; introduction et principes généraux. *Le Journal de Physique IV*, 10:Pr1–1–Pr1–14, 2000.

[107] C. Alba-Simionesco. Étude des propriétés dynamiques des fluides confinés par diffusion quasiélastique de neutrons. *École thématique de la Société Française de la Neutronique*, 12:43–60, 2007.

[108] Toby Perring. Lecture at the oxford neutron school. 2007.

[109] Quentin Berrod, Karine Lagrené, Jacques Ollivier, and Jean-Marc Zanotti. Inelastic and quasi-elastic neutron scattering. application to soft-matter. *EPJ Web of Conferences*, 188:05001, 2018.

[110] C T Chudley and R J Elliott. Neutron scattering from a liquid on a jump diffusion model. *Proceedings of the Physical Society*, 77(2):353–361, 1961.

[111] M. Bée. *Quasielastic Neutron Scattering, Principles and Applications in Solid State Chemistry, Biology and Materials Science.* Taylor & Francis, 1988.

[112] ILL: Neutrons for society. Questions sur la sécurité du réacteur. https://www.ill.eu/fr/reacteur-et-securite/surete/questions-sur-la-securite-du-reacteur.

[113] ILL: Neutrons for society. Instrument description. https://www.ill.eu/users/instruments/instruments-list/sharp/characteristics.

[114] Javier Pérez-Ramírez, Danny Verboekend, Adriana Bonilla, and Sònia Abelló. Zeolite catalysts with tunable hierarchy factor by pore-growth moderators. *Advanced Functional Materials*, 19(24):3972–3979, 2009.

[115] Yang Zhao, Zhaoqi Ye, Lei Wang, Hongbin Zhang, Fangqi Xue, Songhai Xie, Xiao-Ming Cao, Yahong Zhang, and Yi Tang. Engineering fractal MTW zeolite mesocrystal: Particle-based dendritic growth via twinning-plane induced crystallization. *Crystal Growth & Design*, 18(2):1101–1108, 2018.

[116] Sharon Mitchell, Ana B. Pinar, Jeffrey Kenvin, Paolo Crivelli, Jörg Kärger, and Javier Pérez-Ramírez. Structural analysis of hierarchically organized zeolites. *Nature Communications*, 6(1):8633, 2015.

[117] Benoit Coasne, Anne Galarneau, Corine Gerardin, François Fajula, and François Villemot. Molecular simulation of adsorption and transport in hierarchical porous materials. *Langmuir*, 29(25):7864–7875, 2013.

[118] Katie A. Cychosz, Rémy Guillet-Nicolas, Javier García-Martínez, and Matthias Thommes. Recent advances in the textural characterization of hierarchically structured nanoporous materials. *Chemical Society Reviews*, 46(2):389–414, 2017.

[119] Johan A. Martens, Wim Souverijns, Wim Verrelst, Rudy Parton, Gilbert F. Froment, and Pierre A. Jacobs. Selective isomerization of hydrocarbon chains on external surfaces of zeolite crystals. *Angewandte Chemie International Edition*, 34(22):2528–2530, 1995.

[120] Jovana Zecevic, Gina Vanbutsele, Krijn P. de Jong, and Johan A. Martens. Nanoscale intimacy in bifunctional catalysts for selective conversion of hydrocarbons. *Nature*, 528(7581):245–248, 2021.

[121] Céline Chizallet. Achievements and expectations in the field of computational heterogeneous catalysis in an innovation context. *Topics in Catalysis*, 65:69–81, 2021.

[122] Céline Chizallet. Toward the atomic scale simulation of intricate acidic aluminosilicate catalysts. *ACS Catalysis*, 10(10):5579–5601, 2020.

[123] Pavel Kortunov, Sergey Vasenkov, Christian Chmelik, Jörg Kärger, Douglas M. Ruthven, and Jerzy Wloch. Influence of Defects on the External Crystal Surface on Molecular Uptake into MFI-Type Zeolites. *Chemistry of Materials*, 16(18):3552–3558, September 2004.

[124] Berend Smit. Simulating the Adsorption Isotherms of Methane, Ethane, and Propane in the Zeolite Silicalite. *The Journal of Physical Chemistry*, 99(15):5597–5603, April 1995.

[125] Thijs J. H. Vlugt and Merijn Schenk. Influence of Framework Flexibility on the Adsorption Properties of Hydrocarbons in the Zeolite Silicalite. *The Journal of Physical Chemistry B*, 106(49):12757–12763, December 2002.

[126] Aidan P. Thompson, H. Metin Aktulga, Richard Berger, Dan S. Bolintineanu, W. Michael Brown, Paul S. Crozier, Pieter J. in 't Veld, Axel Kohlmeyer, Stan G. Moore, Trung Dac Nguyen, Ray Shan, Mark J. Stevens, Julien Tranchida, Christian Trott, and Steven J. Plimpton. Lammps - a flexible simulation tool for particle-based materials modeling at the atomic, meso, and continuum scales. *Computer Physics Communications*, 271:108171, 2022.

[127] J. Motuzas, A. Julbe, R.D. Noble, C. Guizard, Z.J. Beresnevicius, and D. Cot. Rapid synthesis of silicalite-1 seeds by microwave assisted hydrothermal treatment. *Microporous and Mesoporous Materials*, 80(1):73–83, 2005.

[128] Benoît Coasne, Keith E. Gubbins, and Roland J.-M. Pellenq. Temperature effect on adsorption/desorption isotherms for a simple fluid confined within various nanopores. *Adsorption*, 11:289–294, 2005.

[129] Benoit Coasne, J. Czwartos, M. Sliwinska-Bartkowiak, and Keith E. Gubbins. Effect of pressure on the freezing of pure fluids and mixtures confined in nanopores. *The Journal of Physical Chemistry B*, 113(42):13874–13881, 2009.

[130] H. B. Abdul-Rehman, M. A. Hasanain, and K. F. Loughlin. Quaternary, ternary, binary, and pure component sorption on zeolites. 1. Light alkanes on Linde S-115 silicalite at moderate to high pressures. *Industrial & Engineering Chemistry Research*, 29(7):1525–1535, July 1990.

[131] T Ding, S Ozawa, and Y Ogino. Adsorption equilibria of methane, nitrogen, and carbon dioxide on zsm-5. *Zhejiang Daxue Xuebao*, 22:124, 1988.

[132] T.C. Golden and S Sircar. Gas adsorption on silicalite. *Journal of colloid and interface science*, 162:182–188, 1994.

[133] L.V.C. Rees, P. Brückner, and J. Hampson. Sorption of n_2, ch_4 and co_2 in silicalite-1. *Gas Separation & Purification*, 5:67–75, 1991.

[134] NIST. Nist chemistry webbook. https://webbook.nist.gov/, 2021 (accessed December 5, 2021).

[135] R. M. Barrer and A. B. Robins. Multilayer sorption in terms of an equation of state. *Transactions of the Faraday Society*, 47:773, 1951.

[136] D. D. Do and H. D. Do. Adsorption of argon from sub- to supercritical conditions on graphitized thermal carbon black and in graphitic slit pores: A grand canonical monte carlo simulation study. *The Journal of Chemical Physics*, 123(8):084701, 2005.

[137] Elena García-Pérez, Sondre K. Schnell, Juan M. Castillo, Sofia Calero, Signe Kjelstrup, David Dubbeldam, and Thijs J. H. Vlugt. External Surface Adsorption on Silicalite-1 Zeolite Studied by Molecular Simulation. *The Journal of Physical Chemistry C*, 115(31):15355–15360, August 2011.

[138] Isabella Inzoli, Jean-Marc Simon, and Signe Kjelstrup. Surface Adsorption Isotherms and Surface Excess Densities of n -Butane in Silicalite-1. *Langmuir*, 25(3):1518–1525, February 2009.

[139] Jean Rouquerol, Françoise Rouquerol, Philip Llewellyn, Guillaume Maurin, and Kenneth Sing. *Adsorption by Powders and Porous Solids*. Academic Press, 1999.

[140] Terrell L. Hill. Statistical thermodynamics of the transition region between two phases. II. one component system with a plane interface. *The Journal of Chemical Physics*, 20(1):141–144, 1952.

[141] Terrell L. Hill. Theory of physical adsorption. In W.G. Frankenburg, V.I. Komarewsky, and E.K. Rideal, editors, *Advances in Catalysis*, volume 4 of *Advances in Catalysis*, pages 211–258. Academic Press, 1952.

[142] Terrell L. Hill. Extension of fowler's treatment of surface tension to physical adsorption. *The Journal of Chemical Physics*, 17(7):668–669, 1949.

[143] Brian K. Peterson, Jeremy P. R. B. Walton, and Keith E. Gubbins. Fluid behaviour in narrow pores. *Journal of the Chemical Society, Faraday Transactions 2*, 82(10):1789, 1986.

[144] Douglas M. Ruthven. Diffusion in zeolites. In Laurent Bonneviot and Serge Kaliaguine, editors, *Zeolites: A Refined Tool for Designing Catalytic Sites*, volume 97 of *Studies in Surface Science and Catalysis*, pages 223–234. Elsevier, 1995. ISSN: 0167-2991.

[145] Jorg Karger and Douglas M. Ruthven. On the comparison between macroscopic and n.m.r. measurements of intracrystalline diffusion in zeolites. *Zeolites*, 9(4):267–281, 1989.

[146] Krzysztof Banas, Federico Brandani, Douglas M. Ruthven, Frank Stallmach, and Jörg Kärger. Combining macroscopic and microscopic diffusion studies in zeolites using NMR techniques. *Magnetic Resonance Imaging*, 23(2):227–232, 2005.

[147] Benoit Coasne. Multiscale adsorption and transport in hierarchical porous materials. *New Journal of Chemistry*, 40:4078–4094, 2016.

[148] Keith E Gubbins, Ying-Chun Liu, and Joshua D Moore. The role of molecular modeling in confined systems: impact and prospects. *Physical Chemistry Chemical Physics*, 13:58–85, 2011.

[149] V. Marry, E. Dubois, N. Malikova, J. Breu, and W. Haussler. Anisotropy of water dynamics in clays: Insights from molecular simulations for experimental QENS analysis. *The Journal of Physical Chemistry C*, 117(29):15106–15115, 2013.

[150] Virginie Marry, Emmanuelle Dubois, Natalie Malikova, Serge Durand-Vidal, Stéphane Longeville, and Josef Breu. Water dynamics in hectorite clays: Infuence of temperature studied by coupling neutron spin echo and molecular dynamics. *Environmental Science & Technology*, 45(7):2850–2855, 2011.

[151] Hervé Jobic and Doros N. Theodorou. Diffusion of long n -alkanes in silicalite. a comparison between neutron scattering experiments and hierarchical simulation results. *The Journal of Physical Chemistry B*, 110(5):1964–1967, 2006.

[152] Jorg Karger and Douglas M Ruthven. Diffusion in nanoporous materials: fundamental principles, insights and challenges. *New Journal of Chemistry*, 40:4027–4048, 2016.

[153] B Coasne, S K Jain, and K E Gubbins. Adsorption, structure and dynamics of fluids in ordered and disordered models of porous carbons. *Molecular Physics*, 104:3491–3499, 2006.

[154] David Turnbull and Morrel H. Cohen. Free-volume model of the amorphous phase: Glass transition. *The Journal of Chemical Physics*, 34(1):120–125, 1961.

[155] Hervé Jobic, Marc Bée, and Gordon J. Kearley. Translational and rotational dynamics of methane in ZSM-5 zeolite: A quasi-elastic neutron scattering study. *Zeolites*, 9(4):312–317, 1989.

[156] Anastasios I. Skoulidas and David S. Sholl. Direct tests of the darken approximation for molecular diffusion in zeolites using equilibrium molecular dynamics. *The Journal of Physical Chemistry B*, 105(16):3151–3154, 2001.

[157] R. Larry June, Alexis T. Bell, and Doros N. Theodorou. Transition-state studies of xenon and sulfur hexafluoride diffusion in silicalite. *The Journal of Physical Chemistry*, 95(22):8866–8878, 1991.

[158] Susan J. Goodbody, Kyoko Watanabe, David MacGowan, Jeremy P. R. B. Walton, and Nicholas Quirke. Molecular simulation of methane and butane in silicalite. *Journal of the Chemical Society, Faraday Transactions*, 87(13):1951, 1991.

[159] Steffen Jost, Nils-Karsten Bär, Siegfried Fritzsche, Reinhold Haberlandt, and Jörg Kärger. Diffusion of a mixture of methane and xenon in silicalite: A molecular dynamics study and pulsed field gradient nuclear magnetic resonance experiments. *The Journal of Physical Chemistry B*, 102(33):6375–6381, 1998.

[160] Farid Rizk, Simon Gelin, Anne-Laure Biance, and Laurent Joly. Microscopic origins of the viscosity of a lennard-jones liquid. *Physical Review Letters*, 129(7):074503, 2022.

[161] Kerstin Falk, Daniele Savio, and Michael Moseler. Nonempirical free volume viscosity model for alkane lubricants under severe pressures. *Physical Review Letters*, 124(10):105501, 2020.

[162] Kerstin Falk, Benoit Coasne, Roland Pellenq, Franz-Josef Ulm, and Lydéric Bocquet. Subcontinuum mass transport of condensed hydrocarbons in nanoporous media. *Nature Communications*, 6(1):6949, 2015.

[163] Amaël Obliger, Roland Pellenq, Franz-Josef Ulm, and Benoit Coasne. Free volume theory of hydrocarbon mixture transport in nanoporous materials. *The Journal of Physical Chemistry Letters*, 7(19):3712–3717, 2016.

[164] Noël Jakse and Alain Pasturel. Molecular-dynamics study of liquid nickel above and below the melting point. *The Journal of Chemical Physics*, 123(24):244512, 2005.

[165] Jürgen Horbach and Walter Kob. Relaxation dynamics of a viscous silica melt: The intermediate scattering functions. *Phys. Rev. E*, 64:041503, Sep 2001.

[166] P. G. De Gennes. Liquid dynamics and inelastic scattering of neutrons. *Physica*, 25(7):825–839, 1959.

[167] B. Ruta, G. Baldi, Y. Chushkin, B. Rufflé, L. Cristofolini, A. Fontana, M. Zanatta, and F. Nazzani. Revealing the fast atomic motion of network glasses. *Nature Communications*, 5(1):3939, 2014.

[168] Adolfo J. Banchio, Jacek Gapinski, Adam Patkowski, Wolfgang Häußler, Andrei Fluerasu, Stefano Sacanna, Peter Holmqvist, Gerhard Meier, M. Paul Lettinga, and Gerhard Nägele. Many-body hydrodynamic interactions in charge-stabilized suspensions. *Physical Review Letters*, 96(13):138303, 2006.

[169] C. Alba-Simionesco, A. Toelle, D. Morineau, B. Farago, and G. Coddens. ”de gennes” narrowing in supercooled molecular liquids : Evidence for center-of-mass dominated slow dynamics, 2001.

[170] Alice L. Thorneywork, Simon K. Schnyder, Dirk G. A. L. Aarts, Jürgen Horbach, Roland Roth, and Roel P. A. Dullens. Structure factors in a two-dimensional binary colloidal hard sphere system. *Molecular Physics*, 116(21):3245–3257, 2018.

[171] P. L. Llewellyn, J. P. Coulomb, Y. Grillet, J. Patarin, H. Lauter, H. Reichert, and J. Rouquerol. Adsorption by MFI-type zeolites examined by isothermal microcalorimetry and neutron diffraction. 1. argon, krypton, and methane. *Langmuir*, 9(7):1846–1851, 1993.

[172] P. L. Llewellyn, J. P. Coulomb, Y. Grillet, J. Patarin, G. Andre, and J. Rouquerol. Adsorption by MFI-type zeolites examined by isothermal microcalorimetry and neutron diffraction. 2. nitrogen and carbon monoxide. *Langmuir*, 9(7):1852–1856, 1993.